



**HAL**  
open science

# Morphology development and rheological properties of reactively compatibilized Polyamide 6 / High Density Polyethylene blends

Chloé Épinat

► **To cite this version:**

Chloé Épinat. Morphology development and rheological properties of reactively compatibilized Polyamide 6 / High Density Polyethylene blends. Material chemistry. Université Claude Bernard - Lyon I, 2014. English. NNT : 2014LYO10317 . tel-01128466

**HAL Id: tel-01128466**

**<https://theses.hal.science/tel-01128466>**

Submitted on 9 Mar 2015

**HAL** is a multi-disciplinary open access archive for the deposit and dissemination of scientific research documents, whether they are published or not. The documents may come from teaching and research institutions in France or abroad, or from public or private research centers.

L'archive ouverte pluridisciplinaire **HAL**, est destinée au dépôt et à la diffusion de documents scientifiques de niveau recherche, publiés ou non, émanant des établissements d'enseignement et de recherche français ou étrangers, des laboratoires publics ou privés.

THÈSE DE L'UNIVERSITÉ DE LYON

Délivrée par

l'Université Claude Bernard Lyon1  
École Doctorale Matériaux

DIPLÔME DE DOCTORAT

(arrêté du 7 août 2006)

Soutenue publiquement le 18 décembre 2014 par

Chloé ÉPINAT

MORPHOLOGY DEVELOPMENT AND  
RHEOLOGICAL PROPERTIES OF REACTIVELY  
COMPATIBILIZED POLYAMIDE 6 / HIGH DENSITY  
POLYETHYLENE BLENDS

Devant la commission d'examen formée de :

Philippe CASSAGNAU	<i>Examineur</i>
Mickaël CASTRO	<i>Examineur</i>
Jean-Charles MAJESTÉ	<i>Rapporteur</i>
Pascal MÉDÉRIC	<i>Rapporteur</i>
Denis C. D. ROUX	<i>Examineur</i>
Paul SOTTA	<i>Directeur de thèse</i>
Lise TROUILLET-FONTI	<i>Correspondant industriel</i>







# REMERCIEMENTS

---

Je remercie tout d'abord Ludovic Odoni, Florence Clément, Jean-Yves Delannoy et Didier Long de m'avoir permis de réaliser ce travail au sein du Laboratoire Polymères et Matériaux avancés, UMR 5268 CNRS/Solvay.

Mes plus profonds remerciements vont à mes encadrants Lise Trouillet-Fonti et Paul Sotta qui ont été d'un soutien considérable durant cette thèse.

Lise, quelle chance d'avoir pu travailler à tes côtés! Ta rigueur scientifique et ta méthodologie de travail m'ont guidées et profondément inspirées. Au-delà de ton professionnalisme, ce sont tes qualités humaines exceptionnelles d'écoute et de compréhension qui ont rendu ces années si épanouissantes.

Paul, j'ai beaucoup apprécié ta disponibilité et ton enthousiasme pour m'aider à apporter la rigueur scientifique théorique nécessaire à l'exploitation de mes résultats expérimentaux. Ta sérénité, ta patience et ta pédagogie ont grandement contribué à la réussite de ce projet de thèse.

D'une implication et d'un investissement constant, vous avez su me donner confiance et me transmettre votre goût pour le travail de recherche. Pour tout cela, je vous suis extrêmement reconnaissante, merci à vous deux.

Je remercie très chaleureusement Jean-Charles Majesté et Pascal Médéric d'avoir accepté d'être rapporteurs de ce travail, ainsi que les membres de mon Jury Philippe Casagneau, Mickaël Castro et Denis Roux. Merci pour l'intérêt que vous avez porté à ce travail.

J'adresse des remerciements particuliers à Didier Long, Stéphane Jéol et Alexandra Argoud. Didier, je te remercie pour tout le temps que tu m'as accordé; grâce à toi, les problèmes théoriques d'interfaces ne m'ont pas déstabilisés. Stéphane, je souhaite te remercier sincèrement pour l'expertise et l'aide précieuse que tu as apporté, entre autre, à la confection de mes matériaux. Enfin Alexandra, un grand merci pour ta disponibilité et tes conseils avisés.

Je suis extrêmement reconnaissante à toutes les personnes du R& I Centre Lyon de Solvay pour la qualité des échanges et l'agréable disponibilité de tous.

Je remercie chaleureusement le laboratoire de Microscopie, Magalie Fontana, Clémence Abadie, Rémy Sellier, Baptiste Gros, Nelly Bulgarely et Pauline Grau pour leur aide minutieuse qui m'a permis d'acquérir toutes ces belles images illustrant ma thèse. Rémy, merci de m'avoir fait partager ta passion pour l'univers fascinant de l'infiniment petit.

Merci à l'équipe transformation, Vincent Curtil et Olivier Chaubet ainsi que l'équipe

Synthèse, Olivier Magnat, Rodolphe Sapey-Triomphe, Julie Saunier et Thierry Badel dirigée par Véronique Bossennec. Mes différents passages au LSPP ont été très enrichissants.

Merci à Léo (le roi de la rhéo!) Georges du laboratoire de rhéologie.

Merci à Nadia Delon-Anik et Virginie Reynes de l'équipe Analyses dirigée par Philippe Menez, et particulièrement Frédéric Leguyader et Laetitia Tribolet pour avoir tenté, jusqu'au bout, de percer les mystères de la réaction de compatibilisation.

Merci à Jean-François Thierry et Christophe Moineau pour les échanges très intéressants que nous avons pu avoir pour mieux comprendre nos polymères.

Je tiens également à remercier Elodie Seignobos et Yannick Martinez de la B.U. Engineering Plastics de Solvay, pour les échanges très stimulants autour du stage d'Amandine Houg.

De manière générale, merci à toutes les personnes qui, par leurs petits gestes tout au long de cette thèse, m'ont facilité la tâche au quotidien : merci à Sandrine Rossi, Christiane Prebet, Sylvie Ghiringhelli, Séverine Dauffer, Olivier Andres, Michel Sorin, Mickaël Vest, Arnaud Bamière, Daniel Duchène, Stéphane Lousteau, Didier Tupinier, Olivier Gilbain...

Je souhaite aussi remercier Olivier Boyron et Manel Taam du laboratoire C2PE de l'ESCPE Lyon pour leur disponibilité et leur rapidité sur des analyses.

Le laboratoire du LPMA, et plus généralement APMD, m'a offert un cadre de travail idéal pendant ces trois années de thèse, j'y ai côtoyé de brillantes personnes qui ont su me guider dans des choix pas toujours faciles et qui ont eu une profonde influence sur mon travail de recherche. Je remercie pour ces raisons, l'ensemble des personnes d'APMD présentes au cours de ma thèse, sans exception.

Je souhaite en particulier remercier tous mes amis thésards et post-doc sans qui l'ambiance de travail n'aurait pas été aussi excellente. Je repense au voyage en Thaïlande, aux pauses thé/biscuits bien méritées, aux discussions sur la terrasse, aux gâteaux du jeudi matin, aux sorties sportives (ou pas), aux bières au Ninkasi, à la galette des rois, aux déjeuners internationaux... Du fond du cœur, merci à vous.

Enfin, je remercie tous ceux sans qui tout serait bancal, ceux qui m'ont rappelé tous les jours la richesse de la vie, ceux qui mériteraient 250 pages de remerciements. Je commencerais par ceux qui sont là depuis longtemps, les Montbrisonnais, les Zoozs... Puis ceux apparus au fil de ces trois années, ceux rencontrés grâce au coup de pouce d'un Ar(d)êchois, les Jongleurs, les Montagnards, les Musiciens, les Théâtres, les Crocheteuses, les Artistes en tout genre... Et puis mon penseur, mon éternel rêveur du quotidien; tu m'as permis de percoler à travers ce chemin sinueux et de dévaler des pentes raides, sans peur, comme sur un tapis de poudreuse, douce et onctueuse.

Enfin je ne remercierai jamais assez ma Famille, mes Parents, Marie, Arthur, mes Grands-Pères, mes Grands-Mères, Sandrine et Olivier pour leur infini soutien.

Un immense merci à tous !

# CONTENTS

---

<b>Contents</b>	<b>vii</b>
<b>Introduction</b>	<b>1</b>
<b>Notation</b>	<b>3</b>
<b>1 State of the art</b>	<b>7</b>
1 Thermodynamics of polymer blends . . . . .	8
2 Mechanisms of morphology development in immiscible polymer blends .	11
2.1 Drop break-up mechanisms . . . . .	11
2.2 Coalescence mechanisms . . . . .	16
2.3 Combination of breakup and coalescence . . . . .	19
2.4 Developed morphologies: drop break-up vs. coalescence . . . . .	20
3 Compatibilization of immiscible polymer blends . . . . .	22
3.1 Different compatibilization possibilities . . . . .	22
3.2 Effect of the compatibilization on the morphology development . .	22
3.3 Conclusions on morphology development . . . . .	24
4 Block copolymers . . . . .	25
4.1 Generality on bloc copolymers . . . . .	25
4.2 Incorporation of A and/or B homopolymers into AB bloc copolymers	31
5 Control of the interfacial compatibilization reaction . . . . .	36
5.1 Theoretical approach . . . . .	36
5.2 Diffusion controlled kinetic . . . . .	36
5.3 Reaction controlled kinetics . . . . .	37
5.4 Effect of the copolymer architecture on the chemical reaction . . . .	37
5.5 Interfacial reactivity: summary . . . . .	39
6 Effects of the compatibilization reaction on the morphology development of polymer blends: interfacial roughening and nanodispersions creation .	41
6.1 Interfacial roughening in static conditions . . . . .	41
6.2 Interfacial roughening under shear . . . . .	49
7 Conclusion . . . . .	54
<b>2 Materials and experimental methods</b>	<b>57</b>
1 Introduction . . . . .	57
2 Materials . . . . .	58
2.1 Compatibilization reaction . . . . .	58
2.2 Characteristics of neats polyolefin: HDPE and MA-g-HDPE . . . . .	58
2.3 Polyamide 6 . . . . .	60

3	Experimental . . . . .	64
3.1	Blending Process . . . . .	64
3.2	Morphology characterization . . . . .	64
3.3	Rheological characterization . . . . .	68
3.4	Static annealing of sandwiches . . . . .	70
4	Raw materials stability during process and characterization . . . . .	72
4.1	Stability of polyethylenes . . . . .	72
4.2	Stability of polyamide 6 . . . . .	74
5	Rheological characterization of raw materials . . . . .	77
5.1	Rheological behaviour of polyamide 6 . . . . .	77
5.2	Rheological behaviour of HDPEs . . . . .	79
6	Conclusion . . . . .	82
<b>3</b>	<b>Compatibilization reaction in static conditions</b>	<b>85</b>
1	Article: Nucleation and growth of ordered copolymer structures at reactive interfaces between PA6 and MA-g-HDPE . . . . .	86
2	Discussion, modelling and analysis . . . . .	93
2.1	Interface between two immiscible polymers . . . . .	93
2.2	Equilibrium of copolymer brush at a planar interface: Isolated brush ("Dry brush") [1, 2] . . . . .	94
2.3	Non symmetrical case, curvature effects . . . . .	96
2.4	Case of PA/PE graft copolymers . . . . .	100
2.5	Perspectives: Linear analysis of instabilities . . . . .	106
3	Conclusions . . . . .	107
<b>4</b>	<b>Morphologies</b>	<b>109</b>
1	Studied formulations . . . . .	110
2	Uncompatibilized blends: Results and discussions . . . . .	113
2.1	Blends with PA6-18k . . . . .	115
2.2	Blends with PA6-3k . . . . .	119
2.3	Blends with PA6-31k . . . . .	126
3	Effect of the compatibilization: Results and discussions . . . . .	132
3.1	Conversion rate of the compatibilization reaction . . . . .	136
3.2	Blends with PA6-18k . . . . .	142
3.3	Blends with PA6-3k . . . . .	149
3.4	Blends with PA6-31k . . . . .	156
3.5	Comparison with the static reaction . . . . .	163
4	General conclusion on morphology development in all the studied systems	175
<b>5</b>	<b>Rheological behaviour in the linear regime</b>	<b>181</b>
1	Models for the rheology of non miscible blends . . . . .	182
1.1	Linear rheological behaviour of a pure polymer . . . . .	182
1.2	Gel-like behaviour . . . . .	183
1.3	Dependence of the rheological behavior of polymer blends on the frequency . . . . .	183
1.4	Modeling the contribution of the elastic response of the interfaces: Paliarne's model . . . . .	185
1.5	Dependence of the rheological behaviour of polymer blends on the composition . . . . .	188

## CONTENTS

---

1.6	Analysis of models to predict viscosity evolution as a function of blend composition . . . . .	190
1.7	Objectives of the chapter . . . . .	195
2	Preliminary remarks . . . . .	197
3	Uncompatibilized blends . . . . .	201
3.1	Evolution of the viscosity with the composition . . . . .	201
3.2	Linear viscoelastic behaviour as a function of the frequency . . . . .	203
3.3	Conclusions . . . . .	215
4	Compatibilized blend . . . . .	217
4.1	Evolution of the viscosity with the concentration . . . . .	217
4.2	Linear viscoelastic behaviour of compatibilized blends as a function of the frequency . . . . .	219
4.3	Hypothesis on rheological mechanisms . . . . .	229
5	Prediction of phase inversion . . . . .	233
5.1	Literature on the prediction of phase inversion composition . . . . .	233
5.2	Modified Krieger and Dougherty model for the prediction of blend morphology: phase inversion composition . . . . .	235
5.3	Application to compatibilized and uncompatibilized blends of this study . . . . .	237
6	Conclusion . . . . .	240
	<b>Conclusion</b>	<b>243</b>
	<b>Bibliography</b>	<b>247</b>
	<b>Appendix</b>	<b>259</b>
1	APPENDIX: Linear viscoelastic behaviour of blend components . . . . .	259
2	APPENDIX: Properties of PA6-10k (chap 3) . . . . .	261
3	APPENDIX: Consistency with force measurement on process tool during compounding . . . . .	262
	<b>Résumé en français</b>	<b>265</b>

---



# INTRODUCTION

---

In the past decades, polymers have been widely used to replace metal, wood, ceramics and others materials because of their good processability, properties and low density. Nevertheless, one single polymer cannot always achieve all the properties required for an industrial application, and designing new polymers becomes more and more difficult. Blending polymers is a privileged route for obtaining new polymer materials with enhanced properties. Nevertheless, most often, polymers with sufficiently long chains are immiscible, which leads, after blending, to phase-separated morphologies, poor adhesion between phases and poor final properties. Compatibilization is thus necessary. Reactive compatibilization in which a copolymer is created directly at the interface between both polymers via an in-situ chemical reaction during blending is often used in industry. Indeed, it is well suitable with processes, like extrusion, and allows a one step process. In this study, we chose to study model binary blends of *Polyamide 6/ Maleic Anhydride grafted HDPE (MA-g-HDPE)* in which amine end-groups of PA6 chains react with MA moieties of MA-g-HDPE to form graft-copolymers at the interface during reactive extrusion.

For industrial matters, it is of great interest to be able to predict and control the blend's morphology development during reactive compatibilization in the extruder. Indeed, the final morphology will play a key role on the final properties of the blend. Moreover, the rheological properties of the blends under shear are very important for the processability (blow-moulding...) and depends strongly on the morphology. Improving the knowledge on the relationships between formulation, morphology and rheology could lead to future improvements in both product formulation and process characteristics.

In reactively compatibilized PA6/HDPE blends, different micrometer scale morphologies can be developed during reactive extrusion process following the rheological rules of drop break-up and coalescence: dispersed, stretched dispersed, fibrillar and co-continuous. In addition, recent studies have shown that nano-inclusions of both PE in PA and PA in PE phases, which were attributed to the compatibilization reaction, can be formed in addition to the micron-scale morphology. However, the levers that control the formation of these nano-dispersions (which favour or eliminate the formation) are not yet identified. Similarly, the influence on these nanodispersions on blend properties is not or very poorly described.

The main objective of this study is to be able to understand the levers that control the morphology development and make the link between *formulation, morphology and rheological properties* of reactively compatibilized blends.

The first chapter of this thesis is dedicated to a literature review. First of all, mechanisms of morphology development in reactively compatibilized blends are studied. A focus on bloc copolymers thermodynamical characteristics was also necessary to understand the properties of the copolymer layer created at the interface in reactively compatibilized blends. Then, parameters that control the chemical reaction of compatibilization at the interface during reactive extrusion are presented. Finally, a review of the studies that report the spontaneous formation of morphologies, or nanodispersions due to chemical reaction, is proposed. Thanks to the literature review, several aspects seem to be not fully described yet: this defines more precisely the objectives of the PhD.

Materials of the study were chosen in order to vary in a broad range: the viscosity ratio between the dispersed and the matrix phase (from 0.002 to 540), the architecture of the graft copolymer created by chemical reaction at the interface in case of reactively compatibilized blends and the composition (over the entire composition range of binary PA/PE blends). For that three polyamide 6 of controlled molecular weight were synthesised and two commercial polyolefins were used. Then, compounding conditions and analytical techniques are presented in chapter two.

The first part of the experimental work of this thesis was guided by one question: *how to discriminate the effects due to shearing (drop break-up and coalescence) and due to the compatibilization reaction on the morphology development in reactively compatibilized blends?* Chapter three and four are dedicated to the resolution of this problematic.

In chapter three, the compatibilization reaction in static conditions is studied. We discuss the phenomena of interfacial destabilisation and nucleation and growth of ordered copolymer structures at the interface. Thanks to this study, effects of the reactive compatibilization alone are studied.

The first part of chapter four deals with the study of the morphological development in uncompatibilized binary PA6/HDPE blends. It allows to identify the morphology obtained with only mechanisms of drop break-up and coalescence due to shearing at different viscosity ratios. Finally, morphologies of reactively compatibilized PA6/MA-g-HDPE binary blend, that combine effects of shearing and compatibilization reaction, are analysed with respect to results of chapter three and four. The formation of nanodispersions in one or both phases are discussed. Thus, main parameters that control the morphology development in reactively compatibilized blends are highlighted.

In the last chapter, the linear viscoelastic behaviour of both uncompatibilized and compatibilized blends are studied. The observed relaxation mechanisms are discussed, and in particular those related to interfaces and to interactions between nodules related blends morphologies. Finally, we propose an efficient model to predict the phase inversion composition for both uncompatibilized and compatibilized blends even with viscosity ratio very far from one.

# NOTATION

---

PA6	Polyamide 6
PA6-3k	Polyamide 6, Exhibiting a number average molecular weight $M_n$ of about 3000 g/mol
PA6-18k	Polyamide 6, $M_n \simeq 18000$ g/mol
PA6-31k	Polyamide 6, $M_n \simeq 31000$ g/mol
HDPE	High Density Polyethylene
MA-g-HDPE	Maleic Anhydride grafted High Density Polyethylene
MA	Maleic Anhydride moieties
EG	End-groups
[NH <sub>2</sub> ] = AEG	Amine moieties: Amine End Group of polyamide 6
[COOH] = CEG	Carboxylic End Group of polyamide 6
BEG	Blocker End Group
SEM	Scanning Electron Microscopy
TEM	Transmission Electron Microscopy
TGA	ThermoGravimetric Analysis
SEC	Size Exclusion Chromatography
IR	Infra-Red
$M_n$	Number average molecular weight
$M_w$	Weight average molecular weight
$I_p$	Polydispersity index
$\Gamma$	Interfacial tension
$\phi$	Volume fraction
$\phi_d$	Volume fraction of the dispersed phase
$R$	Average droplet radius
$\rho$	Density
$\eta$	Viscosity
$\eta_i^*$	Complex viscosity, index $i$ can be $m$ for the viscosity of the matrix phase and $d$ for the dispersed phase.
$R_v$	Viscosity ratio $R_v = \eta_d^*/\eta_m^*$

---

$G^*$	Dynamic modulus
$G'$	Elastic modulus
$G''$	Loss modulus
$\omega$	Frequency
$\dot{\gamma}$	Shear rate
$\phi_m$	Maximum close packing
$Ca$	Capillary number
$\chi$	Flory parameter
$\Sigma$	Average interface area per chain

### Nomenclature specific to chapter 1

$\Delta G_m$	Free energy of mixing
$N$	polymerization degree
$\epsilon_{AB}$	Interaction energies
$P_i$	Polarizabilities
$n_A$	monomer unit number
$\tau = \dot{\gamma}/\eta_m$	shear stress
$F$	Driving force for drainage
AFM	Atomic Force Microscopy
DMA	Dynamical Mechanical Analysis
NMR	Nuclear Magnetic Resonance
ODT	Order Disorder transition
SSL	Strong Segregation Limit
PS	Polystyrene
PI	Polyisoprene
PEO	Polyoxyethylene
PBO	Polyoxybutylene
PMMA	PolyMethylMethacrylate
MA= Anh	Maleic anhydride

---

### Nomenclature specific to chapter 3

$k_B$	Boltzmann constant ( $1.38065 \cdot 10^{-23} \text{J} \cdot \text{mol}^{-1} \cdot \text{K}^{-1}$ )
$T$	Temperature
$g$	number of statistical segments
$\xi$	Interfacial thickness
$a$	size of a monomer
$\Gamma_0$	Interfacial tension for an interface free of copolymers
$\gamma_0$	Dimensionless surface tension
$S$	Interfacial area
$\Sigma$	Average interfacial area per chain
$F_{chain}$	Free energy per chain
$N$	Number of statistical segments
$a^3$	monomer volume
$L$	Bloc stretching length
$C$	interfacial curvature
$c$	reduced curvature = inverse of the radius of curvature in unit of monomer size
$R$	Radius of curvature
$p$	number of grafted arms
$f_{brush}$	Free energy of the copolymer brush
$\sigma$	average surface per chain in unit of the surface occupied by one segment
$V_{PA \text{ or } PE}$	Average molar volume
$D$	Equilibrium thickness of copolymer brush



---

This literature review summarizes the helpful elements in the determination of dominant the parameters that govern the morphology development of reactively compatibilized polymer blends, and particularly, nanodispersions. After an introduction to polymer blends basic generalities, mechanisms of morphology formation in immiscible polymer blends, drop break-up and coalescence, are detailed. Then, usual descriptions of the reactive compatibilization effects on these mechanisms are given. A focus on bloc copolymers thermodynamical characteristics was also necessary to understand the properties of the copolymer layer created at interfaces in reactively compatibilized blends. Then, parameters that control the compatibilization reaction kinetics at the interface during reactive extrusion are presented. A review of the studies that report the spontaneous formation of morphologies, or nanodispersions, is proposed. Finally, according to this literature review, the objectives of the present PhD work are presented.

## 1 Thermodynamics of polymer blends

The basic thermodynamic description of the behavior of a mixture of molten polymers was proposed in 1941 by Flory and Huggins. This theory, which is an extension of the theory of regular solutions of simple liquids, is based on three assumptions: (1) Volume does not change during mixing ( $V = v_0$ ), (2) only translational entropy of the chains is considered, and (3) chain conformations in the mixture are the same as in the pure polymer. Some studies have shown that corrections could be made to the theory if these assumptions were not taken into account, especially (3) and (1) [3, 4]. Figure 1.1 schematically shows a polymer mixture according to the Flory-Huggins theory:

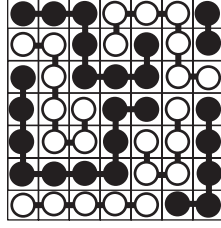


Figure 1.1: Polymer blends according to the Flory-Huggins theory.

For a blend of two polymers exhibiting degrees of polymerisation  $N_A$  and  $N_B$ , the free energy of mixing per site  $\Delta G_m$  is (in  $k_B T$  unit):

$$\frac{\Delta G_m}{k_B T} = \frac{\phi_A}{N_A} \ln \phi_A + \frac{\phi_B}{N_B} \ln \phi_B + \chi_{AB} \phi_A \phi_B \quad (1.1)$$

With  $\phi_i$  the volume fraction of the polymer consisting of units of type  $i$  ( $i = A$  or  $B$ ).

The Flory  $\chi_{AB}$  parameter represents the excess energy per monomer (in  $k_B T$  unit) in the mixture of two polymers A and B. It is defined by the variation of energy per site  $\Delta\epsilon$ , when contacting A and B from pure monomers such as:

$$\chi_{AB} \approx \frac{1}{k_B T} \left[ \epsilon_{AB} - \frac{\epsilon_{AA} + \epsilon_{BB}}{2} \right] \quad (1.2)$$

With  $\epsilon_{AB}, \epsilon_{AA}, \epsilon_{BB}$  the interaction energies associated with the contact of the corresponding monomers.

In the general case (non-polar polymers), molecules interact through van der Waals forces. The attractive interaction energy  $\epsilon_{AB}$  between two sites then depends on the polarizabilities  $P_A$  and  $P_B$  of molecules A and B as  $\epsilon_{AB} = -\kappa P_A P_B$  with  $\kappa$  a positive constant. Therefore, we have  $\chi_{AB} \propto (P_A - P_B)^2 > 0$ : the resulting interaction associated with Van der Waals interactions is repulsive and tends to oppose to the mixture. Contact between A and B is always an excess of energy compared to AA or BB contacts.

In equation 1.1, the first two terms represent the entropy of mixing  $\Delta S_m = k_B \ln \Omega$ ,  $\Omega$  is the number of ways of distributing  $n_A = N\phi_A/N_A$  chains of polymer A (resp. B) on  $N = n_A N_A + n_B N_B$  sites. The last term corresponds to the enthalpic contribution of the mixture, that is to say the energy change that occurs when A and B are brought into contact. For a mixture of large molecules,  $N_A \approx N_B \gg 1$ , the entropy term becomes small

## 1. Thermodynamics of polymer blends

compared to the enthalpy term. Flory parameter thus takes a real importance.

To analyze the stability of a A/B mixture, the change in the free energy of mixing  $\Delta G_m$  (equation 1.1) as a function of the volume fraction of one component of the mixture for various values of  $\chi$  has to be considered. Thus, if we consider the symmetric case where  $N_A = N_B$  :

- Below a certain critical value of  $\chi_{AB}$  ( $< \chi_C$ ) the mixture is stable and there is no phase separation.
- Above this critical value of  $\chi_{AB}$  ( $> \chi_C$ ) the free energy of mixing  $\Delta G_m$  has two minima depending on the composition of the mixture. These minima correspond to volume fractions  $\phi_1$  and  $\phi_2$ .

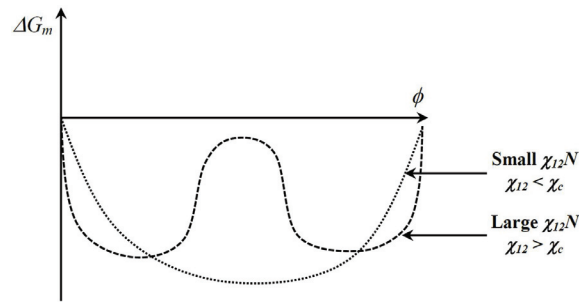


Figure 1.2: Free energy of mixing as a function of the blend composition for small and large values of  $\chi$ .

The stability of a polymer blend depends on the curvature of the  $\Delta G_m$  function, as follows:

- $\frac{\delta^2 \Delta G_m}{\delta \phi^2} > 0$ , the curve is concave (positive curvature): a local concentration fluctuation increases the free energy, and the mixture is stable or metastable.
- $\frac{\delta^2 \Delta G_m}{\delta \phi^2} < 0$ , the curve is convex (negative curvature): a local concentration fluctuation decreases the free energy and thus will grow. The mixture is unstable and separates into two phases.

Since the  $\Delta G_m$  curve has two minima (for  $\chi_{AB} > \chi_C$ ) at compositions  $\phi_1$  and  $\phi_2$ , there exist two inflection points between the positive and negative curvatures at the compositions  $\phi_{S1}$  and  $\phi_{S2}$ , as shown in figure 1.3.

The positions of  $\phi_1$  and  $\phi_2$  as a function of  $\Delta G_m$  (for a given  $\chi N$  or  $T$ ) defines the so called **binodal decomposition curve**. Thus, when  $\phi_1 < \phi < \phi_2$ , the mixture separates into two phases. The inflection points delimit **the spinodal curve**. It is now possible to construct the phase diagram of blend stability: " $\chi N$  as a function of  $\phi$ ". Similarly, knowing that  $\chi N \propto 1/T$  (with  $T$  in Kelvin) for non polar monomers with polarizabilities independent of  $T$ , we can establish the phase diagram  $T$  as a function of  $\phi$  as shown in figure 1.4. All the points inside the spinodal curve represent unstable states where any concentration fluctuation leads to phase separation, called **spinodal decomposition**. All the points located between the spinodal curve and the binodal curve are in a metastable

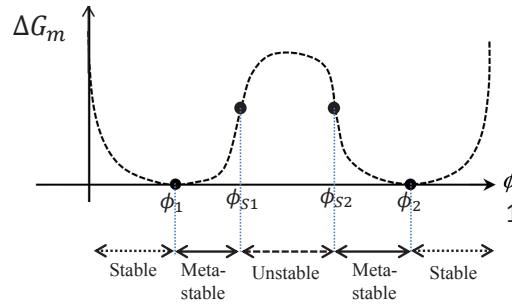


Figure 1.3: Characteristic points and stability domains of  $\Delta G_m$  as a function of composition.

state, phase separation happens by a mechanism of nucleation and growth. Points located outside of the binodal curve are in a stable state. The spinodal curve and the binodal curve are respectively described by the equations:

$$\chi N = \frac{2}{2\phi(1-\phi)} \quad \text{and} \quad \chi N = \frac{2}{2\phi-1} \ln \frac{\phi}{1-\phi} \quad (1.3)$$

The coordinates of the critical point C are:

$$\phi = \frac{1}{2} \quad \text{and} \quad \chi N = 2 \quad (1.4)$$

If  $N_1 \neq N_2$  the decomposition curves have a similar shape but will not be symmetrical.

In general, polymer blends can present an Upper Critical Solution Temperature (UCST) (as described above) and a Lower Critical Solution Temperature (LCST). More complex diagrams are also possible [4]. Figure 1.4 shows a schematic phase diagram of the temperature  $T$  as a function of blend composition for polymer blends [5]. Only UCST is described by the Flory theory [6].

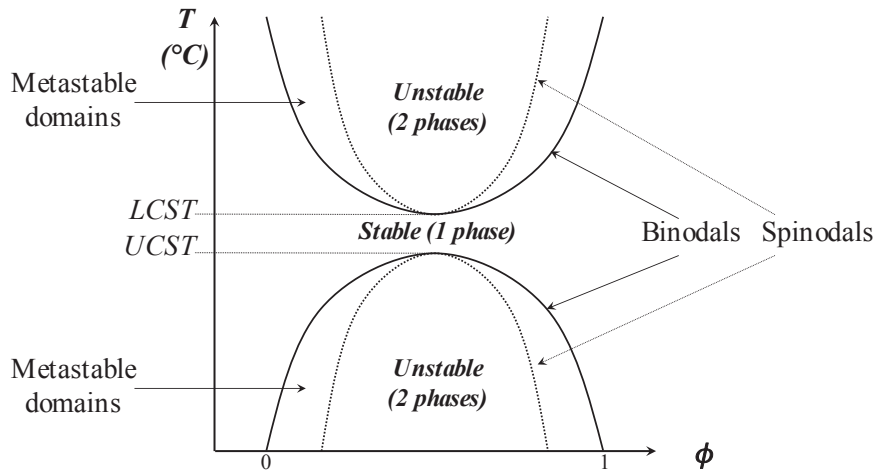


Figure 1.4: Schematic phase diagram of temperature  $T$  as a function of the polymer blend composition.

## 2 Mechanisms of morphology development in immiscible polymer blends

In most applicative cases, polymer blends are prepared by melt-shearing, generally by extrusion. At the end of the blending process, the morphology of the blend, which is generally not in an equilibrium state, is cooled down and frozen to a solid state. This morphology depends not only on the composition of the blend but also on the chemical and physical characteristics of the polymer phases (molecular weight, viscosity, reactivity of the chemical moieties in the case of reactively compatibilized blends...) and strongly on process conditions such as time of mixing, temperature and shear rate imposed in the extruder.

This part of the chapter is largely inspired by the chapter 3 of the book "Mixing and compounding of polymers Theory and Practice" (2009) by H.E.M. Meijer, J.M. Janssen and P.D. Anderson of reference [7].

### 2.1 Drop break-up mechanisms

The blending processes of polymers are theoretically very complicated to study because many uncontrolled parameters have to be considered. This is why the majority of theoretical studies deal with ideal systems of newtonian liquid mixtures: study of Newtonian droplets in a Newtonian matrix under well known conditions of shear and temperature.

Considering a drop of polymer A inbedded in B matrix in a simple shear field, the drop will deform and increase its interfacial area due to viscous forces, this increase has an energetic cost due to the surface tension: the drop will tend to recover its spherical shape to minimize the surface / volume ratio. The deformation is then dependent on the shear stress  $\tau$  exerted on the drop, which will be counteracted by the interfacial stress  $\Gamma/R$  due to the increased surface area of the drop ( $\Gamma$  is the interfacial tension and  $R$  the local radius of curvature). The ratio between these two stresses is called the capillary number  $Ca$ :

$$Ca = \frac{\tau R}{\Gamma} \quad (1.5)$$

with:

- $\tau$  is the shear stress exerted by the matrix on the drop:  $\tau = \dot{\gamma}\eta_m$  with  $\dot{\gamma}$  the shear rate in  $s^{-1}$  and  $\eta_m$  the viscosity of the matrix in Pa.s.
- $\Gamma$  is the interfacial tension in N/m.
- The radius of curvature  $R$  of the drop.

Taylor (1934) [8] was the first to study the critical conditions for the drop break-up in a viscous liquid. Drop break-up occurs when the two competitive stresses ( $\tau$  and  $\Gamma/R$ ) are of the same order of magnitude: the critical capillary number  $Ca_{crit}$  is of the order of unity. There are several possible scenarios with respect to  $Ca_{crit}$ :

- If  $Ca \gg Ca_{crit}$ , the viscous shear stresses predominate over the interfacial stresses. The drops are elongated with the matrix but no interfacial corrugation develop at the interface drop / matrix leading to the drop break-up. This is a DISTRIBUTIVE MIXING.
- $Ca \in [Ca_{crit}, 2Ca_{crit}]$ . When shear forces dominate over the interfacial tension (higher  $Ca$ ), drops are stretched into long filaments until the local radius decreases so that

interfacial tension becomes active ( $Ca \approx Ca_{crit}$ ). There is competition between shear and interfacial stresses and instabilities of the interface lead to the rupture into finer droplets. This is a DISPERSIVE MIXING.

- If  $Ca \ll Ca_{crit}$ , the interfacial stresses predominate over shear and drops will deform slightly but will not break.

Taylor modeled the size of those droplets by introducing, in addition to the capillary number, a rheological parameter expressing the ratio of the viscosity of the dispersed phase  $\eta_d$  on the viscosity of the matrix phase  $\eta_m$ : the viscosity ratio  $R_v$ .

$$R_v = \frac{\eta_d}{\eta_m} \quad (1.6)$$

In reality both dispersive and distributive processes take place simultaneously in a real blend. These two mechanisms are explained below.

*Under shear*, the critical capillary number strongly depends on the viscosity ratio  $R_v$  and  $Ca_{crit}$  reaches a minimum for  $R_v \approx 1$ . Grace [9] measured this dependency in both simple shear and planar elongational flow as shown in figure 1.5. The minimum of the curve shows that it is easier to disperse system when its viscosity ratio is between 0.1 and 1. Viscosity ratio of 4 appears to be the upper limit until which it is possible to break a drop under shear. At higher viscosity ratio, the drop rotates under shear but no longer deforms. *This curves shows that a fluid droplet in a viscous matrix can be elongated by shear and thus broken down to small sizes. Conversely, a fluid matrix cannot deform viscous droplets under shear.* In the case of an *extensional flow* figure 1.5, the capillary number  $Ca$  is only very slightly affected by the viscosity ratio, thus, drop break up can occur whatever the viscosity ratios.

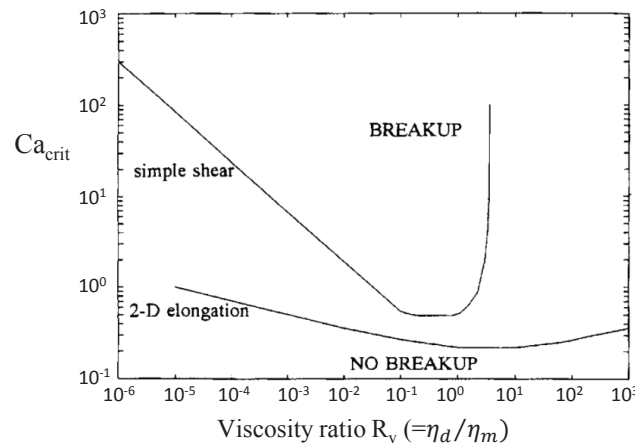


Figure 1.5: Evolution of the critical capillary number  $Ca_{crit}$  as a function of viscosity ratio ( $R_v = \eta_{dispersion}/\eta_{matrix}$ ) in simple shear and 2D (plane) elongation flow [10].

### 2.1.1 Distributive Mixing $Ca \gg Ca_{crit}$ :

The initial morphology is macroscopic drops having the size of one polymer pellet before melting ( $\approx 1\text{mm}$  diameter) in a continuous matrix made of the component which

melts first. Thus, for immiscible polymers it is possible to estimate the value of the initial capillary number:

$$\left. \begin{aligned} \tau = \eta_m \dot{\gamma} = 10^2 \times 10^2 &= 10^4 \text{Pa} \\ \Gamma/R = 10^{-2}/10^{-3} &= 10 \text{Pa} \end{aligned} \right\} Ca = \frac{\eta_m \dot{\gamma} R}{\Gamma} = 10^3 \quad (1.7)$$

With:

- $\tau$  is the shear stress applied to the drop (Pa).
- $\eta_m$  the viscosity of the matrix phase (Pa.s).
- $\dot{\gamma}$  the shear rate ( $s^{-1}$ )
- $\Gamma$  the interfacial tension (N/m) estimated for totally immiscible polymers to  $10^{-2}$ N/m.
- $R$  the radius of curvature of the droplet (m).

If we consider a Newtonian fluid for which  $Ca_{crit} \approx 1$  (thus the viscosity ratio between the nodule and the matrix  $R_v$  is close to 1), we then have a situation where  $Ca \gg Ca_{crit}$ . The shear stress thus dominates the interfacial stresses and the drop deforms with the matrix. Initial nodular drops will then elongate in the early stages of mixing to form ellipsoids and then filaments as shown in figure 1.6.

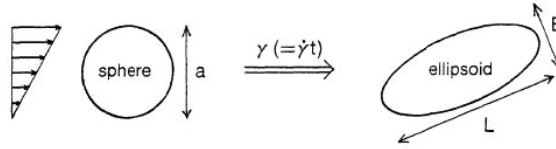


Figure 1.6: Affine deformation of a liquid drop in a simple shear flow.

If the viscosity ratio is different from one, the shape and the extent of the deformed filament can be different from the ideal case studied previously where  $R_v = 1$  [11, 12]:

- For  $R_v > 1$  the deformed drop has rounded ends.
- For  $R_v < 1$  the deformed droplet has pointed ends.

Figure 1.8 in next paragraph show an example of the situations which may occur.

### 2.1.2 Dispersive mixing $Ca \approx Ca_{crit}$ :

Once the drops (millimeter size) are stretched into long and thin filaments, the local radius decreases and the interfacial tension begins to play a role in the capillary number. The global mechanism of thread break-up during stretching is called the transient mechanism. When the local radius of curvature  $R$  of the filament decreases down to  $1 \mu\text{m}$ , the shear stresses begin to be of the same order of magnitude as the interfacial tension. Then:

$$\left. \begin{aligned} \tau = \eta_m \dot{\gamma} = 10^2 \times 10^2 &= 10^4 \text{Pa} \\ \Gamma/R = 10^{-2}/10^{-6} &= 10^4 \text{Pa} \end{aligned} \right\} Ca = \frac{\eta_m \dot{\gamma} R}{\Gamma} = 1 \quad (1.8)$$

Drop break-up and final drop size distribution are then determined by a mechanism: **the capillary wave instability mechanism called the Rayleigh mechanism** described by Taylor (1932) and then by Grace(1971): The filament is elongated, then capillary waves

develop at the interface and thread is gradually cut in a line of "daughter" droplets. Break-up by this mechanisms, which lead to droplets of the same size have been observed in general when the viscosity ratio between the thread and matrix around was close to 1, i.e.  $R_v = 1$ . An example of the Rayleigh mechanism is shown in figure 1.7 which shows a filament of polyamide 6 in a matrix of polystyrene deforming gradually, first forming waves at the interface (Rayleigh disturbance) to finally break into smaller droplets [13]. Between the formed drops, small satellites can be formed. The disturbance development depend on the difference of viscosity between the thread and the fluid around: The smaller the viscosity ratio, the faster the wave develop. Meijer et al. showed that for  $R_v > 1$  more time is needed to develop a disturbance and more extension takes place.

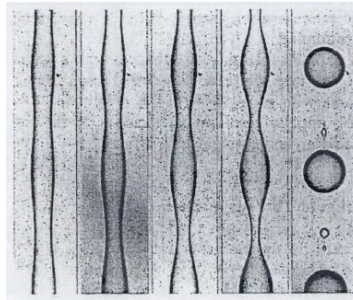


Figure 1.7: Sinusoidal deformation of a Polyamide 6 thread (diameter  $55 \mu\text{m}$ ) in a quiescent PS matrix. Measures performed at  $230 \text{ }^\circ\text{C}$  (left to right) 0, 15, 30, 45 and 60s [13].

An other mechanism has been described in the literature: the break-up mechanism by "**end-pinching**" [7]. Stone et al have widely studied this phenomenon [11, 12]. In this mechanism, two relatively big droplets break off from the extremities of a finite filament. After that, and depending on the viscosity ratio, the "neck" or "intermediately long thread" either continues to break-up or relaxes in shape, which can lead to polydisperse droplet sizes. This mechanism happens when the viscosity ratio is different from one and especially when  $R_v < 1$ . Tjahjadi et al. [14] have shown that, for low viscosity ratios, satellite drops are almost always generated between larger droplets that have been pinched-off. Figure 1.8 shows experiments performed by Stone et al. [11] showing the deformation of a drop under a flow (Simple shear flow correspond to  $\alpha = 0$  and hyperbolic (elongational) flow to  $\alpha = 1$ ) under shear rates between  $0.135 \text{ s}^{-1}$   $0.260 \text{ s}^{-1}$  for different viscosity ratios  $\lambda < 1$ : one can observe the end-pinching of droplets as well as the sharps tips (pointed ends) formed on the elongated threads. The pointed end of the droplet or thread is also responsible of "tip-streaming" which may releases small satellites. This phenomenon is much more discussed and observed for drops with compatibilizers at the interface.

A third mechanism, **the stepwise equilibrium mechanism**, is often used to determine the minimum diameter  $D_{min}$  attainable for a droplet. This mechanism considers that each droplet will be divided into two droplets with equal sizes under shear flow without passing through the stretching step, and this process takes place until droplets become too small to be deformed. In real mixing process this mechanism is very unlikely to happen but it predicts quite realistic sizes. The minimum radius accessible in simple shear stresses depends on the interfacial tension  $\Gamma$ , the estimated maximum deformation  $\dot{\gamma}$  and the critical capillary number  $Ca_{crit}$ . Thus, assuming the droplet to separate into two equal droplets through the stepwise dispersion route, the minimum droplet size is:

$$R_{min} = 2^{-1/2} \frac{Ca_{crit}}{\eta_m \dot{\gamma} / \Gamma} \quad (1.9)$$

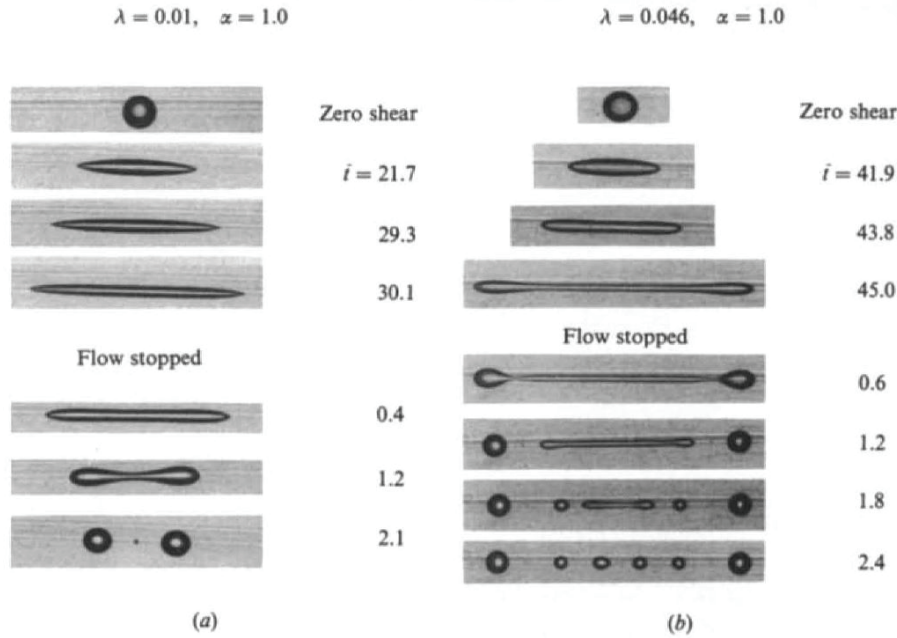


Figure 1.8: Example of deformation of a drop under a flow  $\alpha$  (Simple shear flow corresponds to  $\alpha = 0$  and hyperbolic flow to  $\alpha = 1$ ) under shear rates between  $0.135 \text{ s}^{-1}$   $0.260 \text{ s}^{-1}$  for different viscosity ratio  $\lambda < 1$ . In figure (a) the deformed droplets has very sharp tips and break-up by end-pinching leaving small satellites between drops. In figure (b) the "end-pinching" mechanism is observed and creates droplets of different sizes. [11].

### 2.1.3 Application to viscoelastic systems

In the case of polymer blends, materials are not Newtonians but viscoelastic. Although very similar with the Newtonian fluids in some respect, the evolution of dispersed phase size in polymer blends show some deviations from the Taylor's model which does not take into account polymer viscoelasticity. Indeed, in these systems the shape of the droplet is not only determined by the viscous forces, but also by the pressure distribution around the droplet that originates from the elasticity of the matrix. For the moment, there is no consensus on a theory that can describe the deformability and break-up of viscoelastic drops in viscoelastic matrix. For the viscoelasticity of both the drop and the matrix, it is generally assumed that [15, 10].

- viscoelasticity of both the drop and the matrix phase, retards deformation and breakup.
- when the viscosity ratio is of order of unity the capillary number for break-up ( $Ca_{crit}$ ) is roughly the same as the one for Newtonian drops: viscoelastic effects are not observed [7].
- a higher  $Ca_{crit}$  is observed to break the droplets. This means that for the same shear rate  $\dot{\gamma}$  between viscoelastic than in newtonian blends, bigger dispersions are formed.

- significant deformation and break-up have been observed at higher viscosity ratio values than a value of 4 [7].

Van Puyvelde and Moldenaers (2005) [16] made a review which summarizes the current knowledge on morphology development of viscoelastic blends depending on the viscosity ratio based on Grace's curve:

- When  $R_v=1$  the Regular Rayleigh mechanism leading to droplets of the same size can happen, numerous example are available in the literature.
- When  $R_v < 1$  the mechanisms of morphology development are much less studied. From the study of Newtonian droplets into Newtonian matrix, it appears that end-pinching mechanisms and formation of satellites are likely to happen. Pointed end threads are formed thus tip streaming can also happen.
- When  $R_v > 1$  the mechanisms of morphology development are also much less studied. The upper limit of viscosity ratio for which break-up happen in case of viscoelastic droplets is still discussed.

## 2.2 Coalescence mechanisms

Coalescence is a phenomenon of recombination of two or more drops dispersed in a matrix, increasing the size of morphologies. This phenomenon happens mainly in concentrated blends but can even occur when the concentration of the dispersed phase is quite low [7, 16]. This process comes into competition with the drop break-up mechanism. It can occur in several conditions [17]:

- **In quiescent condition:** In static annealing, two drops will tend to approach themselves with forces such as Van der Waals forces, the Brownian motion or gravity.
- **Under the influence of shear flow:** During the mixing process drops may be brought in contact by the shear flow, to recombine and form a larger droplet. Coalescence takes place in several steps as shown in figure 1.9 [18, 17, 7]. Coalescence is firstly controlled by the collision frequency, the contact force, the contact time (step 1) and then, by the film drainage (step 2), film rupture (step 3) and coalescence (step 4).

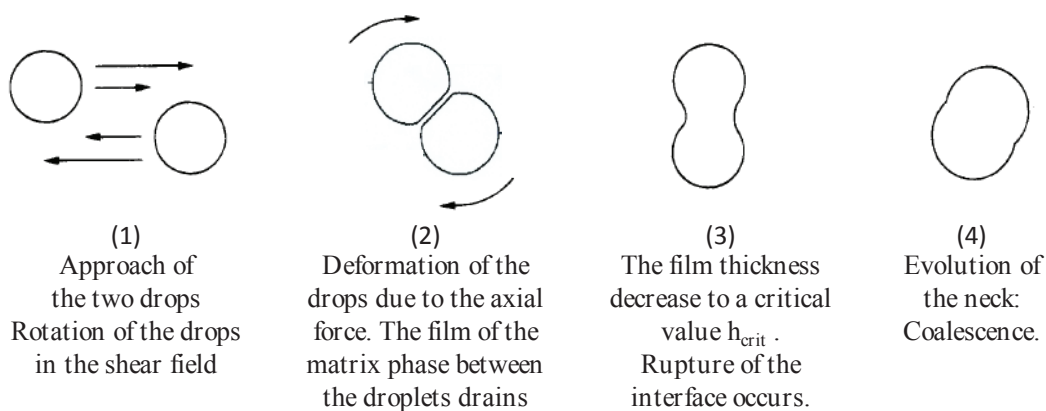


Figure 1.9: Diagram of the coalescence process [18].

### 2.2.1 Film drainage

The understanding of film drainage is an important parameter for the coalescence process [7]:

- At large separation, the drops approach according to the shear rate imposed: the drainage rate  $-dh/dt$  is of the order of  $\dot{\gamma}R$ .
- At a certain separation ( $h_0$ ) hydrodynamic interactions become significant and the collision starts. The driving force for film drainage is now the contact force  $F$  that acts during the interactions times  $t$ .
- The drainage rate  $-dh/dt$  decreases and the film thickness  $h$  asymptotically decays to small values.
- When a critical film thickness  $h_{crit}$  is reached, instabilities grow at the interface and suddenly film rupture occurs: drops coalesce.

The coalescence process strongly depends on the interfacial mobility which allows the drainage of the film. Three cases were studied in the literature and are schematically presented in figure 1.10: immobile, partially mobile and fully mobile interfaces.

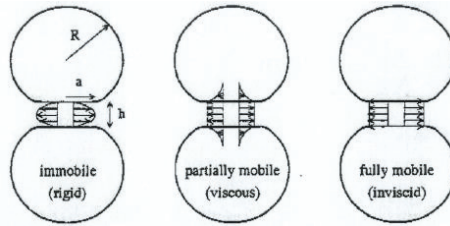


Figure 1.10: Internal flow field of film drainage between colliding deformable droplets with immobile, partially mobile and fully mobile interface [7]

The rates of film drainage were calculated for the immobile interface by MacKay and Mason (1963) [19], and the partially mobile and fully mobile interfaces by Chesters (1988). By integrating the equations from the initial thickness of drainage  $h_0$  and the critical thickness  $h_{crit}$ , the required time of drainage  $t_{drain}$  to reach coalescence are:

**For immobile interface:**

$$t_{drain} \sim \frac{3\eta_c R^2 F}{16\pi\Gamma^2} \left[ \frac{1}{h_{crit}^2} - \frac{1}{h_0^2} \right] \quad (1.10)$$

**For partially mobile interface:**

$$t_{drain} \sim \frac{\pi\eta_d F^{1/2}}{2(2\pi\Gamma/R)^{3/2}} \left[ \frac{1}{h_{crit}} - \frac{1}{h_0} \right] \quad (1.11)$$

**For fully mobile interface:**

$$t_{drain} \sim \frac{3\eta_c R}{2\Gamma} \ln \left[ \frac{h_0}{h_{crit}} \right] \quad (1.12)$$

With:

- $\Gamma$  the interfacial tension
- $R$  the droplet radius
- $\eta_m$  the matrix viscosity
- $\eta_d$  the droplet viscosity
- $F$  the driving force that acts on the droplet. It is estimated from the external simple shear flow to be:  $F \sim 6\pi\eta_m\dot{\gamma}R^2$  with  $\dot{\gamma}$  the shear rate.

The thickness  $h_{crit}$  is defined as:

$$h_{crit} = \left( \frac{AR}{8\pi\Gamma} \right)^{1/3} \quad (1.13)$$

With:

- $A$ , the material dependent Hamaker constant typically  $10^{-20}$ J.

The dependence of  $h_{crit}$  on the drop radius is fairly weak which means that, in any system studied, the minimal film thickness before coalescence is approximately of the same order of magnitude. In our systems we observed the thinner films between uncompatibilized droplet from 100 to 200nm.

In the case of **immobile interface**, the matrix cannot be easily removed from the space between the two droplets. For example, this is the case when the viscosity ratio  $R_v = \eta_d/\eta_m$  is too large. Indeed the drop is too viscous compared to the matrix and acts thus as a "rigid" drop. Conversely, when  $R_v$  is too small, the viscosity of the drop is too small to be seen by the matrix and one can consider this case as a **fully mobile interface**. The model with **partially mobile interfaces** is the only one to include the viscosity of both phases and is thus the most representative for the majority of the polymer/polymer blends having a viscosity ratio close to 1 without any compatibilizer. The drainage regimes may not appear always very intuitive, especially for the case of immobile interfaces drainage regime. Experimental illustrations of the different drainage regime will be studied in chapter 4 and will be discussed in more details.

A high shear rate, which thus increases the collision frequency between the drops, will not necessarily allow coalescence. Indeed, depending on the required time of drainage, the interaction time between two drops  $t_{int}$ , ie the duration of the collision, is approximately inversely proportional to shear rate:

$$t_{int} \sim \frac{1}{\dot{\gamma}} \quad (1.14)$$

Coalescence will thus preferentially take place in zones of extruder where the shear rate and deformation is low.

### 2.2.2 Coalescence probability

After a serie of simplifications, Meijer et al. [7] proposed an expression for the coalescence probability  $P_{coa}$  which is a function of the time of the process  $t_{proc}$ , the collision time  $t_{coll}$  (time necessary for two drops to collide), the time necessary for drainage  $t_{drain}$  and the interaction time  $t_{int}$ :

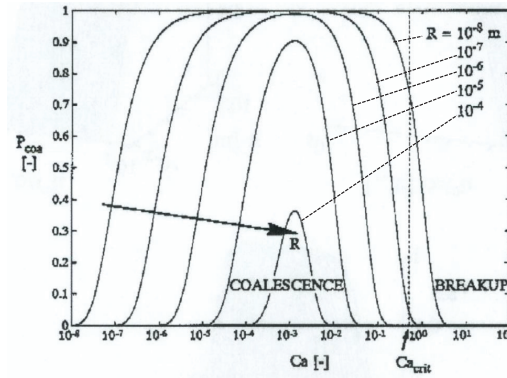


Figure 1.11: Coalescence probability  $P_{coa}$  as a function of the capillary number  $Ca$  for several drop radius  $R$  for a viscosity ratio  $R_v = 1$  (case of a partially immobile interface [7])

$$P_{coa} = P_{coll} \cdot P_{drain} = \exp\left(-\frac{t_{coll}}{t_{proc}} - \frac{t_{drain}}{t_{int}}\right) \quad (1.15)$$

This gives a diagram representing the coalescence probability as a function of the capillary number given in figure 1.11 for different values of droplet radius  $R$ . The diagram shows that the smallest drops (very low  $R$ ) coalesce more easily than largest ones. Besides, one can notice that coalescence occurs at capillary numbers that are smaller than those necessary for drop break-up. Meijer et al. mentioned that for very small drop radii (roughly below  $10^{-7}$  m) these graphs lose validity.

### 2.3 Combination of breakup and coalescence

Figure 1.12 shows the comparison of the minimum droplet sizes resulting from stepwise equilibrium break-up and the maximum droplet size resulting from coalescence of smaller drops after sufficiently long time depending on  $\eta_m \dot{\gamma} / \Gamma$ . It was proposed by Meijer et al. [7] assuming that: (i) the flow acts sufficiently long to reach the final equilibrium state, (ii) the stepwise equilibrium process to reach the minimum drop sizes is considered, (iii) coalescence is restricted to simple shear flow.

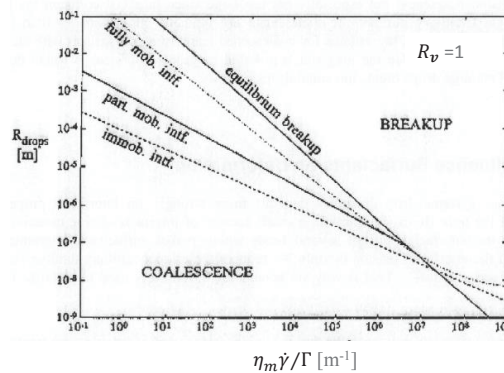


Figure 1.12: Drop size resulting from stepwise equilibrium breakup and coalescence (for different film drainage and  $R_v = 1$ ) after long process time in simple shear [7].

The coalescence lines depend on the drainage regime. The partially mobile interface (full line between the dotted lines) regime is the only one to consider the viscosity ratio. In that case  $R_v = 1$  but the curve may shift in parallel to higher values if the viscosity ratio  $R_v$  decreases and inversely if  $R_v$  increases. The "equilibrium breakup" line (full line) is the minimum attainable drop size considering the stepwise break-up mechanism calculated from  $Ca_{crit}$  with equation 1.9. It also depends on the viscosity ratio and can shift to higher or smaller values in the same way as  $R_v$ . The area between both curves (choosing the drainage regime adapted to the system) gives the possible range of drop sizes after long process time. This means that in that case of  $R_v = 1$  when  $\eta_m \dot{\gamma} / \Gamma$  ranges between  $10^6$  and  $10^7 m^{-1}$ , the maximum size due to the coalescence and the minimum droplet size due to equilibrium break-up are the same. So the droplet distribution size is very homogeneous. At smaller values, the coalescence or the break-up take the lead over the other and a wider distribution of droplet size may be observed. Note that in real mixing process, the transient break-up is more likely to occur and leads to thinner droplets sizes.

Thanks to this figure, it can be concluded that coalescence will thus preferably take place in areas where shear rate is weak (low  $Ca$ ) promoting longer collision times so that the film at the interface can be drained, while stretching and rupture of drops happen at higher  $Ca$  [10]. Both mechanisms are in constant competition in non-compatibilized polymer blends as well as in compatibilized blends, but in this case, other phenomena should be taken into account and will be discussed below.

## 2.4 Developed morphologies: drop break-up vs. coalescence

Without compatibilization, after an intensive mixing, the mechanism of drop break-up and coalescence can lead to multi-scale morphologies: from tens of nanometers to few microns [17]. Various types of morphologies can be developed and in particular *dispersed and co-continuous morphologies* as shown in Figure 1.13. In uncompatibilized blends, when the volume fraction of the dispersed phase increases, the droplet size increases due to coalescence. At a critical value, the phase inversion appears. At compositions close to phase inversion a "co-continuous" morphologies are often observed. It consists in two coexisting, continuous and interconnected phases throughout the whole blend volume. In that case, the two blend components contribute simultaneously to the properties of the blend in all directions [20]. Potschke et al. made an extensive review on the formation of co-continuous structure [21].

The easiest way to characterize qualitatively the morphology is to perform microscopic analyses: optical microscopy, SEM (scanning electron microscopy), TEM (transmission electron microscopy) and AFM (atomic force microscopy)[22, 23, 24]. Unfortunately, these are post-mortem methods which do not give direct information on the morphology development but only on the final morphologies. Microscopy techniques to detect co-continuity have to be used with caution because it does not give information on the entire composition throughout a three-dimensional structure[22, 25]. Moreover, SEM (or TEM) analyses do not result on the quantitative determination of the "degree of cocontinuity" (i.e. the fraction of phase in continuous domain versus in droplets as a function of the composition). Many other indirect methods have been used to characterize co-continuity such as solvent extraction [26, 27], measure of mechanical properties or electrical conductivity [22], dynamic mechanical analysis (DMA) [28], dynamic rheom-

## 2. Mechanisms of morphology development in immiscible polymer blends

---

etry [29, 25, 30, 28]. Recently even X-ray microtomography and laser scanning confocal microscopy (LCMS) were used [31, 32]. The prediction of the phase inversion composition has also been the subject of numerous researches and will be discussed in more details in chapter 5.

These morphologies, which are not stabilized may coalesce during any subsequent heat or stress (like in a second step processing in injection molding, blow molding...). Coalescence may result in phase segregation at the macroscopic scale [23, 17]. So, compatibilization is the way to promote the stabilization and the reproducibility of the morphology, and therefore of the properties (as checked with annealing experiments by Huitric et al. [33]). Compatibilization is thus studied in the following section.

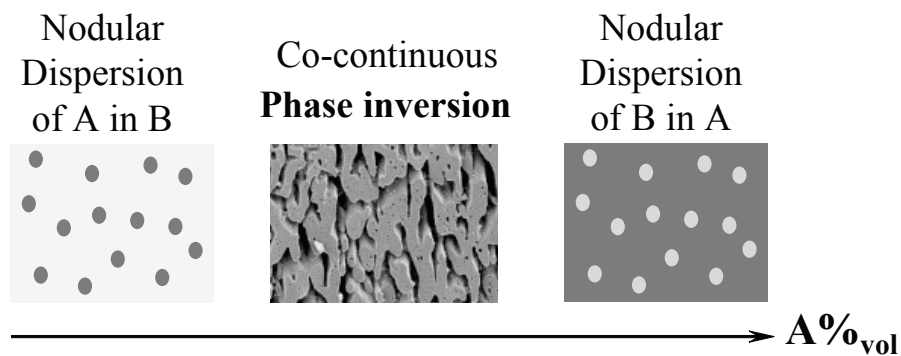


Figure 1.13: Main types of morphologies developed due to the drop break-up and coalescence under shear.

### 3 Compatibilization of immiscible polymer blends

For industrial applications, the morphology expected is often small droplets homogeneously dispersed in a matrix. However, blending two or more immiscible polymers often leads to blends with coarse morphologies, poor adhesion between phases and poor final properties. Compatibilization is thus necessary. The general idea of compatibilization is to add in the blend a component which will locate at the interfaces between incompatible polymers. This stabilizes a large quantity of interfaces in the system, i.e. it stabilizes small size domains. Most generally, this interfacial agent is a copolymer. Nanoparticles or preformed copolymers can also be used. The compatibilization has for main purpose to stabilize the morphologies (during annealing for example), improve adhesion between the blend phases in the solid state and thus facilitate stress transfer, hence improving mechanical properties [15].

#### 3.1 Different compatibilization possibilities

There are several ways of compatibilization for polymer blends:

- The **reactive compatibilization**, in which a copolymer is created directly at the interface between both polymers via an in-situ chemical reaction during blending.
- The **physical compatibilization**, in which a premade copolymer is added to the blend [34][35].
- The **addition of inorganic nano-fillers** which will locate at the interface and play the role of compatibilizer [36].

Reactive compatibilization is often used in industry because it allows a one step process and some chemical reactions have been shown to be effective within the short residence time of process, like twin screw extrusion.

#### 3.2 Effect of the compatibilization on the morphology development

Reactive compatibilization of polymer blends induces several consequences on the well-known drop break-up and coalescence mechanism:

##### Effect on the break-up mechanisms

The break-up mechanisms are mainly affected by the compatibilization because it reduces the interfacial tension. In that case, the energy needed to create interface is reduced and drop break-up is easier. The characteristic size of the morphology is reduced. But the presence of bloc or graft-copolymer at the interface may have several consequences on the drop deformation especially. For example, when a concentration gradient of copolymer is created at the interface of a droplet, Marangoni forces, which tend to restore the balance of chain density, can appear. This leads to a stabilization of the droplet upon further deformation for instance [37]. Moreover, the copolymer concentration gradient caused by the flow field can disturb the break-up mechanisms. Hu et al. [38] for example studied drops of polybutadiene (PB) in polydimethylsiloxane (PDMS) reactively compatibilized with low and high viscosity ratio (resp.  $R_v=0.1$  and  $R_v=2.2$ ). For different copolymer concentrations, they observed different break-up as a function of the viscosity ratio caused by the redistribution of the copolymers at the interface. As shown

### 3. Compatibilization of immiscible polymer blends

in figure 1.14, when  $R_v < 1$ , they observed: (1) usual capillary mode at very low copolymer concentration or no surfactant, (2) tip streaming at modest copolymer concentration and (3) asymmetric end-pinching at higher copolymer concentration. Note that for the second case, they observed that nearly all the copolymer was swept off with the small tip-streamed drops. This phenomenon was observed by other research teams like Eggleton et al. [39]. Meijer et al. [7] reported that "tip-streaming" was very likely to happen when  $R_v < 1$ . In the study of Hu et al. [38] when  $R_v > 1$ , only the normal capillary break-up was observed.

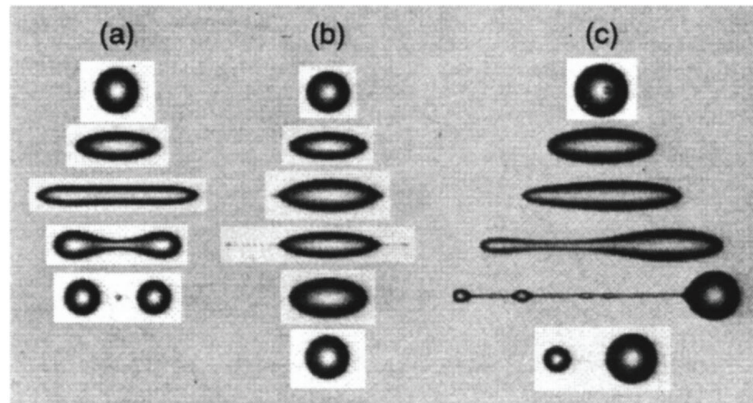


Figure 1.14: Different modes of drop breakup for different concentrations of copolymer at the interface [38]. The viscosity ratio is 0.1. (a) no surfactant: capillary modes (end-pinching) with formation of small satellites, (b) modest copolymer concentration: tip-streaming, (c) Higher copolymer concentration: asymmetric end-pinching.

#### Effect on the coalescence

Compatibilization leads to a dramatic reduction of coalescence and thus to a **stabilization of morphologies**. Two major theories, schematically shown in figure 1.15, were proposed in the literature to describe the suppression of coalescence:

- Milner et al. [40, 41] proposed the existence of **Marangoni stresses**: when the two drops come together the matrix is swept out of the gap which can create a concentration gradient of compatibilizer. The Marangoni stresses created by the interfacial tension gradient, opposed to the squeezing flow direction, slow down the rate of film drainage and suppress (or reduce) coalescence.
- A second hypothesis is based on the compression of the compatibilizer blocks when droplets approach. Elastic repulsion is then created between droplets (steric hindrance) [18, 42].

#### Effect on the co-continuity and phase inversion

When for uncompatibilized blends the droplet size diameter increases with volume fraction of the dispersed phase, for compatibilized blends, droplets sizes seem to be independent of volume fraction [18]: Co-continuity may be directly impacted. The co-continuity formation is still a topic of numerous studies, a general trend toward delaying cocontinuity formation and a narrowing of the composition range at which cocontinuity occurs

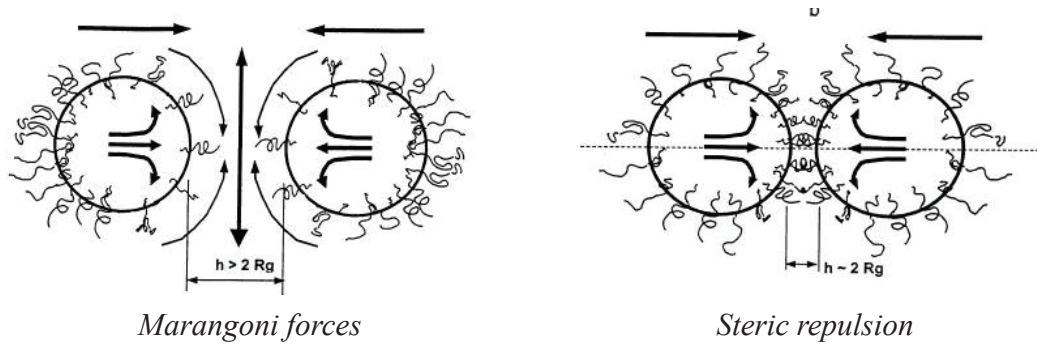


Figure 1.15: Two mechanisms proposed for coalescence suppression in blends compatibilized by addition or creation of block copolymers at the interface: (left) surface tension gradient: Marangoni force, and (right) steric repulsion [42].

is observed. A good summary of published reports on the topic is made by Harrats and Makhlef [20] and a review on the formation of co-continuous structures is proposed by Potschle et al. [21].

#### Other effects

When the compatibilization is done by reactive compatibilization, the reaction of copolymer formation can lead to interfacial fluctuations and creation of micelles or nanodispersions in blends phases. This will be described in more details in section 6 of the present chapter and is precisely the topic of this present work.

### 3.3 Conclusions on morphology development

In uncompatibilized blends, main parameters that control morphology development are: the shear rate, the composition and the viscosity ratio. The mechanism responsible of morphology development is essentially drop break-up and coalescence. In reactively compatibilized blends, when copolymers are created at the interface, these mechanisms can be greatly modified. It appears that the coalescence is limited and the break-up favoured due to the creation of copolymers at the interface. In reactive extrusion, the copolymer layer is formed directly at the interface. The architecture of copolymers created has a direct impact on the compatibilization reaction and on its effects on morphology. Before looking at the reaction and its kinetics itself, it is necessary to have a good knowledge of the chemical and thermodynamic characteristics of the copolymer layer created at the interface. To achieve this, the next section will focus on pure copolymers chemistry and structures.

## 4 Block copolymers

During reactive compatibilization, a large amount of copolymer is created at the interface, sometimes even until the total consumption of the minority phase [43, 44]. Usually, compatibilization is responsible of a size reduction until few hundreds of nanometers. Recently, some teams got, by reactive extrusion, morphologies fully structured at the nanoscale thanks to well-defined copolymers formed in situ [27, 45, 46].

One may wonder whether and how the copolymer layer formed at the interface, for which the thickness is supposed to be of the order of chains radius of gyration (i.e. few tens of nanometers), could affect the formation of the global polymer blend morphologies. What is the symmetry criterion for a copolymer, i.e. how the curvature will change with the architecture? Will copolymers induce a curvature toward its own spontaneous curvature? Will the curvature change if homopolymers penetrate the copolymer brush? Thus a proper understanding of the copolymer layer properties is necessary.

For several decades, scientists were particularly interested in the properties of block copolymers and in particular why the incompatibility of the blocks could lead to the formation of different ordered structures. These theoretical studies allow to understand how the copolymer architecture affects the curvature of the interface and favors certain morphologies compared to others. This section will thus focus on the understanding of pure bloc copolymer behaviour in order to help the understanding of the characteristics of the copolymer layer created at the interface in reactive polymer blends.

### 4.1 Generality on bloc copolymers

Block copolymers are macromolecules constituted of several incompatible blocks linked together by covalent bonds. An unlimited variety of block copolymers of well defined architectures has been synthesized since about fifty years [47], as shown in figure 1.16.

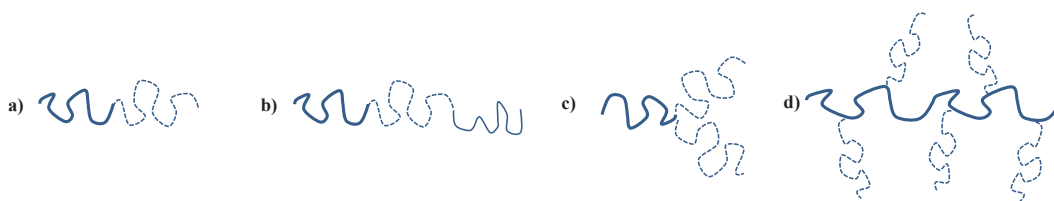


Figure 1.16: Architecture of block copolymers: (a) diblock, (b) triblock (c) grafted (Y type) or (d) grafted comb-like.

Copolymers are synthesized mainly in solvent environment. The morphologies or "microstructures" obtained for pure copolymers can then be entirely nanostructured and depend on the blocks architecture. The main feature of block copolymers is the strong repulsion between the different blocks, even if the repulsion between individual monomers is relatively low according to equation 1.3 [48]. The segregation of blocks is the consequence of this repulsion, but the blocks being chemically bounded, even a total segregation could not lead to a macroscopic phase separation as in the case of two incompatible homopolymers.

The phase behavior of A-B block copolymers is determined by three experimentally controllable factors: the overall degree of polymerization  $N$ , architectural constraints characterized by composition  $f$  (overall volume fraction of the A component), and the A-B segment-segment (Flory-Huggins) interaction parameter  $\chi$  [49]. In the case of a sufficiently strong incompatibility (high  $\chi N$ ), it can form micro-domains rich in A (or B): this is called the microphase separation also called order-disorder transition (ODT) (figure 1.17). When the  $\chi N$  product is large enough to be in the ordered domain ( $\chi N \gg 10$ ), as it will be seen later, the copolymer melt is in the so called strong segregation limit (SSL), this limiting regime will be considered in what follows.

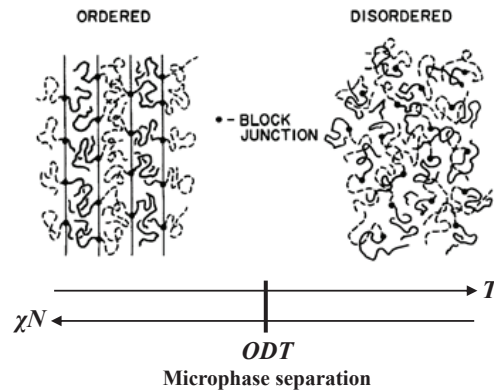


Figure 1.17: Schematic representation of the order - disorder transition for a "symmetrical" copolymer ( $f = 1/2$ ) with a lamellar structure [49].

In the ordered state the copolymer is subjected to several contributions: the repulsive interactions between A and B, a configurational and translational entropy loss related to the location of junction points between A and B at the interface. A repulsive interaction results in a positive parameter  $\chi$  and the entropy loss is inversely proportional to  $N$ . It is then understood that the product  $\chi N$  as a function of  $f$  is the control parameter for microstructures.

Leibler [48] is the first to have determined the phase diagram of block copolymers near the order-disorder transition based on the mean field theory. For a symmetric linear diblock copolymer with a symmetrical composition ( $f = 0.5$ ), the microphase separation occurs when  $\chi N \approx 10.4$ . For asymmetric copolymers,  $f \neq 0.5$ , at a flat interface the energy cost to stretch the longest block is high; the system will therefore prefer to adopt a curved interface. Depending on the composition and the product  $\chi N$ , copolymers can then self-assemble to form a variety of ordered microstructure as shown in figure 1.18: Spherical, cylindrical or lamellar. Several research groups [50] (1994) experimentally demonstrated the existence of a fourth structure commonly observed, the bicontinuous or gyroid phase. The phase diagram is proposed in figure 1.19.

#### 4. Block copolymers

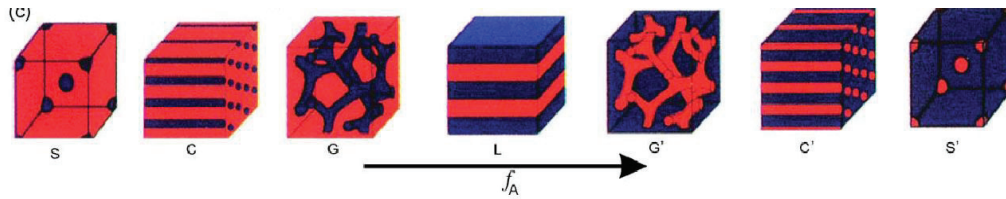


Figure 1.18: Predicting the self-assembly of diblock copolymers by the mean field theory (S) spherical, (c) cylindrical, (g) and Gyroid (L) lamellar [51].

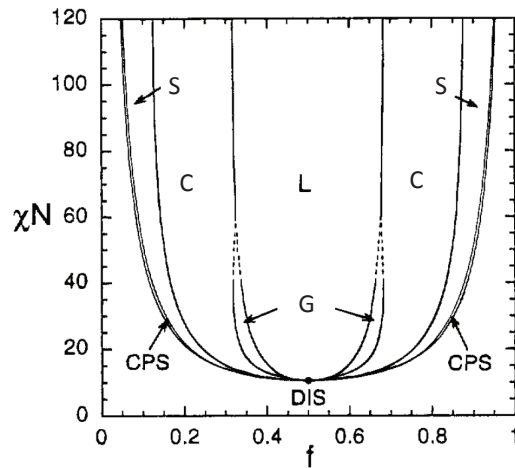


Figure 1.19: Phase diagram for diblock copolymers: lamellar (L), cylindrical (H: hexagonal cylinder), Gyroid (G), spherical (S), CPS for "close packed spheres" and DIS for disordered phase [52].

Experimental studies of Khandpur et al. [53] for polyisoprene-polystyrene (PI-PS) copolymers whose composition  $f$  is close to the ODT, or of May et al. [54] for poly(oxyethylene)-poly(oxybutylene) (PEO-PBO) show very good agreement with the theoretical diagrams (see figure 1.20.)

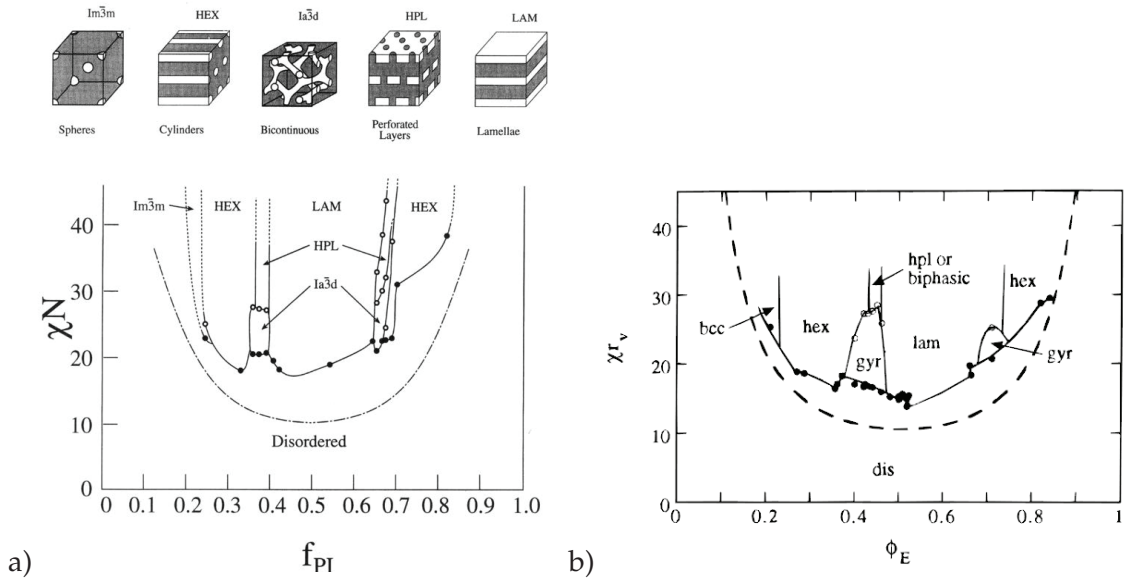


Figure 1.20: a) Experimental phase diagram of  $\chi N$  as a function of  $f$  for diblock copolymer PI-PS. Note: the  $\chi N$  value are higher than Leibler's prediction (dashed line) [53]. b) Experimental phase diagram of  $\chi r_v$  ( $r_v = N =$  length of the copolymer) as a function of  $\phi_E$  (volume fraction of the PEO block) for a diblock copolymer PEO-PBO [54].

#### 4.1.1 Definition of the symmetry criterion: case of linear dibloc copolymers

In a theoretical study of linear diblock copolymers AB, Leibler (1988) defined a first symmetry criterion [1] that promote a small spontaneous curvature of the interface and thus a planar interface at equilibrium. This leads to lamellar bloc copolymer microstructures. This theory is valid in the case of "dry brush" regime (i.e. no homopolymer has penetrated the copolymer blocks) and for monodisperse homopolymers:

$$\frac{V_A^3}{R_{gA}^2} = \frac{V_B^3}{R_{gB}^2} \quad (1.16)$$

With:

- $V_A$  (resp  $V_B$ ) is the average molar volume of block A (resp. B).
- $R_{gA}^2$  the radius of gyration of block A (resp. B).

#### 4.1.2 Definition of the symmetry criterion: case of grafted copolymer with a Y architecture ( $A_2B$ )

In reactive compatibilization of incompatible polymers, graft copolymers are often formed at the interface instead of linear copolymer. This is because one of the reactive polymer contain grafted reactive moieties instead of end-chain reactive moieties. The copolymer created may thus exhibit complex architecture with one backbone containing several branches. Thus, the graft copolymer architecture may influence the curvature of the interface and the symmetry criterion.

Gido et al. [55, 56] have shown that the complex molecular architecture of a polymers chain containing two or more points of grafting could be studied by analogy to the

behaviour of their constitutive basic unit (figure 1.21). If the molecular weight is large enough, the points of grafting will be far enough to behave independently. Thus the chain with multiple grafts can be divided into more basic unit called *Y-shaped copolymer*  $A_2B$  type with two branches of polymer B and one branch of polymer A. Through a series of experiments, Gido et al. [56] generalized the definition of  $\epsilon$  in order to take the difference in the chain length of the Y-shaped copolymer arms into account. In our case, we assume that the two arms of the main chain are of the same length.

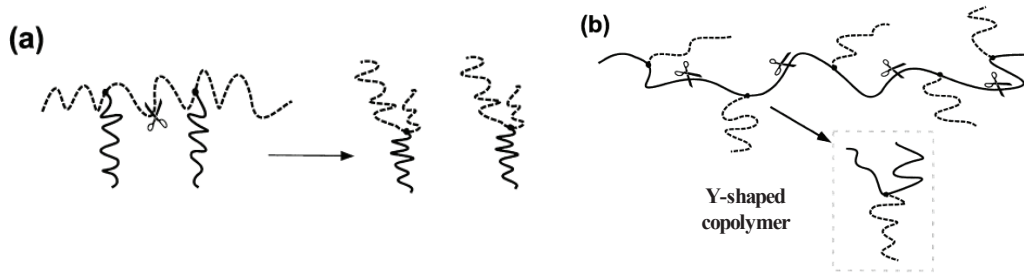


Figure 1.21: Schematic representation of the separation into constitutive basic units of a graft copolymer. In this thesis, the separation considered is where the part with 2 arms of the copolymer have the same length (example b) [56].

#### Theoretical symmetry criterion for Y-shaped graft copolymer, type $A_2B$

Based on Leibler's (1988) work [1], Milner (1994) [57] defined a criterion for zero average curvature for a Y-shaped copolymer with two branches of polymer A and one of polymer B in the strong segregation limit. They considered that the two arms of the polymer A were of the same length. To form a strongly-segregated lamellar phase (flat interface) with such a copolymer, the thermodynamic imposes that the thickness of the A layer is equal to the B layer. The criterion was thus defined as:

$$\frac{V_B^3}{R_{gB}^2} = 16 \frac{V_A^3}{R_{gA}^2} \quad (1.17)$$

in which  $V_A$  is the average molar volume *one branch of A* and  $R_{gA}$  (resp B) the radius of gyration. *This criterion will be discussed in more details in chapter 3.*

Generalizing his calculations on Y copolymers to a star copolymer having  $n_A$  A arms exhibiting **the same length** with a volume  $V_A$  and  $n_B$  B arms with a volume  $V_B$ , Milner[57] determined the phase diagram of a grafted copolymer defined with the asymmetry parameter  $\epsilon$  as a function of volume fraction  $\phi_B$  shown in figure 1.22.

In figure 1.22 sph, cyl, bic, lam represent the spherical, cylindrical, bicontinuous and lamellar phases and the asymmetry parameter  $\epsilon = (n_A/n_B)(l_A/l_B)^{1/2}$  with  $l_A = V_A/R_A^2$ . The volume fraction of B is  $\phi_B = n_B V_B / (n_A V_A + n_B V_B)$ . Thus, when  $n_A = n_B = 1$  the copolymer is linear, when  $n_A = 2$  and  $n_B = 1$  a Y copolymer, etc. Note that the volume fraction to obtain a flat interface is shifted towards higher  $\phi_B$  in the case of a Y-copolymer  $A_2B$  compared to linear diblock copolymer AB.

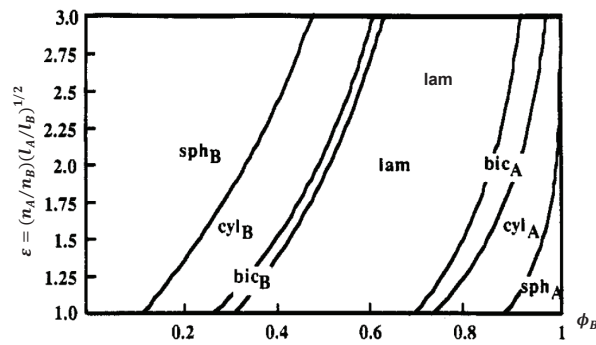


Figure 1.22: Phase diagram of a Y copolymer in the strong segregation limit for copolymers with  $n_A$  A arms and  $n_B$  B arms as a function of the volume fraction of the B monomer [57]. [56].

Later Pochan et al. [58], highlighted the presence of a fifth type of morphology. For this, they conducted an experimental study on a Y-copolymer of polystyrene and polyisoprene : I<sub>2</sub>S (2 arms of polyisoprene and 1 arm of polystyrene). They observed a new I<sub>2</sub>S copolymer morphology for high volume fractions of PS (here  $\phi_S = 0.81$ ). This morphology is in the form of "wormlike micelles" in which the two branches of A (here A = Isoprene I) are forced into the concave side of the interface.

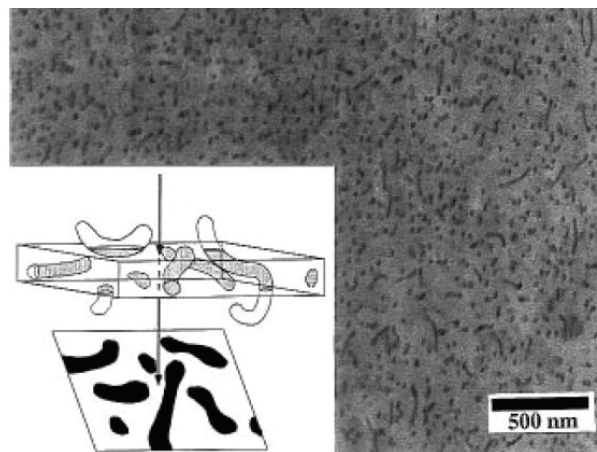


Figure 1.23: TEM micrograph of a "wormlike micelles" morphology for I<sub>2</sub>S copolymer ( $\phi_S = 0.81$ ) [58].

### Experimental examples of symmetric Y-shaped graft copolymer

Recently, Leibler's team [27] designed new materials which exhibit a fully co-continuous morphology at the nanometer scale. Those blends were performed by reactive compatibilization between polyamide and polyethylene. By making the approximation of an Y-shaped copolymer with two branches of PE and one of PA, they gave a criterion of copolymer architecture at the interface to obtain a fully nanostructured co-continuous morphology : "The average fraction of reactive functional groups on the chain skeleton (PE) is chosen such that the average distance between the grafts (PA) is about 2 times the average length of the graft". According to the authors, this criterion, transcribed in equation 1.18, prevents the strong architectural asymmetries and promotes a

large radius of curvature. Later, Freluche et al. [45] indicated that such morphology could only be obtained for PA grafts exhibiting a very low molecular weight, in their case  $Mn_{PA} = 2.5\text{kg}\cdot\text{mol}^{-1}$ . Later the same research team (Gani et al. [46]) mentioned that in all the fully co-continuous nanostructured blends obtained, the molecular weight of the PA graft was lower than twice the molecular weight between entanglement estimated at  $2\text{kg}\cdot\text{mol}^{-1}$  [59].

$$Mn_{PA} = Mn_{PE} \quad (1.18)$$

With  $Mn_{PE}$  the molecular weight of a single PE branch and  $Mn_{PA}$  the molecular weight of the PA branch.

### 4.2 Incorporation of A and/or B homopolymers into AB bloc copolymers

We have seen that copolymers formed at the interface may adopt a spontaneous curvature dictated by several parameters. The question is now: what will be the consequence of the incorporation of unreacted homopolymers on the spontaneous curvature. Two scenarios are possible:

- The copolymer is capable of incorporating the homopolymers in its structure, in the brush of the copolymer and / or between domains. The initial structure will swell.
- The copolymer is unable to incorporate homopolymers, a macrophase separation happen.

One may thus wonder: What are the criteria (length, molecular weight, block parameters / homopolymer interaction ...) for homopolymers to penetrate the copolymer brush? What will be the impact of incorporation on the curvature of the interface? On the final morphology? Will we observe macrophase separation? What are the most favourable morphologies for the incorporation of homopolymers into the structure? Several studies are available in the literature to understand these phenomena in binary mixtures of homopolymers / linear diblock copolymers. However, very few data are available for grafted copolymers / homopolymers. In this section, we will discuss, in a first hand, binary and ternary mixture of linear diblock copolymer / homopolymer, then graft copolymers.

#### 4.2.1 Binary blends of linear diblock copolymers/homopolymers: AB/A

Hashimoto et al. (1990)[60] were one of the first team to study experimentally and theoretically the question. For example, they studied the incorporation of 20 and 50% in weight of monodisperse homopolymers of styrene (hS) into a monodisperse diblock copolymer poly(styrene-b-isoprene) (PS-PI). The initial PS-PI copolymer exhibit a lamellare morphology. Three molecular weights of hS were tested ( $Mn_{hS}$  from 2300 to 16700 g/mol), in all cases the molecular weight were lower or equal to the PS block of the copolymer ( $Mn_S=16700\text{g/mol}$ ). This solubilization of hS causes the PS blocks to swell both laterally and longitudinally. A schematic representation of the various cases considered for the incorporation of hS of increasing molecular weights is given in figure 1.24.

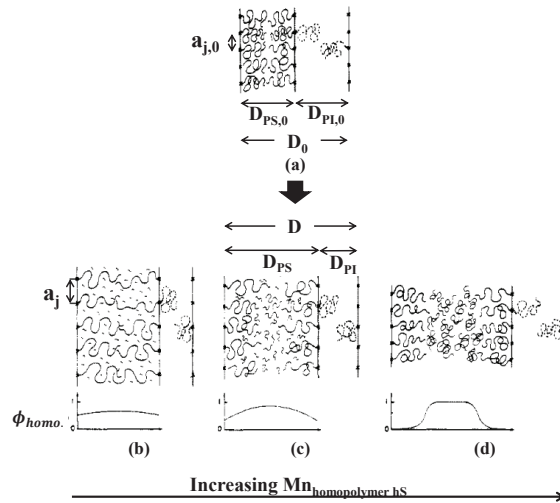


Figure 1.24: Simplified schematic representation of the solubilization of homopolymers PS (hS) in the PS brush of the diblock copolymer (PS/PI) and the spatial segmental distributions of the homopolymers and block copolymers chains in a microdomain space. (a) pure block polymer, (b) uniform solubilization of HS in the PS microdomain ( $Mn_{hS} = 2300\text{g/mol}$ ), (c) intermediate state and (d) localized solubilization of hS in the center of the PS microdomain ( $Mn_{hS} = Mn_S$ )[60].

For the composition hS/SI is 20/80%wt the incorporation of hS did not change the initial lamellar morphology however for the composition 50/50%wt, the morphology was changed from lamellae to cylindrical morphology during incorporation of the shortest homopolymer (case (b) in figure 1.24). In this case, there is a strong increase of the distance between chemical junctions ( $a_j$ ) of the PS block of the copolymer. To maintain a constant bulk density, the inter-domain distance DPI is forced to reduce and even more when the concentration of homopolymers increases. The blocks PI are highly compressed and thus increases the entropic penalty of the PI chains. This free energy conformation penalty is the driving force for the transition from lamellar morphology to cylindrical. The gain in free energy that represents the new conformation of the copolymer blocks must outweigh the energy cost of the formation of a curved interface so that the transition takes place. In this case, the PI chains that were compressed find more space to relax. On the PS side of the copolymer, the PS blocks are confined between homopolymers and the chains are forced to stretch perpendicularly to the interface: there is therefore also a loss of entropy configuration on this side of the copolymer.

A theoretical study of Shull and Winey (1992)[61] has generalized the cases studied by Hashimoto et al. Thus, three incorporation regimes for symmetrical copolymers with lamellar morphologies have been identified. By considering the ratio of the length of the homopolymer  $N_h$  relative to the length of the block copolymer of the same nature  $N_c$ , thus:

- $N_h/N_c < 1$ : The copolymer will be swollen by the homopolymer which will be able to interpenetrate the blocks. Thus the radius of curvature at the interface will decrease which may result in a change in morphology if the volume fraction of homopolymer is high enough. This is the "wet brush" cases defined by Leibler. Figure 1.25 show an example of Tanaka et al.[62] of morphology transition with

## 4. Block copolymers

increasing amount of homopolymer.

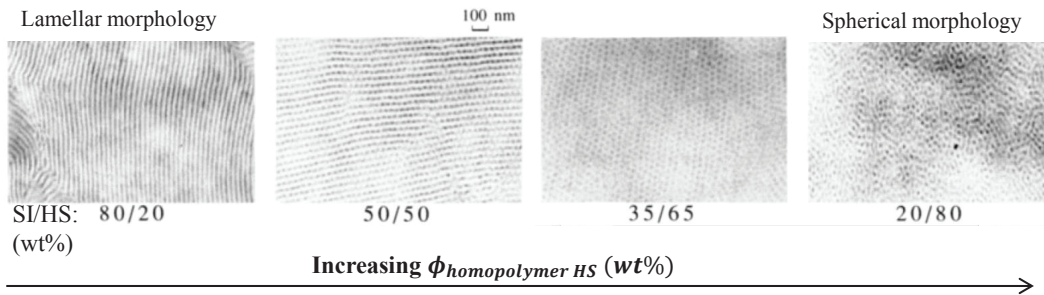


Figure 1.25: Example of morphology transition due to the incorporation of homopolymers for a binary mixture of copolymer PS-PI (block S  $M_n = 15000\text{g/mol}$ ) and styrene homopolymer hS ( $M_{n,hS} = 2200\text{g/mol}$ ) illustrating the case  $N_h/N_c < 1$ . The initial PS-PI copolymer morphology is lamellar [62].

- $N_h/N_c \simeq 1$ : Homopolymer chains will not interpenetrate blocks of the copolymer but no macrophase separation will be observed. They will essentially be located in the middle of micro-domains of the copolymer. For a lamellar microstructure, areas will be able to swell while keeping their basic lamellar structure. This is the "**Dry brush**" cases defined by Leibler. However, if the amount of homopolymer becomes too large, the interface may lose its long range order and may fluctuate as shown by Koizumi et al. [63] in figure 1.26.

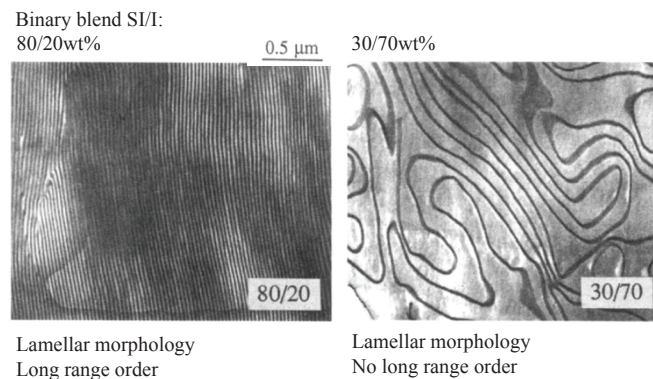


Figure 1.26: TEM image of the binary mixture SI/S illustrating the case  $N_h/N_c \simeq 1$ : there is no transition of morphology but the long range order is not preserved. The dark phase is the PI rich phase and the white phase is the PS rich phase [63].

- $N_h/N_c > 1$ : when the homopolymer is longer than the block copolymer, the entropic penalty to incorporate homopolymer chains is too high, homopolymers will not or very little swell the copolymer blocks. A **macrophase separation** will then be observed: copolymers will organize with their own structuration in one phase and a second phase rich in homopolymer will form ( see figure 1.27). This is especially true if the volume fraction of homopolymer is high. For example in figure 1.27 (Koizumi et al. [64]), the amount of homopolymer (80w%) is much higher than the copolymer one (20wt%).

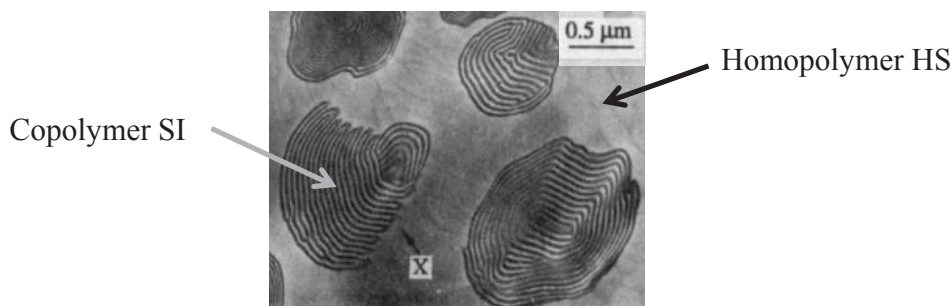


Figure 1.27: TEM image of a mixture of styrene homopolymer (HS) and copolymer (SI) of composition 20/80wt% obtained by rapid evaporation of the toluene solvent at low pressure to illustrate the case  $N_h/N_c > 1$  (dark portion: I rich phase and white: S rich phases)[64].

All these results were confirmed by several teams such as Matsen [65] and Janert and Schick [66]. Cases studied by Hashimoto et al. at the beginning of this paragraph would fall between  $N_h/N_c < 1$  and  $N_h/N_c \simeq 1$ .

#### 4.2.2 Ternary blends of linear diblock copolymers/homopolymers: AB/A/B

Tanaka et al. (1991) [62] studied homopolymer solubilization of low molecular weight into diblock copolymer by comparing binary systems A/AB and ternary A/B/AB. As noted previously, the introduction of low molecular weight homopolymers in a binary mixture A/AB tended to promote a change in conformation (curvature of the interface) because of the entropic penalty generated in both blocks of the copolymer. In ternary mixtures, A and B homopolymers of low molecular weight incorporated in the same amount, are incorporated uniformly in the corresponding blocks of the copolymer (see figure 1.28 for an example of a symmetric copolymer promoting lamellar microstructure). This incorporation results in a uniform expansion of the inter-domain and inter chemical junction distances. Thus there is no change in morphology.

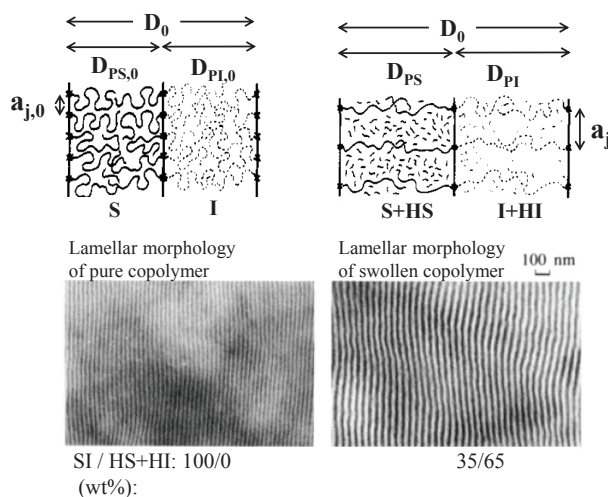


Figure 1.28: TEM images and schematic representation of the solubilization of low molecular weight homopolymers of hI and hS in the SI brush of the copolymer (respective molecular weight 2200,2300 and  $Mn_{PI-PS}=31600$  g/mol so roughly  $Mn_{PI} = Mn_{PS} = 15800$ g/mol): left, the pure copolymer and right, the swollen copolymer [62].

Only few articles describe the incorporation of A and B homopolymers in a AB copolymer which have another structure than lamellae. However, few studies, essentially theoretical studies, showed that in the presence of copolymers having a morphology other than lamellar, i.e. cylindrical, spherical or Gyroid, the curvature of the non-planar interface strongly limits the incorporation of homopolymers, even if the molecular weight is very low [27, 45, 65, 66, 67, 68, 69, 70]. For example, incorporation of homopolymers into spherical domains of an equilibrium spherical copolymer microstructure, would cause a very unfavourable stretching of copolymer blocks located on the outside of the spherical domains, causing a significant loss of free-energy of configuration for these blocks. A very limited quantity can then be incorporated (5 to 10wt% [27]). This kind of situation causes "macrophase separation" as shown in figure 1.27 for example. It appears that polydispersity of both homopolymers and copolymers helps for the incorporation. Janert and Schick [69, 70] tried to establish general ternary diagram of morphology as a function of the composition.

The results show that during the blending of diblock copolymers and their corresponding homopolymers, the four main parameters controlling the formation of morphologies are:

- The overall composition of the blend.
- The composition of the copolymer.
- The molecular weight of the homopolymer and copolymer.
- The initial morphology of the pure copolymer.

### 4.2.3 Blends of grafted copolymers/homopolymers: $A_mB_n/A/B$

Linear diblock copolymers/homopolymer binary blends have been widely studied in the literature and often for model systems (lamellar morphology, equal blocks length, monodisperse polymers ...). However, only few literature exists on copolymers with complex architecture. Yang et al. [71] studied the effects of the incorporation of short polystyrene chain (hS) or polyisoprene (hI) in a pure Y-shaped copolymer with 2 PI branches and one PS branch (noted I<sub>2</sub>S). They showed that hI homopolymers incorporation was more difficult into the PI side with two PI branches than hPS homopolymer incorporation into the PS side with one PS branch. Thus, this swelling asymmetry of the copolymer leads to a shift of the domains phase transition.

## 5 Control of the interfacial compatibilization reaction

Reactive compatibilization is the main route for the compatibilization of immiscible polymers blends. As we have seen in section 3, the layer of copolymer is directly created at the interface of the morphology formed, from reactive homopolymers present in the bulk. In the next section, we will focus on the parameters that control the reaction kinetics at the interface. Indeed, as it will be seen, several criteria will influence the interfacial reaction: the intrinsic reactivity of reactive moieties, polymer chains characteristics on which these function are grafted, the interface, the hydrodynamic conditions (static or shear)...

### 5.1 Theoretical approach

In a theoretical study of heterogeneous polymer blends in static conditions, Fredrickson and Milner (1996) [72] described the different growth regimes of a layer of linear diblock copolymers at the interface between two symmetrical polymers ( $N_A = N_B$ ). The formation of copolymers is controlled successively by:

- (1) For early times: The kinetics of coupling reaction at the interface between reactive moieties controls the amount of copolymers at the interface (represented by  $\Sigma$ , the interfacial coverage) which increases linearly with time.
- (2) For intermediate times: the diffusion of reactive homopolymers to the interface controls the formation of copolymers to fill the depletion hole of reactant created by the first stage.
- (3) For longer times: copolymers gradually form a **copolymer brush at the interface**. It generates a "*potential barrier*" for unreacted homopolymers, which strongly limits and controls the kinetics of the reaction by limiting the diffusion of reactive moieties toward the interface. The potential barrier increases with the chain length.

Theoretical studies of O'Shaughnessy et al. (1996 and 1999) [73, 74] conclude with similar results. In general, authors all agree on the third step of the formation of an energy barrier due to accumulation of copolymers at the interface, which dramatically drops the reaction kinetics [72, 75, 73, 74]. However, the first two steps do not make consensus. In next subsection we thus discuss the papers that study diffusion controlled and then reaction controlled kinetics.

### 5.2 Diffusion controled kinetic

Several theoretical studies on the reaction kinetics are based on the assumption that the reaction kinetics is limited by diffusion of reactive species to the interface. They state that this hypothesis is possible if the chemical reaction is extremely fast [72, 75, 73, 74]. In a theoretical study, Fredrickson (1996) [75] showed that there were two diffusion-controlled regimes of the reaction according to the length of reactive chains ( $N$ ) with respect to the entanglement threshold ( $N_e$ ). If  $N < N_e$  the reaction rate coefficient was higher than if  $N > N_e$ .

However, in most experimental cases, the characteristic reaction times are much longer than the time required for diffusion of reactive moieties to the interface [76, 77, 78, 44, 79, 80]. In this case, the kinetics of copolymer formation is only limited by the chemical reaction kinetics before the formation of the energy barrier due to accumulation of copolymers at the interface.

### 5.3 Reaction controlled kinetics

In polymer blends the quantification of the chemical reaction, i.e. the amount of copolymers created at the interface, is very complicated. Indeed, the reactive functions typically represent only a few percent of the global concentration making the detection with current analytical techniques (IR, NMR, SEC, potentiometric titration, ...) even more difficult.

The nature of reactive functions is crucial for the reactive compatibilization. Macosko et al. (2005) [81, 82] have provided a comprehensive work on reactions at polymer-polymer interfaces for blend compatibilization. For example, the chemical reaction between aliphatic amine and cyclic anhydrides moieties (terminal groups on PS chains) in homogeneous conditions was very fast. The conversion into imide is almost complete at 180 °C in less than 30 seconds under static conditions.

The reactivity at interface of immiscible polymers were also tested during reactive compatibilization. For example, Yin et al. [44] tested the reactivity of two couples of reactive moieties but under shear: PMMA-NCO (PMMA  $\omega$ -isocyanate wherein the reactivity of the isocyanate functional group was deliberately limited) or PMMA-Anh ( $\alpha$ -anhydride PMMA) with a polystyrene containing NH<sub>2</sub> functional groups grafted along the chain (PS-co-PSNH<sub>2</sub>). The conversion rate of reactive moieties was followed by a technique of size exclusion chromatography (SEC) inspired by the work of Guégan et al. (1994) [83]. After 10 minutes of blending at 170 °C in a rheometer (plate-plate geometry at 1Hz), the reactive couple PMMA-NCO/PS-co-PSNH<sub>2</sub> resulted in an interfacial reaction very slow (16.5% conversion into PS-g-PMMA) while the reactive couple PMMA-Anh/PS-co-PSNH<sub>2</sub> led to an almost complete conversion (92% conversion into PS-g-PMMA). The choice of the reactive couple is therefore very important for the final conversion rate.

### 5.4 Effect of the copolymer architecture on the chemical reaction

#### 5.4.1 Location of reactive moieties along the backbone: comparison of reactivity

In a study on the reactive compatibilization, Jeon et al. (2004) [84] compared the reaction kinetics of a linear chain containing one amine reactive end-group (PMMA-NH<sub>2</sub> or PS-NH<sub>2</sub>) which can react either with another linear chain with a maleic anhydride reactive end-group (PMMA-endMA), or with a chain with reactive moieties randomly distributed along the chain (PMMA-midMA). In the first case, a linear diblock copolymer is formed, in the second, a graft copolymer. The reaction rate kinetic constants of linear diblock and grafted copolymers formation (resp.  $k_E$  and  $k_M$ ) were measured by spectrofluorimetry coupled with SEC by mean of anthracene labeling of PMMA chains. The kinetic constants were determined in static conditions and under shear.

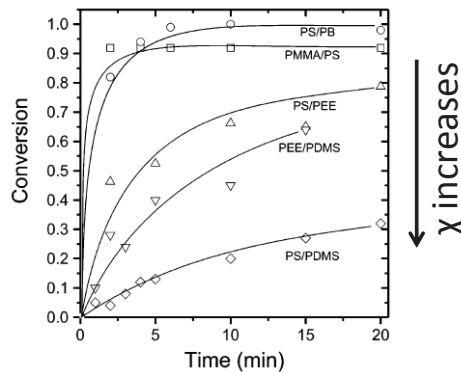
In heterogeneous static conditions,  $k_E/k_M > 10$ . The formation of linear diblock copolymers is largely favourable compared to the formation of grafted copolymers. Their explanation for this very unbalanced result is the higher population of chain ends at the equilibrium interface compared to the central segments. Indeed, Helfand and Tagami (1972) [85] have shown that under static conditions, the density of chain ends at the interface was twice higher than the density of mid-chain segments. Besides, the difference between the formation of linear versus graft copolymer is also explained because functional groups at the center of polymer chains experienced greater hindrance reacting with

complementary functional polymers than those at the ends.

Under shear, a significantly acceleration of reaction kinetics is observed: The reaction rate constant is 1000 times higher than in a static conditions. This increase is due to the fact that the shear continuously generates interface (stretching drops etc ...). However, the difference between  $k_E$  and  $k_M$  is greatly reduced:  $k_E/k_M > 2.6$ .

#### 5.4.2 Influence of the Flory interaction parameter $\chi$

Macosko's team [86] studied the effects on the amine( $\text{NH}_2$ )/ anhydride reaction, of the chemical structure of different monomers on which the reactive moieties are attached. Indeed, changing the Flory interaction parameter  $\chi$  affects the thickness of the interface, hence the interfacial tension and thus affects the interfacial reaction. The Flory interaction parameter  $\chi$  was modified by changing the chemical structure of blend components, keeping a nearly constant molecular weight. The tests were carried out under static conditions between two polymer films both containing reactive moieties at the end and the reaction was characterized by SEC coupled with UV detector. As a conclusion, it has been shown that increasing  $\chi$ , i.e. increases the segregation forces between polymers, decreases the amount of the copolymers formed at the interface.



polymer 1	polymer 2	$\phi_1$	$\chi$ (200 °C)	$a_I$ (nm)	conversion <sup>a</sup> (20 min)
PMMA-anh (22 kg/mol)	PS-NH <sub>2</sub> (15 kg/mol)	0.62	0.017	4.2	0.92
PS-NH <sub>2</sub> (21 kg/mol)	PB-anh (25 kg/mol)	0.70	0.024	3.6	0.98
PS-anh (35 kg/mol)	PEE-NH <sub>2</sub> (18 kg/mol)	0.70	0.036	2.4	0.79
PEE-NH <sub>2</sub> (18 kg/mol)	PDMS-anh (28 kg/mol)	0.70	0.055	1.9	0.64 <sup>b</sup>
PS-NH <sub>2</sub> (15 kg/mol)	PDMS-anh (28 kg/mol)	0.80	0.18	1.0	0.32

<sup>a</sup> Conversion of limiting polymer, based on available functionality. <sup>b</sup> 15 min.

Figure 1.29: Interfacial conversion vs time for melt-mixed blends of two polymers with terminal functionality. Blends characteristics are summarized in table above with  $a_I$  the interfacial thickness and  $\phi_1$  = the volume fraction of polymer 1 [86].

#### 5.4.3 Multiple grafting: influence of grafting heterogeneities

Steurer and Hellman (1998) [43] have studied the reaction kinetics of in-situ grafting at the interface of polystyrene containing several reactive MA moieties along the backbone (PS-g-MA) and amine-terminated polyamide 12 (PA-NH<sub>2</sub>). Several blends were prepared under shear at 250 °C. The authors showed that:

## 5. Control of the interfacial compatibilization reaction

- Not every PA chains are grafted even though less  $\text{NH}_2$  moieties than MA are available in blends. This is because a barrier energy is created after the grafting of the interface which prevents all  $\text{NH}_2$  moieties to access the interface.
- All the PS-g-MA do not receive the same number of grafts: When one maleic anhydride of the backbone has already reacted, the PS-g-MA chain is already grafted at the interface and thus other MA moieties localized on the same chain are in a favourable position to react.

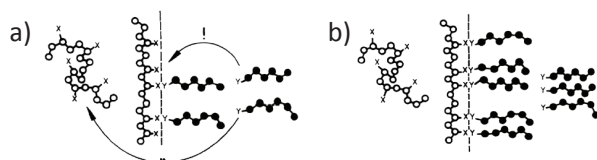


Figure 1.30: Diagram representing the grafting at the interface: (a) The first chains react and form the first grafts (b) The fully grafted chain forms a barrier and prevents new moieties to react [43].

### 5.5 Interfacial reactivity: summary

The reaction kinetics is controlled by:

- 1<sup>st</sup> stage: **The interfacial reaction** between two reactive moieties attached to polymer chains. A copolymer brush is gradually created at the interface.
- 2<sup>nd</sup> stage: **The diffusion of homopolymer chains through the dense brush copolymers accumulated at the interface.** Indeed, these copolymers have ended up creating an energy barrier, mainly due to steric hindrance and chain stretching, preventing the new homopolymers to reach the interface to react, dramatically slowing down the reaction kinetics.

In several theoretical studies, some teams had mentioned that the reaction kinetics could be controlled by the diffusion of reactive species to the interface before the energy barrier due to the accumulation of the copolymers at the interface is formed. However, diffusion calculations and experimental studies have shown that this step is generally not limiting in both static conditions and under shear. The parameters influencing the reaction kinetics are summarized as follow:

**Intrinsic reactivity** Reaction at the interface depend greatly on the reactive moieties. For example, the couple Amine ( $\text{NH}_2$ )/maleic anhydride (MA) is very reactive and the reaction kinetic is very fast. This reaction is thus well adapted for the short times scale or reactive extrusion.

**Copolymer architecture** In the case of graft copolymers, when the reaction is initiated on one of the reactive sites of the chain, the reaction with the other sites of the same chain is favored.

- *In static conditions:* The steric hindrance generated by the architecture of graft copolymers may limit the reaction compared to a linear diblock copolymer.
- *Under shear:* The copolymer architecture (grafted or linear diblock) is much less critical.

**Concentration in reactive moieties** Reaction kinetics increases with the concentration in reactive moieties near the interface. This is for example the case for low molecular weight end functionalized polymers compared to higher molecular weight end functionalized polymers.

**Blocks and homopolymers lengths (molecular weight  $M_n$ )** During the first stage, blocks length does not usually affect the chemical reaction and therefore the coupling kinetics because the diffusion of the reactive species do not come into play. During the second stage, after the formation of a dense copolymer brush at the interface, homopolymers length is more critical. For high molecular weight homopolymers, conversion rates are often lower than for low molecular weight. Note that this can also, at least in part, comes from the fact that when using higher molecular weight, the concentration of reactive functional group in each phase decreases. Thus the probability of reaction is lower.

**Flory interaction parameter  $\chi$**  When  $\chi$  decreases, the reaction rate increases.

**The shear** Shearing greatly accelerates the reaction kinetics. Under shear, the effect of the molecular weight, the architecture, the concentration in reactive moieties near the interface are much less critical than in static conditions.

**Polydispersity** It is important to note that almost all the studies cited were conducted with monodisperse polymers. Using polydisperse polymers could conduct to systems where all the cases studied here would be observed.

It appears that under certain conditions, interfacial fluctuation and then, interfacial roughening are spontaneously created enabling homopolymers to overcome the energy barrier and reaction to progress. Interfacial roughening seems to depend on the architecture of the copolymer created at the interface (molecular weight  $M_n$ , flory parameter  $\chi$ ...). The destabilization of the interface by the creation of copolymer at the interface is thus discussed in next section.

## 6 Effects of the compatibilization reaction on the morphology development of polymer blends: interfacial roughening and nanodispersions creation

As described above, theoretical studies [87, 73, 74, 76, 88, 89] focused mainly on the reaction kinetics at very short times. Thus, researchers have shown that the accumulation of copolymers at the interface slowed down the kinetics, because of an energy barrier created preventing unreacted homopolymers to reach the interface for further reaction. Those studies were completed by experimental studies showing that this slower kinetics were spontaneously compensated, even in static conditions, by an acceleration due to roughening of the interface. Those interfacial fluctuations allow new reactive moieties to reach the interface and therefore the conversion rate to increase under certain conditions [87, 90, 44, 80, 79, 72, 81, 91, 92]. In addition to an acceleration of the reaction kinetics, these interfacial roughening can generate small micelles in blend phases.

Orr et al. (1997) were one of the first academic teams to discuss the fact that different mechanisms could lead to generation of interfaces in polymer blends. In some cases the surface area of the micron scale morphology observed was too small compared to the very large quantity of copolymer formed. In other cases, blends of aliphatic amine terminated polystyrene with anhydride terminated polyisoprene formed a nano-scale microstructure very quickly. Their results implied that, in addition to the usual drop break-up and coalescence process, another mechanism was responsible of interfacial generation. They attributed this mechanism to the coupling reaction that happened at interfaces.

Later, many authors have obtained similar results [93, 94, 95, 44, 96, 34] as Jeon et al. [97] who found that during blend reactive compatibilization, less than 35% of the copolymer formed were located at the interface of the micron scaled domains observed, the rest exists in the matrix as micelles with sizes of 20-50 nm.

In this section, the interest will be focused on how the interfacial roughening is initiated and the mechanisms proposed in the literature to explain the formation of the dual scale morphology and especially the formation of micelles, also called nano-dispersions.

### 6.1 Interfacial roughening in static conditions

During the last two decades, some research teams have noticed that morphologies can be developed in absence of any shear stresses between immiscible polymers able to react at the interface [78, 80, 90]

For example, Macosko's team (Lyu et al., 1999) [90] conducted a series of experiments under static conditions at 200 °C between aliphatic amine terminated polystyrene (PS-NH<sub>2</sub>) and anhydride terminated poly(methyl methacrylate) (PMMA-ah). The molecular weights are respectively  $Mn_{PA-NH_2} \approx 18500$ g/mol and  $Mn_{PMMA-ah} \approx 29000$ g/mol, the polydispersity index 1.05 and 1.03 and the degrees of functionalization are 0.95 and 0.9. After 20 and 60 min, they observed a roughening of the interface which was the consequence of the coupling reaction as shown in figure 1.31. An interesting observation was that, at the interface of the thin domains (figure f) after 1 h of annealing, lamellae

microstructure appeared. It indicates the formation of PS-PMMA block copolymer. No further discussions were made about the microstructures obtained and how they formed. They attributed interfacial roughening to the large decrease in interfacial tension due to the creation of copolymers at the interface. They supposed that local fluctuations may be induced by thermal fluctuations as soon as block copolymer coverage at the interface decreases below the saturation level. This creates new interfacial area that allows new reactive moieties to reach the interface and new copolymers to be formed. The phenomenon of interfacial instabilities continuously creates new interface so that the interface becomes rough.

For this example the  $\chi N$  parameter was estimated to be about 13. They reproduced the same experiment with a system with  $\chi N$  of 34 and did not observed significant roughening in this case. They estimated that the energy barrier created in the case of longer chains (which increases with the  $N$  parameter), is very strong and prevent homopolymers to diffuse to the interface and to reach the saturation level. Thus, based on these 2 experiments, interfacial roughening occurs only for low molecular weight samples. Their work has complemented Jiao's et al [47] by providing more detailed evidence of the existence of the phenomenon of interfacial roughness in static conditions.

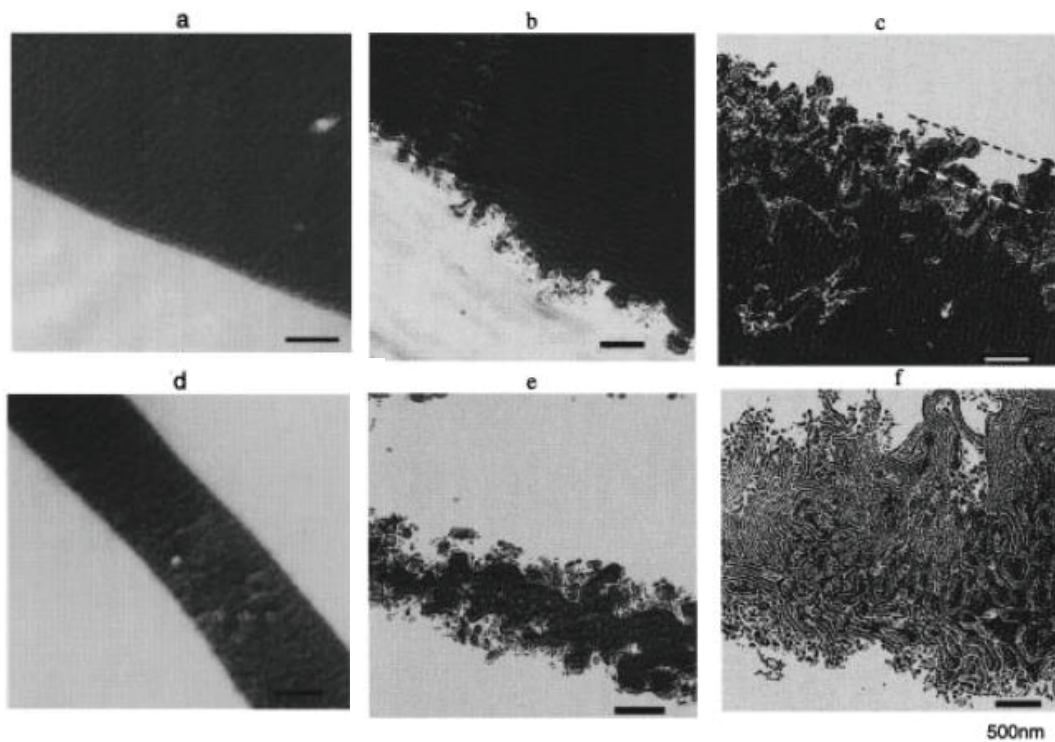


Figure 1.31: Representative morphologies of PA-NH<sub>2</sub>/PMMA-anh blends (in black and grey respectively) after static reaction at 200°C at large domain interface for (a) 0, (b) and 20 (c) and 60 min and at thin sheet interface for (d) 0 (e) and 20 (f) 60min. Two dash lines in (c) approximately indicate the roughening zone. The magnitude of its width is roughly 0.5  $\mu\text{m}$ . The scale bar represents 500 nm for each micrograph. [90]

**Concept of interfacial coverage** In order to determine the reaction rate, several research teams estimated the quantity of copolymers created in situ at the interface called

## 6. Effects of the compatibilization reaction on the morphology development of polymer blends: interfacial roughening and nanodispersions creation

---

interfacial coverage  $\Sigma$  [23, 24, 80, 79, 91, 34].  $\Sigma$  represents the number of copolymer chains at the interface per unit area. Different parameters can be used to calculate  $\Sigma$ . For example, the conversion rate of homopolymers into copolymers was calculated from SEC measurement after pyrene or anthracene labelling with a fluorescence detector [80, 79, 91]. The mean volume diameter  $D_v$  of a dispersion per unit area [79, 34] obtained directly from the SEM images or determination of the thickness of a monolayer of copolymer measured by AFM [80, 34] can also be used to determine  $\Sigma$ .

$\Sigma_{eq}$  corresponds to the theoretical copolymer interfacial coverage of a pure copolymer layer at the equilibrium. The creation of copolymers at the interface contributes to decrease the interfacial tension.

With the present definition of  $\Sigma$ , it is expected to get  $\Sigma$  smaller or equal to  $\Sigma_{eq}$  because, if the number of chain at the interface is higher than the number of chain at equilibrium, chain stretching becomes thermodynamically unfavourable. The rate of interfacial coverage can be determined by the ratio  $\Sigma/\Sigma_{eq}$ .

**Important remark:** In our work (see chapter 3),  $\Sigma$  defines the average interface area per chain, which is thus different from the  $\Sigma$  defined here.

Jérôme's team (Yin et al., 2003) [80] compared the reactive formation of linear diblock copolymer at the interface between two films of polystyrene with amine end-groups (PS-NH<sub>2</sub>) and PMMA chains with anhydride end-groups (PMMA-anh), in static conditions and annealed at 200 °C. Two formulations with varying blocks lengths were studied:

- Linear diblock copolymers of low molecular weight: PMMA-anh (15kg/mol) / PS-NH<sub>2</sub> (17kg/mol).
- Linear diblock copolymers of high molecular weight: PMMA-anh (28kg/mol) / PS-NH<sub>2</sub> (27kg/mol).

The conversion rate of PS-NH<sub>2</sub> into diblock copolymer was measured by SEC with UV detector. The interfacial coverage  $\Sigma$  as a function of time is presented in figure 1.32. They firstly showed that the interfacial reaction was faster for shorter reactive chains and they attributed this result to the higher concentration in reactive moieties, resulting in more efficient collisions. After 40 min of reaction, the formation of diblock copolymers of low molecular weight continued to increase, while for high molecular weight, it levelled off. They estimated the maximum interfacial coverage  $\Sigma_{max}$  at 0.174 and 0.145 chain/nm<sup>2</sup> for respectively the low and high molecular weight diblock copolymers. Figure 1.32 shows that for high molecular weight after 40min  $\Sigma \approx \Sigma_{max}$ , thus an energy barrier to the diffusion of the reactive chains to the interface is formed which strongly limit and control the kinetics of the reaction. This energy barrier results from the entropy loss associated with chain stretching at the interface. Nevertheless, for low molecular weight  $\Sigma > \Sigma_{max}$ : the reaction is not stopped indicating that another mechanism helped the reaction to progress.

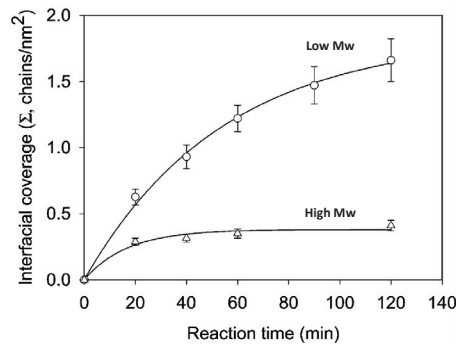


Figure 1.32: Interfacial coverage  $\Sigma$  of low molecular weight, PMMA-anh (15kg/mol) / PS-NH<sub>2</sub> (17kg/mol), and high molecular weight, PMMA-anh (28kg/mol) / PS-NH<sub>2</sub> (27kg/mol), diblock copolymers as a function of reaction time for low and high molecular weight reactive precursor.[80]

To understand this behaviour AFM, after dissolving the PS phase, and TEM images of the interfaces were performed as shown in figure 1.33. For the case of low molecular weights, the interface is very rough while for the long molecular weight it remained almost flat. They related this behaviour to the interaction parameter,  $\chi N$ . Indeed, for low molecular weight  $\chi N = 6$  is small and is favourable to the reaction progress. It leads to a rapid decrease in interfacial tension which results in the roughening of the interface. For the case of high molecular weights  $\chi N = 10$ , the symmetric diblock created at the interface does not allow fluctuations of interface, the energy barrier created limits thus the reaction.

It is thus *interfacial roughening*, very pronounced in the case of low molecular weight, which allows the reaction to progress after the formation of the energy barrier due to the creation of copolymers at the interface.

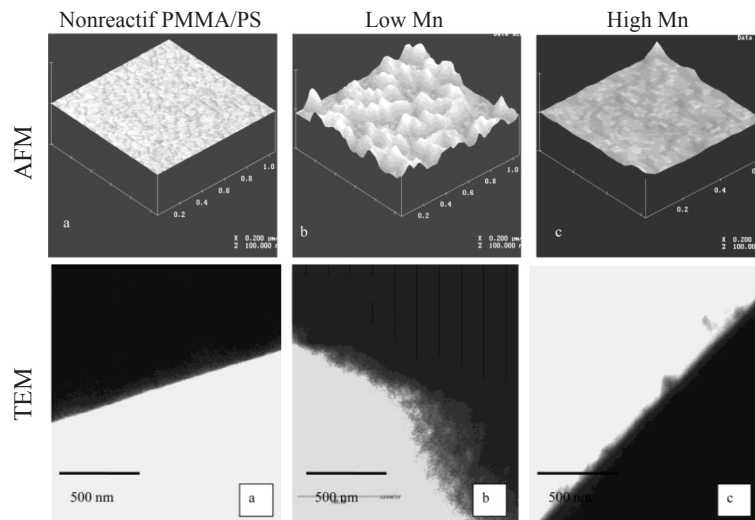


Figure 1.33: AFM images (after dissolving the PS phase) (top) and TEM observations (bottom) of the PMMA/PS interface after 60min at 200 °C in static conditions: (a) nonreactive PMMA/PS, (b) low molecular weight PMMA-anh (15 kg / mol) / PS-NH<sub>2</sub> (17kg / mol) and (c) high molecular weight PMMA-anh (28 kg / mol) / PS-NH<sub>2</sub> (27kg / mol). AFM: the layer of PS has been dissolved by selective solvent (scale bar 100nm). TEM: The dark phase is the PS (scale bar 500nm).[80]

## 6. Effects of the compatibilization reaction on the morphology development of polymer blends: interfacial roughening and nanodispersions creation

Kim et al. (2003) [92] studied the interfacial reaction between two films of end-functional monocarboxylated polystyrene (PS-mCOOH) ( $Mn_{PS-mCOOH} \approx 120\text{kg/mol}$ ) and poly(methyl methacrylates) (PMMA) ( $Mn_{PMMA} \approx 80\text{kg/mol}$ ) with various amounts of poly(methyl methacrylate-g-glycidyl methacrylate) (PMMA-GMA) ( $Mn_{PMMA-GMA} \approx 68\text{kg/mol}$  and  $\sim 12.5$  GMA/chain) which leads to the creation of graft copolymers. The complex viscosity  $\eta^*$  of PS-mCOOH is 40 times lower than that of PMMA (or PMMA-GMA). They measured the complex viscosity  $\eta^*$  during 16 hours at three different temperatures (180, 200 and 220°C) by dynamic rheometry. The strain amplitude was chosen to be 0.5% so that the reaction do not undergo the effect of shearing and happens almost like in static conditions. They showed that micelles (composed of pure graft copolymer or swollen by homopolymers) could be formed after interfacial roughening. Thanks to the viscosity measurement, they proposed three stages for the reaction:

- **Stage I:** The coupling reaction starts and a copolymer layer is formed at the interface.
- **Stage II:** The reactive moieties around the interface are totally consumed. New reactive moieties have to diffuse through the brush-like copolymer layer. Interface becomes corrugated.
- **Stage III:** New homopolymers can diffuse through the copolymer layer due to interfacial roughening and allow the reaction to progress. The interfacial thickness increase. When corrugations become to large, then PS domains can be pinched off from the interface in the PMMA phase. Micelles (10-20 nm) or microemulsions ( $\approx 100\text{nm}$ , which are micelles swollen of homopolymers) are observed as shown in figure 1.35.

The three stages of microemulsions formation are summarized in figure 1.34

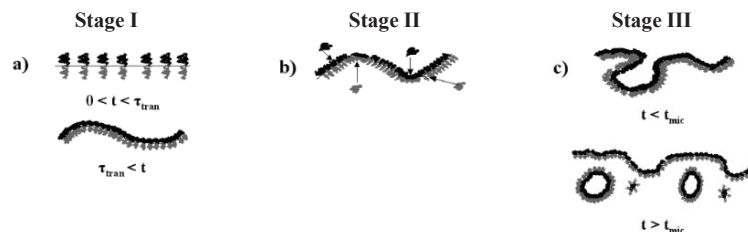


Figure 1.34: Diagram showing interfacial morphology changes between two films of PS-mCOOH / PMMA-GMA annealed (180, 200 or 220°) at different reaction times. a) Stage I: Coupling reaction occurs and formation of a layer of in situ graft copolymers b) Stage II: the interface thickness does not change, but reactant groups diffuse into the brush layer. c) Stage III: pinch-offs are observed at the beginning of this stage, and then microemulsions and micelles are formed at very long reaction times.[92]

As shown in figure 1.34 and discussed by the authors in a second article [98], only microemulsion of PS were observed after pinch-off into the PMMA phase, and not in the PS phase. This was explained by the architecture of the copolymer created: the graft copolymer created is more stable when the two branches of Y-shaped copolymer are located outside the curvature as shown in figure 1.36. Thus by curving the initial flat interface toward the PMMA phase, the two branches find more space to avoid steric hindrance.

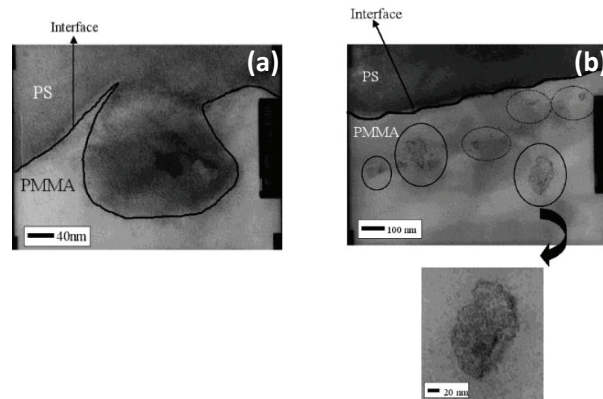


Figure 1.35: TEM images of the interface of a PS-mCOOH / PMMA-GMA blends annealed at  $180^\circ$  after: (a) 6 hours which corresponds to the beginning of stage III, interfacial roughening is clearly observed, however, neither microemulsion nor micelles are observed and (b) 17 hours, corresponding to the end of stage III, here both microemulsions and micelles were observed.[92]

Their main argument for micelle departure is the copolymer architecture. They do not pay much attention to the difference of viscosity between PMMA and PS phase to explain micelles departure or of the sinusoidal stress applied, even though it is very weak, they do not consider its possible effect on micelle departure. Finally, they do not discuss the shape of the micelles which are not really spherical as it could be expected.

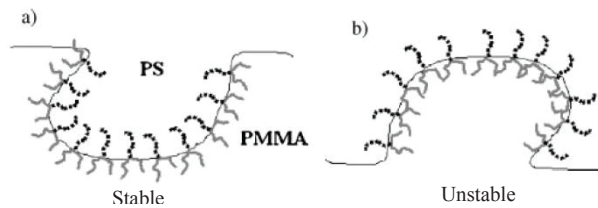


Figure 1.36: Schematic representation of PS-GMA / PMMA-midCOOH Y-shaped copolymer layer in (a) stable configuration (case observed in TEM images) and (b) unstable configuration. [98]

Kramer's team (Kim et al., 2005) [99] has studied the reaction of end-functionalized polymer chains at the interface between polystyrene (PS) ( $M_n=207\text{kg/mol}$ ) and poly(2-vinylpyridine) (P2VP) ( $M_n=152\text{g/mol}$ ) at the melt interface at  $125$  and  $170^\circ\text{C}$  under static conditions. Diblock copolymers were formed at the interface by the reaction of amine end-functionalized deuterated PS (dPS-NH<sub>2</sub>) ( $M_n = 4.3\text{kg/mol}$ ) with anhydride end-functionalized P2VP (P2VP-anh) ( $M_n=4.2\text{kg/mol}$ ). All sample were prepared in solution by spin casting of thick layers of mixtures of P2VP and P2VP-ah (volume ratio of 0.12) and of PS and dPS-NH<sub>2</sub> (volume ratio 0.12). Conditions were chosen such that the system is in the "dry brush" regime. As the density of copolymers created at the interface increases, interfacial tension decreases and the interface becomes unstable inducing interfacial roughening. They showed experimentally that interfacial roughening appears when a certain density of copolymer created at the interface is reached. This density correspond to a zero interfacial tension. After that, thanks to the fresh interfacial area created which allows the reaction to progress, corrugations can grow with a length scale

## 6. Effects of the compatibilization reaction on the morphology development of polymer blends: interfacial roughening and nanodispersions creation

of around 15 nm. This size was comparable to the diameter of diblock copolymers emulsified droplets found near the interface into the P2VP phase as shown in figure 1.37. Due to the symmetric nature of the block copolymer created they observed roughening grow on both side of the interface but only droplet of PS migrate into the P2VP. However there is no clear explanation why the formation of droplets is favoured in the P2VP phase and not in the PS phase.

Kramer's and Macosko's teams [99, 90] are in agreement on the fact that interfacial tension needs to decrease to zero for interfacial roughening to appear.

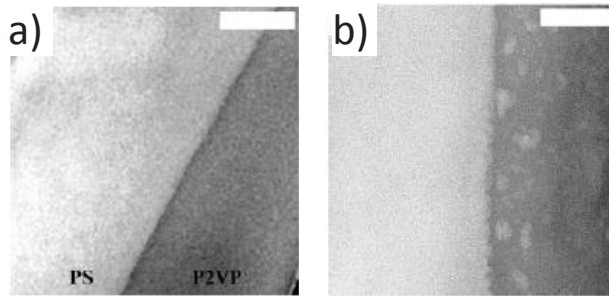


Figure 1.37: TEM images of the interface between the PS (light grey) and P2VP (dark) after annealing at 125°C as a function for different reaction time. (Scale bar 100 nm).[99]

Similarly Macosko's team (Zhang et al., 2005) [91], observed interfacial roughening between a layer of Amine-terminal polystyrene (PS-NH<sub>2</sub>) ( $M_n=18\text{kg/mol}$  and  $I_p=1.2$ ) and a layer of anhydride-terminal poly(methylmethacrylate) (PMMA-anh-pyr) ( $M_n=23\text{kg/mol}$  and  $I_p=1.27$ ) (after static annealing at 175°C. For systems containing enough reactive moieties in bulks, when  $\Sigma < \Sigma_{eq}$  (with maximum interfacial coverage  $\Sigma_{eq}$  estimated to 0.2 chains/nm<sup>2</sup>) slight interfacial fluctuations appeared. After further reaction time,  $\Sigma$  reached  $\Sigma_{eq}$  and interfacial roughness increased sharply. Their experiment suggests emulsification (i.e. micelle departure from the interface) because after that, the interfacial coverage  $\Sigma$  exceeds  $\Sigma_{eq}$  which suggest that new interfacial area is formed and eventually, emulsification. However their TEM micrographs only show emulsification and not micelles departures as show in figure 1.38.

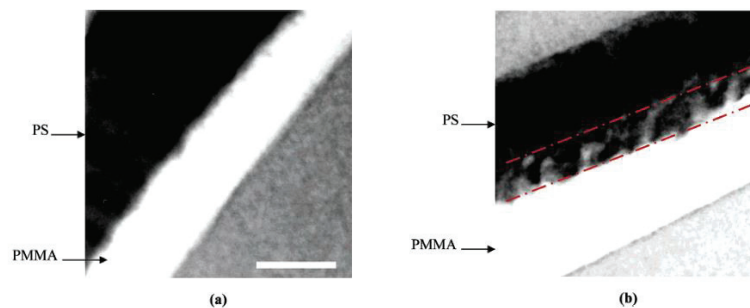


Figure 1.38: Interfacial roughening observed with TEM (a) unreactive PS/PMMA-anh-pyr blend; (b) 100 wt% reactive PS-NH<sub>2</sub>/PMMA-anh-pyr blends. Both samples are annealed at 175°C for 1 h. (Scale bar is 200 nm). [91]

Recently, numerical simulations of the coupling between immiscible polymers leading to the creation of block and graft copolymers of different architectures and symmetry were performed [87, 100, 101]. Berezkin et al. (2012) [100] investigated the mechanism of

interfacial instability caused by saturating layer of copolymers which leads to formation of spontaneous microdomains at the interface. They compared the microstructure development and the different kinetics regimes obtained with different compositions and architectures of block linear or graft-copolymers. Depending on the block length and global copolymer architecture, different microstructures were obtained as shown in figure 1.39. They have found that a lamellae-forming blend leads to very fast exponential kinetics while for microstructures other than lamellae, the kinetics is much slower. Another interesting point is that different morphologies, for example, cylinders and spheres or micelles, can develop at the same interface.

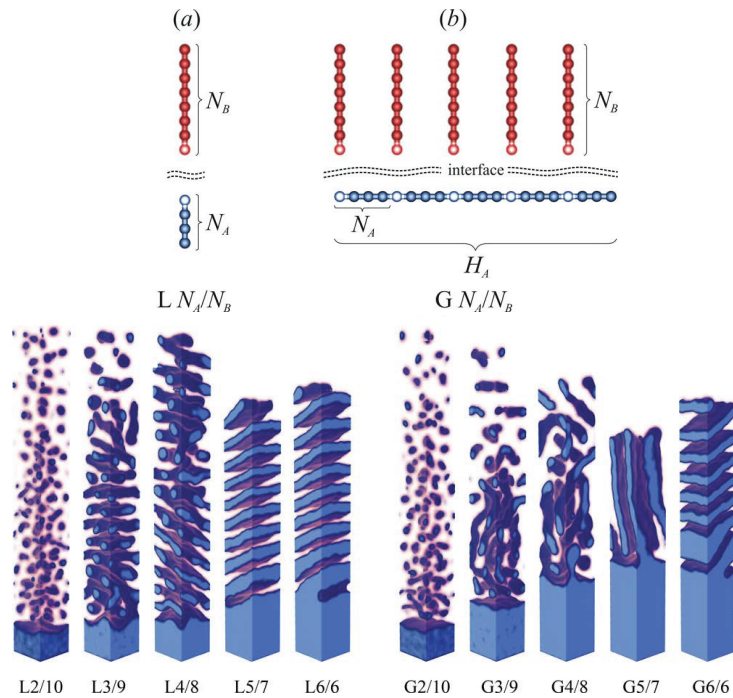


Figure 1.39: Numerical simulation of the microstructure developed at the interface due to the coupling reaction in static conditions forming L=Linear dibloc copolymer and G=Graft copolymers of different architectures. Only the A phase is shown.[100]

To summarize, all the research team previously mentioned [91, 90, 77, 80, 78, 92, 99] have shown the spontaneous formation of interfacial fluctuations during static annealing, and in some case departure of micelles from the interface, only due to the coupling reaction at the interface were possible. Numerical simulations have also been performed [87, 100, 101]. The exact mechanism of interfacial roughening by reactive polymers is still of considerable controversy. Different steps involved in this process during static annealing proposed may be summarized as follow:

- During the compatibilization reaction, a huge amount of copolymers is created at the interface decreasing dramatically the interfacial tension due to chain stretching. In the same time, the copolymer interfacial coverage  $\Sigma$  increases.
- When  $\Sigma = \Sigma_{eq}$  the density of the copolymer layer corresponds roughly to the theoretical copolymer interfacial coverage of a pure copolymer layer at the equilibrium. The surface tension is thus decreased. The value at which interfacial tension decreases is still discussed. It was assumed that  $\Gamma$  is decreased to zero or lower values

## 6. Effects of the compatibilization reaction on the morphology development of polymer blends: interfacial roughening and nanodispersions creation

if  $\Sigma > \Sigma_{eq}$ . A barrier energy to homopolymer is created due to the entropy loss induced by chain stretching: it should be difficult for new reactive species to reach the interface because they have to penetrate the brush-like copolymer layer. Only the smallest chains may perhaps reach the interface.

- However, the interfacial tension is close to 0 so that almost no additional energy is needed to create new interface. Interfacial fluctuations may be initiated. Some authors report that they may be induced by thermal fluctuations. This creates new interfacial area that allows new reactive species to reach the interface and new copolymer to be formed.
- The phenomenon of interfacial instabilities continuously creates new interface so that the interface becomes rough.
- In some cases, small micelles, or swollen micelles, can leave the interface to migrate in one of both phases and create the nanodispersion. The mechanism responsible of micelles departure in static conditions is still unclear in the literature. Macosko's team observed the creation of a lamellar structure at the interface which was also predicted by the numerical simulations of Berezkin et al. .

### 6.2 Interfacial roughening under shear

Industrial reactively compatibilized polymer blends are very often blended under shear via extrusion processes, which induce short process times. In such systems, the interface between immiscible homopolymers is never at the equilibrium because of the ongoing competition between the phenomena of drop break-up and coalescence, enhanced by shearing. Furthermore, Macosko et al. [81], indicate that the reaction rate is up to 1000 times higher during heterogeneous blending in the melt state under shear than in static conditions between two polymer layers. However, several research teams noticed the formation of nanodispersions or subinclusions, in addition to larger scale morphologies, which were not the consequence of the well known break-up and coalescence mechanisms. They attributed these morphologies to an effect of the compatibilization reaction. Different mechanisms were proposed and are summarized below.

In a first study on polysulfone (PSU) / polyamide (PA) blends, Charoensirisomboon et al. (1999) [102] showed that a large amount of linear diblock copolymers formed at the interface escaped the interfacial region to form micelles in the bulk, which was not the case with graft copolymers, this phenomenon was called "Pull-out of copolymer" [103, 104, 105, 106]. A schematic representation of copolymer 'pull-out' is shown in figure 1.40.

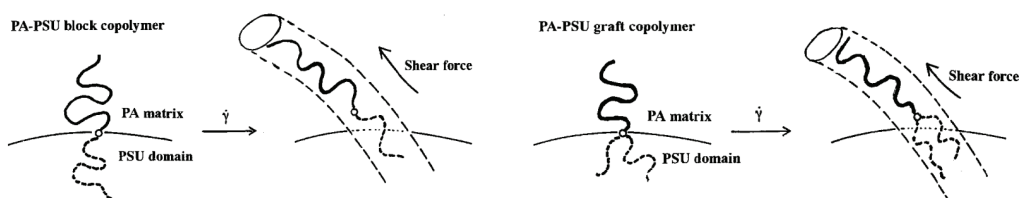


Figure 1.40: Tube model for the pull-out of in situ formed copolymers showing that graft copolymers will be subjected to greater spatial constraints than linear diblock copolymer [103].

Pull-out would be the consequence of hydrodynamic conditions generated during compounding (external shear forces) and depends on the thermodynamic stability of the copolymer at the interface (chain packing and block stretching) and thus on the copolymer architecture (block or graft). Linear and graft copolymers with the 2 arms side at the external side of the curvature would be more subjected to pull-out than when the two arms side in located inside the curvature [107, 108]. Longer blocks (higher molecular weights) should limit the pull-out. However, this mechanism supposes that only one chain of copolymer is pulled-out from the interface by hydrodynamical forces. To the best of our knowledge this interpretation has never been discussed in more recent studies.

Bhadane et al [93] studied Polyamide-NH<sub>2</sub> / Poly(isobutylene-co-p-methylstyrene) blends (PA/IMSM) with different amount of Brominated Poly(isobutylene-co-p-methylstyrene) (BIMSM) prepared using a Brabender internal mixer (90/10%wt). During the in-situ formation of BIMSM-PA graft copolymers at the interface 38 potential Bromine sites are available per BIMSM molecule for reactive grafting with PA.

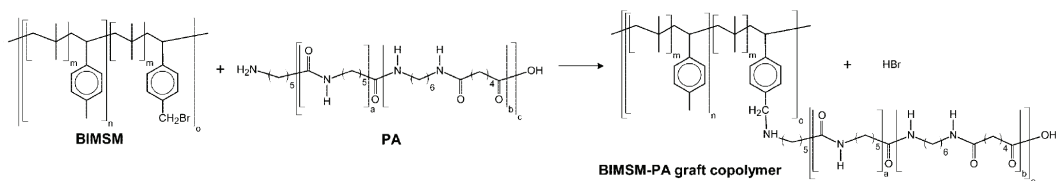


Figure 1.41: Reaction between BIMSM and PA to form a BIMSM-PA graft copolymer [93].

Over the entire composition range of PA/(IMSM/BIMSM) blend tested, small micelles of IMSM were observed in addition to larger domains in the PA phase. The authors explain the micelles formation by a mechanism of “interfacial erosion”. In this case, several PA chains (up to 38) can react with one BIMSM molecule and form a graft copolymer with several segments and highly increases locally the viscosity. They argued that a viscosity mismatch between interfacial region of high viscosity and blend components, would tend to pull out the copolymer away from the interface, during melt mixing. A schematic representation and AFM picture are presented in figure 1.42. Note that these micelles departure could also be due to interfacial roughening as it was observed for several studies in static conditions, but this was not mentioned by authors. The difference between these two mechanisms is the driving force generating nanodispersions: for this study it is the viscosity mismatch between the locally high interfacial viscosity and blend components and in the other case interfacial roughening are due to the chemical reaction at the interface.

6. Effects of the compatibilization reaction on the morphology development of polymer blends: interfacial roughening and nanodispersions creation

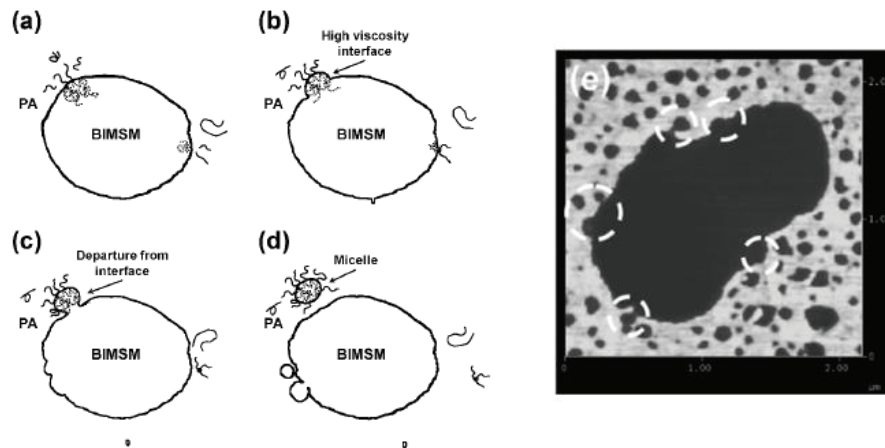


Figure 1.42: Schematic representation of interfacial erosion mechanism responsible of morphology development (left). AFM micrograph in BIMSM/PA blend. Scale  $2.1 \times 2.1 \mu\text{m}$ . [93]

Ten years ago, one of the objective of Leibler's team ([109, 27] was to obtain blends with co-continuous morphologies structured at the nano-meter scale. Their goal was to make stable blends by reactive extrusion with a major composition of polyethylene (80%wt) and continuous nanostructuring of the PA6 (20%wt) to benefit from the thermomechanical resistance of the PA6. They studied highly polydispersed random copolymers of ethylene, ethylacrylate and maleic anhydride (PE-1  $Mn_{PE-1} \approx 9300\text{g/mol}$  with  $IP=5.5$  and 1%wt AM and PE-0.5  $Mn_{PE-0.5} \approx 16000\text{g/mol}$  with  $IP=5$  and 0.5%wt AM) and low molecular weight polyamides 6 with one amine ( $\text{NH}_2$ ) per chain ( $Mn_{PA6} \approx 2500\text{g/mol}$  with  $IP=2$ ). The ratio between the length of the PA6 chain and the distance between graft on the PE backbone was chosen in order to favour a large curvature radius of the interface where grafted copolymers are formed in-situ during blend preparation.

In this study, mainly entirely nanostructured blends have been observed as shown in figure 1.43. Nevertheless, for some blends, a double morphology with nodules of few nanometers were observed concomitantly with larger domains of few microns in blends. An example is shown in figure 1.44. This morphology was explained by the principle of macrophase separation, i.e. by the ability of the copolymer created to incorporate non-reactive homopolymers. Depending on the regime of incorporation (wet or dry brush), homopolymers can be incorporated or not in the brush. In that case the large quantity of PA homopolymers could not be incorporated and homopolymers organized as large domains of PA. This interpretation was also discussed in other studies of Leibler's team. They also showed that nanostructured blends could be swollen by low molecular weight polymers without changing the morphology [45] [109] [46] [110]. In this work, the rheological mechanisms that happen during blend compounding as well as interfacial roughening are not discussed. Results are only discussed in terms of copolymer architecture thermodynamic.

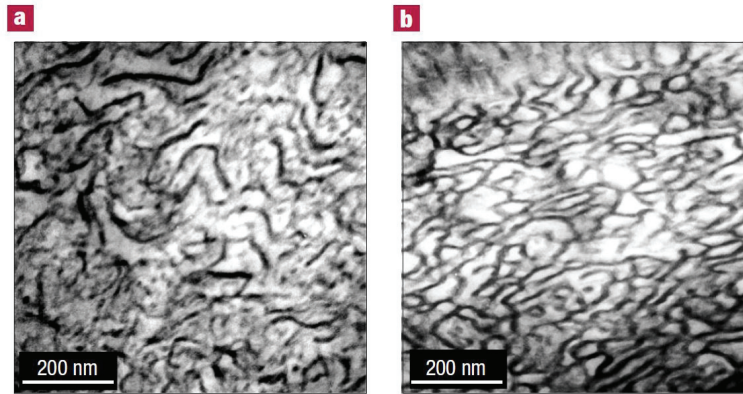


Figure 1.43: TEM micrographs after 1 min of extrusion for (a) 70/30 wt% PE-1/PA6 blend and (b) 60/40 wt% PE-1/PA6 blend [109].

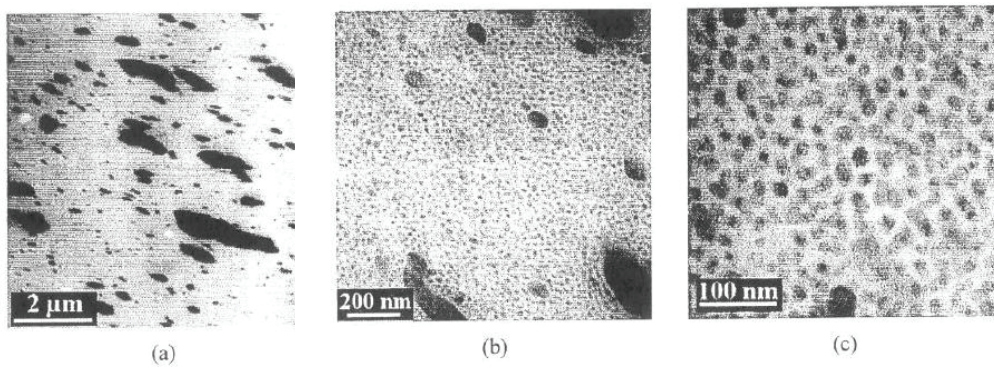


Figure 1.44: TEM micrographs at three magnification after PA6 staining of binary blends PE-0.5/PA6 (80/20wt%) to show the two characteristic sizes of morphology: micron scale PA6 domains and nanostructured organisation of the matrix. [27]

Macosko's team (Zhang et al., 2010) [111] studied a reactive coextruded multilayer system of polystyrene(PS)/ poly(methyl-methacrylate)(PMMA), each component containing 10wt% functional polymer respectively PS-NH<sub>2</sub> (0.71%wt NH<sub>2</sub>) and PMMA-anh (0.84%wt anhydride). The molecular weight  $M_n$  of PS, PMMA, PS-NH<sub>2</sub> and PMMA-anh were respectively 140, 52, 37 and 21kg/mol and IP of 2, 2, 1.21 and 1.24). The reaction conversion was measured by SEC and observed by TEM or SEM. Subsequent steady shear of the multilayer samples was performed and destroyed the layer structure. Micelles and swollen micelles of PS were observed under shear into larger PMMA domains. Authors does not make directly the link with a possible interfacial roughening.

Some other authors also noticed the presence of micelle domains in addition to larger domains in their blends like Sailer et al. (2008) [112] and discussed their possible effect on rheological properties.

The different studies mentioned above show that there is no systematic studies which tried to make the link between interfacial roughening observed in static conditions and micelles obtained in blends under shear.

## 6. Effects of the compatibilization reaction on the morphology development of polymer blends: interfacial roughening and nanodispersions creation

---

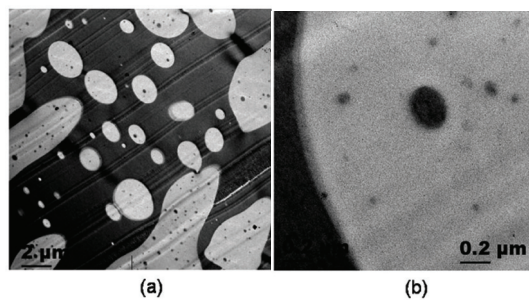


Figure 1.45: TEM image of PS/PMMA reactive multilayer after shearing  $1s^{-1}$  and  $200\text{ }^{\circ}\text{C}$  for 2h. The dark phases are PS, and the white phases are PMMA. The dark inclusions in the PMMA phases are presumed to be micelles and swollen micelles. [111]

## 7 Conclusion

The main objective of this work is to be able to control multi-scale morphologies developed in reactively compatibilized polymer blends.

The main mechanism described in the literature for morphology development, is the well-known mechanism of droplet break-up and coalescence, controlled by classical rheological laws. This mechanism has been widely studied on model systems of single Newtonian droplets in a Newtonian matrix. In viscoelastic polymer blends, examples are numerous for blends with a viscosity ratio close to one, but in general, *only few compositions are studied and do not cover the whole composition range. Besides, systematic studies are missing concerning the morphology development when the viscosity ratio is far from one and over a broad composition range.*

The usual description of the effects of the reactive compatibilization on the morphology development is the following: copolymers created at the interface decrease the interfacial tension and allow the break-up into thinner droplets. They also prevent coalescence and thus stabilize morphologies and improve adhesion between phases at the solid state. However, this description is often limited to systems with a low amount of compatibilizer. Another vision, that has been recently developed, is to synthesize entirely nanostructured polymer blends by reactive extrusion.

A recent study performed in our lab has shown that, in addition to the micron-scale morphology developed by drop break-up/coalescence, a second mechanism due to the chemical compatibilization reaction could lead to formation of nano-dispersions. Figure 1.46 shows that with SEM observations, only the micron-scale morphology can be observed, however, TEM observations allow to observe the concomitant presence of nanodispersions. These nano-dispersions can be very numerous and observed in both phases. In many cases of the literature, nanodispersions are indeed present, but are not taken into account in the discussions. To the best of our knowledge, *no academic research team has already tried to control the formation of nano-dispersions. Only few academic studies have observed that interfacial roughening, or even spontaneous micelles departure from the interface, could happen in static condition no systematic studies were performed to make the link with morphologies observed in reactively compatibilized blends. This literature review leads to the conclusion that, even if mechanisms for the formation of these nano-dispersions have already been proposed in few preliminary studies, there is still no consensus on this point.*

To identify the most promising parameters that control the formation of nanodispersions, we considered studies dealing with the thermodynamical properties of the copolymer layer created at the interface, as well as the compatibilization reaction characteristics (parameters influencing the kinetics and the final conversion of the chemical reaction used for the blend compatibilization). *One of the most promising lever is to optimize the architecture of the copolymer formed at the interface. However, the micron scale morphology is controlled by other parameters like the viscosity ratio, the shear rate, etc...* In reactive compatibilizations copolymer architecture and viscosity ratio are closely related because they both depend on components molecular weight.

Thus, thanks to the literature review, *we formulated blends in which parameters are varied*

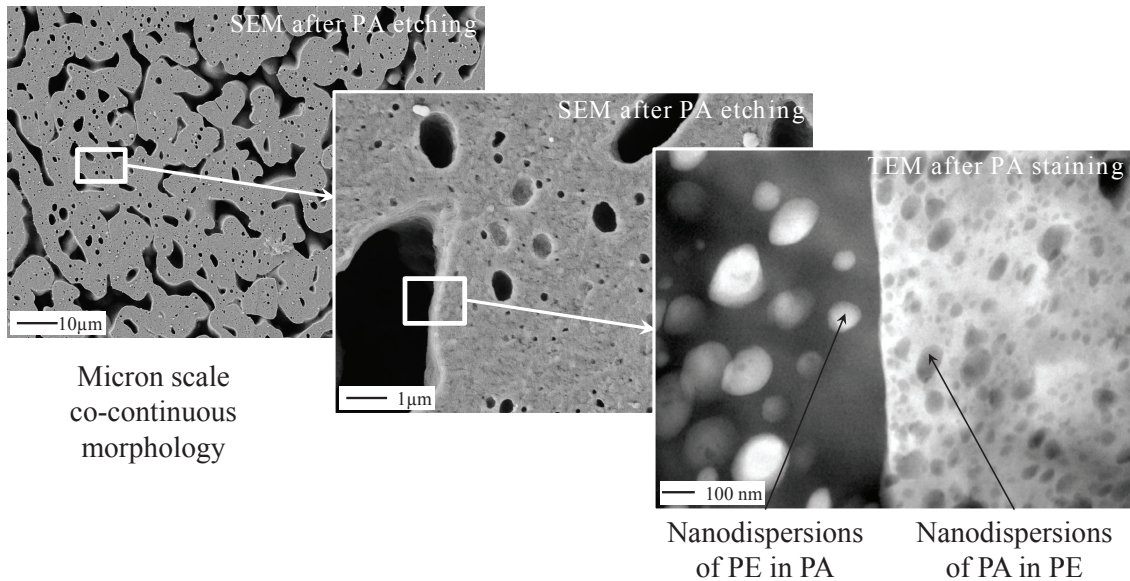


Figure 1.46: SEM micrograph after PA6 etching showing the micron-scale co-continuous morphology and TEM micrograph after PA6 staining showing nanodispersions in both phases of blend PA6-10k/MA-g-HDPE (44/56%vol).

*strategically: by changing only the molecular weight of the linear PA6 in binary blends, the viscosity ratio as well as the copolymer architecture are varied at the same time. In order to perform systematic studies, compositions are varied over a wide range of composition. Those formulations allow to investigate the morphology development of highly compatibilized blends, with very different viscosity ratios over a large composition window.*

However, in compatibilized blends, both effects of rheological processes (shearing) and chemical reaction of compatibilization are responsible of morphology development.

To decorrelate both effects, studies of the corresponding uncompatibilized binary blends, with HDPE instead of the MA-g-HDPE, in which only rheological processes are involved, are performed. It allows to *investigate mechanisms of drop break-up and coalescence when the viscosity ratio is far from one.*

In parallel, studying the compatibilization reaction in static conditions allows to study effects of the chemical coupling reaction at the interface alone. We have seen that some research teams observed spontaneous destabilization of the interface in static conditions. However, the different stages of the process which leads to interfacial fluctuation are not fully understood and, in particular, parameters that control the initiation of interfacial fluctuations. *Another interest of this work is that studying the compatibilization reaction in static conditions between the different PA6 and MA-g-HDPE chosen, could allow to study in more details the effect of different copolymer architectures on the interfacial destabilization.*



## 1 Introduction

In this chapter, the materials used for the study are first presented: three polyamide 6 (PA6), one Maleic-Anhydride grafted High Density Polyethylene (MA-g-HDPE) and one High Density Polyethylene (HDPE). The two polyolefins are commercial grades but the three linear PA6 have been synthesized at Solvay. Thus a deeper description of the characteristics of those three polymers is given. Then, the blending process as well as characterization methods are detailed. Essentially morphological and rheological characterizations of raw materials and blends have been performed. The method used to perform static annealing is also described.

A particular attention has been paid to sensitivity of raw materials constituting blend components to process conditions. Indeed, the extrusion temperature (290 °C) is very high, especially for HDPE, and PA6 is very sensitive to moisture. Thus, the stability of HDPE, MA-g-HDPE and PA6s during process and during rheological measurements (which are performed at 290 °C) were checked. ThermoGravimetric Analysis (TGA), Size Exclusion Chromatography (SEC) and time sweep tests at constant strain and frequency were carried out.

Finally, since blends rheological behaviours were studied in this work, characterizations of the rheological behaviour of pure blend components were performed. A special attention was paid on the rheological behaviour of polyamide 6 which is very sensitive to moisture content.

## 2 Materials

In this work, both uncompatibilized and compatibilized binary blends have been studied:

- Uncompatibilized binary blends: Polyamide-6 (PA6)/High Density Polyethylene (HDPE).
- Compatibilized binary blends: Polyamide-6 (PA6)/HDPE grafted Maleic anhydride (HDPE-g-MA).

### 2.1 Compatibilization reaction

The compatibilization reaction between Maleic Anhydride (MA) moieties of compatibilizer and amine end-groups ( $\text{NH}_2$ ) of PA6 is schematized in figure 2.1. It leads to the formation of PA6-g-HDPE grafted copolymer at the interface between the PA6 and PE phases during processing. The HDPE blocs of the copolymer created are considered to be miscible with the unreacted MA-g-HDPE homopolymers.

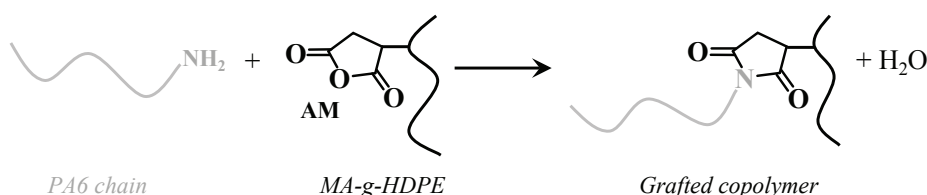


Figure 2.1: Compatibilization reaction

Macosko's team (2005) [82] studied the homogeneous reactive coupling between aliphatic amine terminal and cyclic anhydride terminal chains and found that the reaction was very fast (complete is less than 30s). The same kind of reaction was studied in heterogeneous conditions at polymer interfaces in static conditions [81]. The conversion into imide is almost complete at 180 °C after annealing 2 minutes. Under shear, the coupling reaction can be as much as 1000 times faster than that under static annealing [81, 111].

### 2.2 Characteristics of neats polyolefin: HDPE and MA-g-HDPE

#### 2.2.1 Reactive compatibilizer: MA-g-HDPE

The used Maleic Anhydride grafted High Density Polyethylene (MA-g-HDPE) reactive compatibilizer contained 1% in weight of MA moieties. In neat compatibilizer, the concentration of MA moieties (1% by weight) corresponds to  $2.9 \cdot 10^{-3}$  mol of MA per mole of monomers ( $\text{CH}_2 - \text{CH}_2$ ) that is to say 101 mmol/kg. Considering the molecular mass of the overall MA-g-HDPE ( $M_n \approx 29000$  g/mol), there are  $\approx 1035$  monomers ( $\text{CH}_2 - \text{CH}_2$ ) in average per chain of compatibilizer. By combining both data, there are in average 3 MA moieties per chain of compatibilizer. Thus, there are about 350 monomers ( $\text{CH}_2 - \text{CH}_2$ ) between each grafted MA which represents a molar mass of 9800 g/mol. A schematic representation of the copolymer created between PA6 and MA-g-HDPE with, in average, 3 grafted PA6 chains per HDPE backbones is presented in figure 2.2. In what follows, this copolymer will be studied by analogy to the behaviour of one basic constitutive unit, an Y-shaped PA/PE copolymer, as represented inside the dotted area.

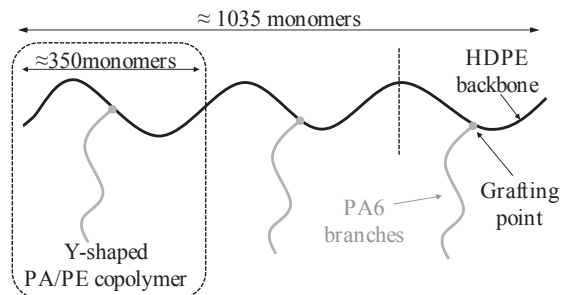


Figure 2.2: Schematic representation of the copolymer created between PA6 and MA-g-HDPE with, in average, 3 grafted PA6 chains per HDPE backbones. Inside dotted area is represented one constitutive unit of the entire copolymer: Y-shaped PA/PE copolymer.

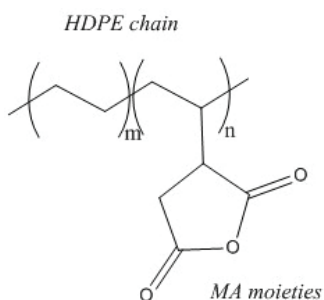


Figure 2.3: Maleic anhydride grafted HDPE.

### 2.2.2 HDPE

High Density Polyethylene (HDPE) is a thermoplastic semi-crystalline polymer (crystallinity amount can reach 85%). It is obtained by polymerization of ethylene gas, compressed at “low” pressure ( $\leq 50$  bar) which leads to the formation of linear macromolecular chains (HDPE can exhibit 1 or 2 short branching like  $-\text{CH}_3$  for 1000 carbon atoms in the main chain) [17]. The molar mass of HDPE monomer is 28 g/mol. Figure 2.4 shows developed formula of HDPE.

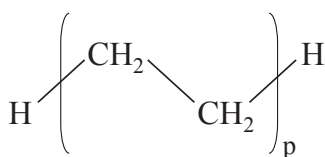


Figure 2.4: Developed formula of HDPE.

### 2.2.3 Characteristics of neat HDPE and MA-g-HDPE

The properties of neat HDPE of the study according to Size Exclusion Chromatography (SEC), to supplier data and to the literature [113][114] are shown in table 2.1. SEC measurements were performed by Olivier Boyron and Manel Taam (CPE Lyon).

Table 2.1: Properties of neat MA-g-HDPE according to literature [113][114], to SEC measurements (absolute values). IP: Index of Polydispersity.

	Mn (g/mol)	Mw (g/mol)	IP	$\rho$ (g/cm <sup>3</sup> ) at T <sub>room</sub>	$\rho$ (g/cm <sup>3</sup> ) at 290 °C
MA-g-HDPE	28900	58 000	2	0.95	0.72
HDPE	15800	35800	2.3	0.95	0.72

## 2.3 Polyamide 6

### 2.3.1 Generality on Polyamide 6

Polyamide 6 (PA6) is a thermoplastic semi-crystalline polymer (crystallinity amount can reach 40 to 50%). The molar mass of PA6 monomer is 113 g/mol. Figure 2.5 shows the developed formula of PA6.

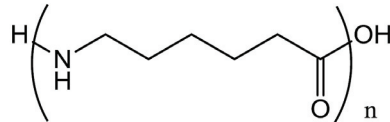


Figure 2.5: Developed formula of PA6.

PA6 is a polar polymer in which hydrogen bonds are formed between amide groups. Its  $T_g$  in the dried state is close to 60 °C. PA6, like other Polyamides, is sensitive to moisture and can absorb up to 9.5% in weight of water at saturation, at room temperature and 100% of hygrometry [17]. Water molecules break H-bonds, increase molecular mobility and thus decrease the glass temperature  $T_g$ . Moreover, at high temperature (typically processing temperature), an excess of water according to the water content at the polycondensation equilibrium of PA6, can induce chains hydrolysis and thus decrease of  $M_n$ . On the other hand, by decreasing the moisture amount below the equilibrium value, post-condensation of PA6 occurs during process, leading to an increase of the average molecular weights. That is why PA6 needs to be dried before processing at a moisture content calculated to be the equilibrium moisture at process temperature.

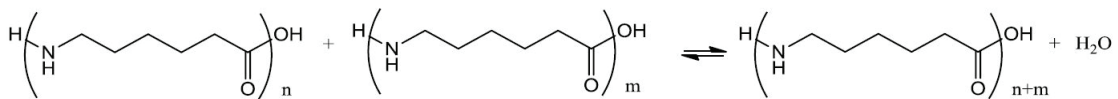


Figure 2.6: Polycondensation equilibrium of PA6

Densities at room temperature and in the melt state of polyamide are summarized in table 2.2:

Table 2.2: Densities of PA6 at room temperature and in the melt state.

	$\rho$ (g/cm <sup>3</sup> ) at T <sub>room</sub>	$\rho$ (g/cm <sup>3</sup> ) at 290 °C
PA6	1.13	0.96

### 2.3.2 Polyamide 6 of the study (coll. S. JEOL, R&I Centre Lyon, LSPP)

#### Synthesis

Polyamide 6 have been synthesized by polyaddition of  $\epsilon$ -caprolactam as shown in figure 2.7 and then polycondensation (see figure 2.6).

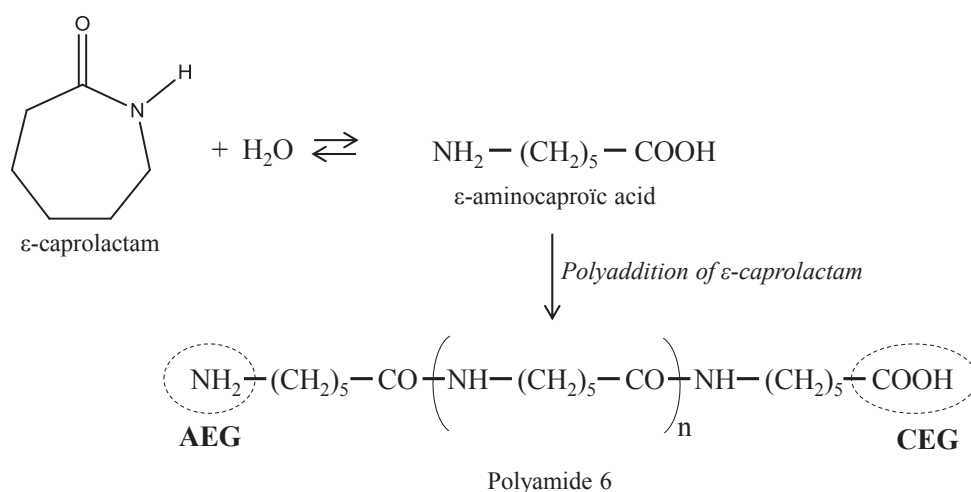


Figure 2.7: Standard polyamide 6 synthesis. AEG= Amine End Groups and CEG=Carboxylic End Groups.

In this thesis, three linear polyamide 6 have been synthesized at Solvay, R&I Centre Lyon:

- PA6-18k,  $M_n \approx 18000$  g/mol and PA6-31k,  $M_n \approx 31000$  g/mol. Each PA6 chain formed will have exactly one Amine End Group (AEG) and one Carboxylic acid End Group (CEG).
- PA6-3k,  $M_n \approx 3000$  g/mol. For PA6-3k, the synthesis protocol has been modified: a mono-fonctionnal comonomer (called Blocker End Group amine  $\text{BEG}_{\text{amine}}$ ) which reacts at chains ends with a part of carboxylic acids end groups of the PA6 chains, has been used. It thus allows to control the progression of the PA6 synthesis reaction and reduces the sensitivity of these short PA6 chains to hydrolysis and condensation reactions.

#### Characterization: End-Group titration

To characterize the PA6 after synthesis, viscosity index measurements (IV), end-group titration (EG) and Size Exclusion Chromatography SEC (Absolute and PS equivalent) were performed on each PA6 ( measurement were performed by Virginie REYNES and

Nadia DELON-ANIK(R& I centre Lyon, Analysis) and Julie SAUNIER and Rodolphe SAPEY-TRIOMPHE( R& I centre Lyon, LSPP)). The structural characteristics(after EG measurements) are reported in table 2.3. The molecular weight  $M_n$  can be deduced from the sum of End-Group (EG).

Table 2.3: Polyamide 6 characteristics after synthesis.

Name	AEG [NH <sub>2</sub> ] (mmol/kg)	$M_{n, \text{equilibrium}}$ (g/mol)
<b>PA6-3k</b>	347	≈ 2900
<b>PA6-18k</b>	55	≈ 18000
<b>PA6-31k</b>	33	≈ 30500

### Characterization: Size Exclusion Chromatography (SEC)

Chromatograms of SEC measurements are shown in figure 2.8. In pure polyamide there are residual cyclic oligomers left from the synthesis even after washing of the reaction medium. These oligomers have very small molecular weight and they do not exhibit any end-group. Thus, they should not be counted in the average molecular weight and oligomer truncation are generally carried out when analysing SEC data of PA6. Due to the very different molecular weight between samples, different oligomers truncation had to be done. Table 2.8 summarizes absolute average molecular weights of PA6 measured by SEC measurement for no oligomers truncation, truncation at 500g/mol and truncation at 1000g/mol.

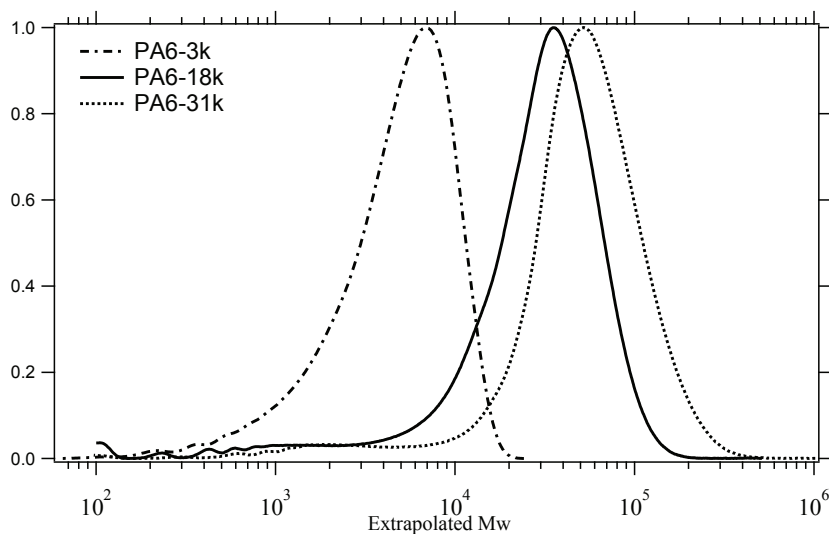


Figure 2.8: Chromatograms of Polyamide 6 PA6-3k, PA6-18K and PA6-31k after synthesis (SEC measurements, Absolute values).

## 2. Materials

Table 2.4: Absolute average molecular weight of PA6 measured by SEC at different oligomers truncation.

Name	No oligomers truncation			Oligomers truncature at 500 g/mol			Oligomers truncature at 1000 g/mol		
	Mn (g/mol)	Mw (g/mol)	Ip	Mn (g/mol)	Mw (g/mol)	Ip	Mn (g/mol)	Mw (g/mol)	Ip
<b>PA6-3k</b>	3500	6600	1.9	4300	6800	1.6	4700	7000	1.5
<b>PA6-18k</b>	8300	36000	4.35	14600	36500	2.5	18000	37000	2
<b>PA6-31k</b>	15300	58000	3.8	21100	58545	2.8	27200	59400	2.2

Globally, the molecular weight determined by both methods (SEC measurement or from end-group titration) are in agreement. However, because PA6 of very different molecular weight are studied in this work and especially PA6 with very low molecular weight (PA6-3k), the average number molecular weight  $M_n$  of polyamide 6 is more precise from the EG measurement. *In this work, the average  $M_n$ s that will be considered are thus the one calculated from the measure of End-Groups titration summarized in table 2.3.*

### Sample preparation before processing or analysis

Before compounding or analysis, pellets of PA6 were dried under a primary vacuum oven at 90 °C to control the moisture amount into the pellet. The moisture amount was calculated to be at equilibrium at process and analysis temperature (290 °C) in order to avoid any post condensation or hydrolysis of PA6 chains.

### Molar ratio $[NH_2]/[MA]$ in compatibilized binary blends

For each blend, the global molar ratio  $[NH_2]/[MA]$  theoretically introduced in the batch mini-extruder was calculated.  $[NH_2]$  concentration is known from the PA6 initial AEG content and the  $[MA]$  content is calculated from supplier data. Then for binary blend, the weight fraction of PA6,  $x$ , and MA-g-HDPE,  $y$ , corresponding to a given  $[NH_2]/[MA]$  ratio can be calculated. For example if the ratio  $[NH_2]/[MA]=1$  mol/mol is targeted, equation 2.1 is used:

$$\left. \begin{array}{l} \frac{x[NH_2]}{y[MA]} = 1 \\ x + y = 1 \end{array} \right\} y = \frac{1}{1 + \frac{[MA]}{[NH_2]}} \quad (2.1)$$

With  $[NH_2]$  and  $[MA]$  expressed in mmol/kg. Considering a melt density at 290 °C of 0.72 g/cm<sup>3</sup> for HDPE chains and 0.96 g/cm<sup>3</sup> for PA6, the corresponding volume fraction of the two polymers can be calculated.

### 3 Experimental

#### 3.1 Blending Process

Blending was carried out using a batch mini extruder (Microcompounder DSM Midi 2000,  $\approx 10$  g per batch). It operates under inert atmosphere ( $N_2$ ) (in collaboration with O. CHAUBET's team, with V. CURTIL, R & I centre Lyon, LSPP). The residence time can be controlled independently from the screw speed, using a recirculating system as shown in figure 2.9. The die characteristics are: diameter between 2.7 and 2.9 mm and length 35mm. Blends were prepared using fixed conditions:

- Screw speed: 100 rpm.
- Time of the process: 4 min.
- Temperature: 290 °C.

After blending, the extruded strand obtained at the exit of the die was quenched in water at room temperature and partially pelletized. Note that after blending in the microcompounder, the strand is pulled manually from the die into the water. Careful precautions were taken to avoid stretching morphologies: the strand has not been pulled out from the die but just accompanied in the water with a speed very close to the speed at which it comes out from the die.

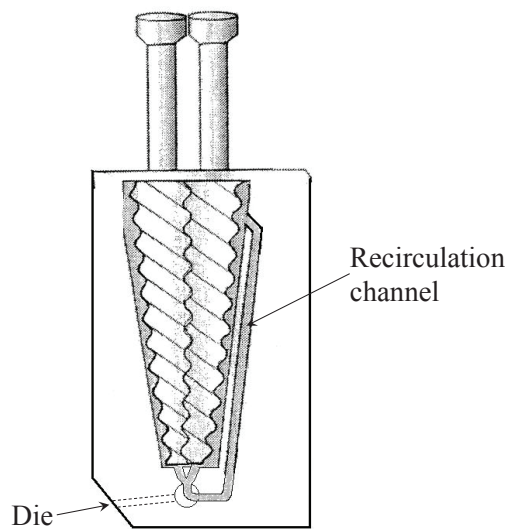


Figure 2.9: Schematic representation the batch mini extruder with recirculation channel.

#### 3.2 Morphology characterization

Blend morphologies were observed using Scanning Electron Microscopy (SEM) and Transmission Electron Microscopy (TEM). This work have been performed in collaboration with Nelly BULGARELLY's team, R & I centre Lyon, Analysis-Laboratory of microscopy.

In polymers blends, the usual range of morphology sizes is from tens of nm to tens of  $\mu m$ . Thus, electron microscopy is the most adapted technique. Whatever the type of electron microscopy used (Scanning or Transmission), an electron beam is emitted by an

electron source and sent on the sample. Various electrons/material interactions are possible, bringing about modifications of the beam as illustrated on figure 2.10.

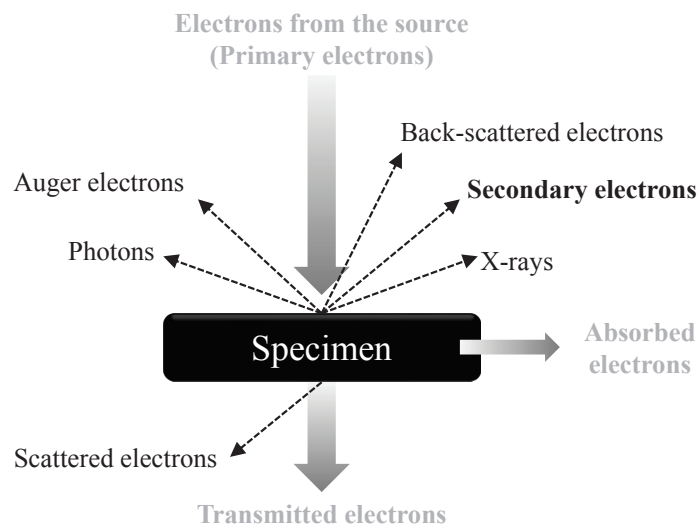


Figure 2.10: Schematic representation of modifications of the primary electrons beam caused by various electrons/material interactions.

In Scanning Electron Microscopy (SEM), depending on the type of interactions, electrons are ejected from more or less superficial layers of the sample leading to different contrasts. In this work, the secondary electrons are used. They are ejected from superficial layers of the sample and give topographic informations. In Transmission Electron Microscopy (TEM), observation were performed in the clear filed mode. With this technique, the transmitted electron beam (i.e. unscattered electrons) is directly observed. Depending on the density of the material present, some of the electrons are scattered and disappear from the beam. The different parts of the sample displayed in varied darkness according their density are observed.

#### 3.2.1 Scanning electron microscopy: SEM

Samples preparation for SEM observation has been done by different ways:

- **Surface Etching:** One pellet of the blend was included in Epoxy resin (Epofix), the surface was then cryotrimmed at  $-150\text{ }^{\circ}\text{C}$  ( $< T_g$  of PA and PE) using a diamond knife in order to obtain a mirror surface. In order to get contrast between both phases, selective dissolution of the minority phase (in terms of volume fraction) was performed:
  - When PA phase is the matrix, the PE phase was etched using a selective solvent, Decahydronaphthalene (Decalin), stirring at  $115\text{ }^{\circ}\text{C}$  for 1h30.
  - When PE phase is the matrix, the PA phase was etched using a selective solvent, Formic Acid, stirring at room temperature for 30 min.

Using this method we are able to observe a small surface (1 mm by 2 mm) initially located inside the pellet. The disadvantage of this technique is that it does not give information on the phase inside the etched nodule.

- **Cryofracture:** Pellets were immersed in liquid nitrogen for 15 min and immediately fractured. With this technique, we were able to differentiate the PE phase from the PA6 phase directly (no need of minor phase etching). Indeed, the cryofractured PA6 phase exhibits a fragile surface with net fractures and the PE phase exhibits a more ductile surface as shown in figures 2.11. With this method, we were able to observe the whole fractured surface of the pellet. This technique allow the observation of stretched nodules and gives information on the morphology inside a nodule, for example, if there are a subdispersions into a nodule. It allow a quick observation of the morphology because the sample preparation is not time consuming.

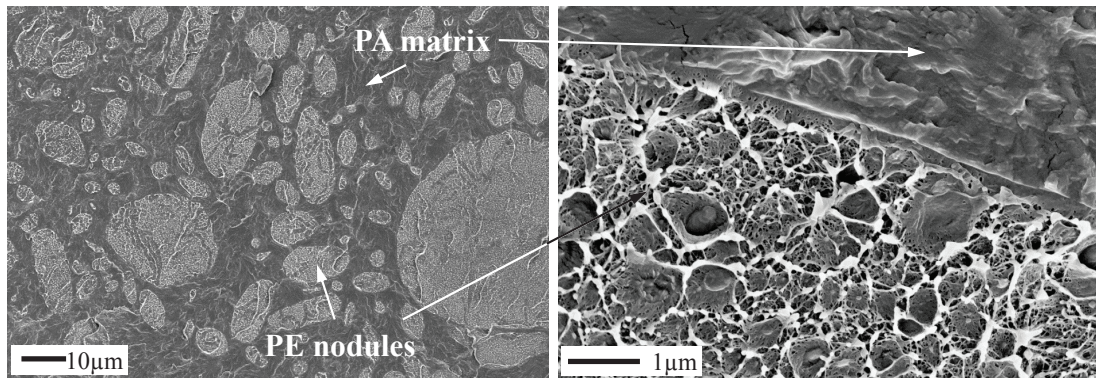


Figure 2.11: Cryofractured surface of PA-3k/MAGPE 50/50 blend showing a morphology of nodules of PE in a PA matrix.

For the observation, samples were coated with platinum and finally imaged using SEM Zeis Ultra 55 in the following conditions:

- Accelerating tension: 3 kV .
- Diaphragm aperture size: 20  $\mu\text{m}$ .
- Two detectors of secondary electrons were used (figure 2.13):
  - **SE2:** Gives a better representation of the surface topology and is thus used in general after surface etching of the minor phase.
  - **InLens:** used in general after cryofracture of the blends.

The pellets obtained after extrusion were observed in the direction shown in figure 2.12.

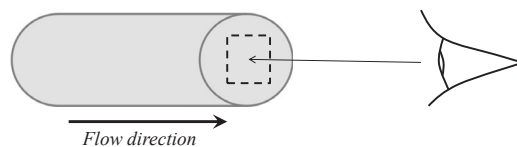


Figure 2.12: Observation of the pellet.

### 3. Experimental

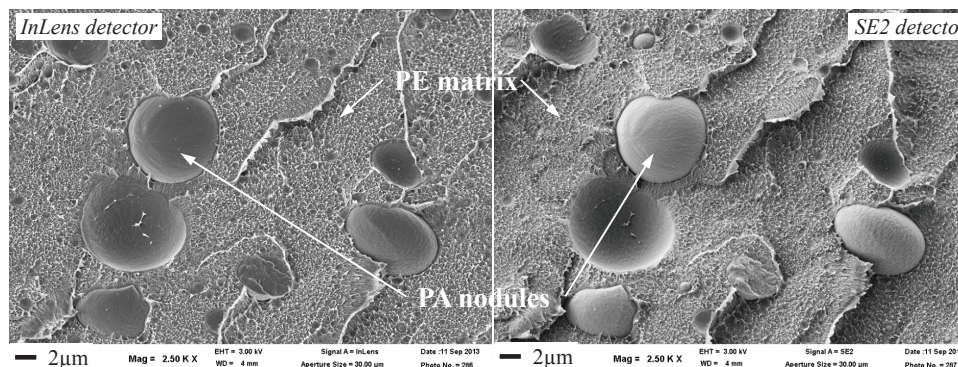


Figure 2.13: Cryofractured surface of PA-3k/PE 10/90 blends showing a morphology of nodules of PA in a PE matrix. The same image is presented here using 2 different kinds of detection to exemplify the difference on the final micrographs: (left) InLens detection and (right) SE2 detection.

#### 3.2.2 Transmission electron microscopy: TEM

Ultrathin sections of 80 nm were cut by ultramicrotomy at  $-80\text{ }^{\circ}\text{C}$  with a diamond knife. Sections were then picked-up on a copper grid (200 mesh). Then, PA6 phase needs to be stained to improve the contrast between PA and PE. In this way, PA phase appears in black and PE phase in white on the pictures. Staining conditions need to be well adjusted in order to get an optimized characterization of the sample. Depending on the kind of morphology, two different staining conditions were used:

- An aqueous solution with 2wt% of phosphotungstic acid ( $H_3PW_{12}O_{40}$ ) and 10% of Ethanol during 90 min at room temperature. This way of staining is more adapted to morphologies of PE nodules in PA matrix when nodules are very thin (below 100 nm) as we can see in figure 2.14 for blend PA6-31K/MA-g-HDPE (80/20 %vol). For coarser PE nodules the second staining conditions can also be used.
- An aqueous solution with 2wt% of phosphotungstic acid ( $H_3PW_{12}O_{40}$ ) and 2% of Benzyl Alcohol during 15 min at room temperature. This way of staining is more adapted for morphologies of PA nodules in PE matrix, especially when the nodules are very thin (below 50 nm) as we can see in figure 2.14 for blend PA6-3k/MA-g-HDPE (20/80 %vol).

Finally, samples were imaged by TEM (Technai Biotwin) under fixed conditions (120kV). Note that observation needs to be performed very carefully since the preparation conditions and observation in TEM are delicate. Otherwise, we may not observe all the nano-dispersions present in the samples and misinterpret the observed morphology.

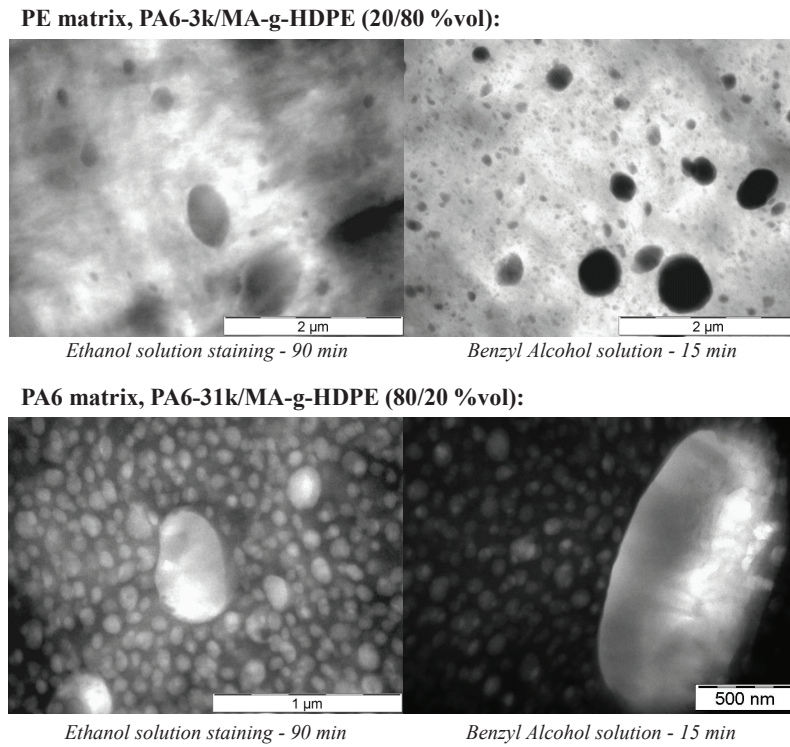


Figure 2.14: TEM characterization of PA6-3k/MA-g-HDPE 20/80 %vol and PA6-31k/MA-g-HDPE 80/20 %vol blends showing the influence of staining conditions on the contrast obtained.

### 3.3 Rheological characterization

#### 3.3.1 Dynamical rheometry

##### Method principle

Dynamical rheometry was performed with the strain-controlled rheometer (ARES) (in collaboration with L. GEORGES, R & I centre Lyon). The rheometer apply a sinusoidal strain deformation with the lower plate,  $\gamma = \gamma_0 \sin(\omega t)$ , and measure the phase shifted sinusoidal stress response with a transducer on the upper plate (or cone),  $\sigma = G^* \gamma_0 \sin(\omega t + \delta)$ . The complex modulus  $G^*$  measures the overall resistance of the material to the applied strain. As the material exhibits viscoelastic behaviour, the response is divided in two parts,  $\sigma = G' \gamma_0 \sin(\omega t) + G'' \gamma_0 \cos(\omega t)$ :

- $G'$  is the storage modulus: elastic component in phase with the strain.
- $G''$  is the loss modulus: viscous component out of phase with the strain.

The dynamic viscosity can thus be calculated as follow:  $|\eta^*| = |G^*|/\omega = (\sqrt{G'^2 + G''^2})/\omega$ . For all measurements, sinusoidal shape of raw signal were checked as well as the final value calculated with respect to the limit of the ARES transducers.

##### Measurements

Dynamical rheometry was performed on the studied polymers to determine the viscoelastic behavior in the linear domain. The rheological characterizations of raw polymers and blends were carried out on a strain-controlled rheometer (ARES) using 3 kind of geometries:

### 3. Experimental

---

- Cone-plate geometry: 25 mm diameter cone, angle=0.1 rad and gap=50.8  $\mu\text{m}$ .
- For very low viscosities: Cone-plate geometry: 50 mm diameter cone, angle=0.04 rad and gap=53  $\mu\text{m}$
- For very viscous or elastic blends if the cone plate geometry was not adapted plate-plate geometries (25 or 50mm diameter) were used.

The heating is controlled by a nitrogen flow. The oven is first preheated and pellets of polymers are placed between the cone and the plate (or plate-plate). Then a melting time of 6min is applied before any measurement. System is opened to atmosphere and the polymer surface is in contact with nitrogen flow.

Measurements have been performed at 290 °C (temperature representative of process conditions) under nitrogen atmosphere.

- **Strain sweep test:** First of all, strain sweep tests were performed on raw materials (PA6, HDPE and MA-g-HDPE) at four constant frequencies, 0.1, 1, 10 and 100rad/s, to determine the linear viscoelasticity domain (strain plateau). The maximum amplitude which can be used to perform frequency sweep tests while staying in the linear domain can then be determined. The higher the frequency, the shorter the plateau. Therefore, the strain amplitude of 15-20% was chosen, because it is the common maximum value of the linear viscoelastic plateau at 100rad/s of raw polymers.
- **Stability in temperature:** The stability of the materials was then validated at constant frequency (10 rad/s) and strain (15-20%) during 10min.
- **Frequency sweep test:** Finally, dynamic frequency sweep tests were performed varying the frequency from 0,1 to 100 rad/s at a strain of 15-20%. This test was repeated at least 3 times for raw polymers and blends.

In the literature [115, 116], it is often mentioned that a small strain amplitude has to be used in polymer blends, typically below 10%, in order to prevent morphologies from being affected by rheological measurements. This is especially true for uncompatibilized blends or blends with low amounts of compatibilizer where coalescence may be effective. Nevertheless, since we are interested in the low frequency rheological behavior, a larger amplitude is needed to get a better response and sensitivity at low frequencies. To check whether the morphology evolves or not during the frequency sweep tests in our reactively compatibilized binary blends, SEM or TEM observations were performed before and after the test for some selected blends. The results are discussed in section 4.

**The viscosity ratio  $R_v$  defines the ratio between the viscosity of the dispersed phase ( $\eta_d^*$ ) and of the matrix phase ( $\eta_m^*$ ) and can be calculated at any frequencies using equation 2.2:**

$$R_v(\omega) = \frac{\eta_d^*(\omega)}{\eta_m^*(\omega)} \quad (2.2)$$

#### 3.3.2 Cox-Merz

In this study, polymer blends are compounded in a batch co-rotative twin screw extruder; they undergo steady shear rate of the order of 100  $\text{s}^{-1}$ . The cone-plate rheometry characterization is performed in dynamic mode at frequencies from 0.05 to 100rad/s in the

linear viscoelastic domain of the polymer tested. To determine the frequency of our rheological measurement which is the most representative of real compounding conditions, the empirical Cox-Merz rule is applied. It was observed by Cox and Merz (1856) that for many polymeric systems, correspondence occurred between the shear rate dependence of the steady shear viscosity,  $\eta(\dot{\gamma})$ , and the frequency dependence of the complex viscosity  $\eta^*(\omega)$  as shown in equation (2.3).

$$\eta(\dot{\gamma}) = \eta^*(\omega) \quad (2.3)$$

Indeed, capillary rheometry tests have been performed on pure MA-g-HDPE and pure HDPE. In capillary rheometry, steady shear rate of  $100 \text{ s}^{-1}$  can be applied to the material to measure steady viscosities. This measured steady viscosity is directly representative of compounding conditions. For those pure polymers the Cox-Merz rule was verified: the complex viscosity measured in dynamic rheometry at  $100 \text{ rad/s}$  is equal to steady viscosity measured at  $100 \text{ s}^{-1}$  in capillary rheometry ( $\eta(100 \text{ s}^{-1}) = \eta^*(100 \text{ rad/s})$ ).

Even though the Cox-Merz rule has not been validated in the particular case of polymer blends, we consider in this study that **the frequency of 100 rad/s, which is the maximum limit of the frequency range accessible with the ARES rheometer, is the most representative of real compounding conditions.** (see appendix 3).

### 3.4 Static annealing of sandwiches

Thin films of different PA6s and MA-g-HDPE with thicknesses of roughly  $20\text{-}100\mu\text{m}$  (10 by 10 cm), were first prepared by compression molding  $\simeq 1\text{g}$  between demolding agent coated stainless steel plates. The films were formed from powder or pellets at  $290 \text{ }^\circ\text{C}$  for 2 min, under a pressure of the platen press varying from 3 to 60 bar depending on the polymer.

The two steps of sample preparation are schematized in figure 2.15.

**Step 1: Sandwich preparation before annealing in the cell at  $290 \text{ }^\circ\text{C}$**  Squares of 1 by 1 cm of each films were then cut and dried 12h in primary vacuum at  $290 \text{ }^\circ\text{C}$ . To make a sandwich, ten sheets were then quickly stacked, alternating PA6 and MA-g-HDPE (only one sort of PA6 per sandwich), and put into a cell. A weight was placed on the top of the sandwich to maintain contact between sheets. The cell was then inerted with argon and hermetically sealed. In order to perform the static annealing, the cell was placed into the oven of a rheometer (ARES) preheated at  $290 \text{ }^\circ\text{C}$ . A very slow rotation was applied to homogenize the heating of the cell. Ten minutes were necessary to reach the temperature of  $290 \text{ }^\circ\text{C}$  into the cell. Three annealing times were performed:

- 10 min (time necessary to reach  $290 \text{ }^\circ\text{C}$ )
- 10 min + 15min
- 10 min + 60min

**Step 2: Preparation for TEM observation after annealing** After heating, the cell was cooled down to room temperature by a cold gas nitrogen flow to room temperature. Sample preparation for TEM observation (second step) was performed: a sample of the center of the sandwich was then cut, in order to perform microscopic characterizations.

### 3. Experimental

---

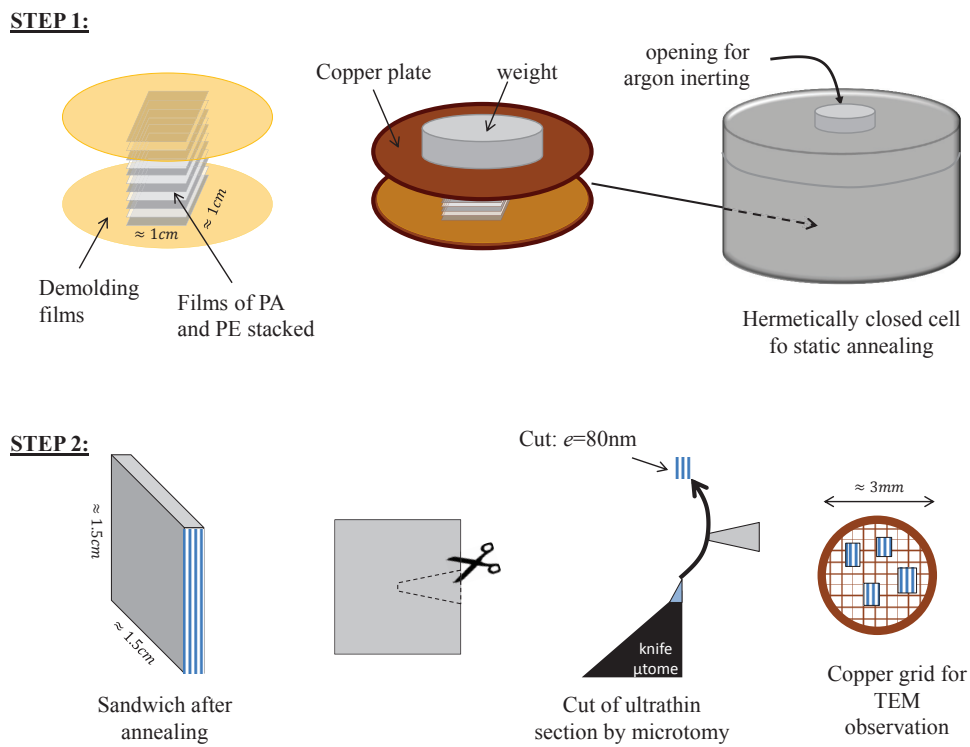


Figure 2.15: Schematic representation of static annealing experiment. Step 1: Sandwich preparation before annealing in the cell at 290 °C. Step 2: Preparation for TEM observation after annealing.

## 4 Raw materials stability during process and characterization

In this work blends were compounded at 290 °C into the microcompounder. We chose to carry out the dynamic rheological measurements at the same temperature because our objective was to be representative of process conditions.

In the melt state, polyamide 6 is very sensitive to moisture content. This parameter constitutes the main risk of PA6 molecular weight evolution. The temperature of 290 °C is high for HDPE. Thus the stability of pure materials (HDPE, MA-g-HDPE and PA6) at extrusion temperature are studied in this section. Then, blends stability (thermal stability and morphology stability) during rheological measurements are discussed.

### 4.1 Stability of polyethylenes

As the extrusion temperature (290 °C) is high for HDPEs, ThermoGravimetric Analyses (TGA), Size Exclusion Chromatography (SEC) and dynamic rheometry were carried out to check the stability of Polyethylene.

#### 4.1.1 ThermoGravimetric Analysis (TGA)

ThermoGravimetric Analyses (TGA) were performed on the HDPE and on MA-g-HDPE before any processing step with the help of Alexandre Corbin (Solvay R& I centre Lyon). Heating ramp from room temperature to 290 °C (extrusion temperature) was carried out at 50 °C/min. Then, an isothermal plateau at 290 °C during 30 minutes under air (to be in the most unfavourable conditions) was applied. The mass loss of each sample was followed during the whole experiment duration. Obtained results are summarized in table 2.5.

Table 2.5: Mass loss of Polyethylene (TGA) under air.

	HDPE	MA-g-HDPE
Mass loss under air	4.3 %	1.8

As both polymers are commercial grade the observed small mass loss could be due to the degradation of PE additives in the formulation.

#### 4.1.2 High Temperature Size Exclusion Chromatography (SEC)

Molecular masses distributions of HDPE and MA-g-HDPE were measured by High Temperature Size Exclusion Chromatography (SEC) before and after processing into the microcompounder by Olivier Boyron and Manel Taal (CPE Lyon). Results obtained are summarized in table 2.6.

Thus, according to table 2.6, the Weight Average Molecular Weight  $M_w$  of both polymers increased and were higher for MA-g-HDPE than for HDPE. These molecular weight changes are accompanied by an increase of the polydispersity index ( $IP$ ). HDPEs and MA-g-HDPE evolved during these high temperature processes.

#### 4. Raw materials stability during process and characterization

Table 2.6: Molecular mass distributions (absolute values) determined by SEC of Polyethylene before and after processing.

	$M_n$ (g/mol)	$M_w$ (g/mol)	$IP$
HDPE before compounding	15800	35800	2.3
HDPE after compounding	8900	43300	4.8
MA-g-HDPE before compounding	28900	58000	2
MA-g-HDPE after compounding	52500	131300	2.5

#### 4.1.3 Dynamic rheometry

##### Stability during processing of pure HDPEs

Frequency sweep tests were performed on HDPE and MA-g-HDPE before and after compounding at 290 °C. Figure 2.16 shows the variation of the dynamic viscosity ( $\eta^*$ ) of commercial HDPEs as a function of frequency ( $\omega$ ) before and after processing.

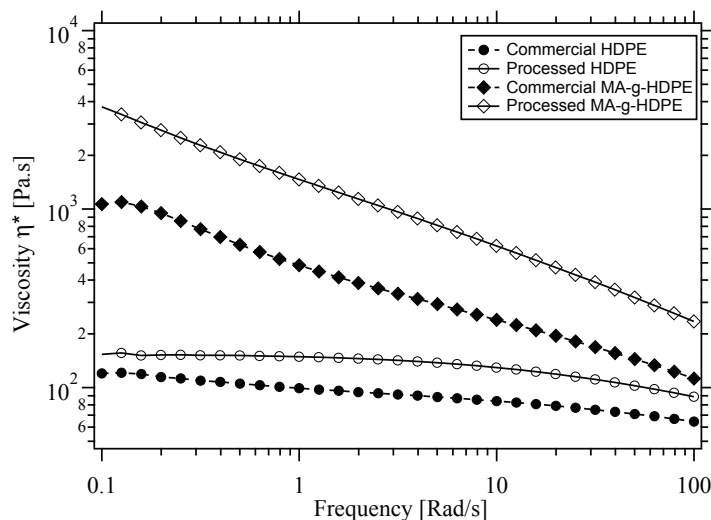


Figure 2.16: Dynamic viscosity as a function of the frequency of commercial and compounded HDPE and MA-g-HDPE at 290 °C.

For both HDPE and MA-g-HDPE, an increase of the viscosity is measured and  $\eta_{MA-g-HDPE}^* > \eta_{HDPE}^*$ , which is in qualitative agreement with the increase of  $M_w$  observed in SEC (table 2.6).

##### Stability during dynamic rheological measurements

In order to test the thermal stability of both HDPE and MA-g-HDPE during rheological measurements at 290 °C, tests of stability versus time were performed by dynamical rheometry. The dynamic viscosity was measured at constant frequency (10 rad/s) and strain (15%) during 20min on raw HDPE and MA-g-HDPE (before processing) as shown in figure 2.17.

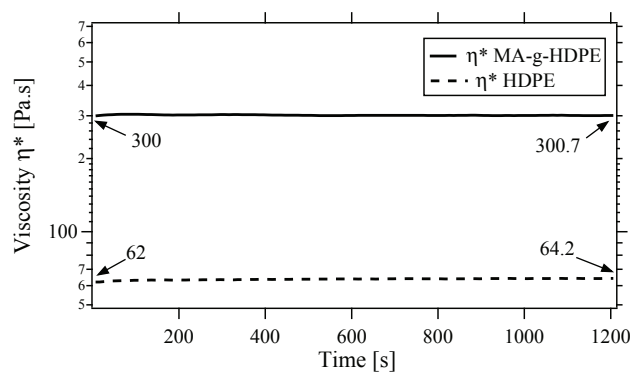


Figure 2.17: Dynamic viscosity,  $G'$  and  $G''$  as a function of time of raw HDPE and MA-g-HDPE (before processing) at 290 °C at constant frequency (10 rad/s) and strain (15%).

During dynamic rheometry experiments, HDPE and MA-g-HDPE viscosities do not evolve and thus do not undergo thermal degradations. Thus, the difference in viscosity observed before and after microcompounding, which can be directly related to the change in  $Mw$ , is not only due to the unfavourable temperature of 290 °C but essentially to the high shearing which is not present during dynamic rheological measurements.

#### 4.1.4 Conclusion on polyethylene stability

For both pure HDPE and MA-g-HDPE after processing into the microcompounder, small mass losses were obtained in TGA at 290 °C. An increase in viscosity was also observed after processing. This increase was greater for the MA-g-HDPE which is consistent with the greater increase in  $Mw$  measured by SEC experiments. During the dynamic rheological experiments at 290 °C no, or few, thermal degradation were observed.

In blends, and especially when the HDPE phase is the dispersed phase (droplets of PE in PA matrix), there is probably a mutual protective effect of each phase to one another (mainly against air during processing). Evolution of molecular weight observed in model conditions as described above, could thus be reduced.

**Thus, measurements of the viscosity and the molecular weights measured before processing will be considered in this work.**

## 4.2 Stability of polyamide 6

### Stability during processing of pure polyamide 6

The main critical parameter for polyamide 6 is the initial moisture content. Thus, pellets were carefully dried at their equilibrium moisture content before any processing or analysis. The moisture content was checked by Karl-Fisher. This allows to avoid any molecular weight evolution during processing by post-condensation or hydrolysis reaction 2.6.

### Stability during dynamic rheological measurements

In order to test the thermal stability of PA6-3k, PA6-18k and PA6-31k during rheological measurements at 290 °C, tests of stability versus time were performed by dynamical rheometry. The dynamic viscosity was measured at constant frequency (10 rad/s) and strain (15%) during 20min. Figure 2.17 shows the stability test as a function of time.

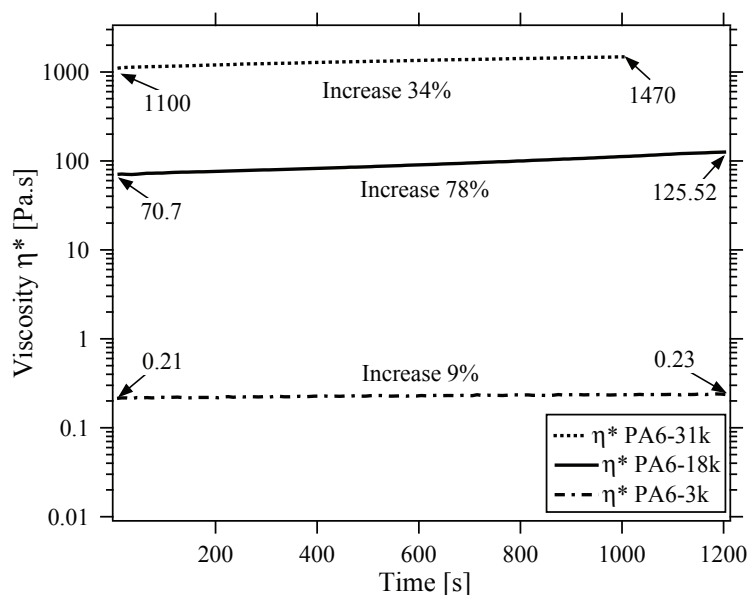


Figure 2.18: Dynamic viscosity as a function of time of pure polyamide 6 at 290 °C at constant frequency (10 rad/s) and strain (20%).

Results are the following:

- PA6-3k dynamic viscosity is almost stable during the 20 minutes.
- PA6-18k and PA6-31 dynamic viscosities increase during the experiment. The greater increase is observed for PA6-18k with an increase of 78%.

While heating into the rheometer oven, the PA6 is continuously dried due to the continuous nitrogen flow surrounding the sample. It is thus not possible to work at the water content corresponding to the equilibrium of polycondensation reaction.

The chemistry of the reaction of polyamide 6 post-condensation depends strongly on the amount of AEG and CEG initially present. Indeed, it controls the maximum molecular weight attainable by post-condensation reaction. While heating during the rheological experiment, the major part of PA6-3k chains are terminated by unreactive blockers end groups and thus, post-condensation reaction is very rapidly limited. On the contrary, post-condensation reaction is very likely to happen for both PA6-18k and PA6-31k. Indeed, a lot of Amine End Groups (AEG) and Carboxylic End Groups (CEG) are available to pursue the reaction if the post-condensation equilibrium with water is not respected. Thus, the increase in viscosity observed for both PA6-18k and PA6-31k is consistent with a molecular weight increase due to post-condensation.

A deeper analysis of the rheological characterization of polyamide 6 will be given in next section. It will be seen that polyamide 6 appears as a very complicated material for studies in dynamic rheological experiments.

### Conclusion on polyamide 6 stability

In this study, we considered that the molecular weight of the polyamide 6 are not changed during compounding because the amount of water can be controlled in microcompounder.

Nevertheless, PA6-18k and PA6-31k greatly evolve during rheological measurements.

In compatibilized blends, many chains of polyamide 6 are grafted to the MA-g-HDPE and thus exhibit much less available amine end-group moieties. We have seen that the post condensation depends strongly on the amount of amine and carboxylic acids end-moieties contents. Thus, when PA6 chains are grafted, post condensation is much less likely to happen. Besides, in blends when the PA6 phase is the dispersed phase (droplets of PA in PE matrix), PA6 is "protected" against the atmospheric environment and continuous drying during rheological measurements by the PE matrix.

## 5 Rheological characterization of raw materials

This section summarizes the rheological characteristics of neat blend components measured by dynamic cone-plate rheometry. Those measurements were needed to study the influence of the rheological properties on the morphology development of blends during compounding. According to the study of polymers stability, we have chosen to use the viscosities measured on unprocessed HDPE, MA-g-HDPE and the three PA6. Besides, polyamide 6 is very sensitive to moisture content which is a critical point for dynamic viscosity measurements. The first part of this section will be dedicated to the rheology of pure PA6 which requires much attention. Then the rheological behaviour of raw HDPE and MA-g-HDPE will be described.

### 5.1 Rheological behaviour of polyamide 6

Very few articles on the rheology of pure polyamide have been published in the literature [117, 118, 119, 120, 121] even though Polyamide 6, for example, constitutes a widely used polymer in industry. Due to its sensitivity to moisture content, this polymer constitutes a difficult material for studies in dynamical rheometry. Indeed, polyamide 6 is synthesised by polycondensation which leads to an equilibrium. In the molten state, this equilibrium is very sensitive to moisture content and can be shifted toward hydrolysis or post-condensation of PA6 chains (see section 2.3.1). Thus the measure of the rheological behaviour of polyamide 6 will depend strongly on the sample history (preparation, drying and manipulation) and on the kind of rheometer used.

In capillary rheometer, the sample is isolated from atmosphere and under pressure, all the water amount initially present is dissolved into the sample. As a consequences, the PA6 can be stable if the moisture content is at equilibrium, or undergo hydrolysis if it is too wet or post-condensation if it is too dry [121]. On the contrary, oscillatory measurements are performed under atmospheric pressure and a nitrogen flow continuously dries the sample, so that water can evaporate and is not entirely dissolved [121, 120]. Thus capillary rheometry should be much more favourable than dynamical rheometry to characterize PA6 in conditions wherein the later remain stable.

However, one of the goal of this thesis was to study the rheological behaviour of PA6/HDPE blends. Only measurements in dynamic rheometry at small deformations, i.e. in the linear regime, could be performed otherwise, in capillary measurement which is in a highly non linear regime, morphologies would be highly modified. The reference blend components (PA6-3k, 18k and 31k and HDPE and MA-g-HDPE) have to be measured in the same conditions. In order to get a better understanding of the morphology development, the measurements are performed at the same temperature as process conditions, i.e. 290 °C.

#### Experimental results on Polyamide 6

The dynamical rheological behaviour of the three polyamide 6, preliminarily dried at the equilibrium moisture content, are shown in figure 2.19. A good repeatability of measurements was complicated to obtain. Observations are the following:

- PA6-31k behaves as a pure viscoelastic polymer. The terminal regime  $G' \propto \omega$  and  $G'' \propto \omega^2$  is observed in the low frequency range (between 0.1 and 1 rad/s).

- PA6-18k behaves as a pure viscoelastic polymer between 10 and 100 rad/s. However, a large plateau is observed between 1 and 10 rad/s.
- PA6-3k the typical behaviour of viscoelastic polymer is not observed. The slope of the loss modulus  $G''$  is a little smaller than one between 1 and 100 rad/s ( $G'' \propto \omega^{0.7}$ ) and the slope of the elastic modulus  $G'$  is very different from 2.

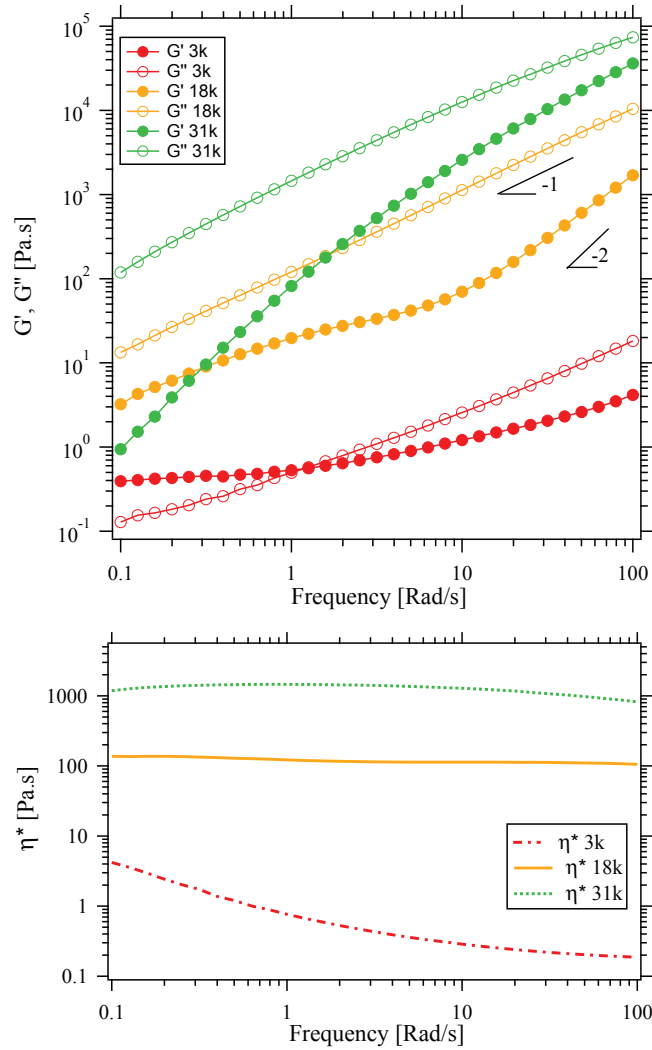


Figure 2.19: Dynamic moduli  $G'$  and  $G''$  and dynamic viscosity  $\eta^*$  as a function of the frequency of PA6-3k, 18k and 31k at 290 °C at constant strain (15%).

### Shoulder induced due to gas bubbles

The solubility of water into the melted polyamide depends on the conditions of pressure and temperature. Under pressure all the initial moisture content can be solubilized. Under atmospheric pressure at 290 °C the water solubility into molten PA6 is quite low. Schaffer et al (2003) [122] estimated the solubility of water in molten nylon at around 1000 to 2000ppm at 272 °C at  $P_{atm}$ .

It thus means that, if the water amount into the PA6 at the beginning of the experiment is higher than 1500 ppm, all the water contained in excess will form vapour bubbles into the materials. At 290 °C, the moisture content to get a stable PA6 for process conditions has to be:

- For PA6-31k:  $\approx 700$  ppm.
- For PA6-18k:  $\approx 2100$  ppm
- For PA6-3k:  $\approx 4400$  ppm.

Thus for PA6-31K, all the initial moisture content should be solubilized into the polymer. However, for both PA6-18k and PA6-3k a large part of this water amount can create bubbles that can be swept away from the molten polymer or stay into the polymer. Thus, the polymer will act as a biphasic blend. Besides, the continuous drying (due to the nitrogen flow), shifts the polycondensation equilibrium toward post-condensation which also releases water. We indeed, observed some bubbles into the melted polymer into the rheometer.

An analysis of the PA6 rheological behaviour based on rheological models is provided in appendix 1. This analysis shows that the shoulder observed in PA6-18k is consistent with the presence of vapour bubbles into the material. Drying the sample allows to remove the shoulder but do not lead to viscosity values corresponding to the viscosity expected for a PA6-18k at equilibrium molecular weight.

To date, there is no ideal experimental conditions in dynamical rheometry independent of the initial moisture amount. This has consequences both on the post-condensation equilibrium (with in addition the continuous drying) and the presence of a shoulders on the  $G'$  modulus. Thus despite the shoulder observed for PA6-18k and 3k, we decided to performed our rheological measurements with PA6 dried at their equilibrium moisture content. *In blends, any potential plateau observed at low frequencies shall thus be interpreted very carefully.*

### 5.2 Rheological behaviour of HDPEs

#### HDPE

The dynamic rheological behaviour of pure HDPE as a function of the frequency is presented in figure 2.20. The loss modulus  $G''$  of the HDPE exhibits the classical rheological behaviour of a viscoelastic polymer in the terminal regime where  $G'' \propto \omega$  and when  $\omega > 10$  rad/s, the storage modulus  $G'$  almost verifies  $G' \propto \omega^2$ . However, at low frequencies ( $\omega < 5$  rad/s),  $G' \neq \omega^2$ . Indeed, a large shoulder followed by a plateau toward low frequencies are observed.

The study of the stability during rheological measurement (see subsection 4.1) has shown that the HDPE is stable during the time scale of the experiment and that thermal degradation was essentially seen during shearing into the extruder. Thus the shoulder observed could hardly be explained by thermal degradation. As in the case of PA6, the shoulder could be due to the presence of air bubbles into the polymer. An analysis based on rheological model is given in appendix 1. It shows that the shoulder is consistent with the presence of gas bubbles. However, we do not exclude that another phenomenon that

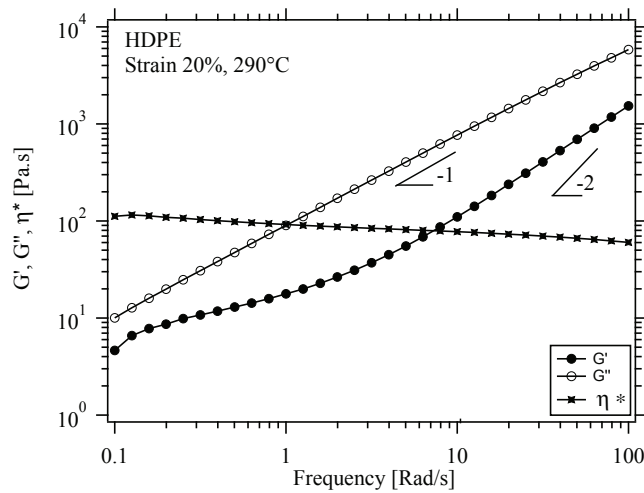


Figure 2.20: Dynamic viscosity,  $G'$  and  $G''$  as a function of the frequency of commercial HDPE at 290 °C at constant strain (20%).

we do not explain for the moment could be responsible of this shoulder.

*In blends, any potential plateau observed at low frequencies shall thus be interpreted very carefully.*

### MA-g-HDPE

The dynamic rheological behaviour of pure MA-g-HDPE as a function of the frequency is presented in figure 2.21.

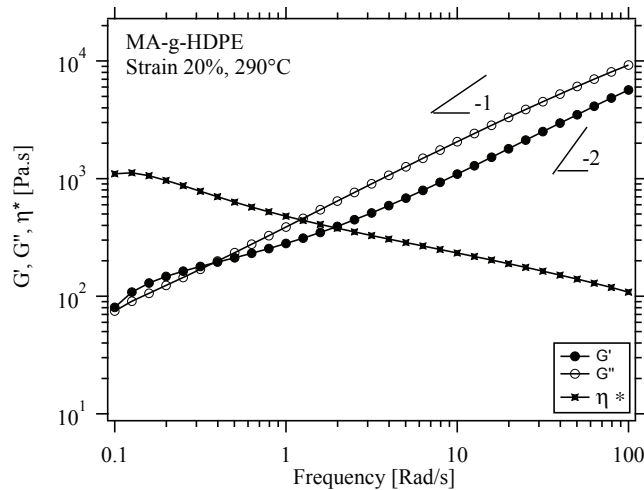


Figure 2.21: Dynamic viscosity,  $G'$  and  $G''$  as a function of the frequency of commercial MA-g-HDPE at 290 °C at constant strain (20%).

As shown in figure 2.21, shoulder of  $G'$  is observed at low frequencies. We cannot exclude the idea that gas bubbles may be responsible for an increase in the elastic modulus at low frequencies but another explanation can be given in the case of MA-g-HDPE. Indeed, the value of the  $G'$  increase seems too high to consider that only gaz bubbles are

responsible (a plateau due to gaz bubbles should be at around 10 Pa.s).

In the case of MA-g-HDPE, the shoulder could be attributed to the shape relaxation of MA micelles formed into a HDPE bulk. Fabre-Argoud [17] calculated the solubility parameter between MA moieties and HDPE bulk, and estimated the Flory interaction parameter  $\chi_{12}$  to be roughly of the order of 1.2 (with  $\delta_{PE}=16 \text{ MPa}^{1/2}$ ). MA-g-HDPE may thus be considered as a polymer containing functional moieties not miscible with HDPE.

Thus, pure MA-g-HDPE can behave like a biphasic blend with micelles of Maleic anhydride (MA grouped as clusters) dispersed into an HDPE bulk. The shape relaxation of MA micelles can be responsible of the large increase in  $G'$ .

*Thus, in blends, careful interpretations of potential plateau at low frequencies have to be done because of the behaviour of pure MA-g-HDPE.*

## 6 Conclusion

The objective of this work is to study the morphology development and the rheological behaviour of binary uncompatibilized PA6/HDPE and compatibilized PA6/MA-g-HDPE blends. For that the characteristics of raw blend components have been presented in this chapter. Both polyolefins of this work are commercial grades. The MA-g-HDPE contains grafted MA moieties and the HDPE was chosen so that its viscosity is close to that of MA-g-HDPE at 100 rad/s. Three polyamide 6 have been synthesized at Solvay. They are linear polyamide 6 with exactly one  $\text{NH}_2$  per chain and their number average molecular weight was calculated thanks to end group titration. To be the most representative of process conditions, viscosities of unprocessed components (i.e. after synthesis or commercial compound) at 100 rad/s are used to calculate viscosity ratios ( $R_v = \eta_a^*/\eta_m^*$ ). Raw materials characteristics are summarized in the following table:

	$M_n$ (g/mol)	AEG [ $\text{NH}_2$ ] (mmol/kg)	[MA] (mmol/kg)	$\eta^*$ at 100rad/s (Pa.s)
PA6-3k	$\approx 2900$	347	-	$\approx 0.2$
PA6-18k	$\approx 18000$	55	-	$\approx 105$
PA6-31k	$\approx 30500$	33	-	$\approx 820$
MA-g-HDPE	$\approx 28900$	-	101	$\approx 108$
HDPE	$\approx 15800$	-	-	$\approx 60$

Blends were compounded by batch mini extrusion at 290 °C. Main experimental methods to characterize blends morphologies and rheological behaviour were then presented. Different methods of microscopy were used to characterize blends morphology: All blends were characterized by Scanning Electron Microscopy (SEM) after minor phase etching and/or after cryofracture. Transmission Electron microscopy (TEM) was used to observe compatibilized blends. A careful attention was paid on the presence of nanodispersions. For that, sample preparation has been optimized in order to get a maximum of informations during observation. Rheological measurements were performed by dynamical rheometry at 290 °C. The method used to perform static annealing has also been described.

The stability of pure HDPE and MA-g-HDPE was checked and it appears that their molecular weights evolve during compounding at 290 °C (SEC measurements) and a small mass loss was obtained by TGA at 290 °C. However, during dynamic rheological experiment they did not evolve. Concerning polyamide 6, they are mainly sensitive to moisture content, thus they should not evolve during compounding. However, they greatly evolved during rheological experiments. This is because the rheometer is directly opened to the atmosphere and PA6 is continuously dried by the nitrogen flow (used to regulate the temperature in the oven). This unbalance the polycondensation equilibrium which is shifted toward post-condensation and can lead to an increase in PA6 molecular weight. These effects could be greatly reduced in blends because of the mutual protective effects of one phase toward the second one.

The linear viscoelastic behaviour of pure blends components are finally presented. Because of its sensitivity to moisture content, a careful attention was paid on the rheo-

## 6. Conclusion

---

logical behaviour of polyamide 6. It appears that the measurements depend strongly on the initial moisture amount. Thus despite the shoulder observed for PA6-18k and 3k, we decided to performed our rheological measurements with PA6 dried at their equilibrium moisture content. Concerning the polyolefins, particular behaviour were also observed. We noticed shoulders at low frequencies on the  $G'$  modulus for both HDPE and MA-g-HDPE. *In blends, any potential plateau observed at low frequencies shall thus be interpreted very carefully.*



# COMPATIBILIZATION REACTION IN STATIC CONDITIONS

---

# 3

In the specific case of reactive compatibilization, two concomitant mechanisms of morphology development can happen during blending, namely (1) the standard mechanism of drop break-up and coalescence of polymer domains under shear that is controlled by classical rheological laws; (2) a mechanism specific to reactively compatibilized blends, which can lead to the formation of nano-scale dispersions in both component domains, in addition to the micro-scale morphology. This phenomenon could be attributed to the chemical reaction. In order to discriminate the mechanisms of morphology development due either to rheological process or to the compatibilization reaction, both mechanisms have been studied separately.

In this chapter, we shall focus on the mechanism responsible of the nanodispersions formation by getting rid of the effect of the shearing and study specifically the effect of the chemical reaction which happens at the interface. For that, static annealing between thin films of MA-g-HDPE and different PA6 are performed during different annealing times. The interface is then observed by TEM. We show in this study the spontaneous nucleation and growth of ordered copolymer structures at the interface. The destabilization of the interface as well as the microstructures observed after annealing as a function of the structure of copolymers are discussed.

In section one, we present a draft of article which presents main results of the study. In section two, results are discussed in more details based on a dry brush model.

## 1 Article: Nucleation and growth of ordered copolymer structures at reactive interfaces between PA6 and MA-g-HDPE

Article submitted to ACS Macro Letters

Authors: Chloé Epinat, Lise Trouillet-Fonti, Stéphane Jéol, Didier R. Long and Paul Sotta

### Abstract

We have studied the effect of the interfacial chemical reaction between PA6 and MA-g-HDPE in static conditions at a macroscopically flat interface. Interface destabilization and the growth of instabilities, somehow similar to myelin figures observed in surfactants put in the presence of water, are observed. For the first time in this system, the nucleation and growth of ordered microphase separated copolymer domains is observed. The morphologies which are formed depend on the architecture of the copolymer, namely essentially on the relative length of the blocks on each side of the interface. We discuss the stability of the plane interface in the case of non-symmetrical formed graft copolymer. The density of copolymers in the interface (coverage) can be estimated accurately from the long period of the formed structures. We confirm the predictions of Berezkin et al. This observation is very important, since it confirms that nanometric domains are certainly formed during reactive extrusion, in addition to purely rheological processes, like Taylor and/or Rayleigh instabilities leading also to micrometric domain formation.

### Introduction

When processing compatibilized polymer blends by reactive extrusion, interface instabilities due to grafting chemical reaction at interfaces may coexist with rheology-driven mechanisms of domain break-up and coalescence under shear [7]. Discriminating both mechanisms may be a key issue in polymer science and engineering in order to better control the process and the obtained morphologies, and therefore the properties of the final products [109]. In this paper we shall focus on the effect of the chemical reaction which happens at the interface in static conditions.

When two reactive polymers react at a planar interface under static heating, the formed copolymers accumulate at the interface, thus decreasing the interfacial tension and promoting interface fluctuations [72, 123, 124]. This leads to interfacial roughening, which was studied in several polymer blends [91, 90, 77, 80, 78, 92, 99]. The kinetics is complex, due to the free energy barrier a chain has to overcome to reach the interface and stretch [89, 73, 74]. After interfacial roughening induced by fluctuations, the formation of an emulsion and/or micelles leaving the interface [92, 99, 91, 93], as well as the formation of microstructures like lamellae, have been observed [90]. Recently, the coupling between immiscible polymers leading to the creation of block and graft copolymers of different architectures and the associated microstructure development, was studied by mesoscale numerical simulations [87, 100, 101]. Reactively compatibilized blends of Polyamide 6 (PA6) and Maleic Anhydride-grafted High Density Polyethylene (MA-g-HDPE), in which graft-copolymers are formed at the interface, are examples of such systems [125].

In this work, we bring new experimental results on the effect of the copolymer architecture on the reaction at the interface in such systems with PA6s of various chain lengths. The destabilization of the interface and the microstructures observed after annealing will be discussed. We show that ordered microphases, such as lamellar and cylindrical phases, can be generated at the interface. Our results offer the first direct experimental confirmation of the numerical predictions by Berezkin et al. [87, 100, 101].

### Materials and methods

We have used MA-g-HDPE (molar mass  $M_n = 29000$  g/mol, index of polydispersity 2.9, concentration of MA moieties 1 wt%, which corresponds to an average of 2.9 MA groups per chain) and we have synthesized four linear PA6s of  $M_n$ s varying from 3000 g.mol<sup>-1</sup> (PA6-3k) up to 31000 g.mol<sup>-1</sup> (PA6-31k) (estimated by end group titration) with an index of polydispersity close to 2, typical of linear polycondensates (Note that a small residual fraction of cyclic oligomers is present in PA6). Sandwiches of 20-100  $\mu$ m thick alternated MA-g-HDPE and dried PA6 films (prepared by compression molding) were submitted to static annealing at 290°C for various durations (10-70 min) under argon atmosphere. Samples were then quenched down to room temperature by cold nitrogen gas flow. Ultrathin sections (80 nm) were cut by cryomicrotomy perpendicularly to initial films, stained with phosphotungstic acid and observed by TEM (Technai Biotwin, voltage 120 kV).

### Experimental results

As a preliminary observation, no evolution was noticed when non-reactive HDPE was used instead of MA-g-HDPE. In addition, there was no adhesion between PA and PE films, resulting in delamination of the samples under ultramicrotomy. The same was observed when MA-g-HDPE was used but the samples were heated up to 160°C only, that is, when only the PE part melted, which prevents the interfacial reaction to occur, except perhaps for few PA chains which happen to be in direct contact with the interface.

After annealing at 290°, no roughening or morphology development was observed for sandwiches with PA6-3k. Interfaces remained flat (see figure 3.1). Nevertheless, no delamination between the PE and PA films was observed, in contrast to the non-reactive cases. Conversely, a strong adhesion between adjacent layers was noticed when preparing thin samples for TEM observation. This can be considered as an indirect proof that a reaction indeed occurred at the interface. Note that some very rare, isolated PA6 droplets of diameter of the order 200 nm, stucked to the otherwise flat interface, start to appear after 10 + 15 min.

In the three other samples with respectively PA6-10k, PA6-18k and PA6-31k, upon static annealing at 290°, interfaces destabilize within less than 10 minutes. Initially flat interfaces proliferate, leading to large scale interfacial roughening, as already described in other systems [91, 90, 77, 80, 78, 92, 99]. In order to distinguish the structures which develop and discuss underlying mechanisms, one then needs to look at small scales. In all three cases, nucleations of local structures, cylinders or lamellae, are observed. Some domains grow into locally ordered mesophase morphologies.

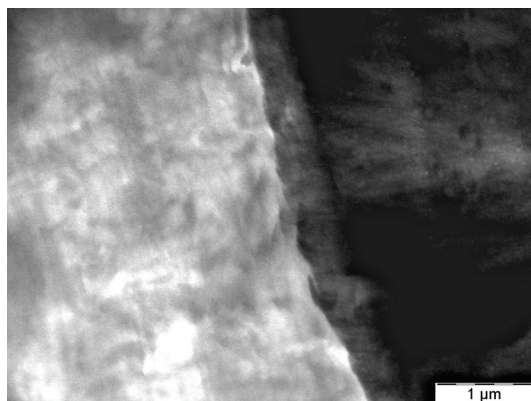


Figure 3.1: Interface between MA-g-HDPE and PA6-3k annealed at 290°C during 10+60 minutes. PA6 phase appears in dark.

For PA6-10k samples (Figure 3.2), the overall thickness of the roughened interface is of the order 500 nm-1  $\mu\text{m}$  after 10 min annealing and reaches 2-3  $\mu\text{m}$  after 60 min.

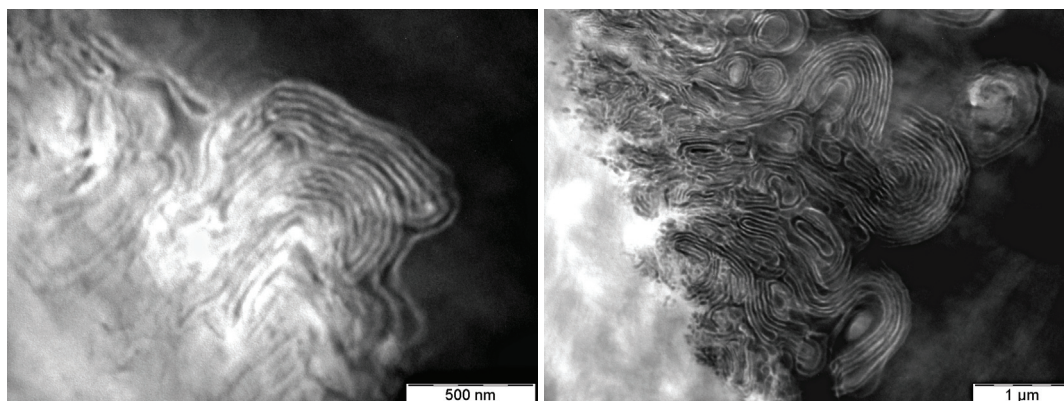


Figure 3.2: Morphology developed at the Interface between MA-g-HDPE and PA6-10k annealed at 290°C during 10 minutes (left) and 10+60 minutes (right). PA6 phase appears in dark.

Closer inspection shows that the morphology which develops mostly consists in tubes or filaments made of concentric cylinders, indicating that the structure is locally lamellar. These tubes seem to grow at a given angle (close to perpendicular) with respect to the initial flat interface and fold in worm-like structures as they develop further. The cylinders/filaments evolve into or coexist with droplets of PA phase inside the PE phase. These cylinders may be reminiscent of focal conic domains observed in smectic liquid crystals, which provides a strong, indirect indication that the structure is indeed locally lamellar [126]. The apparent period of the lamellar array, of order 32.5 nm, and apparent thickness of PA layers, of order 17.5 nm, stay roughly constant throughout annealing (even though it perhaps increases a little).

There is a gradient of morphologies throughout the whole interfacial area, going from foam-like PE phase with PA droplets on the PE side, towards well formed lamellar packings on the PA side.

The observed lamellar structures are reminiscent of myelin figures observed when a concentrated surfactant solution is put in the presence of water [127, 128, 129, 130, 131].

1. Article: Nucleation and growth of ordered copolymer structures at reactive interfaces between PA6 and MA-g-HDPE

---

PA6-18k samples show quite symmetrical patterns (Figure 3.3), with both PA filaments into the PE phase and PE filaments into the PA phase, both initiating perpendicular to the initial locally flat interface and evolving into a locally lamellar structure forming worm-like tubes as in the PA6-10k samples.

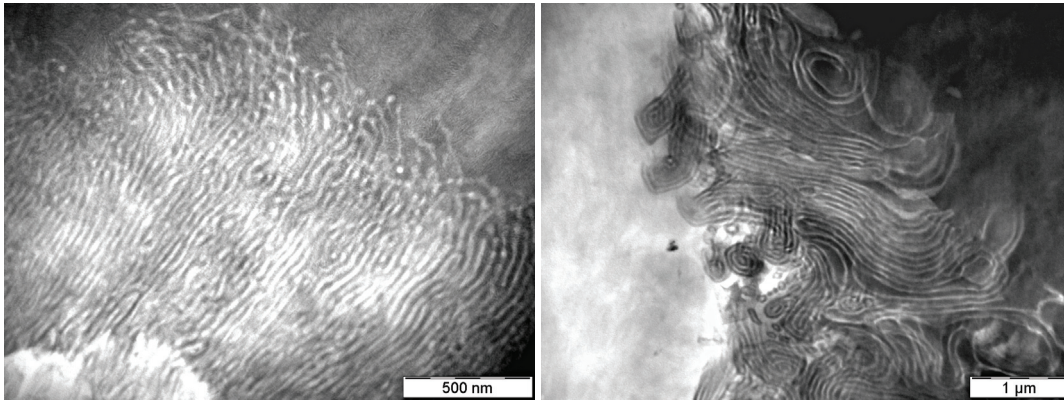


Figure 3.3: Morphology developed at the Interface between MA-g-HDPE and PA6-18k annealed at 290°C during 10 minutes (left) and 10+60 minutes (right). PA6 phase appears in dark.

The apparent period, roughly constant along annealing, is of order 37 - 40 nm, i.e. consistently a little longer than in the 10k case. The diameter of PE filaments inside the PA phase is of order 16.5 to 17 nm. Growth is a little faster than in the 10k case, with overall interface thickness of about 1.5  $\mu\text{m}$  after 10 min annealing.

In PA-31k samples, filaments of PA grow preferentially into the PE phase (Figure 3.4). Growth is slower than in PA6-18k samples. When compared to PA6-10k samples,

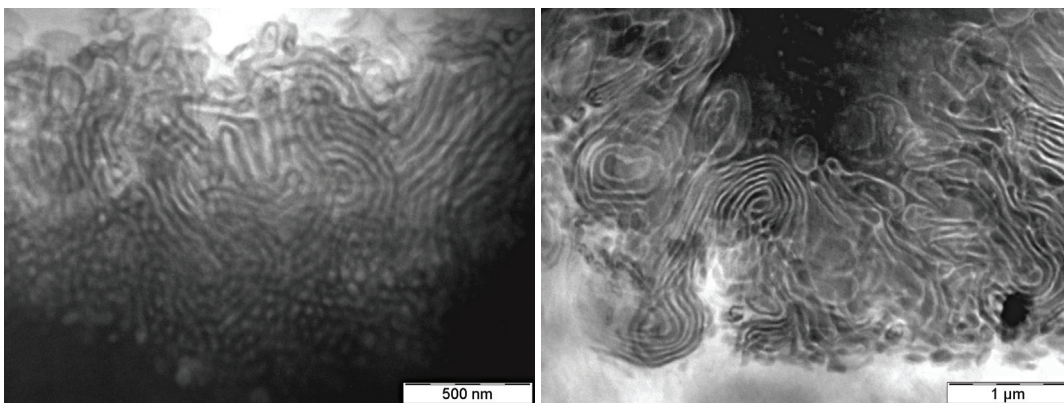


Figure 3.4: Morphology developed at the Interface between MA-g-HDPE and PA6-31k annealed at 290°C during 10 minutes (left) and 10+60 minutes (right). PA6 phase appears in dark.

some clear phase inversion-like phenomenon appears: while PA6-10k samples exhibit preferentially PA droplets (or sections of cylinders) within the PE phase, PA-31k samples show preferentially PE droplets (or isolated filaments) within the PA phase. Apparent period of arrays is of order 47.5 - 50 nm.

## Discussion

Let us now discuss the results, which may be summarized as follows: the formed structures (micelles, cylinders, lamellae) depends on block length; growth occurs at a defined angle with respect to the initial flat interface; the kinetics is faster in the lamellar case; the long periods of the observed arrays are compatible with those of structures observed in pure block copolymers at equilibrium in the strong segregation regime [132].

The apparent long period goes from about 32.5 nm (10k) to 47 nm (31k). It agrees qualitatively with the variation of chain length. Data are not quantitative enough to check a possible power law variation of the period as a function of the average chain length. The apparent long period of the microphase separated domains does not vary significantly with the annealing time (even though it perhaps increases a little). This indicates that structures are nucleated with a copolymer density at the interface (coverage) already close to the final, equilibrium value (corresponding to effectively zero surface tension).

Samples with PA6-18k exhibit both the most symmetric morphologies at the 3 tested annealing times (namely a lamellar morphology) and the fastest growth. Also, a gradual change of microstructure is observed along the normal to a given initial interface. At some point, micelles or cylinders formed at the basis of the interface evolve into lamellae, for example.

This gradual change may results from a gradient of concentration within the interfacial region.

All these observations are in remarkable agreement with the predictions by Berezkin et al. obtained by dissipative particle dynamics (DPD) simulations [87, 100, 101]. Also in agreement with theoretical predictions and simulations is the observed strong slowing down of the kinetics during annealing, related to the increasingly high free energy barrier that chains have to overcome to reach the interface and react [73, 74, 72, 75]. Also, it is observed qualitatively that the kinetics is consistently slower for longer chains.

The copolymer density within the interface (coverage) may be estimated from the value of the long period. Let us assume that interfaces are completely filled by copolymers ('dry brush' approximation). For PA6-10k, assuming that PA lamellae have a thickness  $D \approx 20$  nm and denoting  $a^2$  the average area per chain, the volume occupied by a chain is  $Da^2$ , which, when equated to the number average chain volume  $v_c = M_n/(N_a\rho)$  (where  $M_n$  is in kg/mol,  $N_a$  is Avogadro's number and the density  $\rho$  is of order  $10^3$  kg/m<sup>3</sup>), gives  $a^2 = v_c/D \approx 7.6$  nm<sup>2</sup> or equivalently, an interfacial coverage (number of PA chains per unit area)  $a^{-2} = 0.13$  chain/nm<sup>2</sup>. This value is of the same order as those estimated in other systems [84, 80].

In block copolymers, the microphase separated structures depend on the spontaneous curvature of the interfaces, which is determined by the relative length of segregated blocks [1]. It is observed here that the microphase organized domain morphologies indeed depend on the PA chain length. However, this dependence is not very sensitive, essentially because chain length distributions of our various PA samples overlap quite largely. A criterium for obtaining lamellar structure (zero average curvature) at equilibrium has been proposed for linear diblock copolymers [1] and further extended to star-block copolymers. Assuming that the graft copolymer formed here behaves in the

same way as a Y-shaped copolymer, with a PA block and two PE arms attached to it, this criterium would write  $V_A^3/R_{GA}^2 = 2^4 V_B^3/R_{GB}^2$  [57, 56], where  $V_i$  is the molecular volume of the  $i$  block and  $R_{Gi}$  its radius of gyration, and index A stands for the PA block and B for PE arms. Based on the  $M_n$  value of each PA sample, the predicted equilibrium morphologies would be formed of PA micelles for the PA6-3k sample, PA cylinders for PA6-10k and lamellae for PA6-18k and PA6-31k.

One specific result observed here is that interfaces do not destabilize for the PA6-3k sample. This can be explained in the following way. An initially flat interface becomes instable when copolymers accumulated at the interface have decreased the interfacial tension to zero. This corresponds to the equilibrium state of the brush on both sides of the interface, when block stretching on each side balances the excess contact energy. In the PA6-3k sample, PA chains (blocks) are much shorter than PE blocks. Dense PE block packing, (which would correspond to zero interfacial tension on the PE side), is reached before PA blocks start to interact. Therefore, there is no strong reduction of surface tension, due to chain stretching, on the PA side of the flat interface. Zero overall interfacial tension would correspond to a non-zero spontaneous curvature of the interface, towards the side of the shorter blocks.

For the case of PA6-3k sample, the flat interface does correspond to a metastable state, even though it does not correspond to the absolute minimum of surface tension. Indeed, for an interface with a non-zero (spontaneous) curvature  $C_0$  at equilibrium, the excess energy per unit plane surface associated to a fluctuation mode  $u(q)$  of wave vector  $q$  (within the plane of the interface) is  $\Delta F(u) = \int [(\frac{\gamma}{2}q^2 + \frac{\kappa}{2}q^4) u(q)u(-q) - \kappa C_0 u(q)] d^2q$ . The first term is associated to the excess surface area created by fluctuations, the second term to curvature energy.  $\gamma$  is the surface tension and  $\kappa$  the elastic constant for curvature. For a plane interface,  $C_0 = 0$ . For  $C_0 \neq 0$ , a plane interface ( $u(q) = 0$ ) does not correspond any longer to the most stable state of the interface. However, the  $\Delta F(u)$  curve is concave at the point  $u(q) = 0$  (which corresponds to plane interface), which means that any fluctuation shall increase the free energy, thus corresponding to metastability. Then, to generate a micelle of radius  $R$  from the fluctuating interface, a extra surface area of order  $R^2$  must be created, which corresponds to an excess interface energy  $\gamma R^2$ .

For  $\gamma \approx 10^{-3} \text{ Nm}^{-1}$  (or  $\text{Jm}^{-2}$ ) (estimation for an interface with copolymers) and  $R \approx 10 \text{ nm}$  (order of magnitude of the average chain size), the energy barrier is  $\approx \gamma R^2 \approx 10^{-18} \text{ J} \approx 10 k_B T$ . This shows that the formation of a micelle is kinetically impossible, or has an extremely low probability.

## Conclusion

In conclusion, for the first time in compatibilized polyamide/polyethylene blends, the nucleation and growth of ordered microphase separated copolymer domains at flat interfaces between reactive immiscible blocks, due to chemical reaction under static conditions, has been observed directly and discussed. For long chains, instabilities, somehow similar to myelin figures observed in surfactants put in the presence of water, develop, whereas interfaces with shorter PA6 chains remain metastable. This indicates that, at the considered temperature, the density of graft copolymers at the interface (interface coverage) can reach values which are beyond the equilibrium value, thus leading to negative surface tension and interface destabilization.

The architecture of the copolymer created at the interface not only affects the initiation

of interfacial fluctuations, but also the microstructures which are formed as a result of interface destabilization. These microstructures are similar to those observed in block copolymers, and thus depend on the relative length of the blocks on each side of the interface. Indeed this ratio of lengths determines the local equilibrium curvature of the interface. We confirm the predictions of Berezkin et al [87]. This observation is very important, since it confirms that nanometric domains may be formed during reactive extrusion, in addition to micrometric domain formation formed by purely rheological processes, like Taylor and/or Rayleigh instabilities.

## 2 Discussion, modelling and analysis

In this article we studied four different systems. The main observations were that no interfacial destabilization was observed for sandwiches with PA6-3k. However the interface of the three other cases was destabilized in less than 10 minutes. We observed large interfacial roughening (few micrometers) and at small scales, nucleation of local structures (cylinder or lamellae). The apparent long period of lamellae observed are compatible with those of structures observed in pure block copolymers at equilibrium in the strong segregation limit and are consistent with a "dry brush" approximation. We will thus consider this regime in the following discussion.

This discussion provides a deeper analysis of the effect of the creation of copolymers at the interface in static conditions. We first discuss how the creation of copolymers at the interface decreases the interfacial tension: the effect of bloc stretching, copolymer architecture and initial state of the interface (flat or curved). An energetic approach of the copolymer layer created, confirms the different behaviours between sandwiches with PA6-3k and the three other cases. The symmetry criterion of the copolymer is also discussed. This discussion is completed by the very first conclusions of a theoretical approach of the fluctuation growth at the interface after destabilization.

*Note:* For the study of the compatibilization in static conditions a fourth polyamide 6 has been tested: PA6-10k with  $Mn \approx 10000\text{g/mol}$ . Its characteristics are reported in appendix 2.

### 2.1 Interface between two immiscible polymers

#### 2.1.1 Thickness of the interface [1, 2]

The interface is the region in which A and B effectively interpenetrate through thermal fluctuations (see FIG. 3.5). The energy cost when  $g$  segments of B penetrate into A phase by thermal fluctuations is  $g\chi k_B T$ . This cost should be of order  $k_B T$ , thus  $g\chi k_B T \approx k_B T$ , thus  $g \approx 1/\chi$ . These  $g$  segments form a gaussian statistical coil of size  $\xi \approx ag^{1/2} \approx a/\chi^{1/2}$  ( $a$  is the monomer size), which gives the thickness of the interface:

$$\xi \approx \frac{a}{\chi^{1/2}} \quad (3.1)$$

More complete calculation give [85, 133, 134]:

$$\xi \approx \frac{a}{(6\chi)^{1/2}} \quad (3.2)$$

#### 2.1.2 Surface tension

The total energy for an interface of area  $S$  is of the order:

$$\Gamma_0 S \approx \chi k_B T \frac{\xi S}{a^3} \quad (3.3)$$

$\xi S$  is the volume of the interface,  $\xi S/a^3$  is the number of monomers in the interface,  $\chi k_B T$  represents the order of magnitude of the excess energy per monomer,  $a^3$  is the monomer

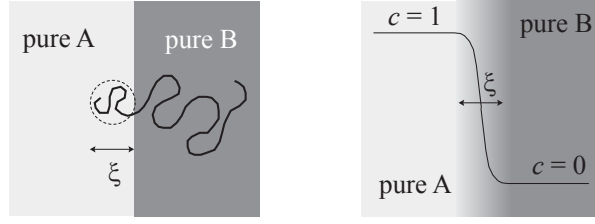


Figure 3.5: Interface between two immiscible polymers A and B.

volume. Thus, per unit area and using Eq. (4.4):

$$\Gamma_0 \approx \frac{k_B T \chi^{1/2}}{a^2} \quad (3.4)$$

More complete calculations (from Eq. (3.2)) give:

$$\Gamma_0 \approx \left(\frac{\chi}{6}\right)^{1/2} \frac{k_B T}{a^2} \quad (3.5)$$

Let us calculate the order of magnitude of the surface tension between polyamide 6 (PA6) and a highly incompatible polymer (such as PE for example). For PA, the molecular weight is  $m = 113$  g/mol and the density of the order  $10^6$  g/m<sup>3</sup>. The monomer volume is (in m<sup>3</sup>):

$$a^3 = \frac{113}{6 \times 10^{23} \times 10^6} \approx 20 \times 10^{-29} \longrightarrow a \approx 0.55 \text{ nm} \quad (3.6)$$

Surface tension (for  $\chi \approx 1$ ), that is, for strongly incompatible polymers):

$$\Gamma_0 \approx \frac{4 \times 10^{-21}}{0.3 \times 10^{-18}} \approx 12 \text{ mJ/m}^2 \quad (3.7)$$

This value is consistent with data of the literature [13]. A dimensionless surface tension  $\gamma_0$  can be defined as:

$$\gamma_0 = \frac{\Gamma_0 a^2}{k_B T} \quad (3.8)$$

$\gamma_0$  represents the contact energy between A and B segments (in  $k_B T$  units). From the value estimated in Eq. (3.7), it is found

$$\gamma_0 \approx \frac{12 \times 10^{-3} \times 0.3 \times 10^{-18}}{4 \times 10^{-21}} \approx 0.9 \approx 1 \quad (3.9)$$

## 2.2 Equilibrium of copolymer brush at a planar interface: Isolated brush ("Dry brush") [1, 2]

We discuss here the origin of the interfacial tension decrease due to the creation of copolymers at the interface. To simplify the system in a first approximation, we consider here linear diblock copolymers isolated from the bulk and study one chain, then the brush alone. It is assumed that no homopolymer penetrates into the copolymer bilayer (dry brush approximation). The free energy *per chain* is:

$$F_{ch} = \Gamma_0 \Sigma + \frac{3}{2} k_B T \frac{L^2}{N a^2} \quad (3.10)$$

## 2. Discussion, modelling and analysis

$\Sigma$  is the average interface area per chain (the overall area of the interface divided by the total number of copolymers see figure 3.6),  $N$  the number of statistical segment and the term  $\Gamma_0\Sigma$  is the excess energy per chain in the interface. The second term is the free energy associated to the stretching of block A (resp. B) at the interface (entropic elasticity of a chain). The first term tends to reduce  $\Sigma$ , i.e. to stretch the blocks in order to minimize the interfacial area. The second term is a free energy cost associated to stretching. Equilibrium results from the balance between both effects. It is given by:

$$\frac{\partial F_{ch}}{\partial \Sigma} = 0 \quad (3.11)$$

Within the layer (the brush), one chain occupies an average volume  $L\Sigma = Na^3$  as shown in figure 3.6. Then, Eq. (3.10) can be expressed as a function of  $\Sigma$  only:

$$F_{ch} = \Gamma_0\Sigma + \frac{3}{2}k_B T \frac{Na^4}{\Sigma^2} \quad (3.12)$$

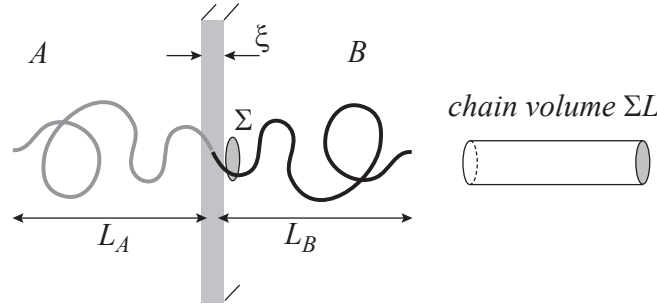


Figure 3.6: A symmetric AB diblock copolymer located at the interface.

The surface tension  $\Gamma$  is defined through the excess energy  $\Delta F_{brush}$  when increasing the surface area  $S \rightarrow S + \Delta S$  as  $\Delta F_{brush} = \Gamma\Delta S$ , i.e.:

$$\Gamma = \left( \frac{\partial F_{brush}}{\partial S} \right)_{Q=cste} \quad (3.13)$$

written for an interface area  $S = 1$  and  $Q$  is the total number of copolymers in the interface of area  $S$ . Thus, the combination of Eq. (3.11) and Eq. (3.13), is equivalent to writing  $\Gamma = 0$  at equilibrium. From Eqs. (3.12) and (3.13):

$$\Gamma = \Gamma_0 - 3k_B T \frac{Na^4}{\Sigma^3} \quad (3.14)$$

Writing  $\Gamma = \Gamma_0 - \Delta\Gamma$ :

$$\Delta\Gamma = \frac{3k_B T N}{a^2} \left( \frac{a^2}{\Sigma} \right)^3 \quad (3.15)$$

We thus understand that, during the experiment in static condition at a flat interface, if the copolymer brush created becomes dense enough to reach the density of a copolymer brush at equilibrium,  $\Gamma$  is decreased to zero. Thus, at equilibrium  $\Gamma=0$  and  $\Delta\Gamma = \Gamma_0$  thus one deduces from Eqs. (3.15):

$$\Sigma_{eq}^3 = 3 \left( \frac{k_B T}{\Gamma_0 a^2} \right) Na^6 \quad (3.16)$$

With the complete numerical factors (eq. 3.5) the average interface area per chain at equilibrium:

$$\Sigma_{eq} = \left( \frac{3k_B T}{\Gamma_0 a^2} \right)^{1/3} N^{1/3} a^2 = \left( \frac{\chi}{54} \right)^{-1/6} N^{1/3} a^2 \quad (3.17)$$

The equilibrium average stretching is given by:

$$L_{eq} = \frac{Na^3}{\Sigma_{eq}} = N^{2/3} a \left( \frac{\Gamma_0 a^2}{k_B T} \right)^{1/3} = \left( \frac{\chi}{54} \right)^{1/6} N^{2/3} a \quad (3.18)$$

Order of magnitude:  $N = 200$ ,  $a = 0.55$  nm,  $\chi \approx 1$  give  $\Sigma_{eq} = 3.6$  nm<sup>2</sup>.

Note that this equilibrium resulting in  $\Gamma = 0$  effectively results from the balance between the raw surface energy  $\Gamma_0$  (simply proportional to the interfacial area) and the copolymer stretching contribution.

### 2.3 Non symmetrical case, curvature effects

In previous subsection we discussed the interfacial tension decrease due to identical chain stretching on both sides of the interface, because a linear diblock copolymer with blocs of equal lengths, was studied at a flat interface. One may thus wonder what are the effects on block stretching of imposing a curvature to an interface which would be plane at equilibrium. Conversely, what is the curvature at equilibrium for an asymmetric copolymer? The present discussion allows to discuss both effects at the same time.

#### 2.3.1 Effect of interface curvature on block stretching

Let us consider a diblock copolymer with block A of length  $N_A$  and block B of length  $N_B$ . If the interface is curved (like in the case of droplets for instance), blocks A (inside the droplet) have an excess of stretching. Stretching of blocks B (outside the droplet) is partially relaxed. Let us denote  $\Sigma_0$  the area per chain occupied at the droplet surface. It is assumed that the interface has locally the geometry of a sphere, with radii of curvature  $R$  in both principal directions. The curvature of the interface is  $C = 2/R$ .

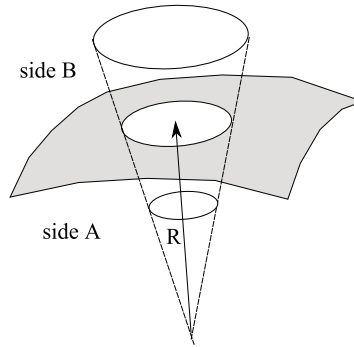


Figure 3.7: Effect of the curvature on the area occupied by both blocs of a grafted copolymer.  $R$  is the radius of curvature of the interface.

The area per chain  $\Sigma(r)$  occupied at a distance  $r$  from the interface (block B) is:

$$\Sigma(r) = \Sigma_0 \frac{(R+r)^2}{R^2} \quad (3.19)$$

## 2. Discussion, modelling and analysis

where  $R$  is the radius of curvature and  $\Sigma_0$  denotes  $\Sigma(r = 0)$ . Conservation of volume (on side B) gives:

$$N_B a^3 = \int_0^{L_B} dr \Sigma(r) = \frac{\Sigma_0}{3R^2} \left[ (R + L_B)^3 - R^3 \right] \quad (3.20)$$

that is, for  $R \gg L_B$  (i.e. not too strong curvature):

$$N_B a^3 = \Sigma_0 L_B \left( 1 + \frac{L_B}{R} + \dots \right) \quad (3.21)$$

and

$$L_B = \frac{N_B a^3}{\Sigma_0} \left( 1 - \frac{N_B a^3}{\Sigma_0 R} + \dots \right) \quad (3.22)$$

Similarly on the A side:

$$L_A = \frac{N_A a^3}{\Sigma_0} \left( 1 + \frac{N_A a^3}{\Sigma_0 R} + \dots \right) \quad (3.23)$$

Now, the free energy  $g$  associated to stretching has to be evaluated. Within a  $r \rightarrow r + dr$  spherical layer, there are in average  $dn(r)$  monomers (for one chain). Since the polymer density in the brush is constant ("dry brush" assumption),  $n$  and  $r$  are related by  $dr \Sigma(r) = dn a^3$  (similarly to previously  $L \Sigma = N a^3$ ), which gives

$$\frac{dr}{dn} = \frac{a^3}{\Sigma(r)} \quad (3.24)$$

For the small subchain of length  $dn$  which is stretched over the length  $dr$  (see schematic representation figure 3.8), the elastic free energy is

$$d\psi = \frac{3}{2} \frac{k_B T}{a^2} \frac{dr}{dn} dr \quad (3.25)$$

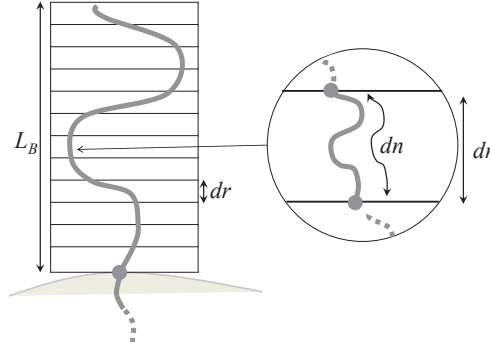


Figure 3.8: Schematic representation of the entire block divided in small subchains of length  $dn$  and stretched over the length  $dr$ .

For the whole block B, the total stretching energy:

$$\psi_B = \frac{3}{2} \frac{k_B T}{a^2} \int_0^{L_B} \frac{dr}{dn} dr \quad (3.26)$$

Inserting Eq. (3.25) and using Eq. (3.19) for  $\Sigma(r)$  (in the approximation  $L_B \ll R$ ) gives:

$$\psi_B \approx \frac{3}{2} \frac{k_B T a}{\Sigma_0} L_B \left( 1 - \frac{L_B}{R} + \dots \right) \approx \frac{3}{2} \frac{k_B T a^4 N_B}{\Sigma_0^2} \left[ 1 - 2 \frac{N_B a^3}{\Sigma_0 R} + \dots \right] \quad (3.27)$$

(in which Eq. (3.22) has been used to substitute  $L_B$ ). Similarly, on the A side:

$$\psi_A \approx \frac{3 k_B T a^4 N_A}{2 \Sigma_0^2} \left[ 1 + 2 \frac{N_A a^3}{\Sigma_0 R} + \dots \right] \quad (3.28)$$

Note the signs in Eqs. (3.27) and (3.28): with the convention of figure 3.7, stretching of block B is decreased, that of block A is increased.

### 2.3.2 General expression for the free energy of the brush

We consider here the general case of grafted copolymers, in which the copolymer which is formed has several ( $p$ ) arms on the B side (two arms for example). In this case, the area per chain is different on each side. For instance, for a graft copolymer with  $p$  B arms, the area per chain on the B side is  $\Sigma_B = \Sigma_A/p$ .

The free energy of the brush  $f_{brush}$  (in the 'dry brush' case) is written *per chain* and in units of  $k_B T$  as a function of the radius of curvature  $R$  (case of a sphere) and of the area occupied per copolymer  $\Sigma_A = p \Sigma_B$ . It contains the stretching free energy of the whole copolymer (one A block +  $p$  B blocks). Altogether it gives [1, 2]:

$$\frac{f_{brush}}{k_B T} = \left( \frac{\Gamma_0 a^2}{k_B T} \right) \frac{\Sigma_A}{a^2} + \frac{3 a^4 N_A}{2 \Sigma_A^2} \left[ 1 + 2 \frac{N_A a^3}{\Sigma_A R} + \dots \right] + \frac{3 p a^4 N_B}{2 \Sigma_B^2} \left[ 1 - 2 \frac{N_B a^3}{\Sigma_B R} + \dots \right] \quad (3.29)$$

or

$$\begin{aligned} \frac{f_{brush}}{k_B T} = & \left( \frac{\Gamma_0 a^2}{k_B T} \right) \frac{\Sigma_A}{a^2} + \frac{3}{2} \left( \frac{a^2}{\Sigma_A} \right)^2 (N_A + p^3 N_B) + 3 \left( \frac{a^2}{\Sigma_A} \right)^3 \frac{a}{R} (N_A^2 - p^4 N_B^2) + \\ & 7 \left( \frac{a^2}{\Sigma_A} \right)^4 \frac{a^2}{R^2} (N_A^3 + p^5 N_B^3) + \dots \end{aligned} \quad (3.30)$$

Writing in dimensionless units  $\sigma = \Sigma_A/a^2$ ,  $\sigma$  representing the average surface per chain in units of the surface occupied by one segment,  $c = a/R$ , the curvature being the inverse of the radius of curvature (in unit of monomer size) and  $\gamma_0 = \Gamma_0 a^2/k_B T$ :

$$\boxed{\frac{f_{brush}}{k_B T} = \gamma_0 \sigma + P_1 \sigma^{-2} + P_2 \sigma^{-3} c + P_3 \sigma^{-4} c^2 + \dots} \quad (3.31)$$

with the coefficients

$$P_1 = \frac{3}{2} (N_A + p^3 N_B) \quad (3.32)$$

$$P_2 = 3 (N_A^2 - p^4 N_B^2) \quad (3.33)$$

$$P_3 = 7 (N_A^3 + p^5 N_B^3) \quad (3.34)$$

In Eq. (3.31), the first term is the excess energy per chain in the interface, the second is the free energy associated to the stretching of both block, the third is associated to the spontaneous curvature of the interface and the fourth the curvature elasticity.

The expression in Eq. (3.31) allows discussing the effect of the asymmetry of the copolymer on the equilibrium curvature of the interface, and determining the equilibrium area per chain. It also gives the curvature elastic constant of the interface.

Eq. 3.31 shows that it exists a value of the reduced surface  $\sigma$  and the curvature  $c$  for which  $f_{brush} = 0$ . This state corresponds to the equilibrium state. It directly gives the curvature at equilibrium of the considered graft copolymer and the surface occupied by one chain, thus indirectly the block stretching. It also gives the possibility to estimate the excess energy when a brush is curved with a curvature different from its equilibrium curvature.

Let us first determine the overall minimum of  $f_{brush}$ , which gives the equilibrium values  $\sigma_{eq}$  and  $c_{eq}$ . For a given  $\sigma$  value,  $f_{brush}$  may be written:

$$\frac{f_{brush}}{k_B T} = \gamma_0 \sigma + \left( P_1 - \frac{P_2^2}{4P_3} \right) \sigma^{-2} + P_3 \sigma^{-4} \left( c + \frac{P_2 \sigma}{2P_3} \right) \quad (3.35)$$

which gives for each  $\sigma$  value a curvature  $c_{min}(\sigma) = -\frac{P_2 \sigma}{2P_3}$  corresponding to the minimum of the function. For  $c = c_{min}(\sigma)$ ,  $f_{brush}$  is

$$\frac{f_{brush}}{k_B T} = \gamma_0 \sigma + \left( P_1 - \frac{P_2^2}{4P_3} \right) \sigma^{-2} \quad (3.36)$$

and has an overall minimum given by  $\partial f_{brush} / \partial \sigma = 0$ , which gives

$$\sigma_{eq}^{-3} = \frac{\gamma_0}{2 \left( P_1 - \frac{P_2^2}{4P_3} \right)} \quad (3.37)$$

Then the equilibrium curvature is

$$c_{eq} = -\frac{P_2 \sigma_{eq}}{2P_3} \quad (3.38)$$

with  $\sigma_{eq}$  given by Eq. (3.37).

### 2.3.3 Condition for zero average curvature

The condition to have a planar interface at equilibrium is that  $F_{brush}$  has a minimum for  $c_{eq} = 0$ , i.e. the coefficient  $P_2$  must be zero. It gives:

$$N_A^2 = p^4 N_B^2 \quad (3.39)$$

Thus for a linear diblock copolymer  $p=1$ , this gives  $N_A=N_B$ , for a Y-shape grafted copolymer with  $p=2$ , it gives  $N_{PA}=4N_{PE}$ . This criterion may be more conveniently expressed as a function of measurable quantities as, for example, for a grafted copolymer with two arms of PA (=A) and one arm of PE (=B) as [57]:

$$\boxed{\frac{V_{PA}^3}{R_{gPA}^2} = 16 \frac{V_{PE}^3}{R_{gPE}^2}} \quad (3.40)$$

in which  $V_{PE}$  is the average molar volume of **one** PE arm and  $V_{PA}$  is the average molar volume of the PA arm.  $R_{gPE}^2$  and  $R_{gPA}^2$  are the corresponding squared radii of gyration. The advantages of Eq. 3.40 is that  $V$  and  $R_g$  are experimentally measurable values.

## 2.4 Case of PA/PE graft copolymers

Let us now discuss the previous theoretical analysis with actual parameters values corresponding to our systems, regarding the results obtained in static conditions at a flat interface between MA-g-HDPE and different PA6 (PA6-3k, 10k, 18k and 31k) presented in the article (see section 1).

### 2.4.1 Chosen parameters and hypothesis on the systems studied

Several hypothesis are made. First of all the dry brush regime is considered, thus, it is supposed that no homopolymer can penetrate the copolymer brush created at the interface. Then, polydispersity is not considered but rather an average number average molecular weight  $M_n$ . Besides, it is assumed that the graft copolymer behaves in the same way as a Y-shaped copolymer with one block PA and two HDPE arms as shown in fig. 3.9.

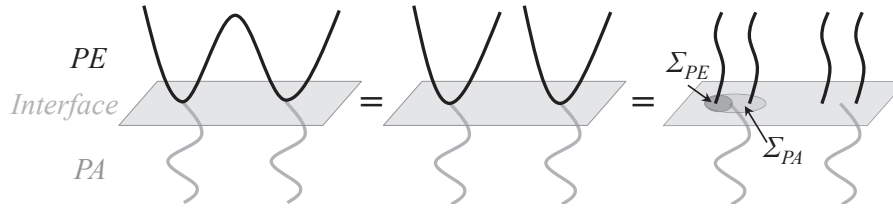


Figure 3.9: Hypothesis on the copolymer architecture considered for the calculations.

To discuss the effect of relative block length, one has to determine the numbers of statistical segments for each block ( $N_{PA}$  and  $N_{PE}$ ), corresponding to the molar masses under study.

- For PE at 413 K = 140°C, Fetters et al. [135] give  $C_\infty = 7.38$  and  $a_{PE} = 13.7 \text{ \AA}$  (length of the Kuhn statistical segment). For PE, the elementary chemical unit is one  $-\text{CH}_2-$  group, of molar mass  $m_0 = 14 \text{ g}$  and length  $l_0 = 1.54 \text{ \AA}$ . The average molar mass between grafting points (MA groups) along MA-g-HDPE chain is  $M_n \approx 9700$ . Using the definition of  $C_\infty$ :

$$\langle R^2 \rangle_0 = C_\infty \frac{M}{m_0} l_0^2 = C_\infty N_b l_0^2 = N a^2 \quad (3.41)$$

We estimate the number  $N_{PE}$  of statistical segments corresponding to  $M_n \approx 9700$  which gives  $N_{PE \text{ 2arms}} \approx 64$ . Each PE arm is half this length, which gives about  $N_{PE} \approx 32$  statistical segments for each branch on the PE side.

- For PA6 at 270°C, the same estimation from tabulated values [59, 135] give a kuhn statistical segment length  $a_{PA} \approx 0.92 \text{ nm}$  and the statistical segments values  $N_{PA}$  are estimated as shown in table 3.1.

From these values, the equilibrium thickness  $D$  of the PA layer given by  $D = 2L_{eq} \approx N_{PA}^{2/3} a_{PA}$ , with  $L_{eq}$  given by eq.3.18 and  $\chi \approx 1$ , can be estimated for each value of the average molecular weight  $M_n$ . Results are summarized in table 3.1. For sandwiches exhibiting lamellae (10k, 18k and 31k), it is found that  $D$  varies from about  $\approx 20 \text{ nm}$  (for

## 2. Discussion, modelling and analysis

Table 3.1: Table of polyamide samples of the studied samples.  $\langle R^2 \rangle_0^{1/2}$  calculated from Fetters et al.  $N$ : number of statistical segments.

Denomination	$M_n$	$\langle R^2 \rangle_0^{1/2}$ [ nm ]	$N_{PA}$	$D \approx N_{PA}^{2/3} a_{PA}$ [ nm ]
3k	3000	5.06	30.12	8.93
10k	10000	9.23	100.4	19.92
18k	18000	12.39	180.7	29.47
31k	31000	16.26	311.3	42.35

$M_n = 10000 \text{ g.mol}^{-1}$ ) up to about 42 nm (for  $M_n = 31000 \text{ g.mol}^{-1}$ ). The variation of the apparent long period of the observed patterns agrees qualitatively with the variation of chain length. Data are not quantitative enough to check a possible power law variation of the period as a function of the average chain length.

### 2.4.2 Zero average curvature

The condition for zero mean curvature is given by Eq. 3.40, then using  $V_i = Mn_i/\rho_i$  ( $i=PA$  or  $PE$ ) where  $\rho$  is the density in the melt state at  $290^\circ\text{C}$  ( $\rho_{PA \text{ at } 290^\circ\text{C}} = 0.96 \text{ g.cm}^{-3}$  and  $\rho_{PE \text{ at } 290^\circ\text{C}} = 0.72 \text{ g.cm}^{-3}$ ) and ratios  $\langle R^2 \rangle_0/Mn$  tabulated by Fetter et al.[59] ( $\langle R_{PA6}^2 \rangle = 0.852 Mn_{PA6} (\text{\AA}^2)$  and  $\langle R_{PE}^2 \rangle = 1.25 Mn_{PE} (\text{\AA}^2)$ ) we find  $V_{PA}^3/R_{gPA}^2 = 1.325 Mn_{PA}^2$  and  $V_{PE}^3/R_{gPE}^2 = 2.14 Mn_{PE}^2$  (with lengths in  $\text{\AA}$  and  $Mn$  in  $\text{g mol}^{-1}$ ), which gives for the zero mean curvature condition:

$$\boxed{Mn_{PA} \approx 5.1 Mn_{PE}} \quad (3.42)$$

Ratios  $Mn_{PA}/Mn_{PE}$  and  $N_{PA}/N_{PE}$  are given in table 3.2.

Table 3.2: Estimation of the ratio  $Mn_{PA}/Mn_{PE}$  for the four systems of MA-g-HDPE and PA6-3k, 10k, 18k and 31k.  $Mn_{PE}$  is taken  $\approx 4800 \text{ g/mol}$ ,  $N_{PA}$  are taken in table 3.1 and  $N_{PE} \approx 32$ .

Denomination	$M_n$	$Mn_{PA}/Mn_{PE}$	$N_{PA}/N_{PE}$
3k	3000	0.6	0.9
10k	10000	2.04	3.1
18k	18000	3.67	5.6
31k	31000	6.32	9.7

### 2.4.3 Free energy of brushes: determination of equilibrium positions

The free energy of brushes created by the four systems can be estimated from eq. 3.31.  $f_{brush}$  is expressed as a function of the reduced surface  $\sigma = \Sigma_A/a^2$  and the curvature  $c = a/R$ . The minimum of the function for both  $\sigma$  and  $c$  corresponds to the equilibrium state of stretching and curvature.

The average numbers of statistical bond  $N_A = N_{PA}$  have been estimated in table 3.1 and  $N_B = N_{PE} \approx 32$ , the number of branch  $p=2$  and  $\gamma_0 \approx 1$  (see eq. 3.9), the function

$f_{brush}$  is plotted as a function of  $c$  and  $\sigma$  for the four systems in the contour maps in figure 3.10. The minimum coordinates of the function are reported in table 3.3.

We see that in all cases, when  $\sigma = \sigma_{eq}$  the energy is minimum and when the brush is compressed  $\sigma < \sigma_{eq}$  the energetic cost is huge and  $f_{brush}$  increases very rapidly. When the brush is relaxed  $\sigma > \sigma_{eq}$  (surface is increased) this also makes the free energy increase, but in reactive blends when area is created new reactive species are directly formed as long as chemical reaction can progress which decreases  $\sigma$  as long as reactive moieties are available.

The sign of the value of the curvature indicates that cases of PA6-3k and 10k are curved toward the PA6 side and cases of PA6-18k and 31k are curved toward the PE side. The value of the curvature found for cases 10k, 18k and 31k are much closer to zero than 3k. Thus at a flat interface, which at the scale of a copolymer chain starts at  $\approx 100\text{nm}$ ,  $f_{brush}$  for PA6-3k is metastable. This shows that for PA6-3k, only a very curved interface ( $R \approx 36\text{ nm}$ ) allows to form a dense brush which decreases the interfacial tension to zero.

Table 3.3: Estimation of the minimum coordinates of the function  $f_{brush}$  for the four systems.

Denomination	$\sigma$	$c (\times 10^{-3})$
3k	9.0	-25
10k	10.2	-7
18k	10.9	5
31k	11.7	6

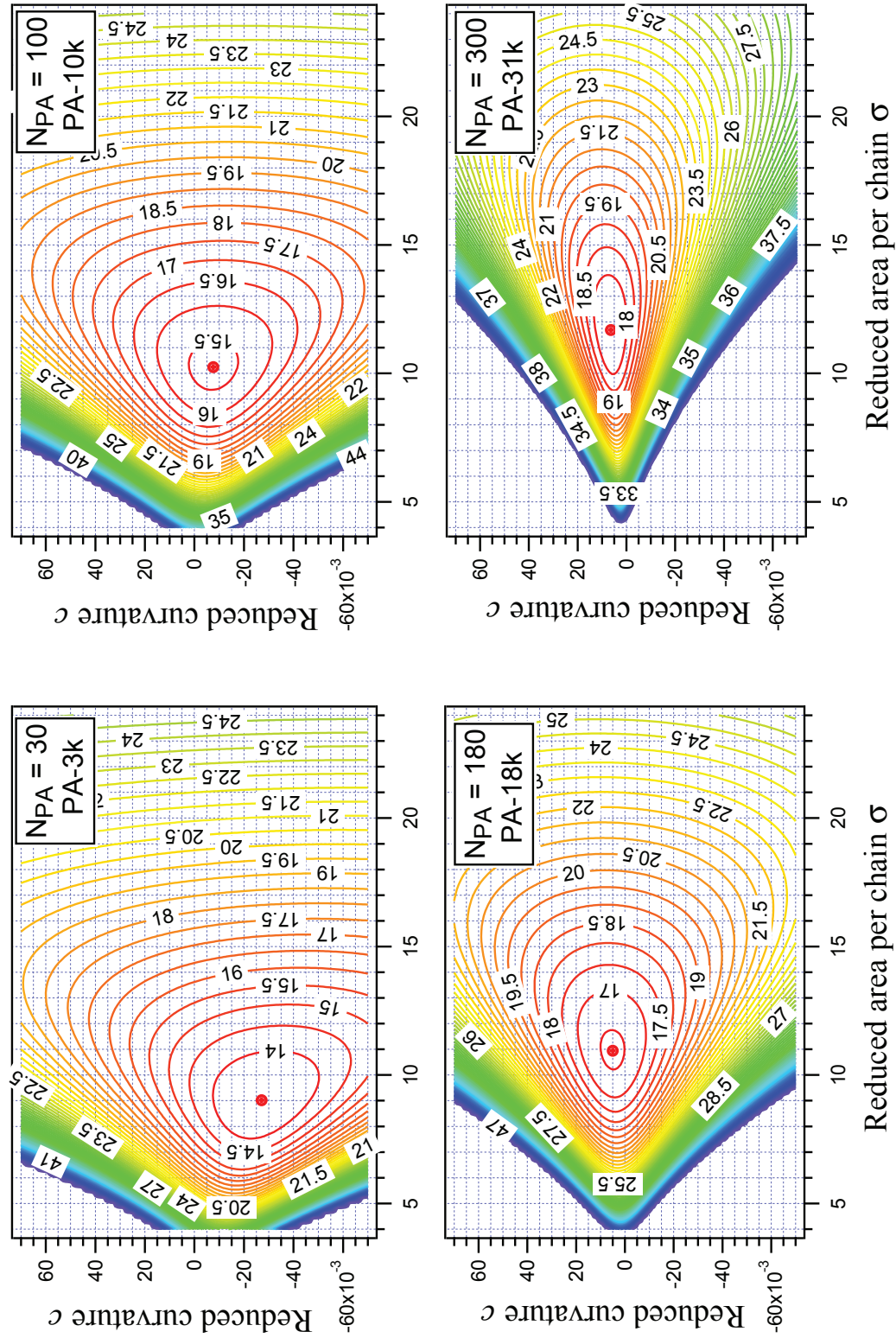


Figure 3.10: Contour maps of the free energy of the brush  $f_{brush}$  as a function of the reduced area per chain  $\sigma$  and the reduced curvature  $c$  for the four systems studied with  $\gamma_0 \approx 1$  and  $p=2$ .

### 2.4.4 Spontaneous morphology at equilibrium

The copolymer morphologies at equilibrium depends on the curvature of the interface at equilibrium; as the equilibrium curvature  $c$  increases, the following structures are successively observed: Lamellar (around  $c=0$ ), Bicontinuous, Cylinders and Spheres (micelles).

Milner [57] has estimated a phase diagram which summarizes the domain of existence of the different structures in terms of volume fraction and copolymer asymmetry.

For our systems, the volume fractions corresponding to each copolymer architecture are summarized in table 3.4.

The asymmetry parameter  $\epsilon$  is defined as  $\epsilon = (n_{PE}/n_{PA})(l_{PE}/l_{PA})^{1/2}$  with  $l_{PE} = V_{PE}/R_{gPE}^2$  (resp.  $l_{PA}$ ). With:

- On the PA side:  $l_{PA} = \frac{Mn_{PA}/\rho_{PA}}{R_{PA}^2} = \frac{Mn_{PA}}{\rho_{PA}*1.25Mn_{PA}} = \frac{1}{0.96*0.853} = 1.22$
- On the PE side:  $l_{PE} = \frac{Mn_{PE}/\rho_{PE}}{R_{PE}^2} = \frac{Mn_{PE}}{\rho_{PE}*1.25Mn_{PE}} = \frac{1}{0.72*1.25} = 1.11$

For a Y-shaped copolymer  $PE_2PA$  with two arms of PE ( $n_{PE} = 2$ ) and one arm of PA ( $n_{PA} = 1$ ), the value of our asymmetry parameter is thus  $\epsilon \approx 1.91$ . We can then predict the morphology that copolymers should theoretically adopt as a function of the composition. Corresponding points are reported in figure 3.11

Table 3.4: Estimation of the volume fraction of PA6/MA-g-HDPE for each of our copolymers.

Denomination	$M_n$	PA6/MA-g-HDPE (%vol)
3k	3000	20/80
10k	10000	44/56
18k	18000	58/42
31k	31000	70/30

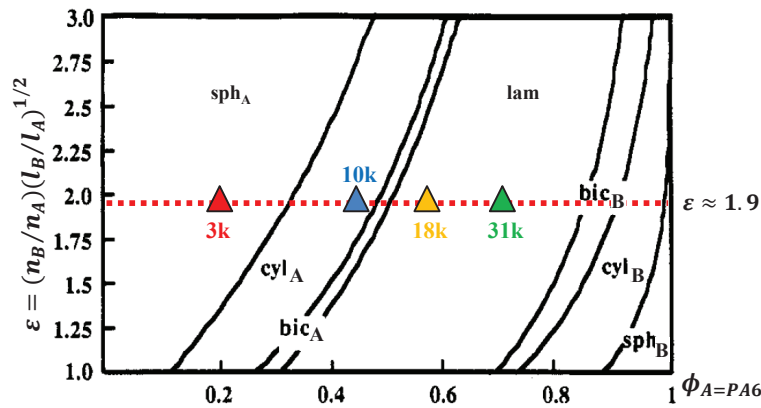


Figure 3.11: Milner phase diagram [57]. Determination of the theoretical morphology adopted by the four Y-shaped copolymers (2 arms of B=PE, 1 arm of A=PA) of the study in the strong segregation limit, with  $n_{PE} = 2$  PE arms of roughly 4800g/mol and  $n_{PA} = 1$  PA arm of the average molecular weight 3000g/mol for 3k (resp. 10k, 18k and 31k) as a function of the estimated PA6 volume fraction. We made the hypothesis that all chains are grafted with a molar ratio  $[NH_2]/[MA]=1$ .

### 2.4.5 Discussion

From the previous results, one obvious conclusion is that copolymers with PA6-3k behaviour is predicted to be very different from the three other cases. Indeed, its architecture is far from the architecture which predicts a zero average curvature at equilibrium. Indeed, Milner's diagram shows that the morphology at equilibrium is micelles of PA6 while for the three other systems quite symmetrical morphologies (cylinders or lamellae) are predicted.

In sandwiches with PA6-10k, 18k and 31k, quite symmetrical morphologies were indeed observed, which is consistent with the theoretical prediction for Y-shaped graft copolymers. In real systems, the difference in the morphology observed is less sensitive to chain length because the chain distribution of the three PA6 samples overlap quite largely, as shown in the SEC chromatograms in figure 3.12.

However, the PA6-3k did not exhibit interfacial destabilization and the SEC spectra show that the molecular weight distribution almost do not overlap the others. This very different behaviour is also consistent with theoretical predictions which predict a very different morphology at equilibrium than the other one. Note that the symmetry criterion defined by Leibler's team ( $Mn_{PA} = Mn_{PE}$  see chapter 1) is thus not adapted to describe symmetrical morphologies for our systems.

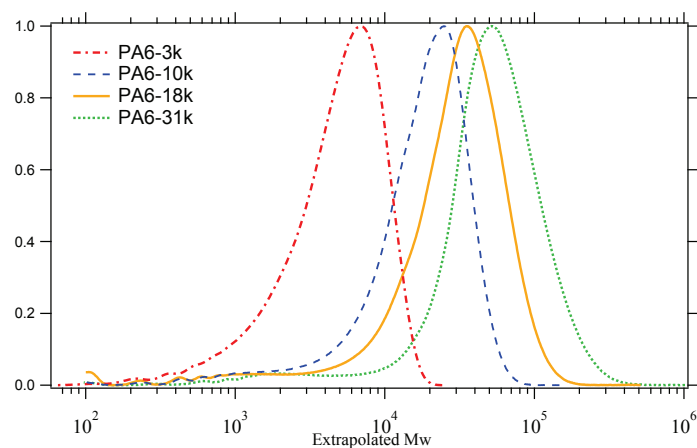


Figure 3.12: Chromatograms of Polyamide 6: PA6-3k (red), PA6-10k (blue), PA6-18K (yellow) and PA6-31K (green) (SEC measurement, absolute values).

## 2.5 Perspectives: Linear analysis of instabilities

Very preliminary linear analysis of the instability initiation and growth is in progress. First discussions led to several temporary first conclusions:

- The driving force for the decrease of surface tension is the energy gain due to the reaction at the interface. It is thus the driving force for the initiation of instabilities.
- A creation of a dense copolymer layer is possible due to the very fast chemical reaction between reactive moieties  $\text{NH}_2$  and MA.
- Instabilities are initiated when the interfacial tension  $\Gamma$  becomes zero or even negative. We did not discuss quantitatively the most negative value that  $\Gamma$  may reach kinetically.
- An estimation of the wavelength of the fastest growing instability (by an analyse in terms of wave vector  $q$ ) exhibits a wavelength of few tens of nanometers. This is consistent with the length of few copolymer blocks (in terms of radius of gyration).
- The characteristic time of the fastest growing mode after destabilization is very fast compared to the time scale of the experiment: few milliseconds compared to few minutes.
- For a nearly symmetrical copolymer, longer chains length (i.e.  $N \approx 1000$ ) may create an energy barrier which may slow down the reaction kinetics and prevent the formation of a dense copolymers brush. For small values (i.e.  $N \approx 100$ ) a stationary regime is reached due to the creation of instabilities.

## 3 Conclusions

In this chapter we have studied the effect of the interfacial chemical reaction between PA6 and MA-g-HDPE in static conditions at a macroscopically flat interface. We observed the nucleation and growth of ordered microphase separated copolymer domains at flat interfaces due to chemical reaction under static conditions for three of the four case studied. For the longer PA6 chains (PA6-10k, 18k and 31k) instabilities developed, whereas interfaces with shorter PA6 chains (PA6-3k) remain metastable.

At the considered temperature, the interfacial destabilization was initiated due to the fast chemical reaction and the creation of a dense brush of copolymers at the interface. The brush density can reach values which are beyond the equilibrium value, thus leading to zero or negative surface tension and interface destabilization. The architecture of the copolymer created at the interface not only affects the initiation of interfacial fluctuations, but also the microstructures which are formed as a result of interface destabilization. These microstructures are similar to those observed in block copolymers, and thus depend on the relative length of the blocks on each side of the interface. Indeed this ratio of lengths determines the local equilibrium curvature of the interface.

We found that the copolymer architecture created by the systems with 10k, 18k and 31k are not far from the architecture which favours symmetrical morphologies, i.e. zero average spontaneous interface curvature. This is well consistent with the destabilization of the interface and the quite symmetrical patterns observed for the three systems. However, the architecture of the copolymers formed in systems with PA6-3k favour a very strong curvature toward the PA6 blocks (micelles of PA). Thus, at a flat interface, a dense copolymer brush on both side of the interface cannot be formed and thus cannot generate destabilization. In conclusion, we show that in our case the copolymer asymmetry can inhibit instabilities.



---

In the specific case of reactive compatibilization, two concomitant mechanisms of morphology development can happen during blending, namely (1) the standard mechanism of drop break-up and coalescence of polymer domains under shear that is controlled by classical rheological laws; (2) a mechanism specific to reactively compatibilized blends, which leads to the formation of nano-scale dispersions in both component domains, in addition to the micro-scale morphology. This phenomenon could be attributed to the chemical reaction. In order to discriminate the mechanisms of morphology development due either to rheological process or to the compatibilization reaction, both mechanisms have been studied separately.

In this chapter, we first focus on the mechanism of morphology development only due to shearing, that is drop break-up and coalescence. For that, we study uncompatibilized PA6/HDPE blends over a broad range of compositions for three PA6 of very different molecular weights, in order to study the influence of the viscosity ratio on mechanisms of morphology development. This first part combined with results of chapter three, provide an overview of both effects of shearing alone and effects of the compatibilization reaction alone.

In the second part of this chapter, morphologies of reactively compatibilized PA6/MA-g-HDPE are described. In order to identify the mechanisms responsible of morphology development in those blends, morphologies are first compared to typical sizes and phase inversion compositions observed in uncompatibilized blends morphologies. Points that cannot be explained by the mechanism of drop break-up alone, and particularly nanodispersions, are identified. Morphologies are then compared to results obtained in chapter 3 on the morphology development in static condition only due to the compatibilization reaction. The influences of viscosity ratio and copolymer architecture formed at the interface are discussed. Thanks to this study, main parameters that control the morphology development in reactively compatibilized blend, and especially the formation of nanodispersions, are highlighted.

## 1 Studied formulations

In this work three series of uncompatibilized blends are compared to three series of compatibilized blends:

- Uncompatibilized blends: **PA6-31k/HDPE, PA6-18k/HDPE, PA6-3k/HDPE**. All blend compositions are reported in table 4.1.
- Compatibilized blends: **PA6-31k/MA-g-HDPE, PA6-18k/MA-g-HDPE, PA6-3k/MA-g-HDPE**. Blends compositions are reported in table 4.2.

Materials properties have been described in chapter 2. The compositions in terms of volume fraction were calculated with the density in the melt state of PA6 and HDPE at 290 °C:  $\rho_{PA\ 290\ ^\circ C} = 0.96\ \text{g/cm}^3$  and  $\rho_{PE\ 290\ ^\circ C} = 0.72\ \text{g/cm}^3$ . As a reminder  $R_v$  is defined as the viscosity ratio in the linear regime at 100 rad/s between the dispersed phase and the matrix ( $R_v = \eta_d/\eta_m$ ). Thus  $R_v(\text{PA/PE})$  and  $R_v(\text{PE/PA})$  are respectively used when PA forms a dispersed phase in PE matrix and vice versa.

Blends will be named by, first, the name of the polymer composing both phases and secondly, the volume fraction in the melt state of the blend. For sake of simplicity, the name of polymers have been shorten in blends names as follow:

- **PA6-3k, PA6-18k and PA6-31k** will be called respectively **PA-3k, PA-18k and PA-31K**.
- **HDPE** will be called **PE**.
- **MA-g-HDPE** will be called **MAGPE**.

For example a blend composed of 20%vol of PA6-18k and 80%vol of MA-g-HDPE will be called: PA-18k/MAGPE 20/80.

In compatibilized blends copolymers are created at the interface due to the reaction between MA moieties of the MA-g-HDPE and  $\text{NH}_2$  end-groups of the PA6. The characteristics of raw materials are as follow:

- As mentionned in chapter 2 all PA6 chains contain one amine-end group per chain.
- MA-g-HDPE, contains in average about 3 maleic anhydride moieties per chain (value calculated from GPC measurements and supplier data). For this calculation, we considered the value of 1%wt of maleic anhydride (given by the supplier). Note that the real percentage of MA moieties effectively reactive is probably lower than 1%wt (see discussion in section 3.1 of the present chapter).

The reaction between MA moieties and  $\text{NH}_2$  moieties of PA6 can be extremely fast at process temperature(chapter2 subsection 2.1)[82, 81]. Thus, in our blends, a large amount of copolymer can be created at the interface. Given that our three PA6 have very different average molecular weights, the architecture of the created copolymers, will be very different. Figure 4.1 is a schematic representation of the copolymers formed at the interface during reaction between MA-g-HDPE and PA6-3K, PA6-18K or PA6-31k. In table 4.2, the compatibilized blends compositions are reported as well as the theoretical molar ratio  $[\text{NH}_2]/[\text{MA}]$  (Amine end group/maleic anhydride) initially present in the blends. Note that the viscosity ratios are slightly modified compared to the uncompatibilized blends because the dynamic viscosity at 290 °C and 100rad/s of PEHD and PEHD-g-AM are respectively,  $\eta_{PEHD}^* = 60\ \text{Pa/s}$  and  $\eta_{PEHD-g-AM}^* = 105\ \text{Pa/s}$ .

## 1. Studied formulations

Table 4.1: Uncompatibilized binary blends: PA6/HDPE

Name	Composition (%vol)	Composition (%wt)	Viscosity ratio	
	PA6/PEHD	PA6/PEHD	$R_v$ (PA/PE)	$R_v$ (PE/PA)
PA-31k/PE 80/20	80/20	84.2/15.8	13	0.07
PA-31k/PE 69/31	69/31	75.7/24.3	13	0.07
PA-31k/PE 58/42	58/42	64.9/35.1	13	0.07
PA-31k/PE 50/50	50/50	57.1/42.9	13	0.07
PA-31k/PE 40/60	40/60	47.1/52.9	13 </td <td>0.07</td>	0.07
PA-31k/PE 20/80	20/80	25/75	13	0.07
PA-18k/PE 80/20	80/20	84.2/15.8	1.7	0.6
PA-18k/PE 69/31	69/31	75.7/24.3	1.7	0.6
PA-18k/PE 58/42	58/42	64.9/35.1	1.7	0.6
PA-18k/PE 50/50	50/50	57.1/42.9	1.7	0.6
PA-18k/PE 40/60	40/60	47.1/52.9	1.7	0.6
PA-18k/PE 20/80	20/80	25/75	1.7	0.6
PA-3k/PE 80/20	80/20	84.2/15.8	0.003	300
PA-3k/PE 69/31	69/31	75.7/24.3	0.003	300
PA-3k/PE 50/50	50/50	57.1/42.9	0.003	300
PA-3k/PE 40/60	40/60	47.1/52.9	0.003	300
PA-3k/PE 30/70	30/70	36.4/63.6	0.003	300
PA-3k/PE 20/80	20/80	25/75	0.003	300
PA-3k/PE 10/90	10/90	12.9/87.1	0.003	300

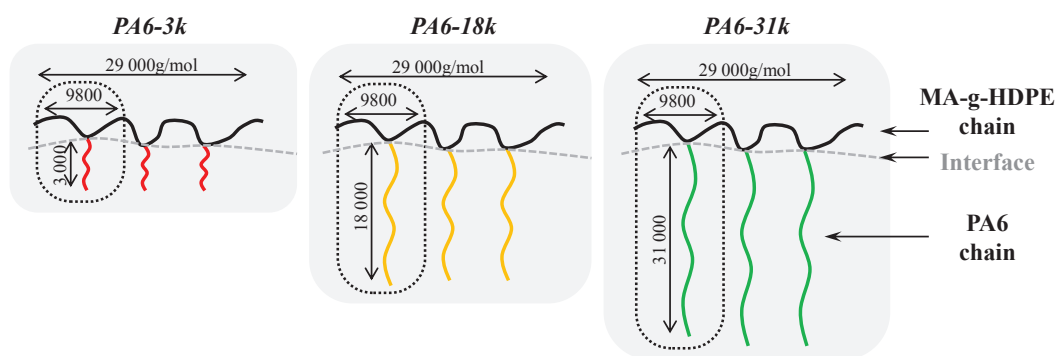


Figure 4.1: Schematic representations of graft copolymers formed during the reaction between MA moieties of the MA-g-HDPE and  $\text{NH}_2$  moieties of the PA6. The numbers indicated correspond to average molecular weights ( $M_n$ ) of the PA6 branch, the total length of the HDPE backbone and the HDPE unit to consider in the Y-shape copolymer. These numbers can be widely distributed due to the polydispersity of the PA6 and the MA-g-HDPE and due to the statistical heterogeneity of the grafting.

Table 4.2: Compatibilized binary blends: PA6/MA-g-HDPE

Name	Composition	Composition	Viscosity ratio		Ratio (NH <sub>2</sub> )/(MA)
	(%vol)	(%wt)	$R_v$ (PA/PE)	$R_v$ (PE/PA)	
PA-31k/MAGPE 80/20	80/20	84.2/15.8	7.6	0.13	1.7
PA-31k/MAGPE 69/31	69/31	75.7/24.3	7.6	0.13	1
PA-31k/MAGPE 58/42	58/42	64.9/35.1	7.6	0.13	0.6
PA-31k/MAGPE 50/50	50/50	57.1/42.9	7.6	0.13	0.4
PA-31k/MAGPE 40/60	40/60	47.1/52.9	7.6	0.13	0.3
PA-31k/MAGPE 20/80	20/80	25/75	7.6	0.13	0.1
PA-18k/MAGPE 80/20	80/20	84.2/15.8	1	1	2.9
PA-18k/MAGPE 69/31	69/31	75.7/24.3	1	1	1.6
PA-18k/MAGPE 58/42	58/42	64.9/35.1	1	1	1
PA-18k/MAGPE 50/50	50/50	57.1/42.9	1	1	0.7
PA-18k/MAGPE 47.5/52.5	47.5/52.5	54.7/45.3	1	1	0.65
PA-18k/MAGPE 45/55	45/55	52.2/47.8	1	1	0.6
PA-18k/MAGPE 40/60	40/60	47.1/52.9	1	1	0.5
PA-18k/MAGPE 20/80	20/80	25/75	1	1	0.2
PA-3k/MAGPE 80/20	80/20	84.2/15.8	0.002	540	18
PA-3k/MAGPE 69/31	69/31	75.7/24.3	0.002	540	8.9
PA-3k/MAGPE 50/50	50/50	57.1/42.9	0.002	540	4.5
PA-3k/MAGPE 40/60	40/60	47.1/52.9	0.002	540	3
PA-3k/MAGPE 30/70	30/70	36.4/63.6	0.002	540	1.9
PA-3k/MAGPE 20/80	20/80	25/75	0.002	540	1
PA-3k/MAGPE 10/90	10/90	12.9/87.1	0.002	540	0.5
PA-3k/MAGPE 5/95	5/95	6.6/93.4	0.002	540	0.25

## 2 Uncompatibilized blends: Results and discussions

In this section, we have studied three series of binary PA6/HDPE blends covering a wide range of viscosity ratios  $R_v$  from 0.003 to 300 as shown in table 4.1.

In uncompatibilized blends, morphology development is the consequence of drops break-up and coalescence mechanisms under shear (see chapter 1). This mechanism is controlled by rheological processes and depends essentially on the viscosity ratio and the shear rate  $\dot{\gamma}$  imposed in blends.

Meijer et al.[7] proposed an expression to estimate the minimum achievable diameter  $D_{min} = 2R_{min}$  of a drop (see equation 1.9 in chapter 1 section 2.1):  $R_{min} = 2^{-1/2}Ca_{crit}/(\eta_m\dot{\gamma}/\Gamma)$ . The value of  $Ca_{crit}$  can be estimated with Grace's curve ( $Ca_{crit}$  as a function of the viscosity ratio, see figure 1.5 in chapter 1). Values of the critical capillary number in both simple shear and 2D elongation are deduced from Grace's curve using blends viscosity ratios at  $\dot{\gamma} = 100\text{rad/s}$  (see figure 4.2) and are reported in table 4.3.

The estimated values of  $D_{min}$  are reported in table 4.3. For uncompatibilized blends, the value of the interfacial tension  $\Gamma$  was estimated at  $\sim 10\text{mN/m}$ . Note that the expression of  $D_{min}$  does not take into account the coalescence and Grace's curve was designed for blends of newtonian fluids. The calculated  $D_{min}$  is given as a rough estimation.

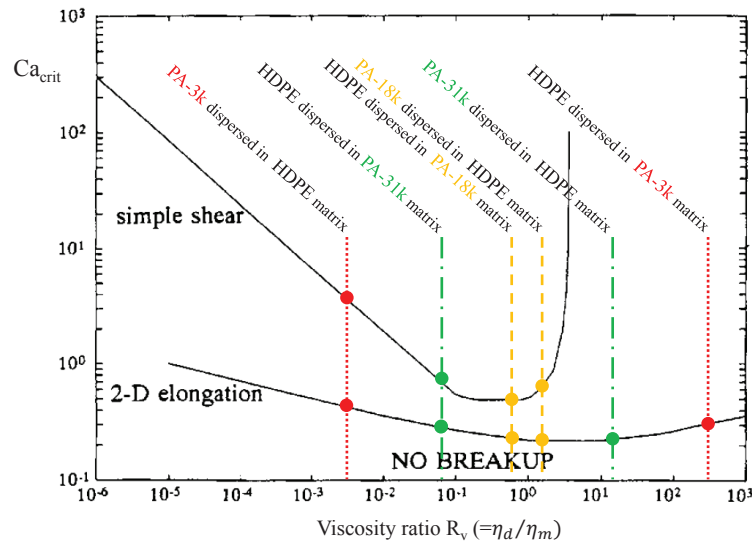


Figure 4.2: Grace's curve representing the critical capillary number  $Ca_{crit}$  as a function of the viscosity ratio measured at  $100\text{rad/s}$ . Lines corresponding to the different blends viscosity ratios studied in this work are reported.

The three series of uncompatibilized blends were observed by SEM after batch mini extrusion. Conditions of observation are described in chapter 2 subsection 3.2. For each series, the obtained morphologies will be described and discussed with respect to the mechanisms of drop break-up and coalescence successively for blends PA6-18k/HDPE, PA6-3k/HDPE and PA6-31k/HDPE.

Experimental SEM micrographs of the three series that will be discussed are summarized in figure 4.3. This figure is given to help the reader, given the large number of blends which has been studied.

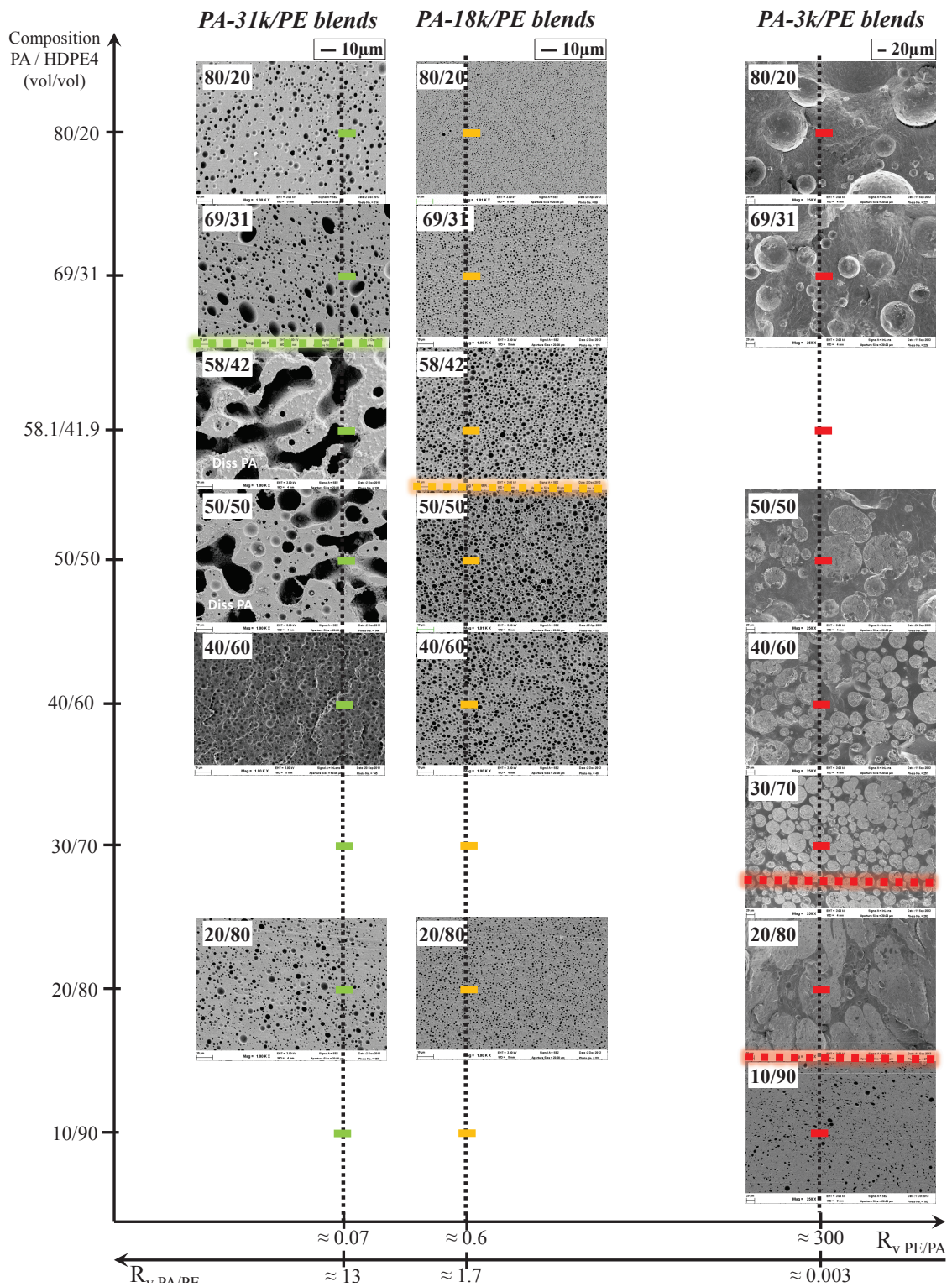


Figure 4.3: Comparison of PA-31k/PE, PA-18k/PE and PA-3k/PE uncompatibilized blends. For a better visualization, SEM micrographs of either sample surface after minor phase etching or sample surface after cryofracture are presented. Due to the different characteristic sizes of the morphologies, different magnification scales have been used: x1000 for PA-31k/PE and PA-18k/PE blends and x250 for PA-3k/PE blends.

## 2. Uncompatibilized blends: Results and discussions

Table 4.3: Determination of the critical capillary number  $Ca_{crit}$  for uncompatibilized binary blends PA6-31k/HDPE, PA6-18k/HDPE and PA6-3k/HDPE and minimum diameter accessible  $D_{min}$  using equation 1.9 for both simple shear and 2D elongation. The interfacial tension  $\Gamma=10mN/m$  and the shear rate  $\dot{\gamma}=100s^{-1}$ , component viscosities are taken at 100rad/s.

		PA6-31k/HDPE		PA6-18k/HDPE		PA6-3k/HDPE	
		HDPE matrix	PA6-31k matrix	HDPE matrix	PA6-18k matrix	HDPE matrix	PA6-3k matrix
	$\eta_m$ 100rad/s [Pa.s]	60	820	60	105	60	0.2
	$R_v$	13	0.07	1.7	0.6	0.003	300
Simple shear	$Ca_{crit}$	Off limits	0.6	0.6	0.5	3	Off limits
	$D_{min}$	Large	100nm	1.4 $\mu$ m	800nm	8 $\mu$ m	Large
2D elongation	$Ca_{crit}$	0.21	0.3	0.21	0.21	0.5	0.3
	$D_{min}$	500nm	50nm	500nm	500nm	1 $\mu$ m	200 $\mu$ m

### 2.1 Blends with PA6-18k

We present first blends with PA6-18k, which correspond to the most symmetrical case in terms of viscosity ratio. Figure 4.6, shows the morphologies obtained for a large set of compositions for PA6-18k/HDPE blends at different magnification scales. On SEM micrographs, the minor phase has been etched. Blends of PA6-18k and PEHD have the particularity to have a viscosity ratio close to 1.

In this series, phase inversion happened between blend PA-18k/PE 58/42 and 50/50, thus between 50%vol and 58%vol of PA6-18k. Globally, sizes of morphologies have developed more or less symmetrically on each side of the phase inversion composition. Thus the description made for the morphology development of the dispersion of PE in PA is also valid for PA in PE.

For blends with a low concentration of dispersed phase, homogeneously dispersed nodular PE dispersions in PA are observed for PA-18k/PE 80/20, with diameters of droplets from 400 to 800nm. For PA-18k/PE 20/80 thin nodules, from 200nm to 1.5 $\mu$ m, are also observed. Droplet sizes are in the range of the minimum sizes attainable by break-up predicted in table 4.3 ( $\sim$ 500nm for elongationnal flow and  $\sim$ 800nm to 1.5 $\mu$ m in simple shear). This is consistent with the fact that at low volume fraction of the dispersed phase  $\phi_d$ , the probability of coalescence is lower compared to the break-up, thus minimum sizes attainable by break-up can be reached.

For more concentrated blends, when the volume fraction of the dispersed phase  $\phi_d$  ( $d$  can be HDPE or PA6-18k) increases, the average sizes of nodular dispersion increase and become more polydisperse. Morphologies are in average larger than predicted (see table 4.3). Indeed, when  $\phi_d$  increases, the probability of coalescence increases as well. Theoretically the minimum sizes attainable by break-up can be reached but droplets, in the case of a viscosity ratio close to one, can also instantaneously coalesce. Thus, since the expression proposed by Meijer et al. (see equation 1.9) does not include the coalescence mechanism, the minimum size attainable cannot be observed in the blend. When  $\phi_d$  increases, the mechanisms of drop break-up and coalescence are continuously in com-

petition.

The phase inversion is observed within the composition range of blends PA-18k/PE 50/50 and 58/42 which is very consistent with the viscosity ratio between both phases close to 1. Only 8%vol separate those two blends, which constitute a narrow windows of composition in which phase inversion occurs for uncompatibilized blends. This is consistent with the fact that coalescence and break-up mechanisms are very balanced when  $R_v \simeq 1$ .

Note also that, for a very small fraction of nodules of PA dispersed into the PE matrix in blend PA-18k/PE 50/50, small nodules of PE (from 200nm to 500nm) are observed as shown in figure 4.4. This is not observed when PA6-18k is the matrix. This phenomenon of sub-inclusion, which constitutes only a minor fraction here, will be discussed later.

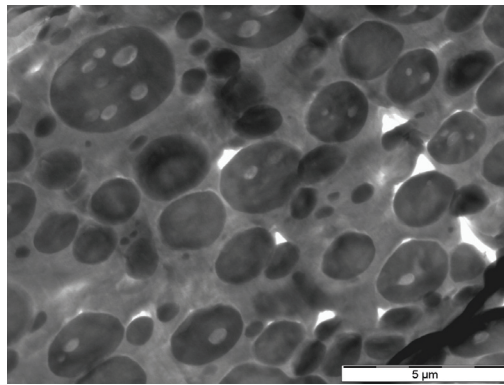


Figure 4.4: TEM micrograph of PA-18k/PE 50/50 blend. The PA6 phase is stained and appears in dark. The very white domain are holes due to the sample preparation for observation.

Thus in this blend series, the same mechanisms seems to be responsible of the final morphology, both when PE is dispersed in PA and when PA is dispersed in PE. Besides, in each of the six blends, nodules are rather homogeneous in size, which is consistent with a capillary-wave instability mechanism (Rayleigh mechanism). Indeed, this mechanism leads to the formation of droplets of the same size when the viscosity ratio is close to 1. This case corresponds to the model mechanism of drop break-up that has been described in the literature for the case of first "dispersive mixing" and then "distributive mixing" (chapter 1 subsections 2.1.1 and 2.1.2). A schematic representation of this mechanism is proposed in figure 4.5 [7].



Figure 4.5: Schematic representation of the capillary wave instability mechanism (Rayleigh) leading to drop break-up, that is consistent with the morphology development in uncompatibilized PA6-18k/HDPE blends with a viscosity ratio  $R_v \simeq 1$ .

### **Summary of PA6-18k/HDPE blends**

- Morphologies develop symmetrically with respect to phase inversion, which occurs at a composition close to 50/50 (%vol).
- The obtained nodular morphologies, homogeneous in size, are quite consistent with capillary-wave instability mechanism (Rayleigh mechanism).
- Droplets sizes increase when the volume fraction of the dispersed phase increases on approaching phase inversion, which is consistent with increased probability of coalescence.

This series of blends exhibits the most generic behaviour described in the literature.

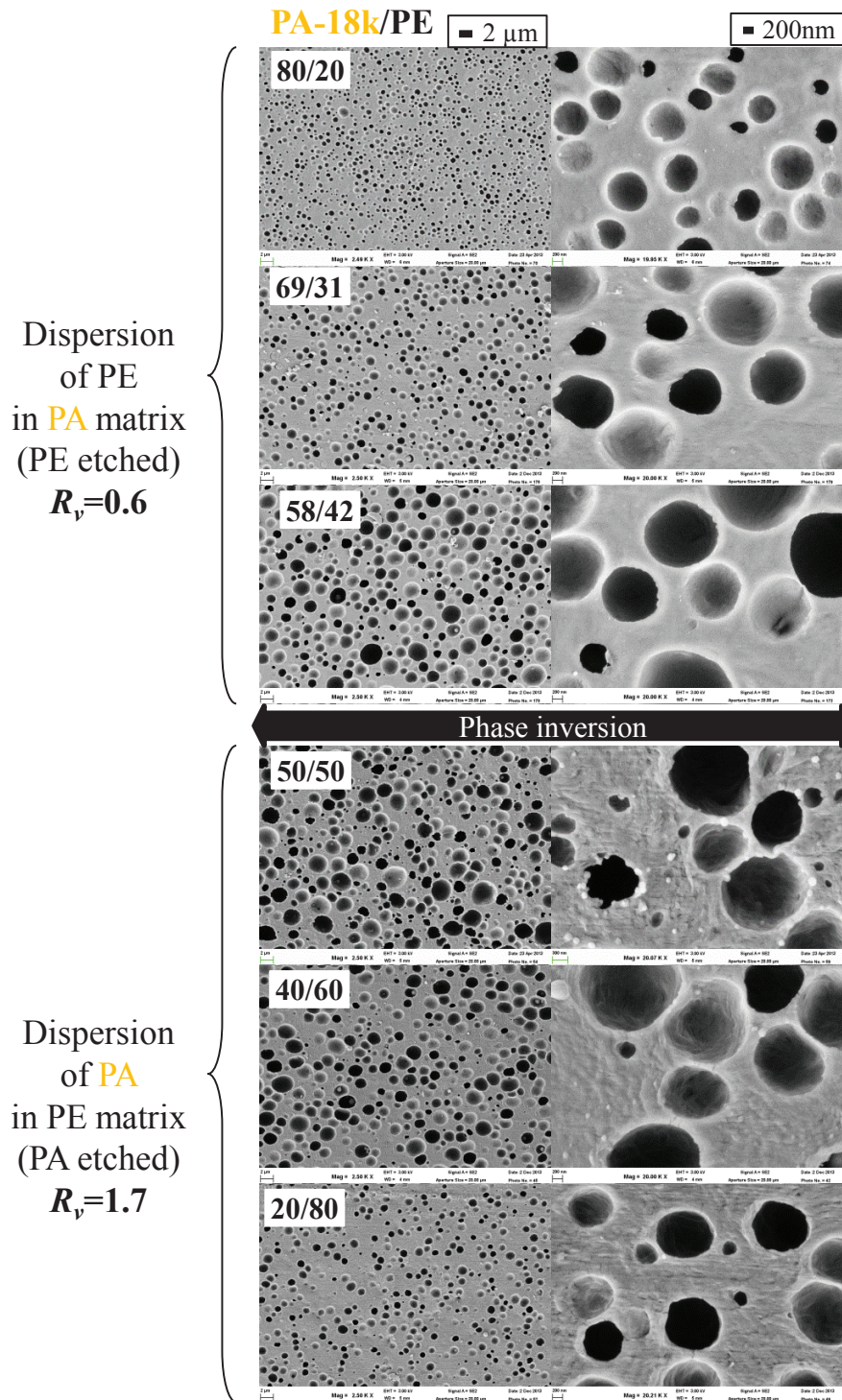


Figure 4.6: SEM micrographs of uncompatibilized binary blends of PA6-18k/HDPE after minor phase etching. Left column correspond to a magnification of  $\times 2500$  and right of  $\times 20000$ . The scale bar is reported on top of the figure. The name of each blend is reported on the corresponding micrograph and corresponds to the volume fraction in the melt state of each phase.

### 2.2 Blends with PA6-3k

Figure 4.7 shows the morphologies obtained for a large set of compositions for uncompatibilized PA6-3k/HDPE binary blends. For better visualizing the morphologies:

- For blends exhibiting a dispersion of PE in a PA matrix (blends PA-3k/PE 80/20 to 20/80): SEM images of cryofractured surfaces are shown. PA6 is the darker phase and PE phase appears in white and with a fibrillar surface.
- For blends exhibiting a dispersion of PA in a PE matrix (blend PA-3k/PE 10/90): the PA phase, constituting the minor phase, has been etched.

This series of uncompatibilized binary blends is particularly interesting because  $R_v \neq 1$  for both dispersions of PE in PA matrix and dispersions of PA in PE matrix (respectively  $R_{vPEinPA} = 300$  and  $R_{vPAinPE} = 0.003$ , see table 4.1). Only few examples of experimental studies dealing with these ranges of very high or very low viscosity ratios have been described in the literature.

The following morphologies are observed for each blend:

- Dispersion of HDPE in PA6-3k matrix: blends PA-3k/PE 80/20, 69/31, 50/50, 40/60, 30/70.
- Co-continuous: blend PA-3k/PE 20/80.
- Dispersion of PA6-3k in HDPE matrix: blend PA-3k/PE 10/90.

Let us now observe more precisely and discuss each of the three kinds of morphologies observed.

#### Dispersion of HDPE in PA6-3k matrix ( $R_v = 300$ : $\eta_d \gg \eta_m$ )

There are several remarkable and unexpected observations in the 5 blends exhibiting a HDPE dispersion in PA6-3k matrix. First of all, the presence of elongationnal flow in our process is confirmed. Indeed, theoretically, under simple shear the PE phase could not be dispersed in the PA matrix because the viscosity ratio is much higher than the critical value of 4, defined in Grace's curve in figure 1.5 (chapter 1 subsection 2.1). Nevertheless, SEM observations show that break-up happened since, for each composition, droplets with a diameter smaller than  $200\mu\text{m}$  are observed. This reflects the fact that, **elongational flow is also present in our process** and allows the break-up at viscosity ratios much higher than 4. The estimation of the minimum size attainable in table 4.3 using the curve of  $Ca_{crit}$  in the case of 2D elongationnal flow is  $D_{min}=200\mu\text{m}$ , which is close to the diameters observed for biggest droplets observed in blends PA-3k/PE 80/20 to 50/50.

The second remarkable effect is that, when the volume fraction of the dispersed HDPE phase increases toward phase inversion composition, sizes of the dispersions decreases. For blends at low concentrations (80/20, 69/31 and 50/50), very big droplets of PE in PA matrix are observed (from 5 to  $200\mu\text{m}$ ) but when  $\phi_d$  increases (40/60 and 30/70), sizes decreases: for blend PA-3k/PE 30/70, for example, the maximum size observed is now  $D_{max}=60\mu\text{m}$  ( $\approx 100\mu\text{m}$  for blend 40/60 and  $\approx 150\mu\text{m}$  for blend 50/50). This means that break-up becomes more efficient for concentrated blends. In blends with PA6-18k (see subsection 2.1), where the break-up and coalescence were balanced, we observed the opposite trend. The size of the dispersed phase was increasing with increasing  $\phi_d$  due to the increasing probability of coalescence.

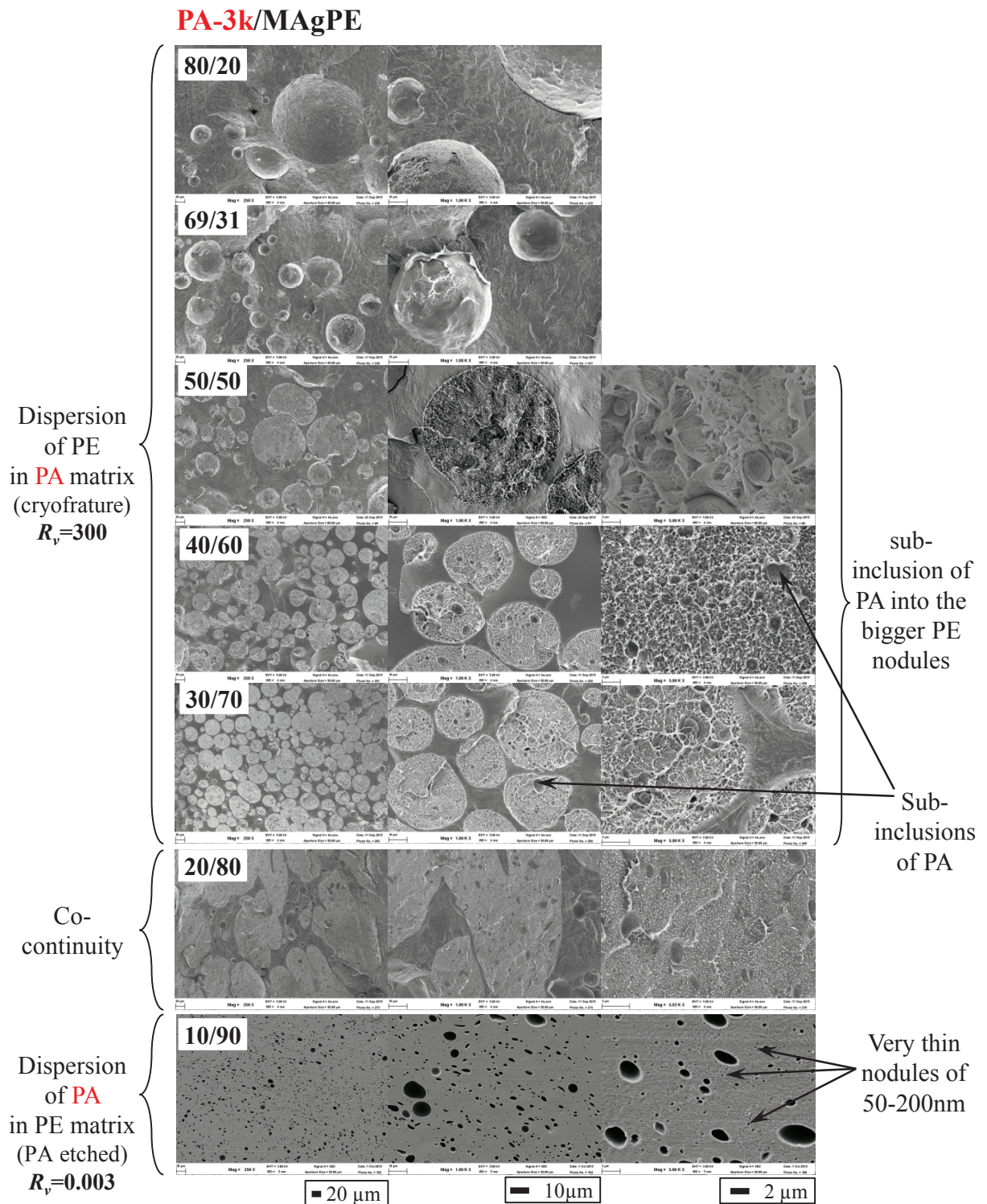


Figure 4.7: SEM micrographs of uncompatibilized binary PA6-3k/HDPE blends: after minor phase etching for blends 10/90 and after cryofracture for blends 80/20 to 20/80. Left column corresponds to a magnification of x250, middle to x1000 and right of x5000. The scale bar is reported on the bottom of the figure. The name of each blend is reported on the corresponding micrograph and corresponds to the volume fraction in the melt state of each phase.

## 2. Uncompatibilized blends: Results and discussions

The explanation could come from the large difference between the viscosity of both phases. Indeed, droplets of HDPE are  $\sim 300$  times more viscous than the PA6-3k matrix (respectively,  $\eta_{HDPE}^*_{100rad/s} \simeq 60$  Pa.s and  $\eta_{PA-3k}^*_{100rad/s} \simeq 0.2$  Pa.s). Thus, when highly viscous droplets are added to a fluid matrix, this could increase the overall viscosity of the matrix felt by a single droplet:  $\eta_{matrix}$  becomes  $\eta_{blend}$ . Thus the local shear rate applied on the droplet is highly amplified and leads to the break-up into thinner droplets. We estimated the value of the minimum droplet size attainable by break-up due to elongational flow (with equation 1.9) by replacing the value of the matrix  $\eta_m$ , which was equal to  $\eta_{PA-3k}^*_{100rad/s}$ , by the value of the complex viscosity of each blend measured by cone plate rheometry at 100rad/s (see chapter 5). The values are reported in table 4.4. Although a little bit smaller, they are more consistent with real minimum sizes observed compared to the case where  $\eta_m=0.2$  Pa.s and  $D_{min}=300\mu m$ . Indeed, in average in all blends the minimum PE droplet size observed is around  $5\mu m$ . Thus, it reflects the fact that when  $R_v \gg 1$ , the viscosity of the matrix to take into account is not the one of the pure component which constitutes the matrix phase, but rather the blend viscosity itself, which is a mean value between both pure components (see chapter 5). Jansen et al. (2000) [136] reported the same observation. They studied the effect of breakup on concentrated emulsions of oil in water for different viscosity ratios. They observed that in the case of most concentrated blends the critical shear rate for breakup decreased by more than an order of magnitude. This means that the final object sizes are smaller than the prediction of Grace's curve. They explained these effects by means of a mean fields model, which assumes that break-up of a droplet in concentrated emulsion is determined by the average emulsion viscosity rather than the continuous phase viscosity. They furthermore observed that drop with viscosity ratio of 22 were seen to break-up in simple shear as soon as the emulsion concentration was raised to 40%. This observation is really consistent with ours.

Table 4.4: Minimum diameter attainable  $D_{min}$  using  $\eta_m = \eta_{blend}^*$  instead of  $\eta_m = \eta_{pure PA6-3k}$  taken at 100rad/s and Grace's curve in 2D elongation. Estimation of  $D_{min}$  using equation 1.9. The interfacial tension  $\Gamma=10mN/m$  and the shear rate  $\dot{\gamma}=100s^{-1}$ .

	PA6-3k	80/20	69/31	50/50	40/60	30/70
$\eta^*_{blend 100rad/s}$ [Pa.s]	0.2	2.5	5.4	9.7	11.8	20.4
$\eta^*_{m 100rad/s}$ [Pa.s]		2.5	5.4	9.7	11.8	20.4
$R_v$		24	11.1	6.2	5.1	2.9
$Ca_{crit}$ (2D elongation)		0.3	0.21	0.21	0.21	0.21
$D_{min}$		24 $\mu m$	8 $\mu m$	4 $\mu m$	3.5 $\mu m$	2 $\mu m$

The last remarkable observation is the obvious inhibition of the coalescence. Indeed, the phase inversion occurs within the composition range of blends PA-3k/HDPE 30/70 to 10/90.

In blends with PA6 3k in which the viscosity ratio is very different from one, the composition at phase inversion is shifted towards low PA volume fraction, as will be

discussed in chapter 5. The PA phase remains continuous in blends in which its volume fraction is significantly lower than 0.5. This is clearly observed for example in blend PA-3k/PE 30/70 (Figure 4.8). In this case, relatively large PE droplets (20 to 50  $\mu\text{m}$  in diameter) are separated by very thin, much less viscous PA films. The thickness of these films is observed as small as 100 nm in some cases (see figure 4.8).

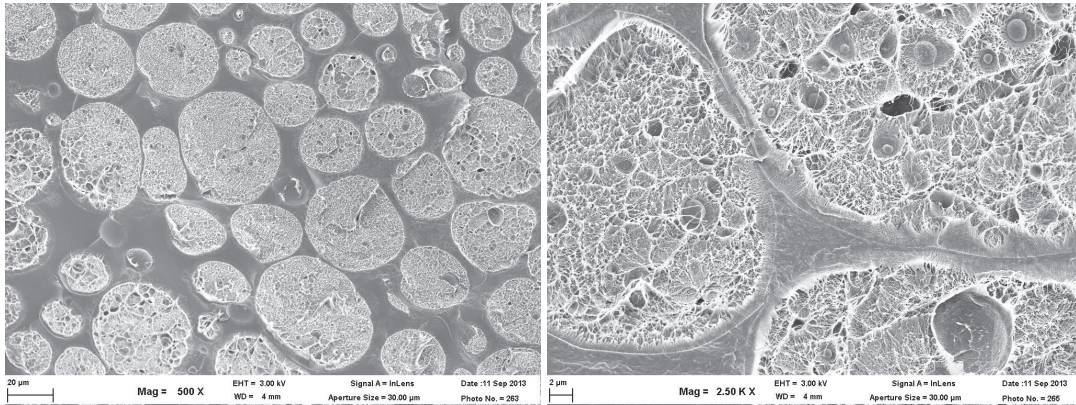


Figure 4.8: SEM micrographs of cryofractured PA-3k/PE 30/70 blend showing the dispersion of HDPE into the very fluid PA6-3k matrix. Right micrograph at higher magnification shows the subdispersion of PA6-3k into the bigger PE nodules and the very thin films of PA6-3k remaining between the large droplets.

Semi-empirical models for phase inversion, based on macroscopic rheological considerations, will be discussed in Chapter 5. It may also be discussed here from a different, more microscopic point of view.

In the blend PA6-3k/PE 30/70 3k, large droplets (20 to 50  $\mu\text{m}$  in diameter) are separated by very thin, much less viscous PA films confined in between nearly flat, parallel interfaces. The occurrence of such a particular morphology is possible because drainage of thin films in between neighboring droplets is very slow, therefore reducing drastically coalescence of PE droplets. In this particular situation, the time needed to drain the confined film may be roughly estimated as follows.

Let us first consider the case of rigid interfaces (this would be the case for infinitely viscous droplets).

The driving force for coalescence is mainly the normal pressure applied to the film. The problem of drainage of a film leading to coalescence has been studied by several authors (see [7] and refs cited therein). When two droplets of diameter  $D$  collide at a distance  $h \ll D$ , a region of contact is created (see Fig. 4.9). As the thickness of the film becomes much smaller than the size  $a$  of the contact zone, draining the film involves a lubrication problem, with an excess normal pressure developing as a result of strong (Poiseuille) shear flow in the film. This excess pressure tends to separate interfaces from each other and thus opposes coalescence.

For an immobile interface, mass conservation imposes that, to drain a film of thickness  $h$  at a velocity  $\dot{h} = \frac{\partial h}{\partial t}$ , the radial fluid velocity is:

$$v(r, z) = \frac{r}{h} \dot{h} \left( 1 - \frac{4z^2}{h^2} \right) \quad (4.1)$$

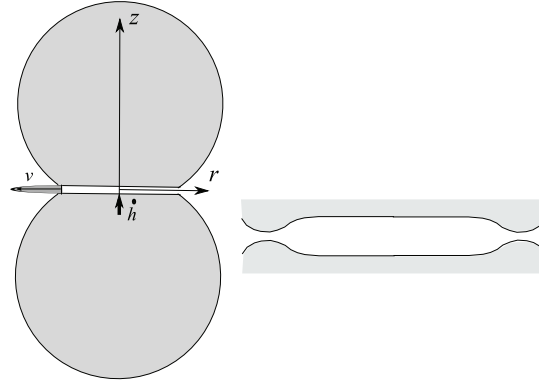


Figure 4.9: Left: Contact of two droplets separated by a thin film of thickness  $h$ . The parabolic velocity profile within the film is schematized. Right: dimple formed at the rim of the contact zone, due to the maximum lubrication pressure at the center (after [137]).

The Navier-Stokes equation then gives the excess pressure  $p(r)$  in the film:

$$\frac{\partial p}{\partial r} = \eta \frac{\partial^2 v}{\partial z^2} \quad (4.2)$$

and the profile of the excess pressure is of the form:

$$p(r) = \frac{3\eta}{h^3} \dot{\gamma} (r^2 - a^2) \quad (4.3)$$

where  $a$  is the radius of the contact zone. By integrating the pressure field, a total force  $F$  is obtained:

$$F = \frac{3\pi\eta}{2h^3} \dot{\gamma} a^4 \quad (4.4)$$

This force opposes coalescence. It grows as  $h^3$ , and therefore diverges as interfaces come closer to each other. Thus, for a given external applied force, the approaching velocity becomes slower and slower as  $h$  decreases. Equating the force  $F$  to the external force applied during the process  $F_{ext} \approx \eta \dot{\gamma} a^2$  gives:

$$\frac{1}{h^3} \frac{\partial h}{\partial t} \approx \frac{\dot{\gamma}}{a^2} \quad (4.5)$$

which upon integration gives an estimate of the coalescence time  $t_c$ :

$$t_c \approx \dot{\gamma}^{-1} \frac{a^2}{h_c^2} \quad (4.6)$$

$h_c$  being the critical thickness when coalescence eventually occurs. Thus, for  $a \approx 10 \mu\text{m}$  and  $h_c \approx 10 \text{ nm}$ , we obtain  $\dot{\gamma} t_c \approx 10^6$ . Thus, the coalescence time is  $10^6$  times larger than the time scale  $\dot{\gamma}^{-1}$  of the estimated maximum shear during the process. This explains why coalescence may be very difficult (slow) in this situation.

On the other hand, in case of mobile interfaces, it may be shown that the lubrication force  $F$  diverges as  $1/h$  instead of  $1/h^3$ , making the coalescence time much shorter. Thus, **long coalescence times are related to the viscosity of the droplets, not to the viscosity of the fluid within the film to drain**. This rather counter intuitive result explains that it is difficult to drain PA films in the morphology shown in figure 4.8, even though PA has

a very low viscosity in this case.

Also, by numerically solving the Reynolds equation of this lubrication problem, it has been shown that a dimple develops at the rim of the contact zone [137]. This is due to the fact that the normal pressure (which tends to separate the interfaces from each other) is maximum at the center of the contact zone (see fig. 4.9). This may explain the inclusion of sub-droplets of PA, from 200nm to  $2\mu\text{m}$ , that are dispersed into the bigger PE nodules for blends PA-3k/PE 50/50, 40/60, 30/70 and 20/80 (cf. figure 4.8 right). A schematic representation of the coalescence process with trapping of small subinclusion is presented in figure 4.10.

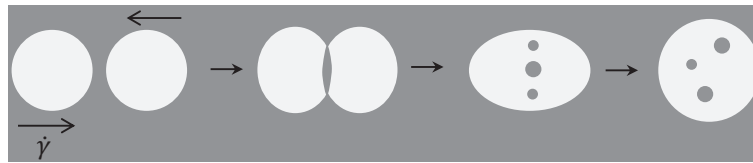


Figure 4.10: Schematic representation of the coalescence of two nodules of HDPE into the fluid PA6-3k matrix ( $R_v \gg 1$ ): trapping of smaller nodules of PA6-3k into HDPE droplets.

#### Dispersion of PA6-3k in HDPE matrix ( $R_v = 0.003$ : $\eta_d \ll \eta_m$ )

Blends PA-3k/PE 10/90 is the only one blend exhibiting a PA6-3k dispersion into an HDPE matrix. Figure 4.11 shows this morphology at higher magnifications. We can notice a bimodal distribution of droplet sizes: Large nodules of in average  $2\text{-}4\mu\text{m}$  (until  $10\mu\text{m}$  for few nodules) and very thin nodules of around 50 to 200nm are observed. Note also that a part of large droplets do not exhibit a nodular shape.

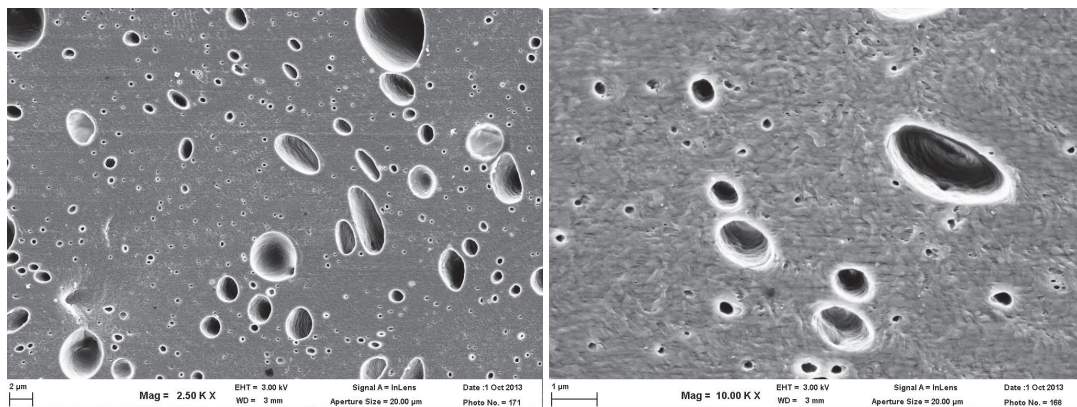


Figure 4.11: SEM micrographs of PA-3k/PE 10/90 blend after minor phase etching, to show the heterogeneous droplet sizes at two magnifications: left  $\times 2500$  and right  $\times 10000$ . Very thin nodules of PA are observed.

Under simple shear, the smallest attainable size  $D_{min}$  is supposed to be around  $\simeq 8\mu\text{m}$  and under elongational flow  $\simeq 1\mu\text{m}$ . In average, the size of larger nodules is closer to the prediction for elongationnal flow. But, the very thin droplets of 50 to 200nm are unexpected. In the literature it is mentioned that when  $R_v \ll 1$ , faster capillary waves may develop on the filament, and thus different mechanism like end-pinching could lead to

break-up of the elongated droplet. When nodules are created by this mechanism, the filament between droplets may relax to form bigger droplets or continue to break, leading to heterogeneous droplet size distribution. It also favours the creation of very small satellites between broken droplets [11] (see figure 1.8 in chapter 1). This mechanism is very consistent to explain the bimodal morphology observed: the larger nodules are formed by end-pinching and the very thin droplets may correspond to the previously mentioned satellites. A schematic representation of the break-up mechanism by end-pinching and formation of satellites between droplets is shown in figure 4.12 [7].



Figure 4.12: Schematic representation of the break-up mechanism by end-pinching and formation of satellites between droplets that is consistent with the morphology development in uncompatibilized PA6-3k/HDPE blends when PA6-3k is dispersed in HDPE matrix with a viscosity ratio  $R_v \ll 1$ .

Due to the large size polydispersity the probability of coalescence of larger nodules will be higher than for the very thin nodules. This contributes to increase even more the size polydispersity. A schematic representation of the coalescence of the morphology created by end-pinching is shown in figure 4.13.



Figure 4.13: Schematic representation of coalescence in the morphology created by end-pinching ( $R_v \ll 1$ ).

### Summary of PA6-3k/HDPE blends

Our study constitutes a good example of the morphology development in binary blends of viscoelastic polymers at  $R_v$  very different from one. The main observations are:

- when  $R_v \gg 1$ :
  - Break-up is observed even if, theoretically, in simple shear for mixture of Newtonian fluids, break-up cannot happen when  $R_v > 4$ . This is due to elongation flow present in the process. Nevertheless, droplet morphology remains coarse (from 5 to 200 $\mu\text{m}$ ).
  - Droplet sizes decreases when  $\phi_d$  increases. Break-up was thus more efficient in concentrated blends. This is due to the fact that the viscosity of droplet is much higher than the matrix.
  - Coalescence is highly inhibited due to the "fully immobile" drainage regime. A consequence of this drainage regime is that, sub-dispersions of PA in the nodular dispersion of PE are observed. Besides, phase inversion is shifted to high volume fraction of PA6-3K. The composition at phase inversion will be studied in chapter 5.

- when  $R_v \ll 1$ :
  - Sizes of morphologies are very polydisperse: bigger nodules of around 2-4 $\mu\text{m}$  and very thin nodules of around 50 to 200nm are observed. The mechanisms of end-pinching with formation of small satellites between droplets may be responsible for the very polydisperse morphologies.

### 2.3 Blends with PA6-31k

Figure 4.14, shows the morphologies obtained for a large set of compositions for uncompatibilized PA6-31k/HDPE binary blends. Three magnifications of SEM micrographs are shown, the minor phase has been etched.

The following series of uncompatibilized binary blends have also the particularity to exhibit a viscosity ratios far from 1 for both dispersions of PE in PA matrix ( $R_v=0.07$ ) and dispersion of PA in PE matrix ( $R_v=13$ ). Compared to blends with PA6-3K, the PA6 is the most viscous phase and viscosity ratios are closer to one.

#### Dispersion of HDPE in PA6-31k matrix ( $R_v=0.07$ : $\eta_d < \eta_m$ )

A HDPE dispersion in PA6-31k matrix is observed for blends 80/20 and 69/31. For both blends, we observe a bimodal distribution of droplet sizes: larger droplets in the range of 1 $\mu\text{m}$  to 20 $\mu\text{m}$  for some droplets in the case of blend 69/31 and very thin nodules of around 200nm are also observed. Besides, the size of larger droplets increases with HDPE volume fraction. The last observation is consistent with an increased probability of coalescence between droplets and means that even if  $R_v < 1$  the drainage regime to consider is not unfaourable to coalescence.

As for PA6-3k/HDPE blends when  $R_v \ll 1$  (dispersion of fluid PA6-3k into HDPE matrix), a bimodal distribution of droplet sizes was observed. Thus the mechanism of end-pinching with satellites formation between droplet is also very consistent to describe the morphologies obtained (see figure 4.12). Note that the minimum diameter predicted was  $\sim 50$ -100nm (for elongationnal and simple shear see table 4.3). These sizes are consistent with the small satellites observed but not at all with the larger sizes observed. This show the limitation of the use of this prediction when mechanism of morphology development are very different from the usual Rayleigh capillary wave instabilities.

Figure 4.15 shows a comparison between blends PA-18k/PE 69/31 (left) and PA-31k/PE 69/31 (right) at the same composition for two magnifications. In blends with PA6-18k, the Rayleigh capillary wave instability mechanism was well adapted to describe the roughly homogeneous sizes of morphology obtained. We see in blend with PA6-31k that the mechanism of morphology formation is very different and is consistent with the "end-pinching" mechanism with formation of small satellites between drops.

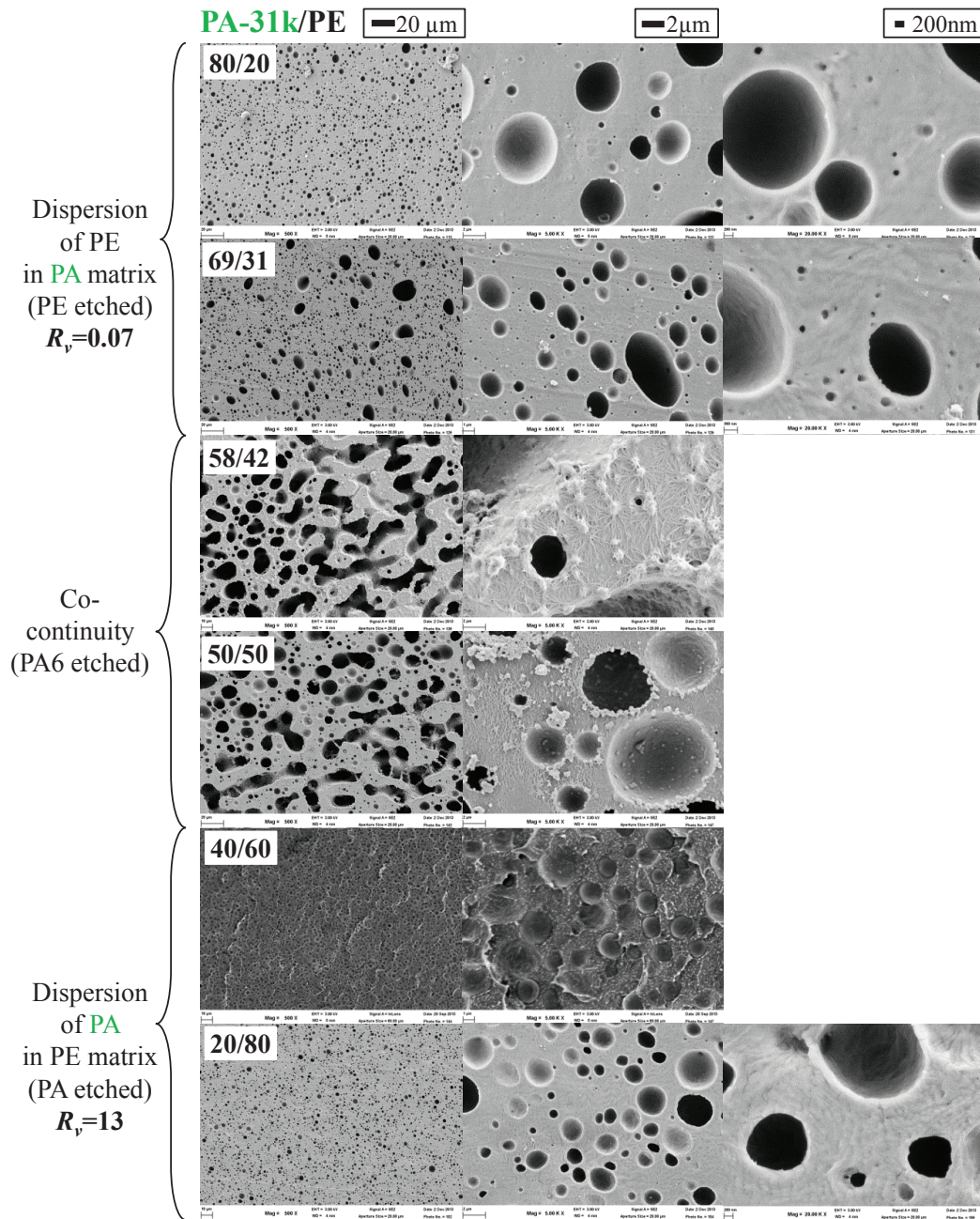


Figure 4.14: SEM micrographs of uncompatibilized binary blends of PA6-31k/HDPE after minor phase etching. Left column corresponds to a magnification of x500, middle to x5000 and right of x20000. The scale bar is reported on the top of the figure. The name of each blend is reported on the corresponding micrograph and corresponds to the volume fraction in the melt state of each phase.

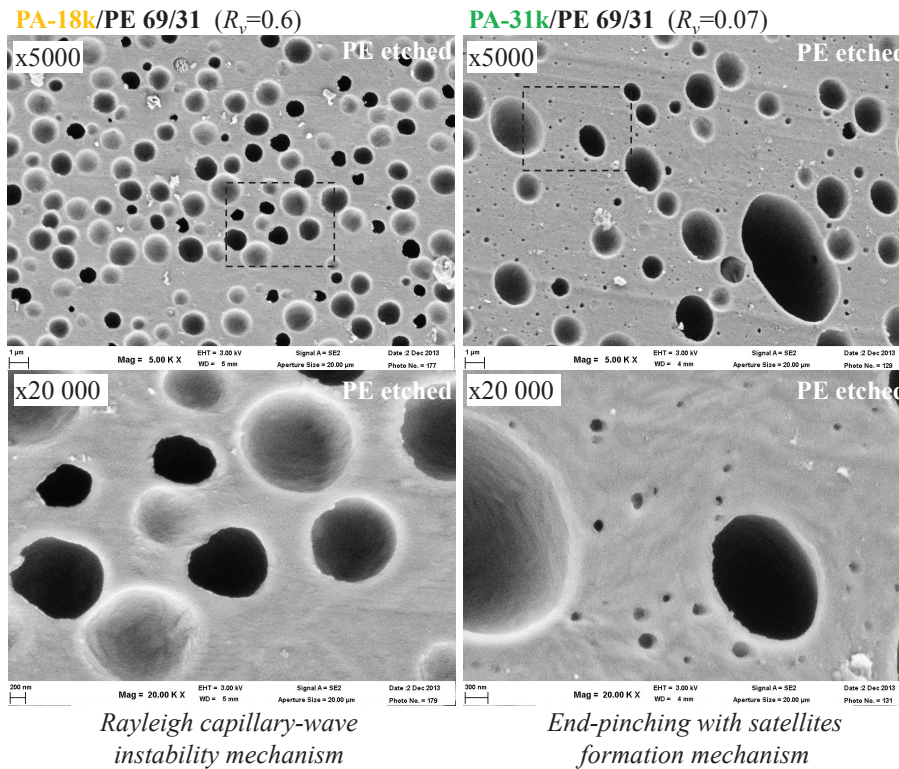


Figure 4.15: SEM micrographs of uncompatibilized binary after minor phase etching at two magnifications (x5000 and x20000): on the left, blend PA-18k/PE 69/31 and right, PA-31k/PE 69/31. Comparison of the final morphology probably obtained with two different mechanisms: Rayleigh mechanism and end-pinching mechanism.

#### Dispersion of PA6-31k in HDPE matrix ( $R_v = 13$ : $\eta_d > \eta_m$ )

PA-31k/PE 20/80 and 40/60 blends exhibit a nodular dispersion of PA6-31k into a HDPE matrix. The morphologies reveal a large size polydispersity (from 500nm to 5 $\mu$ m) but we do not observe very thin nodules which could be associated with satellite formations (as it has been observed in blends PA-31k/PE 80/20 and 69/31).

Observed droplet sizes are consistent with predicted sizes with Grace's curve in 2D elongation which predicts  $D_{min} \simeq 500$  nm. Once again the morphology confirms that elongation flow may also be responsible of droplet break-up. Indeed, under simple shear theoretically, dispersion of PA6-31k in the HDPE matrix with a viscosity ratio of 13 is not possible. In that case several factors are also in line with a favoured break-up. First, the addition of more viscous droplets into the matrix may increase the global viscosity, although much less than in the case of PA6-3k/HDPE blend where  $R_v = 300$ . Secondly, the viscosity ratio is closer than one compared to the case of PA6-3k/HDPE blends, break-up is thus less unfavourable. Finally, another hypothesis may be that the viscoelastic nature of both phases makes the break-up possible at higher viscosity ratio under shear, as suggested in the literature [138].

Figure 4.16 shows the comparison between PA-18k/PE 20/80 and PA-31k/PE 20/80 blends, at the same composition and for two magnifications. In blends with PA6-18k, the

## 2. Uncompatibilized blends: Results and discussions

Rayleigh capillary wave instability mechanism was well adapted to describe the roughly homogeneous sizes of morphology obtained. In blend with PA6-31k, we see that the morphology obtained are not very different but size are a bit more polydisperse. Thus, an asymmetric Rayleigh capillary wave instability mechanism could be responsible for such morphologies. Indeed, when  $R_v > 1$ , the formation of the Rayleigh instabilities on the elongated droplet can be delayed due to the difference of viscosity between the dispersed phase and the matrix. The deformation of the droplet can thus be perturbed compared to the case when  $R_v=1$ .

Thus, even though  $R_v > 1$ , it seems that the morphology development is much closer to the morphology development of PA6-18k/HDPE blends with  $R_v = 1$  than to the one of PA6-3k/HDPE blends when  $R_v \gg 1$ .

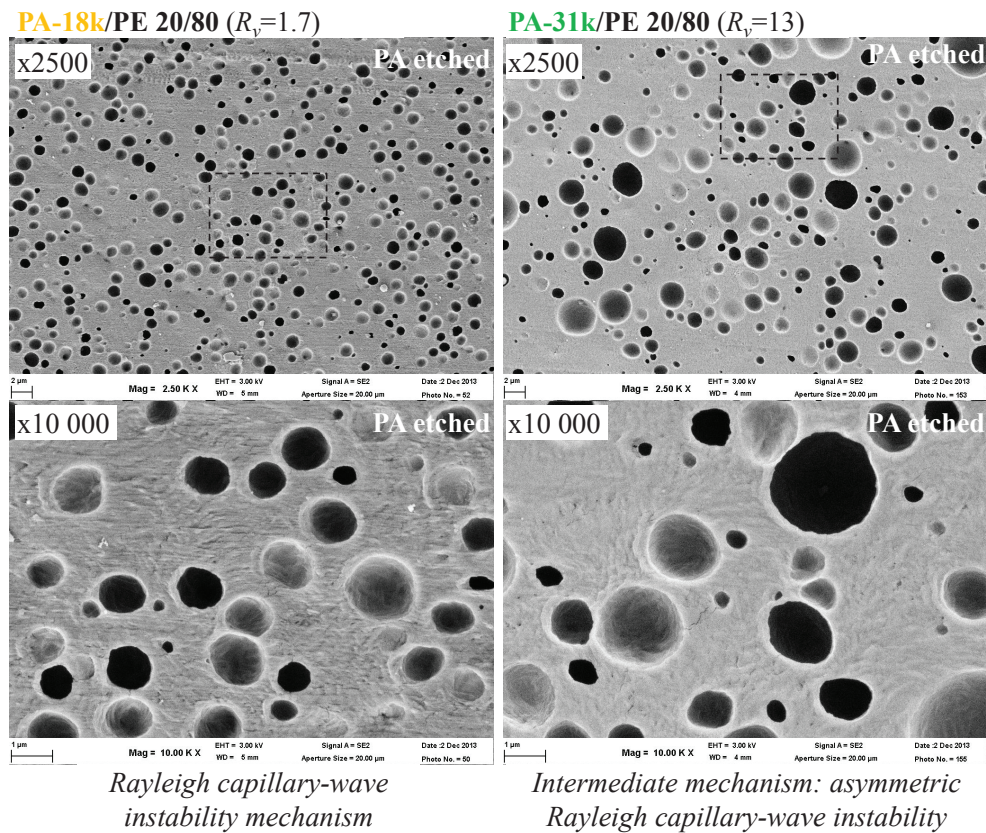


Figure 4.16: SEM micrograph of uncompatibilized binary after minor phase etching at two magnifications (x2500 and x10000): on the left, PA-18k/PE 20/80 blend and right, PA-31k/PE 20/80. Comparison of the final morphology probably obtained with slightly different Rayleigh mechanisms.

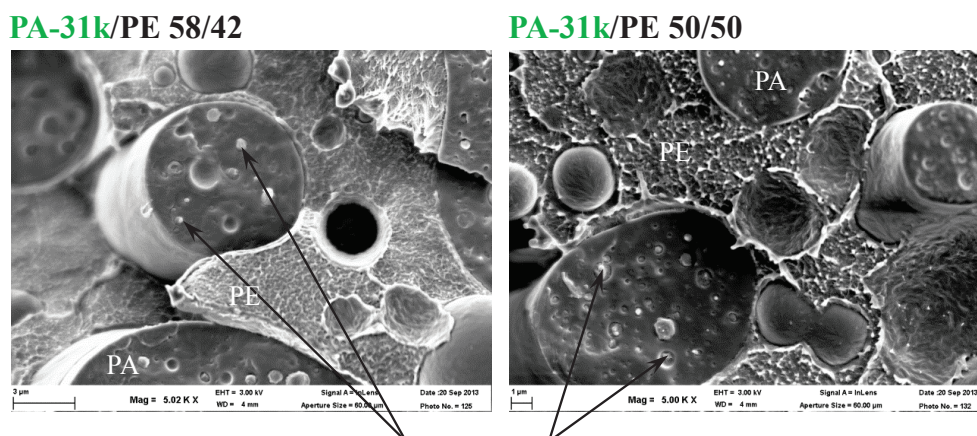
### Phase inversion

Observation of PA-31k/PE 58/42 and 50/50 blends in figure 4.14 shows that the morphology is co-continuous. A large window of compositions corresponding to co-continuity is thus observed between 40%vol and 69%vol of PA6-31k. However, more precise information concerning the morphology are given by the techniques of sample preparation before observation. Indeed, as the morphology is co-continuous it is possible, a priori, to

use both formic acid or decalin to dissolve respectively either the PA6 or the PE phase. But when the PE phase was dissolved for both blends, samples totally collapsed and when the PA6 phase was dissolved, samples remained as shown in figure 4.14. Thus the phase inversion, i.e. the composition at which the matrix phase is reversed, happened within the 11%vol separating blend PA-31k/PE 69/31 and 58/42. Thus, compared to blends with PA6-18k, the phase inversion composition have been shifted to smaller compositions of HDPE and morphologies partially co-continuous are observed over a larger window of compositions.

Another interesting observation is the presence of small HDPE subdispersions (from 200nm to 1-2 $\mu$ m) into the larger PA6-31k zones of the co-continuous morphologies as shown in figure 4.17. These subdispersions are also observed on micrographs with a magnification x5000 (middle) for blend 58/42 and 50/50 in figure 4.14: the very small droplets on the surface are reminiscence of the subdispersions which were inside the dissolved phase; during dissolution they are not entirely washed out and remain as a deposit on the surface.

This case, where the viscosity of the PA6-31k dispersed phase is more viscous than the HDPE matrix phase, shows similarities with the case of blend with PA6-3k when  $R_v \gg 1$ . During coalescence of two PA6 domains, a thin HDPE films can be trapped between droplets and break-up to form smaller HDPE subdispersions into the new larger PA6 droplet formed.



Subdispersions of HDPE into PA6-31k

Figure 4.17: SEM micrographs of co-continuous uncompatibilized binary blends of PA-31k/PE 58/42 and 50/50 after cryofracture (magnification x5000): subdispersions of HDPE in the PA large domains are observed.

### Summary of PA6-31k/HDPE blends

Once again, our study provides a good example of the morphology development in binary blends of viscoelastic polymers at  $R_v$  different from one (but less different than with PA6-3k). Main observations are:

- when  $R_v < 1$ , dispersion of HDPE in PA6-31k:
  - Very polydisperse sizes of morphology: bigger nodules of around 0.6-20 $\mu$ m and very thin nodules of  $\approx$ 200nm are observed. The mechanisms of end-

pinching with formation of small satellites between droplets is probably responsible of the very polydisperse sizes of morphology.

- A large window of partially co-continuity is observed (between 40 and 70%vol of PA6-31k): the phase inversion is observed at low volume fraction of HDPE (between 58 and 69%vol of PA6-31k).
- when  $R_v > 1$ , dispersion of PA6-31k in HDPE:
  - Break-up is observed even if, theoretically, in simple shear for mixture of Newtonian fluids, break-up cannot happen when  $R_v > 4$ . This is probably due to elongationnal flow present in the process.
  - Asymmetric Rayleigh capillary wave instability mechanism are consistent with the polydispersed sizes of morphology observed.
  - Sub-dispersions of PE in the PA6 domains were observed. We supposed that this is the consequence of the coalescence of more viscous PA6-31k domains of which traps smaller HDPE nodules.

### 3 Effect of the compatibilization: Results and discussions

In the literature, we have seen that, during compatibilization, the creation of a block or graft-copolymer at the interface can have several effects:

- **Reduce interfacial tension and prevent coalescence:** This leads to smaller sizes and more homogeneous morphologies as compared to uncompatibilized blends. In the literature, the role of block or graft-copolymers on the deformation, break-up and coalescence has been studied but there is a lack of systematic experimental studies to understand the role of the copolymer architecture on the final morphology.
- The accumulation of copolymers at the interface can lead to **interfacial fluctuations and be responsible for the creation of nanodispersions**. Creation of small micelles in addition to a micron-scale morphology attributed to the compatibilization reaction have been reported in the literature but not fully analysed.

Those two mechanisms can happen simultaneously during reactive extrusion. Systematic studies of blends morphological development which take into consideration both mechanisms have never been carried out before. Comparing compatibilized blends to their respective uncompatibilized counterpart, may allow to discriminate the effect of compatibilization.

In this section, we have studied three series of binary compatibilized PA6/MA-g-HDPE blends covering a wide range of viscosity ratios  $R_v$  from 0.002 to 540 as shown in table 4.5. These blends are complementary to the uncompatibilized blends discussed in last section (see section 2).

The same table can be proposed for the prediction of the minimum droplet sizes achievable  $D_{min}$  as for uncompatibilized blends. However, for compatibilized blends, the interfacial tension  $\Gamma$  was estimated to be  $\sim 1\text{mN/m}$ .  $Ca_{crit}$  for both simple shear and 2D elongation as a function of the viscosity ratio were estimated from Grace's curve as shown in figure 4.2. Value of minimum diameters  $D_{min}$  were calculated with equation 1.9 (chapter 1. Estimated values of  $Ca_{crit}$  and  $D_{min}$  are reported in table 4.5. Note that the viscosity ratios are slightly changed compared to the uncompatibilized blends because the dynamic viscosity at 290 °C and 100rad/s of PEHD and PEHD-g-AM are respectively,  $\eta_{PEHD}^* = 60 \text{ Pa/s}$  and  $\eta_{PEHD-g-AM}^* = 108 \text{ Pa/s}$ .

The three series of compatibilized blends were observed by TEM and SEM after batch mini extrusion. Conditions of observation are described in chapter 2 subsection 3.2. In order to identify the effects that control the morphology development in reactively compatibilized blends (PA6-18k/MA-g-HDPE, PA6-3k/MA-g-HDPE and PA6-31k/MA-g-HDPE), the description of experimental results and discussions will be organized as follows:

- Firstly, morphologies obtained for compatibilized blends will be described.
- Secondly, morphologies of uncompatibilized and compositions exhibiting the same composition ratio of compatibilized blends will be compared.
- Then, differences identified between uncompatibilized and compatibilized blends morphologies will be deeply analysed in order to identify which mechanisms could be responsible of morphology development:

### 3. Effect of the compatibilization: Results and discussions

- In subsections 3.2, 3.3 and 3.4, only the mechanism due to rheological process (usual drop break-up/coalescence discussed in section 2) will be discussed and we shall endeavour to identify morphologies that could not be explained only by these mechanisms.
- In subsections 3.5, the results obtained in chapter 3 will be integrated to the discussion.

Thus a state of the art of mechanisms involved in the morphology development in reactively compatibilized blends will be proposed using the results obtained in chapter 3, discussions on uncompatibilized and compatibilized blends morphologies (sections 2 and subsections 3.2, 3.3 and 3.4) and comparisons between morphologies obtained (subsections 3.2, 3.3 and 3.4). All the necessary information will be combined to try to develop a scenario of morphology development in reactively compatibilized blends.

Experimental TEM micrographs of the three series that will be discussed are summarized in figure 4.19. This figure is given to help the reader given the large number of studied blends .

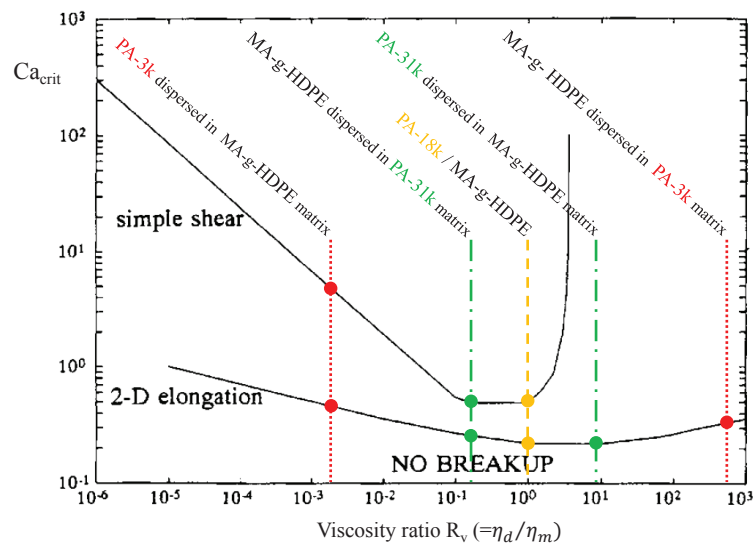


Figure 4.18: Grace's curve representing the critical capillary number  $Ca_{crit}$  as a function of the viscosity ratio measured at 100rad/s. Lines corresponding to the different blends viscosity ratios studied in this work are reported.

Table 4.5: Determination of the critical capillary number  $Ca_{crit}$  for compatibilized binary blends PA6-31k/MA-g-HDPE, PA6-18k/MA-g-HDPE and PA6-3k/MA-g-HDPE and minimum diameter accessible  $D_{min}$  using equation 1.9 for both simple shear and 2D elongation. The interfacial tension  $\Gamma=1mN/m$  and the shear rate  $\dot{\gamma}=100s^{-1}$ , blend components viscosities are taken at 100rad/s.

		PA6-31k/MA-g-HDPE		PA6-18k/MA-g-HDPE		PA6-3k/MA-g-HDPE	
		MA-g-HDPE matrix	PA6-31k matrix	MA-g-HDPE matrix	PA6-18k matrix	MA-g-HDPE matrix	PA6-3k matrix
$\eta_{m\ 100rad/s}$ [Pa.s]		108	820	108	105	108	0.2
$R_v$		7.6	0.13	1	1	0.002	540
Simple shear	$Ca_{crit}$	Off limits	0.5	0.5	0.5	4	Off limits
	$D_{min}$	Large	10nm	65nm	65nm	0.5 $\mu$ m	Large
2D elongation	$Ca_{crit}$	0.21	0.25	0.21	0.21	0.48	0.31
	$D_{min}$	30nm	4nm	30nm	30nm	60nm	20 $\mu$ m

### 3. Effect of the compatibilization: Results and discussions

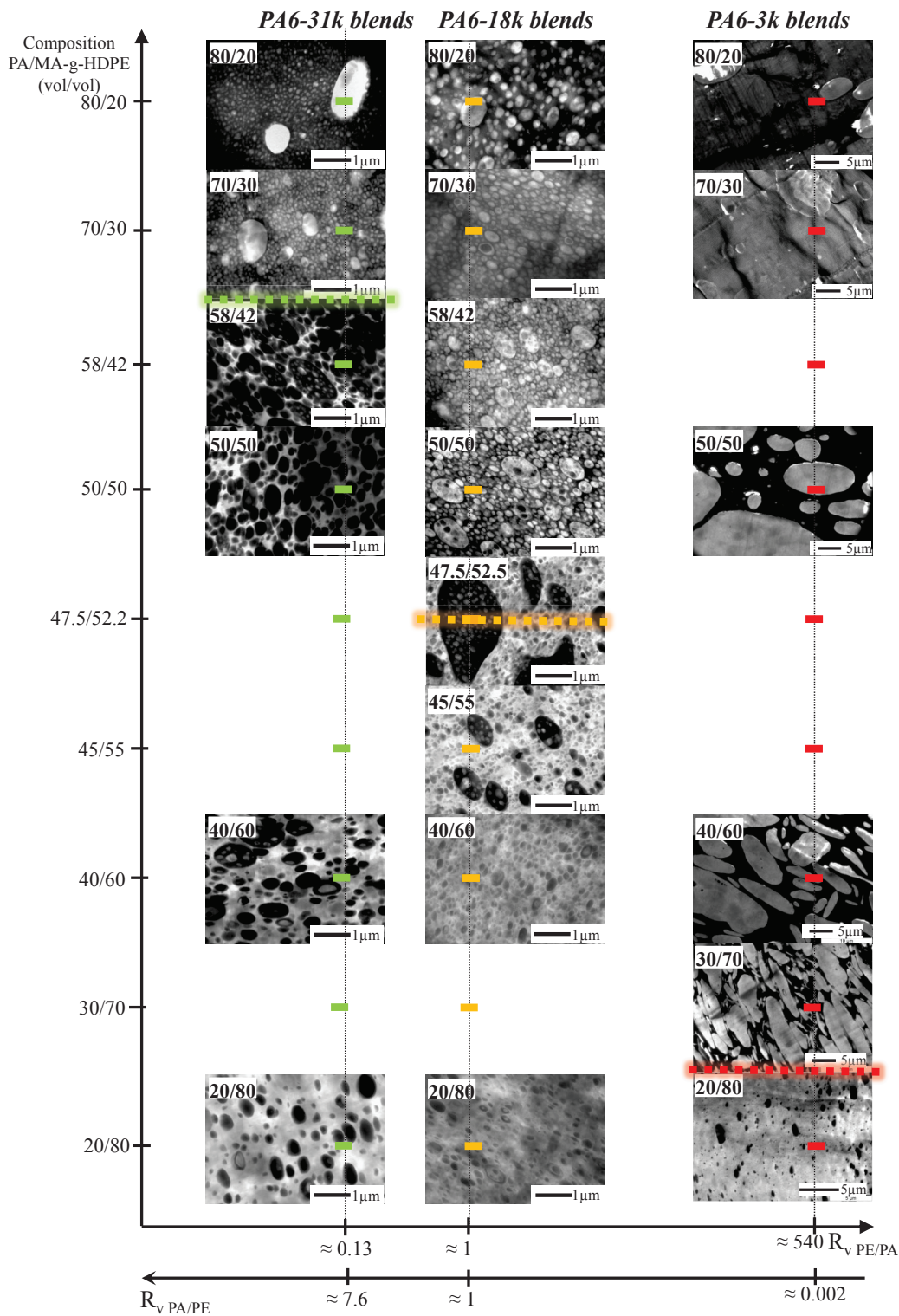


Figure 4.19: Comparison of PA-31k/MAGPE, PA-18k/MAGPE and PA-3k/MAGPE compatibilized blends. TEM micrographs after PA6 staining are presented, PA6 appears in dark. Due to the different characteristic sizes of morphology, different magnification are presented:  $\times 16000$  for PA-31k/PE and PA-18k/PE blends and  $\times 2500$  for PA-3k/PE blends.

### 3.1 Conversion rate of the compatibilization reaction

Microscopic observations may give a good idea of the efficiency of the compatibilization but only give a local qualitative information. They do not give access to the conversion rate of the reaction.

During the compatibilization reaction, maleic anhydride moieties of the MA-g-HDPE react with amine-end group of the PA6; the MA moieties disappear in order to form an imide moieties. The compatibilization reaction is schematized in figure 4.20.

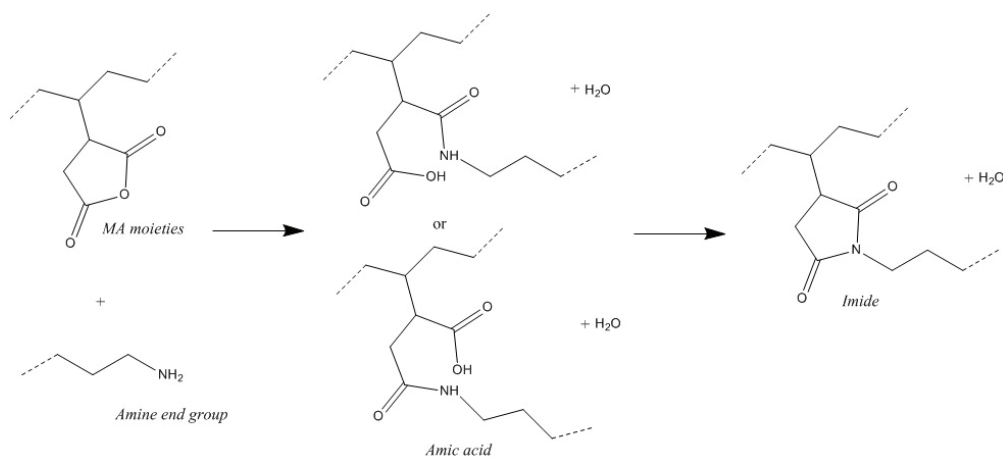


Figure 4.20: Compatibilization reaction

Transmission Infrared Spectroscopy (IR) has been proposed in the literature to follow the consumption of MA moieties after reaction, and thus estimate the compatibilization reaction conversion [125, 139, 140, 141, 142]. For that, the decrease after reaction of the area of the absorption band characteristic of anhydride carbonyl at  $1791\text{cm}^{-1}$  was followed.

However, in the MA-g-HDPE used for this study, maleic anhydride is present in a mixture of two forms, the maleic anhydride and the dicarboxylic acid forms, as shown in figure 4.21. Figure 4.22 shows the IR spectra obtained for the MA-g-HDPE. According to the literature, the bands  $\nu\text{C}=\text{O}$  were assigned as follow:

- $\nu\text{C}=\text{O}$   $1791\text{ cm}^{-1}$ : symmetrical vibration of maleic anhydride (sym AM).
- $\nu\text{C}=\text{O}$   $1713\text{ cm}^{-1}$ : vibration of the carboxylic acid (COOH)(acide).
- $\nu\text{C}=\text{O}$   $1866\text{ cm}^{-1}$ : asymmetrical vibration of maleic anhydride (asym AM).

### 3. Effect of the compatibilization: Results and discussions

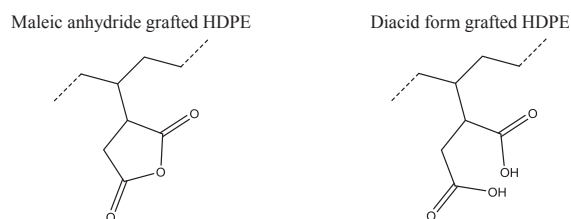


Figure 4.21: Developed formulae of the maleic anhydride form and the acid form of the maleic anhydride grafted to the HDPE.

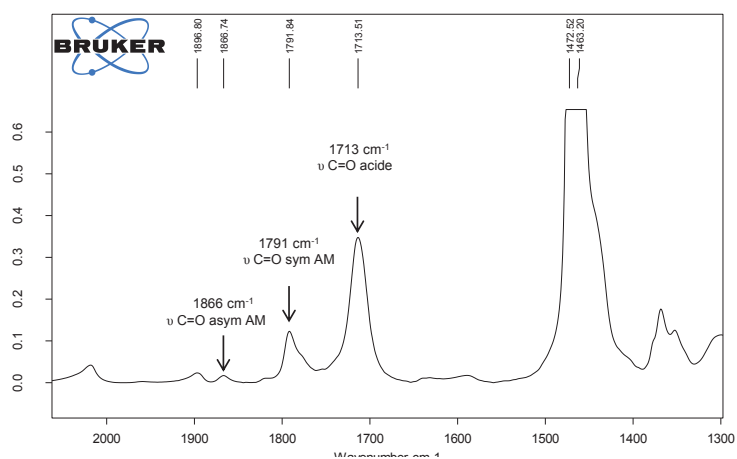


Figure 4.22: IR spectra of pure MA-g-HDPE. Zoom between 2000 and 1300cm<sup>-1</sup>. Symmetrical vibration of maleic anhydride (sym AM), vibration of the carboxylic acid (COOH)(acide), asymmetrical vibration of maleic anhydride (asym AM).

Consequences on the compatibilization reaction are:

- During the compatibilization reaction, the reaction kinetics of  $\text{NH}_2$  with the maleic anhydride is much faster than with the corresponding carboxylic acids ( $\text{COOH}$ ). However, a fraction of carboxylic acid may even react with amine end groups of PA6. Thus not only the band of maleic anhydride ( $1791\text{ cm}^{-1}$ ) should be followed but also the band at the diacid ( $1713\text{ cm}^{-1}$ ) to calculate the conversion rate.
- In addition, during the blend compounding (into the microcompounder), water is present at the beginning due to the PA6, and is also created in the environment. At high temperature, this water can be responsible of further hydrolysis of maleic anhydride moieties as shown in figure 4.23. Those maleic anhydride moieties could therefore disappear, which results on the IR spectra by a decrease of the area of the absorption band at  $1791\text{ cm}^{-1}$ . However, instead of being transformed into imide moieties (band at  $1770\text{ cm}^{-1}$ ) they could transform into the acid form (band at  $1713\text{ cm}^{-1}$ ): the acid area absorption band should thus increase. As a consequence, this maleic anhydride should not be counted in the conversion rate.

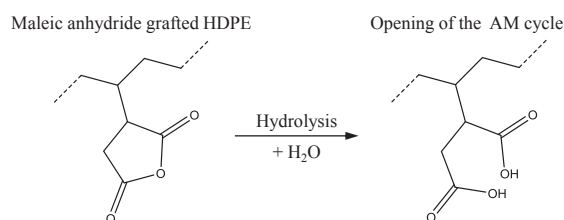


Figure 4.23: Schematic representation of the creation of two carboxylic acids by the hydrolysis of the maleic anhydride grafted.

Thus, for a proper quantification of the reaction, not only the band at  $1791\text{ cm}^{-1}$  should be followed but also the band at  $1713\text{ cm}^{-1}$ : the initial amount of both forms has to be quantified as well as the one after reaction. However, figure 4.24 showing pure IR spectra of PA6-3k and 18k, shows that the range of wavelengths characteristic of MA and  $\text{COOH}$  moieties in MA-g-HDPE, corresponds to the beginning of an absorption bands of PA6, which may vary in width, depending on the thickness of the film sample. This situation is even more critical for  $\text{COOH}$  band which are seen at smaller wavelengths than MA bands.

**Thus, a quantitative analysis of MA conversion by IR spectroscopy for PA6/MA-g-HDPE is not possible. Only qualitative data on the reaction rate can be extracted from the study of IR spectra of reacted and unreacted blends.**

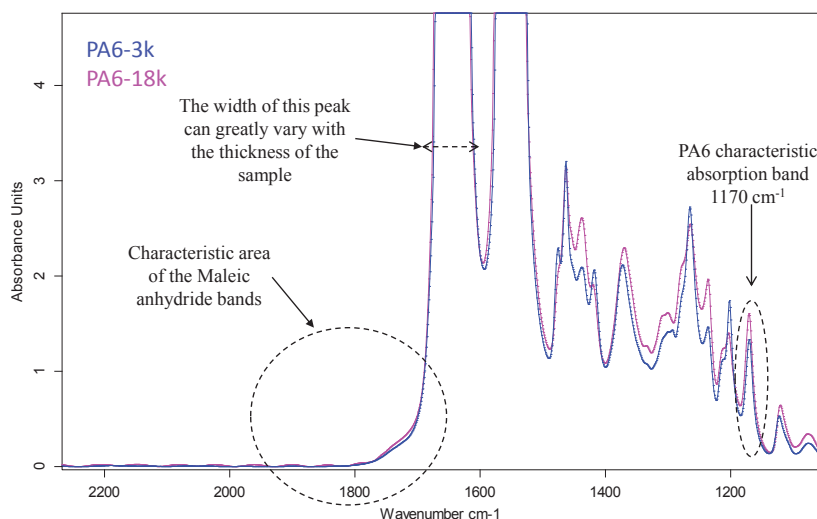


Figure 4.24: IR spectra of pure PA6-3K and PA6-18k. Zoom between 2200 and 1100 $\text{cm}^{-1}$  to show the critical zone where the maleic anhydride bands are expected. The characteristic band at 1170 $\text{cm}^{-1}$  used for the normalization is identified.

#### Study of binary PA6/MA-g-HDPE blends

Several binary blends of PA6 and MA-g-HDPE have been analyzed by IR for this study. General observations are:

- As expected, the smaller the volume fraction of MA-g-HDPE, the less visible the carboxylic acid band.
- In all blends, the acid band is practically masked by the very intense PA6 band and the quantitative analysis is impossible.
- The intensities of bands of interest (maleic anhydride and imide) are very low, they can sometimes be mingled with bands of the background noise.
- When the concentration of MA-g-HDPE increases in blends, the vibration of the acid carboxylic at 1713  $\text{cm}^{-1}$  is shifted to smaller wave lengths: until 1700  $\text{cm}^{-1}$  with 75%vol of MA-g-HDPE. It is indeed known that the band position of the carboxylic acid may vary depending on the possibilities of forming hydrogen bonds with the environment. Formation of H bond with PA6 may be responsible for the shifting of the COOH band.

For example, two binary blends exhibiting molar stoichiometry of 1 between MA moieties of the MA-g-HDPE (that can be in the form of MA or COOH) and  $\text{NH}_2$  end-groups of PA6 are described in what follows. Figures 4.25 and 4.26 show the IR spectra of binary blends: PA-18k/MAGPE 58/42 and PA-3k/MAGPE 20/80. In order to eliminate the possible effect of sample thickness variation in blends, all the considered absorption bands are normalized by one of the absorption band of the PA6 at 1170  $\text{cm}^{-1}$ . For each blend, a particular attention was paid in the IR spectra of blend after microcompounding to:

- The decrease of the maleic anhydride band at 1791  $\text{cm}^{-1}$ .
- The appearance of band at 1770  $\text{cm}^{-1}$  characteristic of the formation of the imide moieties.

- The changes on the carboxylic acid band at  $1713\text{ cm}^{-1}$ : shift toward lower wavelength and/or modification of intensity.

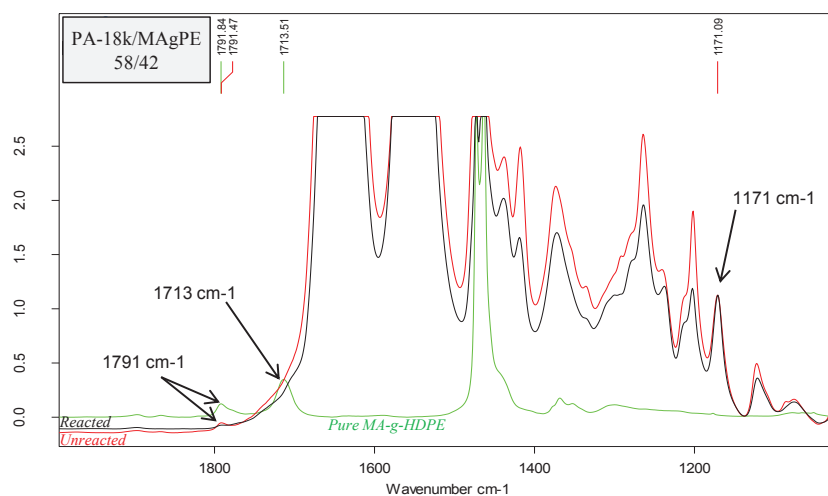


Figure 4.25: IR spectra of binary blend PA-18k/MAGPE 58/42, for which the molar ratio  $[MA]/[NH_2]$  is 1, before (red) and after (black) reaction (= after compounding). Comparison with IR spectra of pure MA-g-HDPE (green).

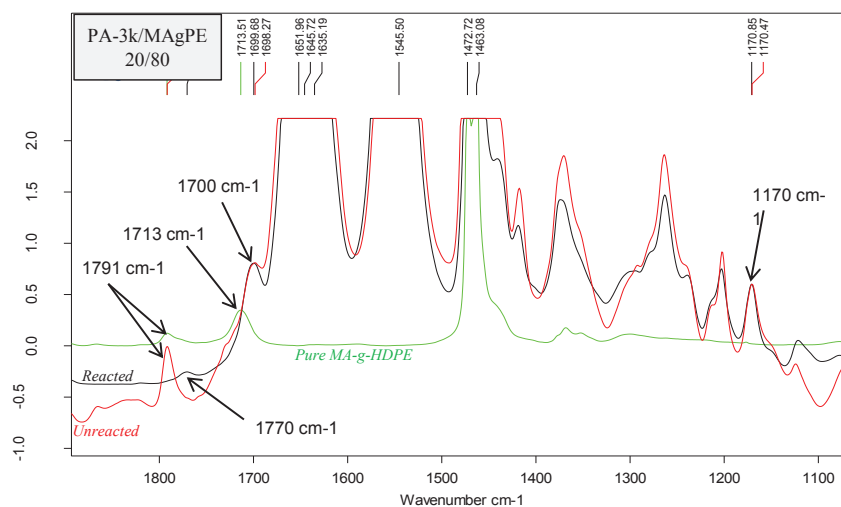


Figure 4.26: IR spectra of binary blend PA-3k/MAGPE 20/80, for which the molar ratio  $[MA]/[NH_2]$  is 1, before (red) and after (black) reaction (= after compounding). Comparison with IR spectra of pure MA-g-HDPE (green).

From the IR spectra of **PA-18k/MAGPE 58/42 blend**:

- The intensity ratio of bands at  $1791\text{ cm}^{-1}/1170\text{ cm}^{-1}$  decreased by a factor of 2.
- Characteristic band due to the creation of imide moieties at  $1770\text{ cm}^{-1}$  is not observed.
- Characteristic band due to the creation of carboxylic acid moieties at  $1713\text{ cm}^{-1}$  are unusable because the signal is too weak.

Thus the only qualitative conclusion that could be made is that the maleic anhydride has reacted but we have no information on the final conversion of the reaction.

The IR spectra of PA-3k/MAGPE 20/80 is more interesting:

- The band at  $1791\text{ cm}^{-1}$  of maleic anhydride almost totally disappeared.
- A band at  $1770\text{ cm}^{-1}$  due to the creation of imide has clearly been formed.
- The band at  $1700\text{ cm}^{-1}$  which corresponds to the shifted band of carboxylic acid at  $1713\text{ cm}^{-1}$  is clearly visible and the ratio of band area  $1700\text{ cm}^{-1}/1170\text{ cm}^{-1}$  did not evolve.

Thus, in this blend we have the proof that almost all the maleic anhydride moieties initially present in the blend have reacted and that the formation of imide moieties, reflecting the formation of copolymers, is confirmed. The relative intensity of the acid band did not evolve which means two things: first, the carboxylic acids did not react during compounding because otherwise the intensity of the band would have decreased and secondly, there was no creation of further carboxylic acid moieties in the blends.

**As a conclusion, this technique allows a qualitative observation that the reaction of compatibilization indeed happened. This is particularly relevant as the volume fraction of MA-g-HDPE increases. We have seen that PE reactive moieties which are in the form MA moieties almost quantitatively reacted during compounding. However, we have also seen that a fraction of the MA-g-HDPE was initially under the form of diacid. This form being less reactive than the maleic anhydride, there is a significant fraction of the MA-g-HDPE that do not react during compounding. In the case of PA-3k/MAGPE 20/80, the initial MA moieties transformed predominantly into imide moieties and the possible hydrolysis of MA moieties into dicarboxylic acid during compounding is not significant.**

## 3.2 Blends with PA6-18k

### 3.2.1 Experimental results: PA6-18k/MA-g-HDPE blends

Figure 4.27, shows the morphologies obtained for a large set of compositions for PA6-18k/MA-g-HDPE blends. On TEM micrographs the PA6 phase has been stained and appears in dark, while the PE phase appears in white.

#### Dispersion of MA-g-HDPE in PA6-18k phase

The global morphologies of blends 80/20 to 50/50 are dispersions of MA-g-HDPE in PA6-18k matrix as shown in figure 4.27. However, TEM micrographs reveal more complex morphologies on the whole composition range, that will be described in details in what follows.

The less concentrated blend, blend PA-18K/MAGPE 80/20, exhibits nodular dispersions of MAGPE. PE nodules sizes have been observed between 80nm to 600nm which is consistent with the sizes prediction in table 4.5. Droplets of roughly the same sizes are observed in the more concentrated blends, blends PA-18k/MAGPE 70/30, 58/42 and 50/50, and constitute the majority of nodules observed. Besides distances between nodules decrease and nodules become more homogeneously dispersed in space, due to the increase in volume fraction of the dispersed phase. However, we denote in dilute blends, blends 80/20 and 70/30, that some small PA nodules are observed inside PE nodules as shown in figure 4.28.

In more concentrated blends, blends PA-18k/MAGPE 58/42 and 50/50, a second population of larger PE nodules from 300nm to 1.8 $\mu$ m is observed. These nodules are filled with a subdispersion of small PA nodules from 80nm to 200nm. The PA nodules into the bigger PE nodules are distributed, in size and in space, similarly as small PE nodules population, with similar nodules sizes and distances between droplets. All the phenomena described above can be well observed in the TEM micrographs at higher magnification in figure 4.29.

With the calculation of the molar ratio between amine-end group of PA and the maleic anhydride moieties in blends, the blend PA-18k/MAGPE 58/42 is supposed to be equimolar. We did not succeed in the quantification of the conversion rate of the reaction, but the sizes of the population of small PE nodules, from 80nm to 300nm, which is not far from twice the radius of gyration of a PE chain for the smallest ones ( $R_{gPE} \approx 18\text{nm}$  [59]), suggests that only few homopolymers of MA-g-HDPE chains are trapped into these nodules (this MA-g-HDPE can be reactive or unreactive as discussed in subsection 3.1). Moreover, distance between PE nodules are in average from 40nm to 80nm which is even closer to twice the radius of gyration of PA6-18k ( $R_{gPA} \approx 12\text{nm}$  [59]). Thus, it can be concluded that a large quantity of copolymers are created at the interface, leading to a very high conversion rate of the reaction.

### 3. Effect of the compatibilization: Results and discussions

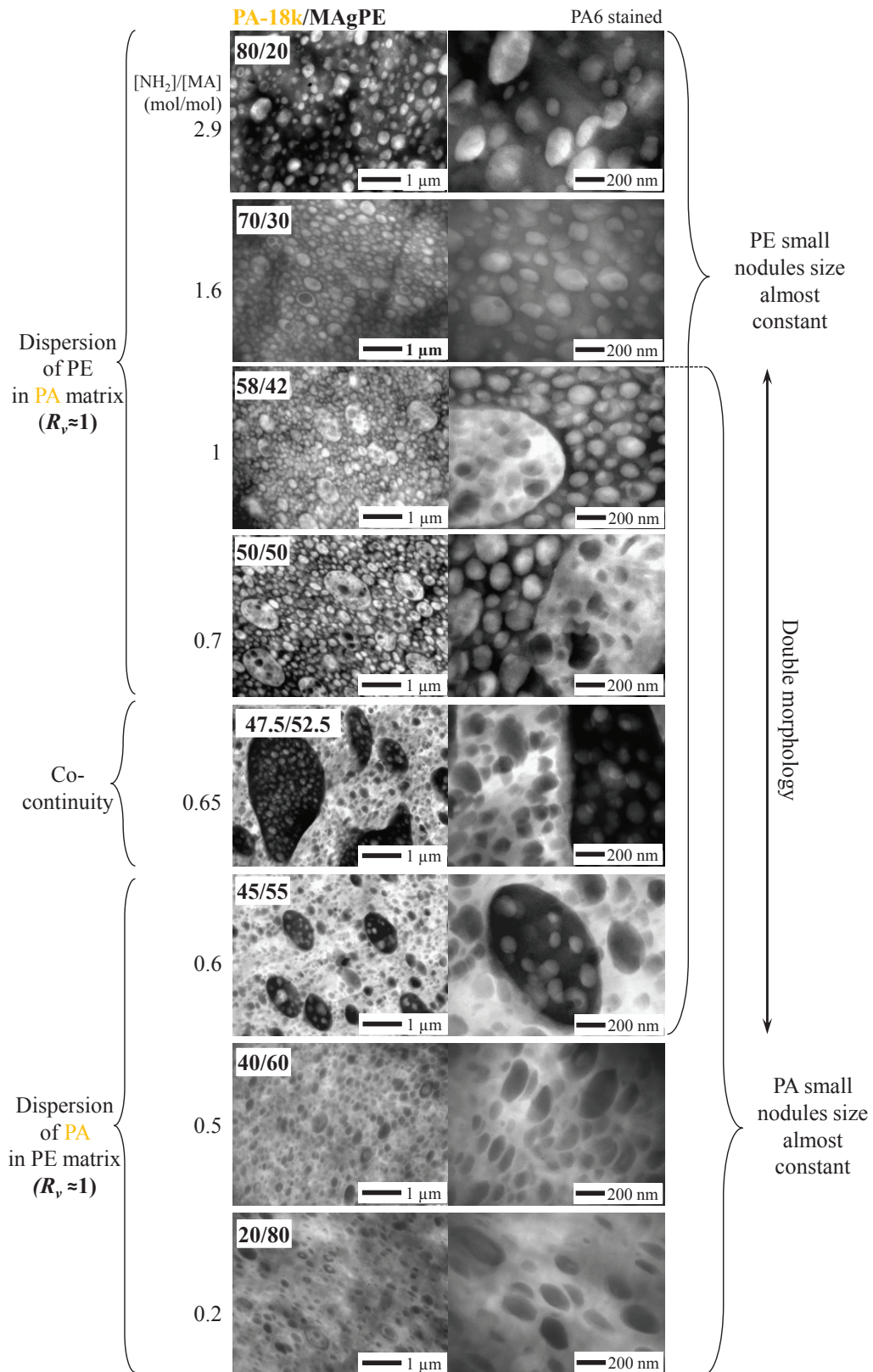


Figure 4.27: TEM micrographs of compatibilized binary blends of PA6-18k/MA-g-HDPE after PA6 staining (dark domains). Two magnifications are presented. The name of each blend is reported on the corresponding micrograph and correspond to the volume fraction in the melt state of each phase. The molar ratio between amine end groups and maleic anhydride  $[NH_2]/[MA]$  is also reported.

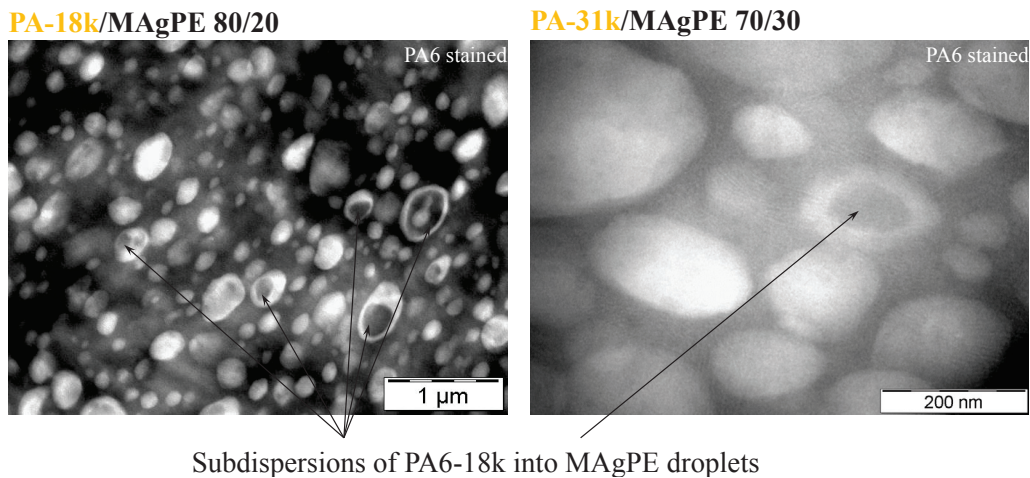


Figure 4.28: TEM micrographs of blends PA-18k/MAgPE 80/20 and 70/30 after PA6 staining (dark domains) to show that few PE nodules contain PA subdispersions (magnifications: left  $\times 20k$ , right  $\times 135k$ ).

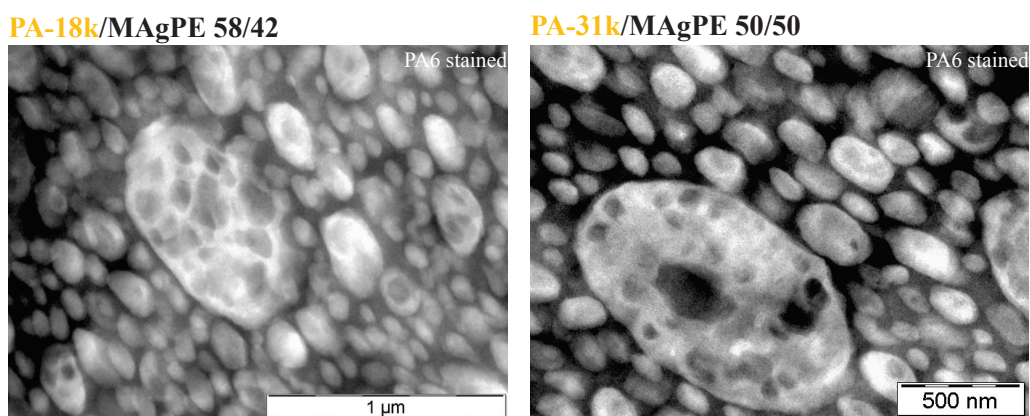


Figure 4.29: TEM micrographs of blends PA-18k/MAgPE 58/42 and 50/50 after PA6 staining (dark domains) showing the multiscale morphology: large PE droplets filled with PA subdispersions and small PE population. (magnification:  $\times 43000$ ).

#### Phase inversion

In those blends, a very precise composition at phase inversion has been detected: Blend PA-18k/MAGPE 47.5/52.5 exhibits a co-continuous morphology as shown in the SEM micrograph in figure 4.30. Blends PA-18k/MAGPE 50/50 and 45/55 exhibit respectively nodular dispersions of PE in PA and PA in PE. Thus the phase inversion composition happened between these 5%vol separating these blends. At the magnification of the figure 4.30, the co-continuous domains of PE (which appears in lighter) and PA (which appears in dark) are of the order of the micrometer. But the TEM micrograph shown in figure 4.27 shows that a very large amount of nanodispersions of both PE in the PA phase and PA in the PE phase are observed. The observations are the same as the one mentioned above: the distribution in size and in space of both nodules and distances between nodules are the same for both sides. It has not been quantified, but the amount of sub-dispersions is huge in both phases and distances between nodules is close to twice the radius of gyration of either MA-g-HDPE or PA6-18k.

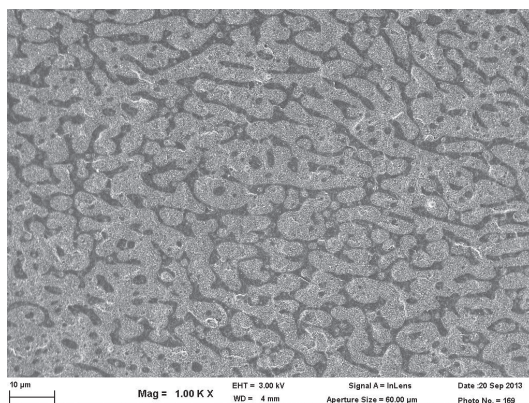


Figure 4.30: SEM micrograph of the cryofractured surface of PA-18k/MAGPE 47.5/52.5 binary blend (x1000).

#### Dispersion of PA6-18k in MA-g-HDPE phase

This morphology was observed for blends PA-18k/MAGPE 20/80, 40/60 and 45/55. Similar observations as for blends exhibiting dispersions of PE in PA matrix are made:

- The size of the small PA droplets are constant for the four blends and of the order of 50nm to 400 nm. In dilute blends PA-18k/MAGPE 20/80 and 30/70, one can observe sub dispersions of PE into the small PA nodules as shown in figure 4.31.
- The distance between droplets decreases (some distances are as low as 20nm for blend PA-18k/MAGPE 45/55) and nodules become more homogeneously dispersed in space due to the increased volume fraction of the dispersed phase.
- Blend PA-18k/MAGPE 45/55 exhibits a double morphology: the large majority of PA nodules exhibit a size between 50 to 400nm but some larger PA nodules, from 400 to 800nm, filled with smaller PE droplets (60 to 200nm) are observed: size and distribution of the small nodules inside are consistent with what has been observed previously for blends 58/42, 50/50 and 47.5/52.5.

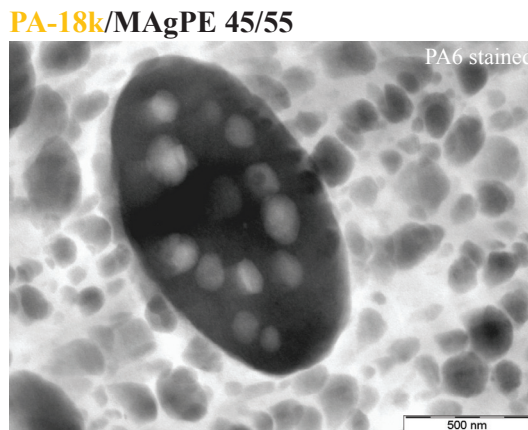


Figure 4.31: TEM micrographs of blends PA-18k/MAgPE 45/55 after PA6 staining (dark domains) showing the multiscale morphology: concomitant presence of small and large PA droplet population, and large PA droplets filled with PE nanodispersions. (magnification:  $\times 43000$ ).

### 3.2.2 Comparison with uncompatibilized blends

#### Comparison of experimental results: PA6-18k/HDPE vs. PA6-18k/MA-g-HDPE

Figure 4.32 shows the comparison between uncompatibilized and compatibilized binary blends with PA6-18k. On SEM micrographs, the minor phase has been etched. It is important to note that for compatibilized blends, Transmission Electron Microscopy was much more adapted to observe the small nodules which are hardly observable on SEM micrographs. The comparison between experimental results obtained for uncompatibilized and compatibilized blends shows that:

- Sizes of compatibilized blends decreased by more than a factor 10.
- The development of morphologies are symmetrical with respect to the phase inversion: the same trends are observed on both sides.
- For both series, the phase inversion is observed close to the composition of 50/50: the shift in phase inversion composition is consistent with the slight change in the PE phase viscosity which is smaller for pure HDPE.
- Where in uncompatibilized blend droplets sizes increase approaching the phase inversion, in compatibilized blends, droplet sizes of the smaller population remain almost constant. This phenomenon is indeed observed:
  - In blends PA-18k/MAgPE 70/30, 58/42 and 50/50 where a majority of the PE nodules keep almost the sizes observed for blend 80/20, i.e. from 80nm to 400nm.
  - In blends PA-18k/MAgPE 47.5/52.5, 45/55 and 40/60 where a majority of the PA nodules keep almost the sizes observed for blend 20/80, i.e. from 50nm to 400nm.
- In compatibilized blends, small sub-inclusions are observed into some nodules of dilute blends. However, when the concentration in dispersed phase increases (i.e. for composition between more or less 10%vol of the phase inversion composition), a

second population of larger nodules filled with smaller sub-inclusions of the matrix phase is observed. **This behavior was not observed in uncompatibilized blends.**

#### **Discussion on the comparison of mechanisms responsible for the morphology development**

The changes in morphology sizes attest of a significant conversion rate of the reaction. The morphology development has thus been modified due to the creation of copolymers at the interface. Thus, in comparison to the uncompatibilized blends, some points are consistent with the usual description of compatibilization effects:

- The size reduction by at least a factor 10 is consistent with the reduction of interfacial tension. This constitutes a direct proof that the compatibilization reaction occurred.
- The constant sizes of the smallest population of nodules when increasing  $\phi_d$  is consistent with an inhibition of coalescence due to the presence of copolymers. Thus whatever the side of the graft copolymers considered, the inhibition of coalescence is very efficient.
- Given the homogeneity in size and in space of the small population of both PE nodules in PA (for blends 80/20 to 47.5/52.5) and PA nodules in PE (for blends 45.7/52.5 to 20/80) the simple Rayleigh break-up mechanism could satisfactorily explain the formation of small nodules. Besides, with a surface tension decreased to  $\sim 1\text{mN/m}$ , the minimum size attainable by elongation is  $\sim 30\text{nm}$  which is consistent with the smallest sizes observed.

However, the presence of subdispersions, in small quantity for dilute blends, but in large quantity in concentrated blends, was not observed in the case uncompatibilized blends. Besides, the multiscale morphology observed in concentrated blends (larger population of nodules filled with smaller nodules) cannot be explained by the Rayleigh capillary wave instabilities mechanisms. This also applies for the co-continuous blend PA-18k/PE 45.5/52.5 which is fully filled in both phases of nanodispersions. As a consequence **sub-inclusions in such large amount are developed through the compatibilization reaction.** Indeed, the study of the compatibilization reaction between PA6-18 and MA-g-HDPE in chapter 3 has shown that, at a flat interface in static conditions, after 10 minutes annealing at 290 °C, the interface was greatly destabilized: lamellar structures had formed over a thickness of few micrometers. Thus there may be a strong link between this destabilization due to the compatibilization reaction and the nanodispersions observed on both sides of the interface, for concentrated blends especially.

This, point will be discussed in more details in subsection 3.5.

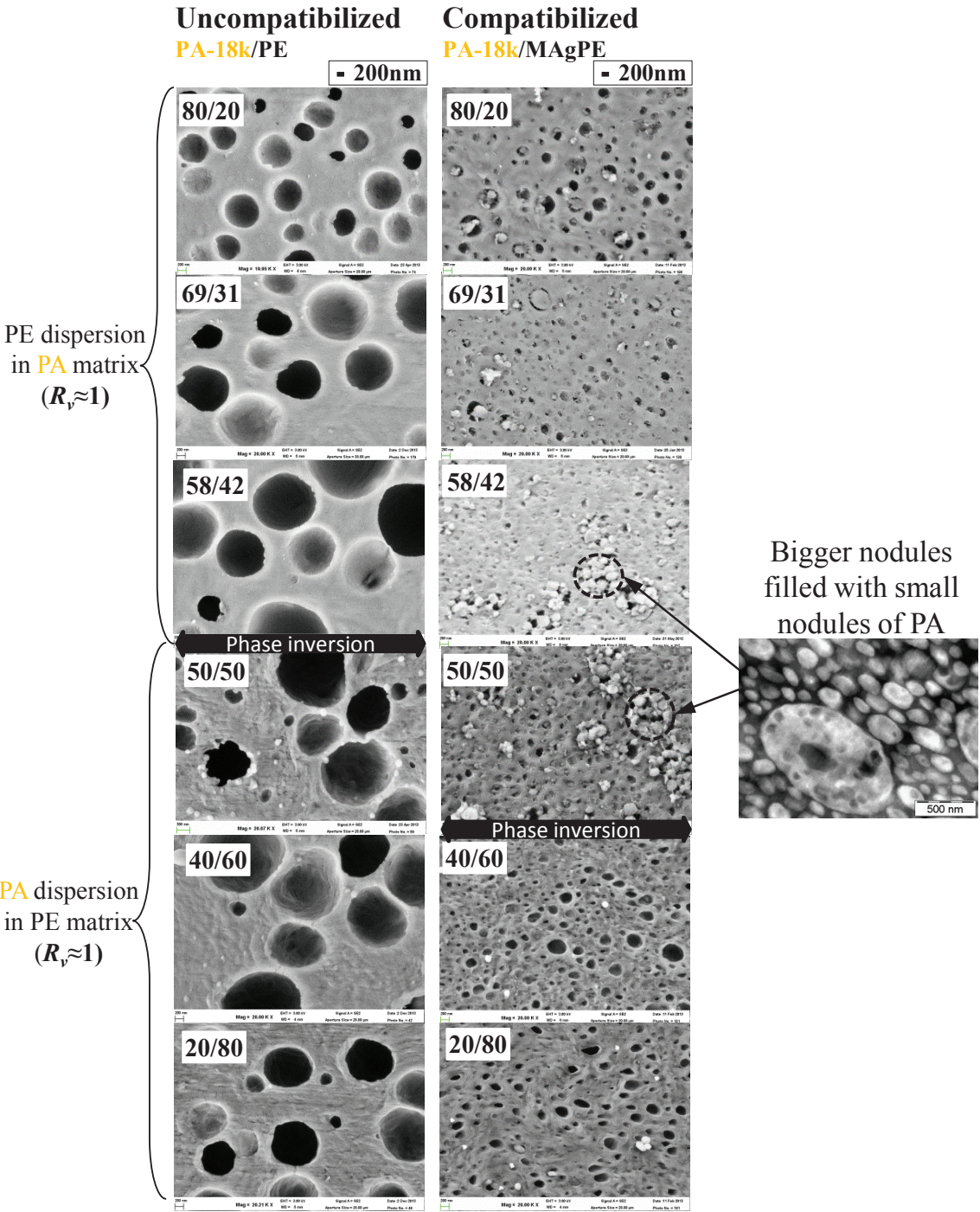


Figure 4.32: Comparison of uncompatibilized binary blends PA-18k/PE and compatibilized binary blends PA-18k/MAGPE. SEM micrographs after minor phase etching at the same magnification  $\times 20000$ .

## 3.3 Blends with PA6-3k

### 3.3.1 Experimental results: PA6-3k/MA-g-HDPE

Figure 4.33, shows the morphologies obtained for a large set of compositions for PA6-3k/MA-g-HDPE blends. On TEM micrographs the PA6 phase has been stained and appears in dark, while the PE phase appears in white. For blends PA-3k/MAGPE 80/20, 70/30, 50/50, 40/60 and 30/70 the right column shows a higher magnification of the morphologies focussed in the biggest PE nodules.

#### Dispersion of MA-g-HDPE in PA6-3k phase

As shown in Figure 4.33, blends PA-3k/MAGPE 80/20, 70/30, 50/50, 40/60 and 30/70 exhibit dispersions of MA-g-HDPE domains (which appears in white) into a PA6-3k matrix (which appears in dark). For blends PA-3k/MAGPE 80/20 to 50/50 the shape of the dispersions are not always nodular but sometime slightly elongated and the sizes vary from 2 $\mu\text{m}$  to 30 $\mu\text{m}$ . For more concentrated blends, blends PA-3k/MAGPE 40/60 and 30/70, almost all the nodules adopt an elongated shape and the sizes decrease: for blend PA-3k/MAGPE 30/70 the width and the length of nodules are in the range of respectively: 400nm to 15 $\mu\text{m}$  and 1 $\mu\text{m}$  to 20 $\mu\text{m}$ . Those sizes are consistent with the prediction made in table 4.5 for elongational flow. The films of PA6-3k between these droplets are very thin, down to few tens of nanometers which is of the order of twice the radius of gyration of PA6-3k chains ( $R_{g, PA} \approx 5 \text{ nm}$  [59]), and can be squeezed over a very long distance, several micrometers sometimes as shown in figure 4.34.

Looking more carefully at the large PE droplets on TEM micrographs of figure 4.33 (right column) and figure 4.34, one can notice an interesting phenomenon: "stripes", from 100 to 200 nm wide, composed of a large number of tiny nodules of PA of 5 to 50nm and randomly crossing the nodules are observed. A signature of this particular phenomenon, which was only noticed for these specific blends, was also observed on the SEM micrographs after cryofracture. Usually, when PE nodules are cryo-fractured, they leave a filamentous (=ductile) surface which globally appears in white, from a low magnification point of view. In almost all the pictures of blends PA-3k/MAGPE 50/50 to 30/70, darker stripes making sorts of pathway (few hundreds of nm) through the nodules were observed. Figure 4.35 illustrates the phenomenon.

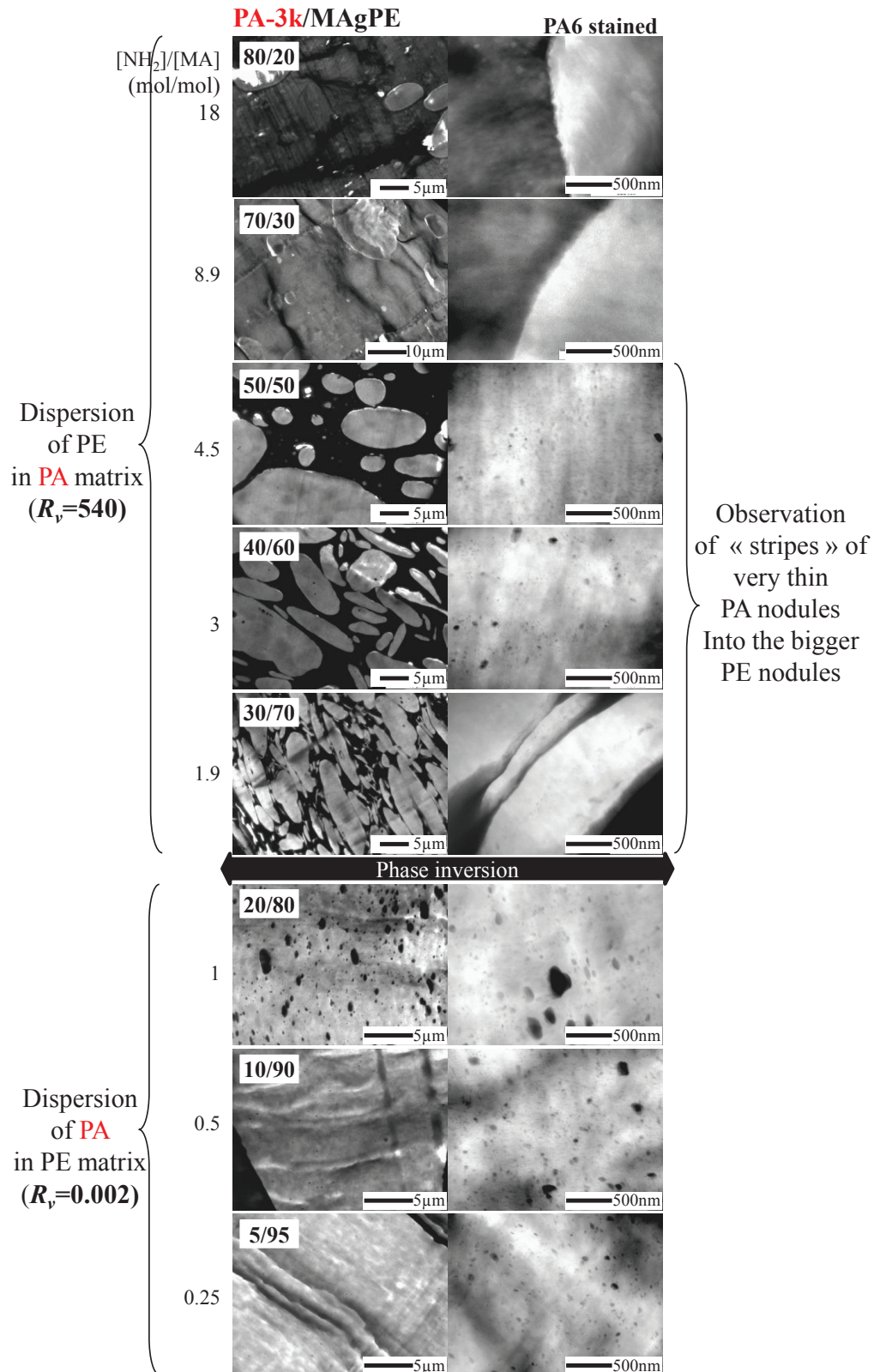


Figure 4.33: TEM micrographs of compatibilized PA6-3k/MA-g-HDPE binary blends after PA6 staining (dark domains). Two magnifications are presented. The name of each blend is reported on the corresponding micrograph and corresponds to the volume fraction in the melt state of each phase. The molar ratio between amine end groups and maleic anhydride  $[NH_2]/[MA]$  is also reported.

### 3. Effect of the compatibilization: Results and discussions

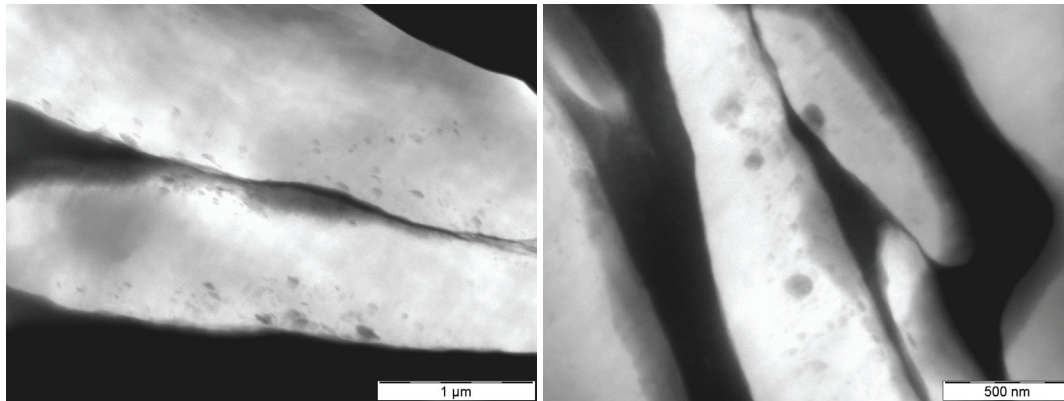
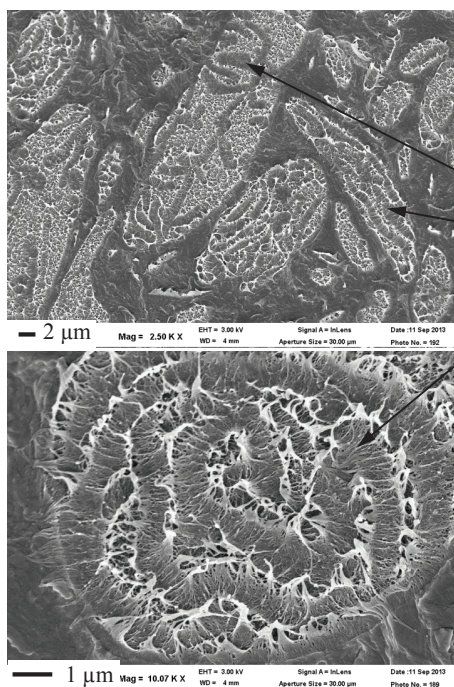


Figure 4.34: TEM micrographs of binary blends PA-3k/MAGPE 40/60(left, x26000) and 30/70(right, x43000) after PA6 staining, illustrating the very thin films of PA6 matrix squeezed between large PE domains.

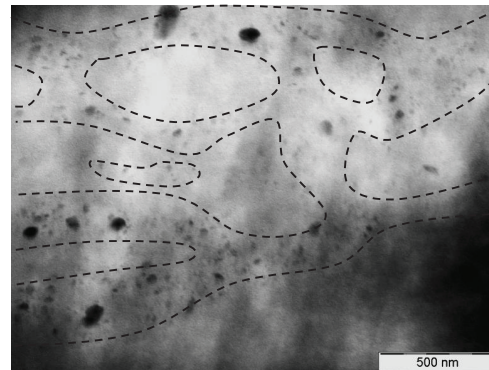
#### Cryofracture

PA matrix (black) and PE nodules (white)



#### TEM

(PA6 stained)



#### "Stripes" of PA6-3k micelles

The dotted lines represent the boundaries within which there is a multitude of very thin PA6-3k droplets (=micelles) inside a larger MA-g-HDPE nodules of few  $\mu\text{m}$ .

These stripes are observed by darker paths on the micrographs after cryofracture.

Figure 4.35: Cryofractured surfaces (left, x2500 and x10000) and TEM micrograph after PA6 staining (right, x43000) of binary blend PA-3k/MAGPE 40/60 illustrating the "stripes" (width=100 to 200 nm), composed of a large number of tiny PA nodules of 5 to 50nm.

### Dispersions of PA6-3k in MA-g-HDPE phase

Blends PA-3k/MAGPE 5/95, 10/90 and 20/80 exhibit a morphology with nodular dispersions of PA6-3k in a MA-g-HDPE matrix as shown in figure 4.33. A first observation at low magnification of TEM micrographs shows that only blend 20/80 exhibits nodules of PA6-3k in the matrix. The sizes of the nodules are quite big, from 200nm to 20 $\mu$ m and their shape is not really nodular but a bit elongated. Nevertheless, an observation at a higher magnification shows that the matrix is filled with a lot of very thin droplets, that we could call "micelles", for which the size can vary from 5 to 50nm. Micelles are observed for the three blends and an example in blend 10/90 is shown in figure 4.36. Blends PA-3k/MAGPE 10/90 and 5/95 are almost entirely composed of micelles of PA in PE phase.

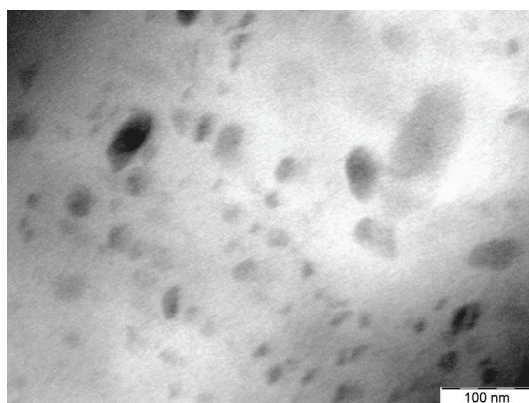


Figure 4.36: TEM micrograph of binary blend PA-3k/MAGPE 10/90 at high magnification ( $\times 160000$ ): micelles of PA6-3k in the MA-g-HDPE matrix.

Theoretically, the droplet size attainable from calculations using the critical capillary number (see table 4.5) under shear is  $\sim 500$ nm but under elongational flow it is  $\sim 60$ nm. The sizes observed here (5 to 50nm) are in average smaller than calculated predictions. The radius of gyration of a chain of PA6-3k is approximately  $\langle R_g \text{ PA} \rangle = \sqrt{0.852 M n_{\text{PA}}} \approx 5$  nm[59]. This means that the small nodules observed are probably micelles of pure graft copolymers (=micelles) or copolymers slightly swollen by unreacted PA6-3k chains.

The molar ratio  $[\text{NH}_2]/[\text{MA}]$  in blend PA-3k/MAGPE 20/80 is supposed to be 1 (see table 4.2). Thus potentially all PA6 chains should be observed under the form of micelles of pure copolymers. However, few PA nodules of hundreds of nanometers are still observed suggesting that all PA6 chains have not been converted into copolymers. The Infra-red analysis of blend discussed in subsection 3.1, has qualitatively shown that the compatibilization reaction was effective. However, the analysis of IR spectra of pure MA-g-HDPE showed that a part of the 1%wt of MA moieties may initially be under the form of the corresponding carboxylic acid, much less reactive than the maleic anhydride form. Thus, when blends are formulated with a ratio  $[\text{NH}_2]/[\text{MA}]=1$  the amount of MA reactive moieties is very probably overestimated. This explains why in blend 20/80, the IR measurement shows that all the MA moieties reacted but the morphology still exhibits few PA droplets of few hundreds of nanometers.

In blends 10/90 and 5/95, where the  $[\text{MA}]$  is in excess compared to the  $[\text{NH}_2]$  we observe almost only PA6-3k micelles.

#### 3.3.2 Comparison with uncompatibilized blends

##### Comparison of experimental results: PA6-3k/HDPE vs. PA6-3k/MA-g-HDPE

Figure 4.37 shows the comparison between uncompatibilized and compatibilized binary blends with PA6-3k. SEM micrographs of cryofractured surfaces or after minor phase etching are presented. For compatibilized blends, TEM was much more adapted to observe micelles of PA into the PE phase which cannot be observed on SEM micrographs. To summarize the observations, when compatibilized blends are compared to the corresponding uncompatibilized blend:

- Characteristic sizes of compatibilized blends are approximately one order of magnitude smaller than the uncompatibilized blends exhibiting the same PA/PE composition ratio.
- When PE or MA-g-HDPE are dispersed into the PA6-3k:
  - Even if  $R_v \gg 1$  The PE phase has been dispersed for both series.
  - Very thin films of PA between large PE nodules are observed.
  - The droplets sizes decreases when  $\phi_{PE}$  increases on approaching phase inversion. In uncompatibilized blends, when  $\phi_{PE}$  increases, neighbouring nodular droplets are slightly deformed. In compatibilized blends, droplets adopt an elongated shape.
  - Sub-inclusions of PA6-3k of 200nm to 2 $\mu$ m were observed into large HDPE nodules in uncompatibilized blends. "Stripes" (of 100 to 200 nm wide), composed of a large number of PA micelles of 5 to 50nm are observed in the biggest MA-g-HDPE nodules in compatibilized blends.
- Phase inversion is observed between 20 and 30%vol for compatibilized blends and 10 and 30%vol of PE for uncompatibilized blends.
- When PA6-3k is dispersed into PE or MA-g-HDPE phase:
  - Uncompatibilized PA-3k/HDPE 20/80 blend was co-continuous while PA-3k/MAgPE 20/80 blend exhibits a nodular dispersions of PA in PE matrix in the compatibilized blend.
  - In uncompatibilized blends, very polydisperse sizes of PA dispersions were observed: bigger nodules of around 2-4 $\mu$ m and very thin nodules of around 50 to 200nm were observed. In compatibilized blends, almost only micelles of 5 to 50nm, i.e. nodules composed of pure copolymers, were observed.

##### Discussion on the comparison of mechanisms responsible for the morphology development

The changes in morphology sizes attest that morphology development has been modified due to the creation of copolymers at the interface. Thus, in comparison to the uncompatibilized blends, the main conclusions that can be drawn from these observations are:

- The size reduction by a factor of  $\sim 10$  is consistent with the creation of copolymers at the interface.
- When PE or MA-g-HDPE are dispersed into the PA6-3k:

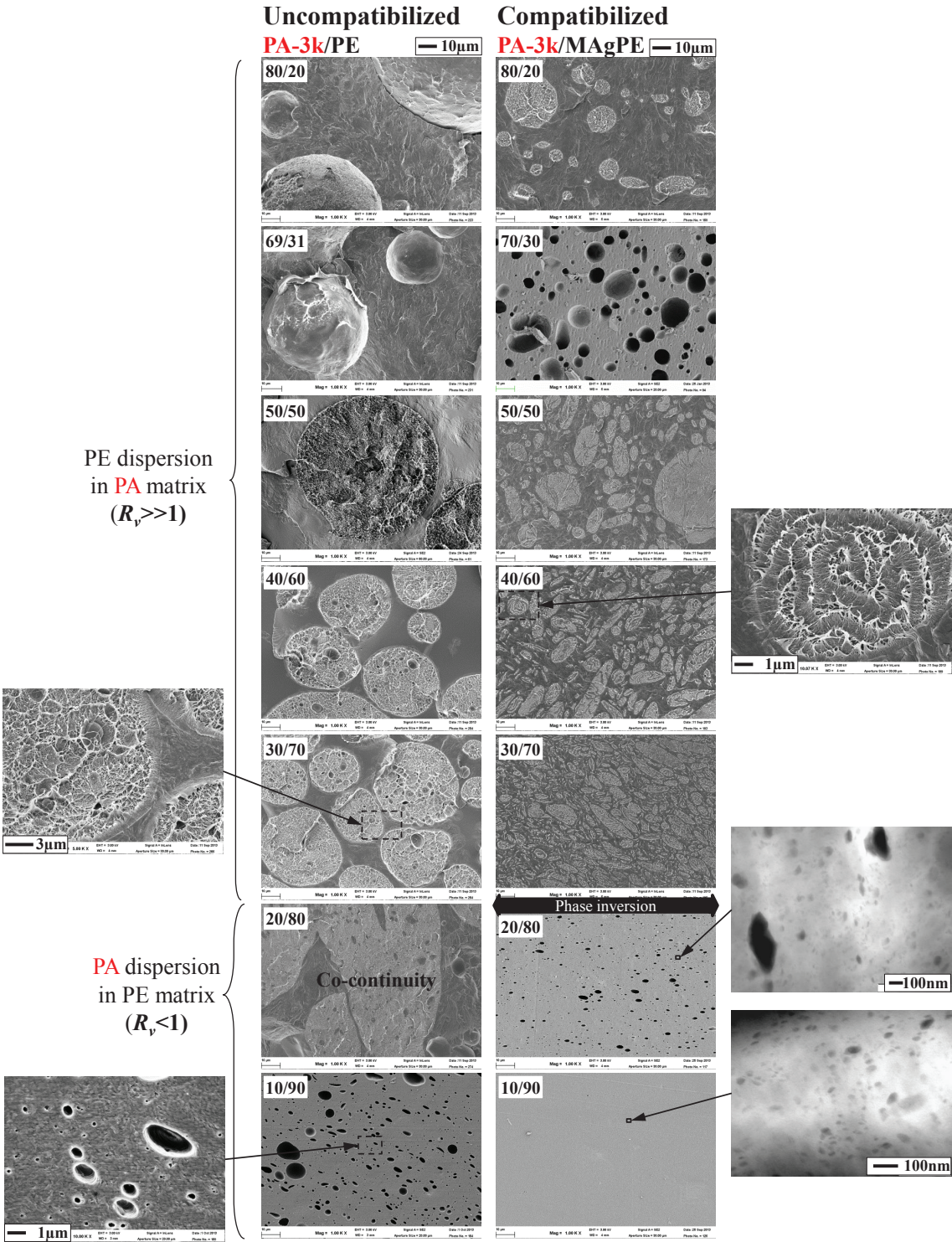


Figure 4.37: Comparison of uncompatibilized binary PA-3k/PE blends and compatibilized binary PA-3k/MAgPE blends. SEM micrograph (after minor phase etching or cryofracture) at the same magnification x1000.

- In both cases break-up of PE phase happened even though the viscosity of the PE phase is much higher than the viscosity of the PA phase. As discussed for uncompatibilized blends, this may be explained by elongationnal flow present in the process.
  - Coalescence is very unfavourable in both cases due to the very high viscosity ratio (PA6 remains the matrix until high volume fractions: 70%vol): the immobile interface drainage regime can be considered as discussed in subsection 2.2. Besides, the long films which do not coalesce between elongated droplets indicates that coalescence is even more inhibited due to the presence of compatibilizer at the interface.
  - The fact that nodules sizes decrease when  $\phi_{PE}$  increases is due to the promoting of break-up induced by the addition of droplets much more viscous than the matrix: this increases the global viscosity.
  - The presence of micelles organized in "stripes" into bigger droplets of MA-g-HDPE is not easily explained by the mechanisms of break-up and coalescence modified with the presence of copolymers at the interface. Indeed, on the one hand, micelles sizes are smaller than the predicted sizes even in elongationnal flow and on the other hand, the stress felt by the subdispersion inside a larger droplet is much lower than the stress imposed by the matrix. Thus, such a thin size could not be explained by classical break-up mechanisms alone.
- When PA6-3k is dispersed into PE or MA-g-HDPE phase:
- Coalescence of PA6 domains is inhibited due to the creation of copolymers: as a consequence blend at 20/80 was co-continuous for the uncompatibilized blend while it is a dispersion of PA into a PE matrix in the compatibilized one. The co-continuity windows is probably reduced in the compatibilized series.
  - In uncompatibilized blends, end-pinching mechanism with formation of small satellites between drop was adapted to describe the very polydisperse morphology composed of nodules of 2 to 4 $\mu$ m but also very small nodules of around 50 to 100nm. Predictions of table 4.3 in elongational flow were in quite good agreement with the larger droplets sizes observed. But sizes of small satellites were far from the predictions. In compatibilized blends, the minimum size attainable in elongation is supposed to be 60 nm but the typical sizes observed are smaller, 5 to 50 nm and could correspond to micelles of pure copolymers. Thus, the morphology development in compatibilized blends seems to be favourable to the development of very small nodules rather than larger ones. The mechanism of end-pinching could hardly explain the very large quantity of micelles. In the literature several authors reported that when  $R_v < 1$ , tip-streaming can occur [38, 39, 7]. Tip-streaming leads to the formation of very small drops at the end of a drop as shown in chapter 1, figure 1.14 picture (b). This mechanism could describe the morphology observed.

The study of the compatibilization reaction between PA6-3k and MA-g-HDPE in chapter 3 has shown that, at a flat interface in static conditions, the interface was not destabilized. We discussed the fact that with this architecture of copolymer (very short PA6-3k compared to long HDPE backbone), only a very high curvature of the interface, of the order of the radius of gyration of a PA6-3k chain, could lead to a destabilization and the

creation of micelles of PA6-3k into MA-g-HDPE. Thus, only very curved interfaces like the end of the drop from which the tip-streaming occurs could be curved enough to favor the spontaneous creation of micelles. Thus there may be a strong link between the observation made in static conditions and the blend morphology developed. This, point will be discussed in more details in subsection 3.5.

### 3.4 Blends with PA6-31k

#### 3.4.1 Experimental results: PA6-31k/MA-g-HDPE

Figure 4.38, shows the morphologies obtained for a large set of compositions for PA6-31k/MA-g-HDPE blends. On TEM micrographs the PA6 phase has been stained and appears in dark, while the PE phase appears in white.

#### Dispersion of MA-g-HDPE in PA6-31k phase

As shown in figure 4.38 the morphology of blends PA-31k/MAGPE 80/20 and 70/30 is particular because two typical sizes are observed:

- A very homogeneous nodular dispersion of thin MA-g-HDPE droplets into the PA6-31k matrix is observed. The size of this dispersion is in average from 30nm to 100nm. The distance between these nodules is also very regular and homogeneous, and goes in average from 20nm to 100nm. According to Fetters et al. [59] the gyration radius of PA6-31k and MA-g-HDPE are  $R_g PA-31k \approx 16\text{nm}$  and  $R_g MAGPE \approx 18\text{nm}$ . As a consequence, sizes observed for both nodules and distances between nodules correspond roughly to twice the gyration radius of chains. The molar ratio  $[\text{NH}_2]/[\text{MA}]$  is equimolar for blend 70/30 and  $\sim 1.7$  for blend 80/20, thus in this blend,  $\text{NH}_2$  moieties are in excess. The small PE droplets observed may thus be mainly composed almost by pure bloc copolymers. The matrix surrounding droplets can be pure grafted PA6 chains of the copolymer, or eventually, slightly swollen by homopolymers of PA6-31k in blend 80/20. Note also that small PE nodules are very well organized, one can sometime even guess typical sphere packing organization with respect to the distance of twice  $R_g PA$  between spheres. Static annealing of those blends has been performed and show an even better organization.
- In addition, larger droplets of MA-g-HDPE are observed (from 0.5 to  $2\mu\text{m}$  in PA-31k/MAGPE 80/20 blend and from 300nm to  $1.5\mu\text{m}$  for PA-31k/MAGPE 69/31 blend). No subdispersions insides droplets are observed so they seem to be composed only of pure unreacted MA-g-HDPE. As discussed previously, a part of MA moieties grafted on MA-g-HDPE may not be reactive (dicarboxylic acids). In both blends the MA-g-HDPE has been introduced with a molare ratio  $[\text{NH}_2]/[\text{MA}]$  of 1 or 1.7, thus in both cases, reactive  $[\text{NH}_2]$  moieties are in excess. All reactive MA moieties may react to form PE micelles, and chains with corresponding dicarboxylic acids, which are thus unreactives, may segregate and form the larger MA-g-HDPE droplets.

Blend PA-31K/MAGPE 80/20 displays a particularity observed on the cryofractured surface (see figure4.39): the larger PE nodules remaining exhibit the typical morphology observed after cryofracture of nodules with no cohesion at the interface. Indeed, usually when copolymers are present at the interface, this lead to a fracture inside the nodules and not at the interfaces. In figure 4.39, we observe that

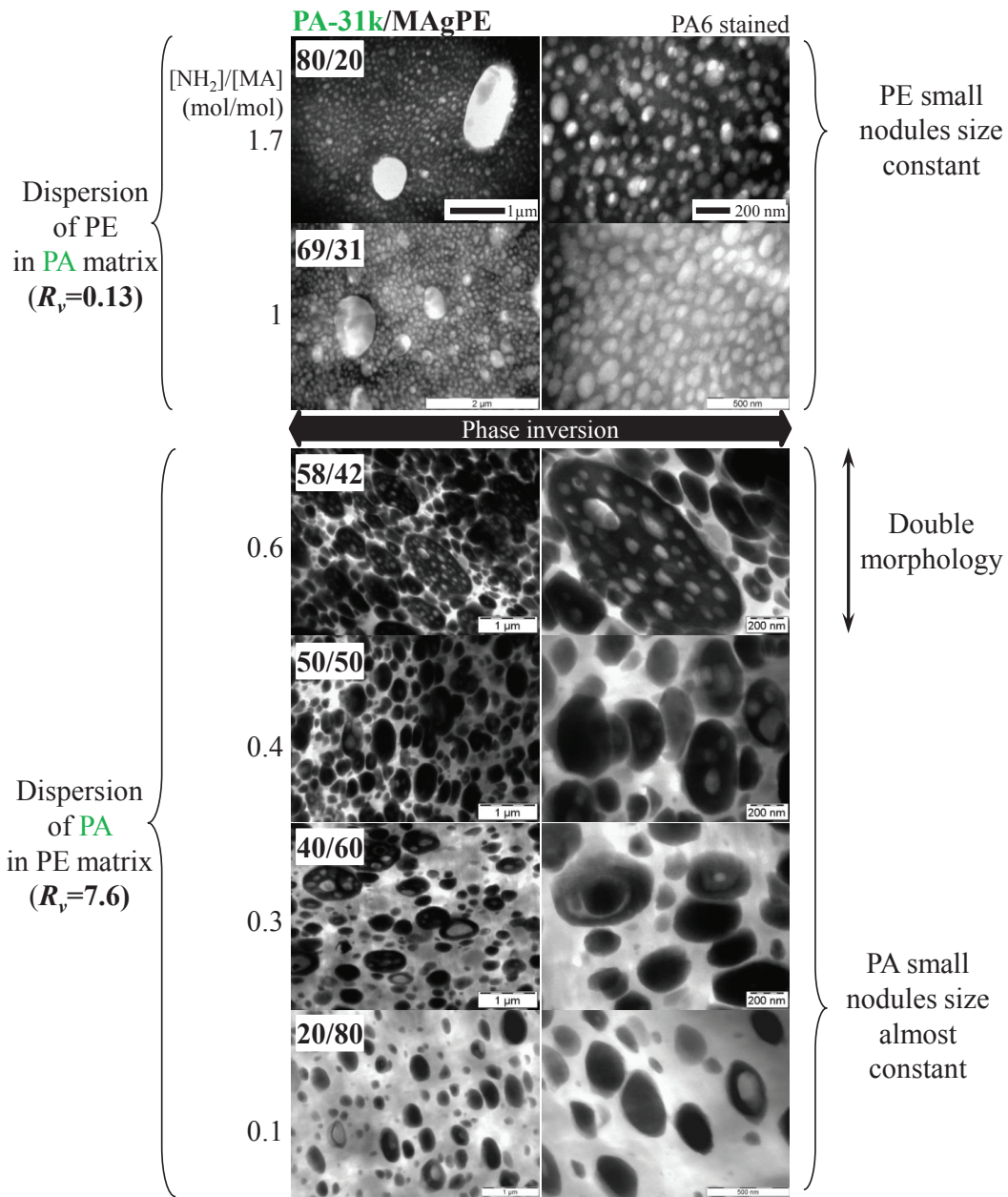


Figure 4.38: TEM micrographs of compatibilized binary PA6-31k/MA-g-HDPE blends after PA6 staining (dark domains). Two magnifications are presented. The name of each blend is reported on the corresponding micrographs and correspond to the volume fraction in the melt state of each phase. The molar ratio between amine end groups and maleic anhydride [NH<sub>2</sub>]/[MA] is also reported.

larger nodules have been either extracted with the upper part of the cryofracture or remained in the lower part, with their rounded shape of full nodule, which is characteristic of interface with low or no cohesion. This observation is consistent with TEM micrographs, where holes were observed at the interface between some nodules and the matrix. These holes are typically formed during sample preparation by cryo ultramicrotomy when there is no cohesion at the interface.

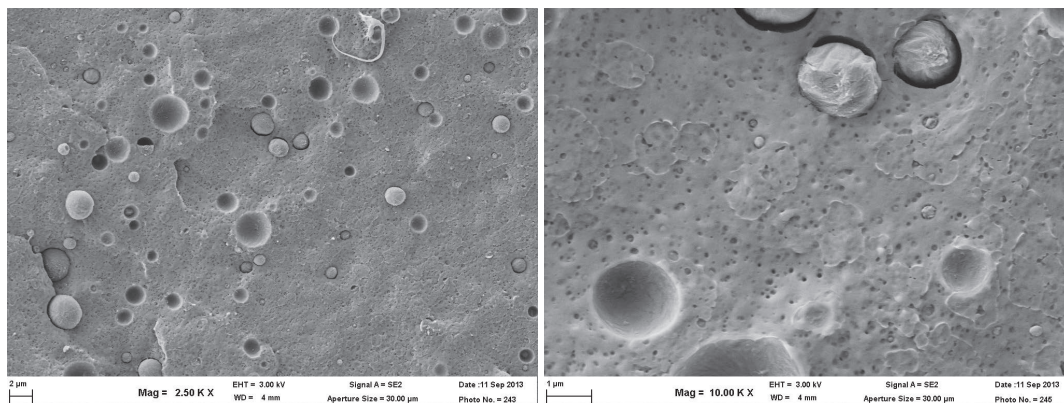


Figure 4.39: SEM micrographs of the cryofractured surface of blend PA-31k/MAGPE 80/20 at 2 different magnifications:  $\times 2500$  and  $\times 10000$ . Bigger nodules exhibit the typical morphology observed for nodules when there is no cohesion at the interface.

### Phase inversion

Phase inversion happened between blends PA-31k/MAGPE 70/30 and 58/42 thus 12%vol separate those two blend. No co-continuous morphology was observed.

### Dispersion of PA6-31k in MA-g-HDPE phase

Blends PA-31k/MAGPE 20/80 to 58/42 exhibit PA6-31k dispersions into a MA-g-HDPE matrix. The typical sizes of morphology obtained are rather polydisperse and vary from 80nm to 1 $\mu$ m. Even though it has not been quantified, microscopy observations indicates that the fraction of large nodules increases when the volume fraction of the dispersed phase increases. In less concentrated blends, PA-31k/MAGPE 20/80 and 40/60, droplets are not homogeneously dispersed in space, but rather organized as lines of nodules following one another. The distance between nodules along these lines can sometimes decrease down to 20nm as shown in figure 4.40 for blend PA-31k/MAGPE 40/60. This distance is sometimes even smaller than twice the gyration radius of the MA-g-HDPE chain ( $(R_{gPE} \approx 18\text{nm})$  [59]). In concentrated blends (PA-31k/MAGPE 50/50 and 58/42) dispersion of PA6-31k loses their nodular shape and are slightly deformed, as "squeezed" on each other like a foam. Distances between nodules are very thin of the order of 20nm.

The typical size of PA6-31k nodules in which no subdispersions are observed, are in average bigger than twice the gyration radius of chains of PA6-31k ( $(R_{gPA-31k} \approx 16\text{nm})$ ). This means that a lot of PA6 homopolymers are trapped into those nodules and have not reacted. However the theoretical molar ratio  $[\text{NH}_2]/[\text{AM}]$  shows that, in the four blends, Maleic anhydride are in excess and should theoretically promote a great  $\text{NH}_2$  conversion rate. Thus obviously, the reaction did not happen entirely.

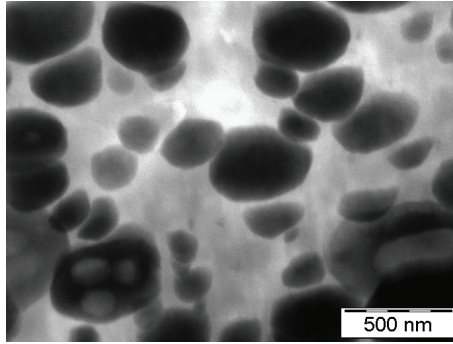


Figure 4.40: TEM micrographs of blend PA-31k/MAgPE 40/60 showing the "in line" organisation of PA6-31k nodules and the very thin distance between nodules. PA6 has been stained and appears in black (magnification:  $\times 43k$ ).

Another interesting observation is that, in the four blends, small subinclusions of PE of 20 to 200nm into some PA droplets are observed. These subinclusions are preferentially observed in larger PA droplets, but were also observed in droplet with a diameter  $< 200\text{nm}$ . The amount of subdispersions observed increases when the volume fraction of PA6-31k dispersed in PA increases. In blend 58/42, all PA droplets with a sizes larger than 300nm (i.e. from 300nm to  $1\mu\text{m}$ ) were filled with PE subdispersions. These PE nodules exhibit exactly the same morphology than small PE nodules (20 to 100nm) into PA observed in blends 80/20 and 69/31 in which PA is the matrix as shown in figure 4.41.

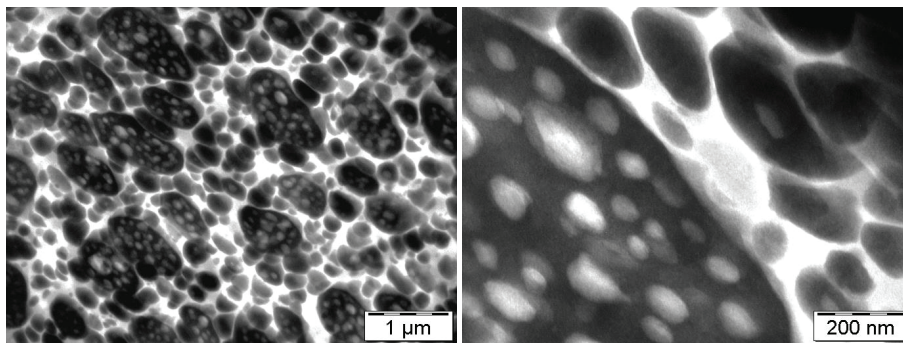


Figure 4.41: TEM micrographs of blend PA-31k/MAgPE 58/42 showing PE subdispersions into large PA nodules at 2 magnifications ( $\times 16k$  and  $\times 87k$ ). PA6 has been stained and appears in black.

#### 3.4.2 Comparison with uncompatibilized blends

##### Comparison of experimental results: PA6-31k/HDPE vs. PA6-31k/MA-g-HDPE

Figure 4.42 shows the comparison between uncompatibilized and compatibilized binary blends with PA6-31k. SEM micrographs of cryofractured surfaces or after minor phase etching are presented. For compatibilized blends, TEM was much more adapted to observe thin MA-g-HDPE nodular dispersions into the PA6-31k matrix. The comparison between compatibilized blends and the corresponding uncompatibilized blend leads to the following observations:

- When PE or MA-g-HDPE are dispersed into the PA6-31k:

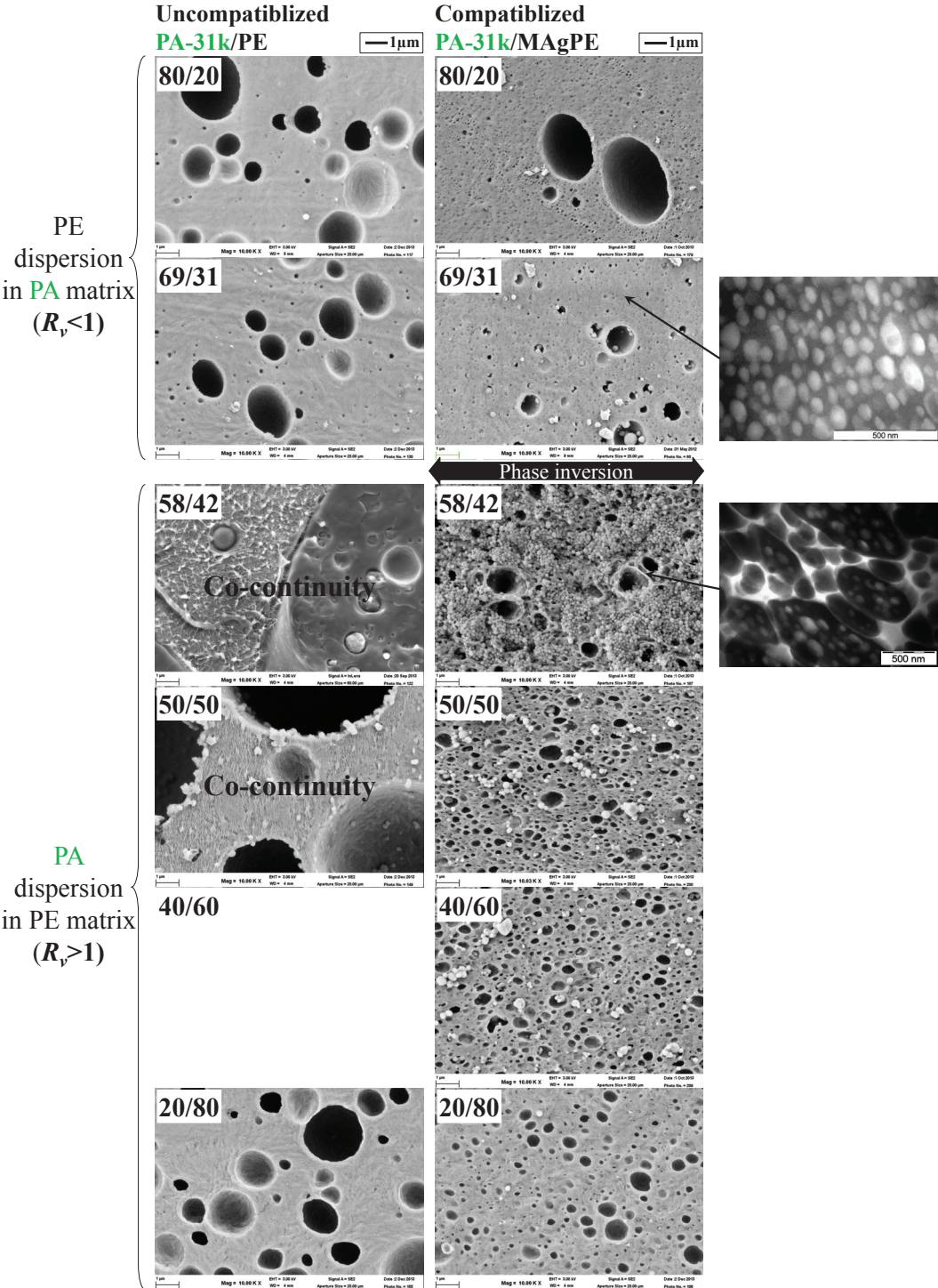


Figure 4.42: Comparison of uncompatibilized binary blends PA-31k/PE and compatibilized binary blends PA-31k/MAGPE. SEM micrograph (after minor phase etching or cryofracture).

- In uncompatibilized blends, we observed the concomitant presence of large (1 to 20  $\mu\text{m}$ ) and small ( $\sim 200\text{nm}$ ) HDPE nodules, like a "bimodal" distribution". In compatibilized blends, a very homogeneous nodular dispersion of small droplets of MA-g-HDPE (20 to 100nm) into the PA6-31k matrix is observed but also some larger droplet of pure MA-g-HDPE remain.
- Nevertheless, although it has not been quantified, the bimodal distribution is totally different between compatibilized and uncompatibilized because compatibilized blends are almost entirely composed of small nodules, which is not the case for uncompatibilized blends, where only few small nodules are observed.
- For both series, the phase inversion is observed at high PA6-31k volume fraction: between 58 and 69%vol.
- When PA6-31k is dispersed into HDPE or MA-g-HDPE phase:
  - Blends PA-31k/HDPE 50/50 and 58/42 were co-continuous in the uncompatibilized blends and they become a nodular dispersion on the compatibilized blend.
  - Global droplets sizes were reduced in compatibilized blends. The example of blends with 20%vol of PA indicates that a size reduction by a factor 5 to 10 is observed.
  - In uncompatibilized blends, sub-inclusion of PA6-31k (200nm to 2 $\mu\text{m}$ ) into HDPE large domains were observed especially in co-continuous blends. In compatibilized blends, small sub inclusions (20 to 200nm) are observed for compositions into PA6-31k droplets, and especially in larger PA droplets for compositions close to phase inversion. The subinclusion sizes and distribution are very similar to the sizes of small MA-g-HDPE nodules observed in blends 80/20 and 69/31 when small PE nodules are dispersed in PA6-31k matrix.

#### **Discussion on the comparison of mechanisms responsible for the morphology development**

The changes in morphology sizes attest that reaction happened and that the morphology development has been modified due to the creation of copolymers at the interface. Thus compared to what has been seen in compatibilized blends, the main conclusions that can be drawn from these observations are:

- The size reduction is consistent with the creation of copolymers at the interface and reduction in interfacial tension.
- When PE or MA-g-HDPE are dispersed into the PA6-31k:
  - In uncompatibilized blends, the bimodal morphology was attributed to the result of end-pinching break-up mechanism with formation of small satellites between droplets. In compatibilized blends, the amount of very thin MA-g-HDPE nodules (10 to 100nm) is much higher than in uncompatibilized blends. In the description of the results, we made the hypothesis that if those very thin nodules have indeed copolymers at the interface, the morphology observed is constituted of almost only pure copolymers. Sizes predictions in table 4.5 predict that, under shear or under elongational flow, the minimum sizes attainable are  $<10\text{nm}$  which is not theoretically possible given the radius of gyration

of both MA-g-HDPE and PA6-31k. But this small  $D_{min}$  is consistent with the small PE droplet sizes observed experimentally. However, after observation of cryofractured surface, we also observe in blends PA-31k/MAGPE 80/20 and 70/30, larger PE droplets (300nm to 2 $\mu$ m) which seem to exhibit no cohesion at the interface (i.e., as if no of few copolymers were created at the interface). Besides, their sizes are much larger than the theoretical minimum sizes attainable for compatibilized blends. They are indeed closer to the sizes observed for the corresponding uncompatibilized blend. By taking into consideration that probably a part of the HDPE chains of MA-g-HDPE are not reactive (see subsection 3.1), the large PE nodules observed may correspond to this fraction. It thus means that the mechanism of morphology development have depleted all the reactive chains contained into MA-g-HDPE to form graft copolymers contained in the population of small PE nodules. In the literature, Hu et al. [38] and Eggleton et al. [39] showed that when  $Rv < 1$ , the mechanism of "tip-streaming" occurred for droplets with surfactant and observed that nearly all of the copolymer was swept off with the small tip-streamed drops. *Tip-streaming could thus explain the morphology formed, but the very large amount and homogeneity in size and in space of the small MA-g-HDPE nodules need to be discussed in more details.*

- When PA6-31k is dispersed into PE or MA-g-HDPE phase:
  - The viscosity of the PE phase is 8 times higher than the viscosity of the PA phase but we have here the evidence that break-up happened because of elongational flow present in the process.
  - Coalescence of PA6 domains is inhibited due to the formation of copolymers at the interface. As a consequence, PA-31k/MAGPE 50/50 and 58/42 exhibit nodular dispersions of PA in PE whereas uncompatibilized blends exhibiting the corresponding composition were co-continuous.
  - The mechanism of Rayleigh capillary wave instability (slightly perturbed by the fact that  $R_v > 1$ ) was appropriate to describe the morphology development of uncompatibilize blends. However, *the presence of small PE subdispersions in almost all compatibilized blends exhibiting PA dispersion in MA-g-HDPE matrix, cannot be easily explained only by the usual mechanisms of drop break-up and coalescence.*

The study of the compatibilization reaction between PA6-31k and MA-g-HDPE in chapter 3 has shown that, at a flat interface in static conditions, after 10 minutes annealing at 290 °C, the interface was greatly destabilized: PA-31k samples show preferentially PE droplets (or isolated filaments) within the PA phase. This observation is consistent with the fact that, in compatibilized PA6-31k/MA-g-HDPE blends, a lot of small PE droplets are observed and are not easily explained by only usual drop-break-up mechanisms. This observation suggests that there may be a strong link between the observation made in static conditions and the morphology observed in compatibilized blends.

This point will be discussed in more details in subsection 3.5.

#### 3.5 Comparison with the static reaction

The comparison between the morphologies of uncompatibilized and compatibilized blends has shown that the global type of morphology (i.e. nodular dispersions, co-continuous...), and thus, the position of phase inversion, was the same. This suggests that mechanisms of drop break-up and coalescence due to rheological process control the micron-scale morphology in both uncompatibilized and compatibilized blends. However, in the three compatibilized blends studied, several observations like dispersions sizes or unexpected nanodispersions in one of the phase or in both phases could not be explained only by the classical mechanisms of drop break-up and coalescence. These observations appeared to be strongly related to the observations made in chapter 3 where the compatibilization reaction was studied in static conditions between thin films of PA6 and MA-g-HDPE.

In chapter 3, we have observed the nucleation and growth of ordered microphase separated copolymer domains at a flat interface. These morphologies were only due to the chemical compatibilization reaction in static conditions after annealing at 290 °C. We showed that the destabilization of the interface and the morphology growth depends on the relative length of the copolymer blocks. An initially flat interface becomes unstable when copolymers accumulated at the interface have decreased the interfacial tension to zero. This corresponds to the equilibrium state of the brush on both sides of the interface, when blocks stretching on each side balances the excess contact energy. Following the destabilization, morphologies can grow from the interface. For the three PA6 studied, main observations were:

- For the very asymmetric copolymer created by the graft copolymer between PA6-3k and MA-g-HDPE, the dense chain packing could not be attained leading to no destabilization of the interface (dense PE block packing is reached before PA blocks start to interact). We discussed the fact that only a very curved initial interface could lead to interfacial destabilization and spontaneous morphology creation.
- For PA6-18k and PA6-31k the destabilization and morphology growth at a plane interface was very effective. After annealing only 10 min, the interface was already greatly destabilized. The PA6-18k samples showed quite symmetrical patterns (lamellae essentially). In PA6-31k samples, the tendency was more to the growth of PE filaments (or sections of cylinders) within the PA phase. However, differences between morphologies formed from PA6-18k and PA6-31k were not very pronounced, essentially because chain length distributions of our various PA samples overlap quite largely. Since the morphology grew under thermodynamic equilibrium, the morphology observed reflect the relative symmetry of the copolymer created.

**How do interfacial instabilities and morphologies observed in static conditions behave under shear and be related to the morphologies obtained in blends?**

It is useful here to decompose the process of morphology growth in static conditions in two steps: (1) the destabilization of the interface and (2) the microstructure growth.

Let us first discuss the process of destabilization of the interface due to the creation of copolymers. Under shear, the coupling reaction is greatly accelerated. Indeed, Macosko et al. [81], indicate that the reaction rate between two polymer layers is up to 1000 times higher during heterogeneous blending in the melt state under shear than in static conditions. Thus, one can expect a significant increase of the conversion rate of the reactions within the experimental timescale used in this study. The accumulation of copolymers at the interface is very fast and if the copolymer architecture is not too unbalanced, the interfacial tension is rapidly decreased to zero. Interfacial fluctuations can be quickly initiated. The shear rate enhance the diffusion of new reactive moieties to the interface for the reaction to progress: Interfacial fluctuation can rapidly grow. Until this point of the process, we assume that shearing only accelerates the process compared to reaction in static conditions.

Let us now discuss the morphology growth after the very first interfacial fluctuations. Figure 4.43 shows a comparison between the morphology obtained after 10+15minutes annealing between films of PA6-18k and MA-g-HDPE and the morphology obtained for the reactively compatibilized PA-18k/MAGPE 47.5/52.5 blend. The comparison shows that there is no similitude between both micrographs: the lamellar structures obtained in static conditions are not observed in the compatibilized blend where nodular nanodispersions are rather observed. Thus even if the same precursors were used for both experiments, the shearing led to very different morphologies. In static conditions, the lamellar structure was already observed after only 10 minutes annealing which indicates that the first step of interface destabilization was very effective. The second step of the process is thus modified by the shearing.

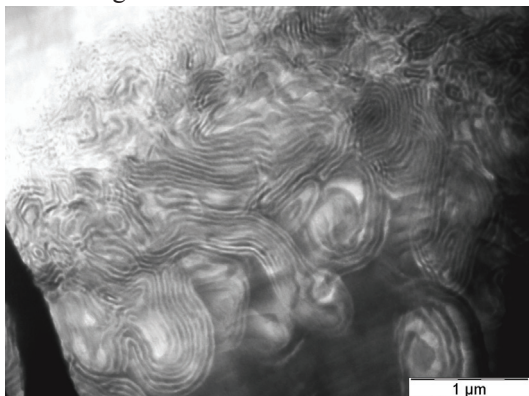
Indeed because, under shear, conditions are far from thermodynamic equilibrium, the equilibrium microstructures observed in static conditions cannot form and grow. The hydrodynamic convection flow imposed by the shearing on the fluctuated surface can break-off fluctuations from the interface. The surface of small nodules broken-off, called nanodispersions, is entirely covered by copolymers that were accumulating at the surface of the fluctuation. As a consequence, the concentration in copolymers of the remaining micronic interface (from which the nanodispersion have left), remains almost flat and covered by a low density of copolymers: nanodispersions break-off process have depleted all the copolymers that were present on this interface. As long as reactive moieties are available in the bulk, reaction progresses and nanodispersions break-off in a self-sustaining process. A schematic representation of the 2 steps process is schematized in figure 4.44: the first step being common to both static and shear conditions, and the second being dependent of the shearing. Of course, the first step should be greatly accelerated during reactive compatibilization under shear.

Two experimental results confirm some hypothesis mentioned above. First of all, the fact that nanodispersion break-off depletes the micronic surface in copolymers and that nanodispersions are created as long as reactive moieties are available in bulks was

### 3. Effect of the compatibilization: Results and discussions

---

Sandwich PA6-18k and MA-g-HDPE  
Annealing 10+15min



Blend PA-18k/MAGPE 47.5/52.5

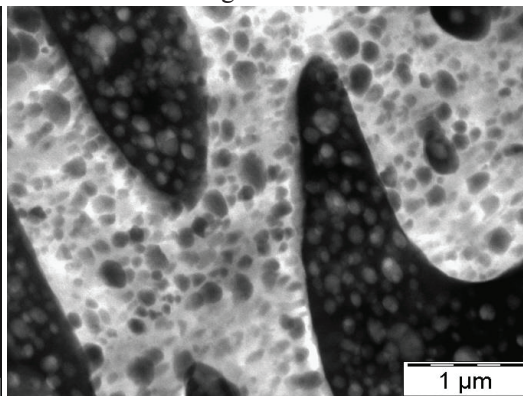


Figure 4.43: Comparison between the morphologies obtained after static annealing for 10+15min on sandwiches with PA-18k and reactively compatibilized PA-18k/MAGPE 47.5/52.5 blend. This comparison shows that the morphology obtained is very different even if the same reactive moieties and same component have been used. PA6 has been stained and appears in dark.

verified by simply annealing some blends pellets during two hours at 290 °C. This experiment allows to check if no more interfacial fluctuations can happen at the interface of nodules formed. Figure 4.45 shows the morphology after compounding and after two hours annealing at 290 °C of PA-18k/MAGPE 58/42 and 70/30 blends. Apart from an homogenisation of droplet shapes and distribution, no more interfacial fluctuations are observed meaning that there remained not enough reactive moieties in bulks to react. This observation confirms the fact that nanodispersions created by the mechanism of interfacial fluctuation totally deplete the micronic interface of bigger nodules.

The second one is that very first interfacial fluctuations seem to be observed in some regions of static interfaces annealed only 10 minutes. Even though the interfaces have already been destabilized over a large area, the fluctuations observed (surrounded by dotted lines) in figures 4.46 and 4.47, should be quite representative of the fluctuations that we describe before break-off under shear.

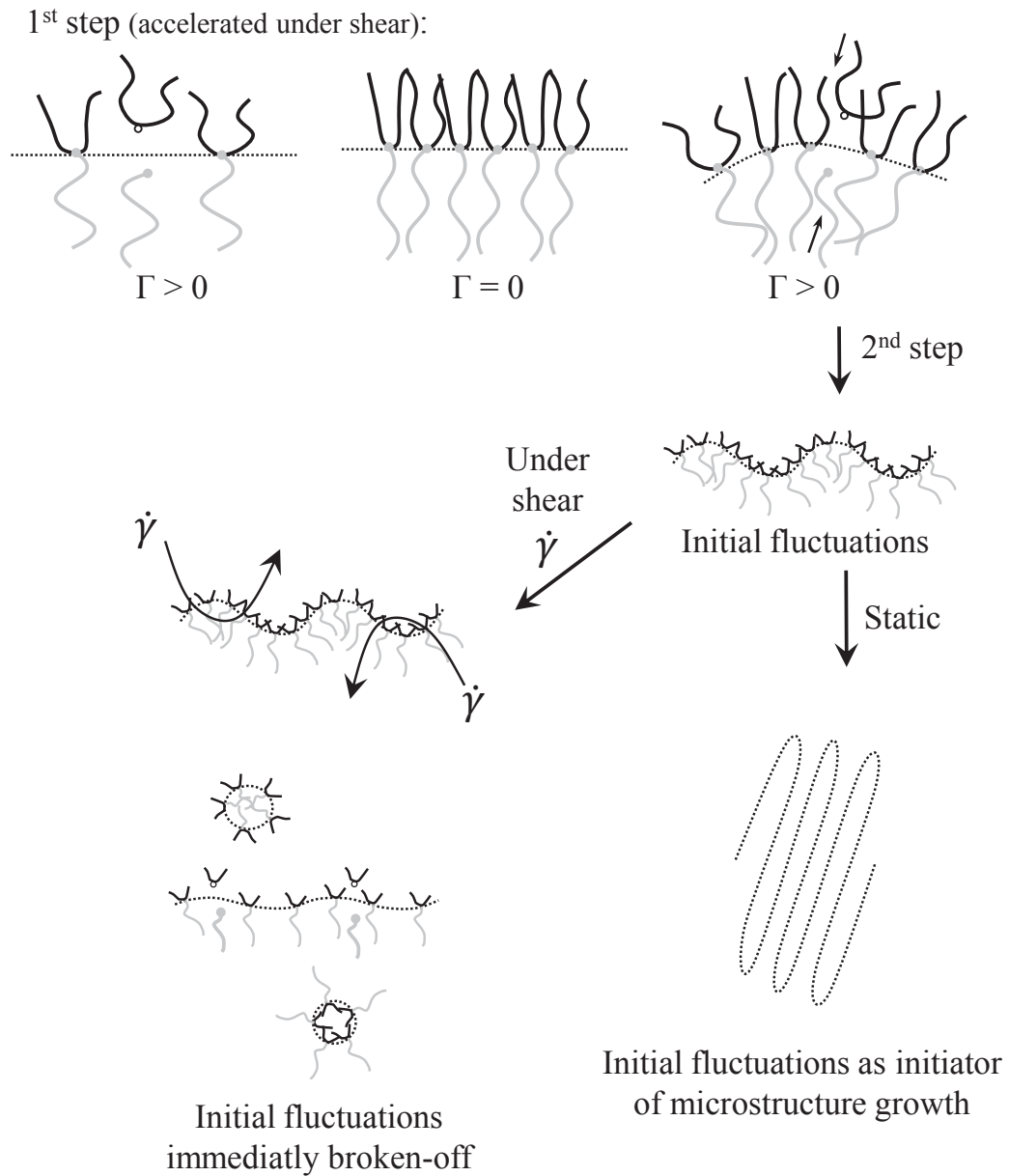


Figure 4.44: Schematic representation of the 2 steps process of first, destabilization and nanodispersions break-off under shear or second, destabilization and microstructure growth in static conditions.

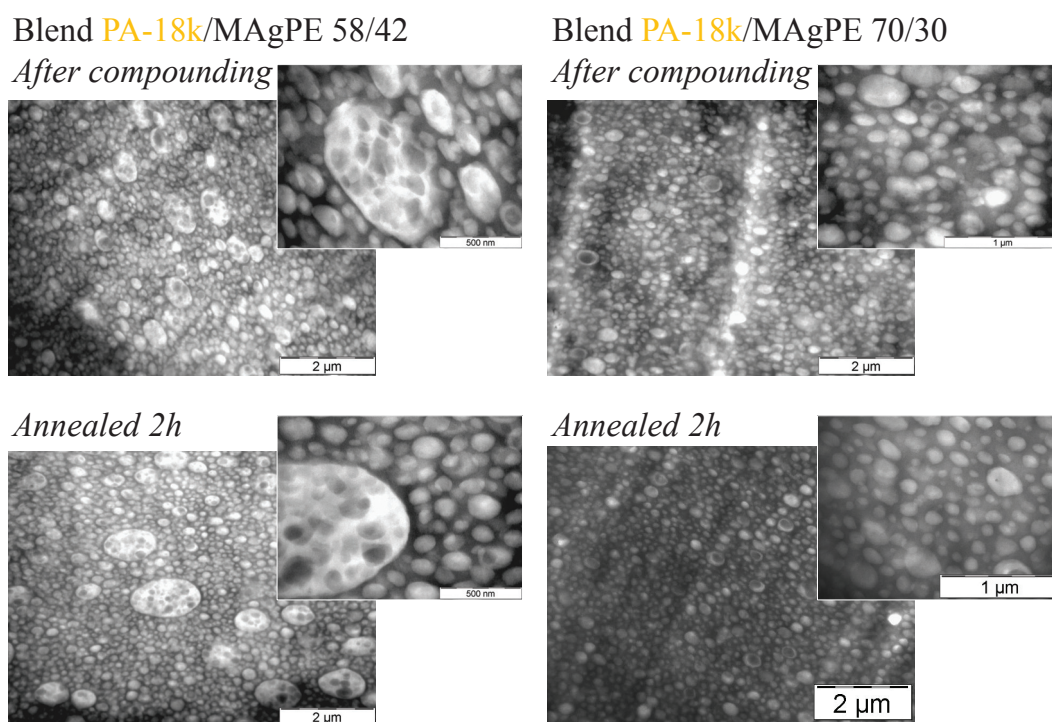
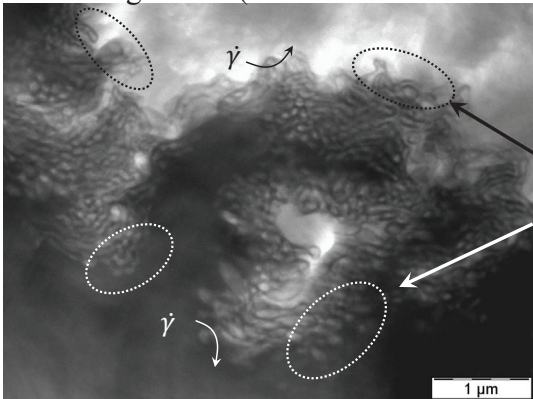


Figure 4.45: TEM micrographs of the blends PA-18k/MAgPE 58/42 and 70/30 after compounding and after 2 hours annealing. PA6 has been stained (black domains). Homogenisation of droplet shapes and distribution is observed but no more interfacial fluctuations or lamellar structure are created.

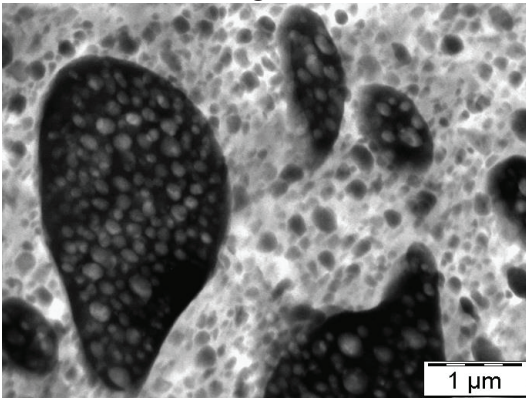
Sandwich **PA6-18k** and MA-g-HDPE

Annealing 10min (Zone where lamellar morphology did not grow)



Representative of the very first fluctuations leading to the break off of **PE or PA nanodispersions** with  $\gamma$  in binary blends

Blend **PA-18k**/MAGPE 47.5/52.5



Blend **PA-18k**/MAGPE 50/50

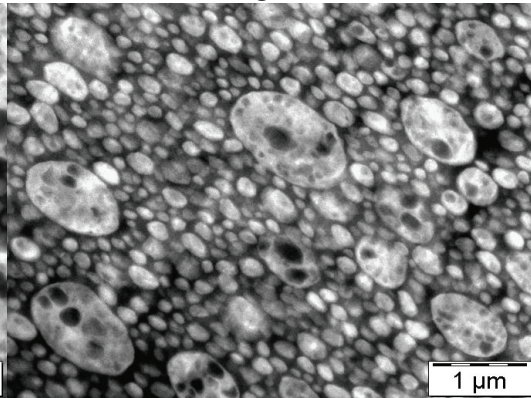
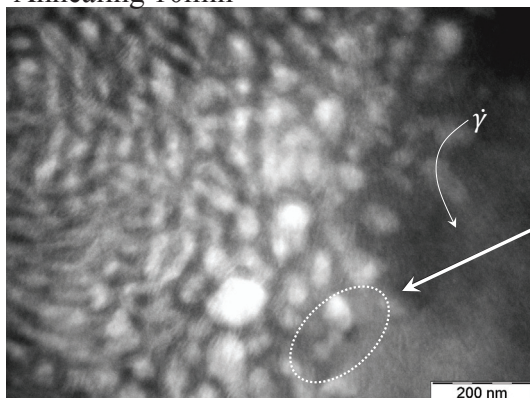


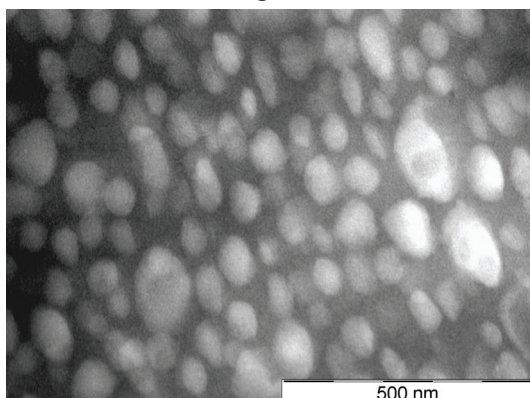
Figure 4.46: TEM micrographs of the interfacial microstructures obtained after 10 minutes static annealing between two films of PA6-18k and MA-g-HDPE. For the comparison, two micrographs of blends of PA-18k/MAGPE exhibiting nanodispersions are shown: sizes of fluctuations and nanodispersions are consistent. All micrographs are shown after PA6 etching at the same magnification:  $\times 16000$ .

Sandwich PA6-31k and MA-g-HDPE  
Annealing 10min



Representative of the very first fluctuations leading to the break off of **PE nanodispersions** with  $\dot{\gamma}$  in binary blends

Blend PA-31k/MAGPE 70/30



Blend PA-31k/MAGPE 58/42

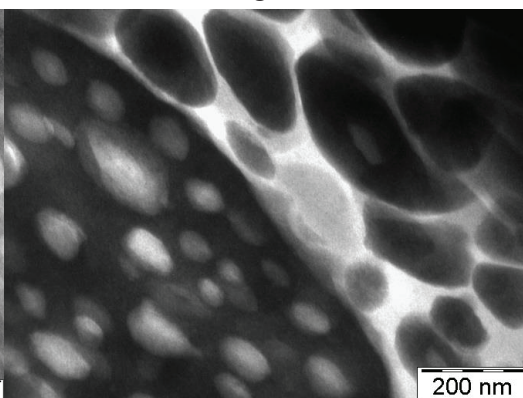


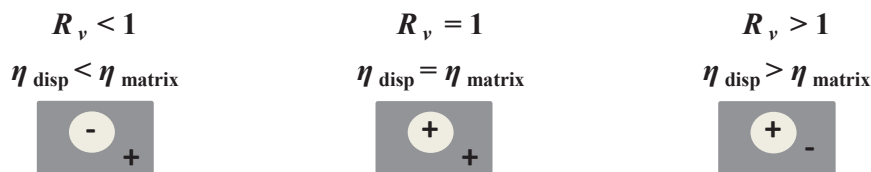
Figure 4.47: TEM micrographs of the interfacial microstructures obtained after 10 minutes static annealing between two films of PA6-31k and MA-g-HDPE. For the comparison, two micrographs of blends of PA-31k/MAGPE exhibiting nanodispersions are shown: sizes of fluctuations and nanodispersions are consistent. All micrographs are shown after PA6 etching at the same magnification: x87k.

**What are the levers that control nanodispersions formation?**

Thanks to observations of reactively compatibilized blends with PA6-3K, 18k and 31k in the whole composition range, we identified that two main levers control the nanodispersion formation and break-off:

- **The copolymer architecture:** Indeed, the copolymer architecture is crucial. First of all, the decrease in interfacial tension followed by the destabilization is mainly controlled by the asymmetry of the copolymer formed. If the copolymer is too asymmetric, the dense chain packing on both side of the interface could not be reached and the interfacial tension could not decrease to zero. Besides, if copolymers chains are too long, it is also possible that the energetic barrier created prevents other reactive species to reach the interface due to steric hindrance and thus do not allow the interfacial tension to decrease to zero. With components of this study, the last case has not been observed. Secondly, if destabilization happens, the architecture of the copolymers may favour the growth of the initial regular destabilization to a spontaneous curvature toward the side of the shorter bloc. This could be for example the case for an Y-shape copolymer with 1 arms of PA6-31k and 2 arms of HDPE: the HDPE branches being smaller than the PA6-31k branch, the curvature would be favoured toward the HDPE side.
- **The viscosity ratio:** Indeed, as in the case of usual drop break-up mechanism, we assume that nanodispersions would break-off on the side preferred by viscosity ratio. Indeed, theoretically the initial fluctuations are regular on both side of the interface, however if there is a difference of viscosity on both sides, the more viscous phase will apply a larger stress and thus favour the nanodispersions break-off in this phase. If the viscosity ratio is close to unity, then nanodispersions can break-off on both sides of the interface. It appears that the stress needed for nanodispersions break-off is probably much lower than the stress needed for nodule break-up, because nanodispersions can break-off inside a nodule were the stress transfer is lower.

Figure 4.48 summarizes the different cases encountered in our polymer blends and the possibility or not to create nanodispersions in the matrix phase, inside the dispersion or both. The more functional moieties present in the blend, the more phenomena are amplified. If only few reactive moieties are present, the phenomena should decrease and get closer to the behaviour of uncompatibilized blends.



**If destabilisation is possible:**

*Nanodispersions in the matrix phase?*

<b>Yes</b> , both for composition close or far from the phase inversion composition.	<b>Yes</b> , both for composition close or far from the phase inversion composition.	<b>No or few</b> , because the viscosity of the matrix is not favourable to break-off.
--	--	--

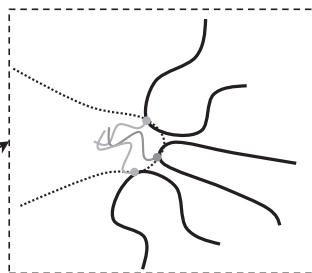
*Nanodispersions inside the droplet?*

<b>No or few</b> , because the viscosity inside the nodule is not favourable to break-off.	<b>Yes</b> , the creation is highly favoured close to phase inversion composition where larger interfaces of micronic domains are observed.	<b>Yes</b> , possible when the composition is far from phase inversion but the process is highly favoured close to phase inversion composition where larger interfaces of micronic domains are observed.
--	---	--

**If no destabilisation occurs:**

In any case, if the copolymer do not allow fluctuation, creation of nanodispersions by the mechanism of nanodisperion break-off is not possible.

△ This case favours the mechanism of **tip-streaming** which leads to dispersions of the same size as nanodispersions. Then at the tips the curvature is locally very high thus enables the destabilization of interface with very asymmetric copolymers (if the shorter branch is located inside the droplet).



△ When  $R_v > 1$ , small droplets (-) of the fluid matrix can be trapped into viscous droplets (+) when 2 viscous droplet coalesce. This creates a system such as:



Thus nanodispersion break-off of phase (-) into (+) is theoretically possible but will not undergo a high shear stress due to the fact that this droplet is inside another droplet.

Figure 4.48: Summary of the different cases encountered in polymer blends and the possibility or not to create nanodispersions.

### Nanodispersions break-off in reactively compatibilized PA6-3K/MA-g-HDPE, PA6-18K/MA-g-HDPE and PA6-31K/MA-g-HDPE blends

In blends with PA6-18k,  $R_v \simeq 1$  and the copolymer architecture allows a great destabilization of the interface. Thus nanodispersions are observed in both matrix and dispersed phase in the whole composition range. Nanodispersions are very numerous close to the phase inversion composition.

In blends with PA6-31k,  $R_v < 1$  when PE is dispersed in PA and  $R_v > 1$  when PA is dispersed in PE and the copolymer architecture allows a great destabilization of the interface. Besides, PA6-31k branches are longer than the HDPE backbone, thus a most stable curvature should correspond to a spontaneous curvature towards the HDPE side. Thus, when PE is dispersed in PA, both nanodispersions break-off and tip-streaming may happen simultaneously, both phenomena are favoured by copolymer architecture. This explains the very numerous and small sizes of PE droplets observed. When PA is dispersed in PE, nanodispersions are observed into the PA dispersed phase especially for compositions close to phase inversion compositions. This is because nanodispersions break-off is favoured into the dispersed phase but not in the matrix phase since neither the matrix viscosity nor the copolymer architecture are favourable. Besides, we saw in uncompatibilized blends that small PE nodules could be trapped into larger PA droplet due to the coalescence process of two PA6 droplets. These small nodules can also eventually fluctuate and form nanodispersions into the droplet.

Finally in blends with PA6-3k,  $R_v \gg 1$  when PE is dispersed in PA and  $R_v \ll 1$  when PA is dispersed in PE. Besides, the copolymer architecture is highly asymmetric and does not allow the decrease in interfacial tension to zero except for highly curved interface (curvature of the order of few gyration radius of PA6-3k chains). Thus, When PE is dispersed in PA, nanodispersion break-off is not possible. To explain the stripes of micelles observed in large PE droplets let us first analyse blends with a PA dispersion in PE. When PA is dispersed in PE, the mechanism of tip-streaming can happen. The very sharp tip of the nodule becomes thus favourable to the destabilisation of the interface and to the spontaneous formation of equilibrium microstructure which is, in the case of PA6-3k/MA-g-HDPE, micelles of PA in PE. Thus, tip streaming due to the viscosity ratio favours also the spontaneous generation of micelles of PA in PE. This indeed corresponds to the observations.

The stripes of micelles observed in the coarse PE nodules in blends PA-3k/MAGPE 50/50, 40/60 and 30/70 may come from the trapped polymer film which broke up during the coalescence of two big PE nodules. Even if the phase inside the nodule does not directly undergo the shearing, the large PE droplets rotates and thus moves the nodules that are trapped inside with its rotation. When the PA nodules moves, nanodispersions are broken off from the tips. A schematic representation of the process is proposed in figure 4.49

Nanodispersions break-off observed in the three series of reactively compatibilized blends are summarized in figure 4.50. A schematic representation of the mechanisms proposed are depicted with illustrations with TEM micrographs of different blends.

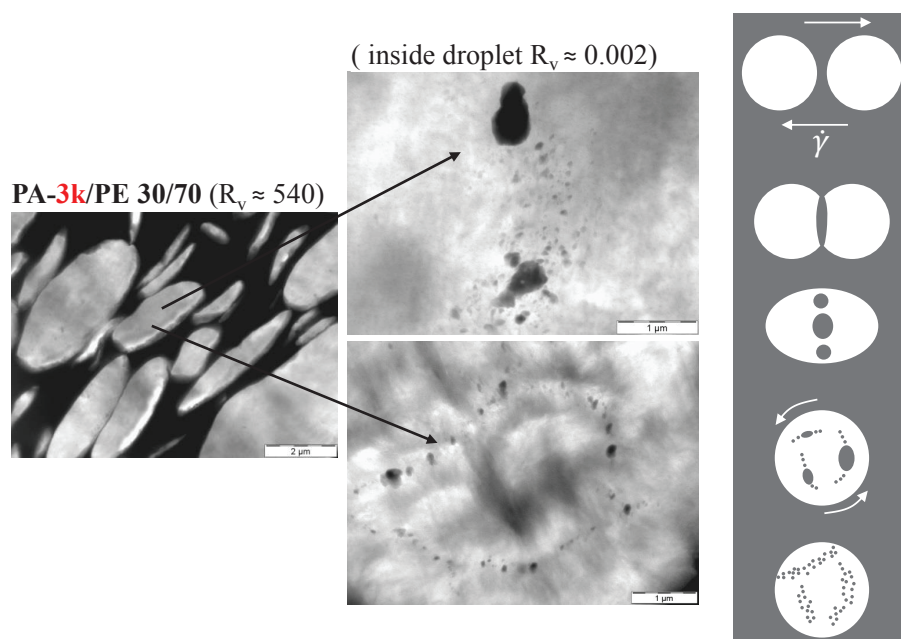
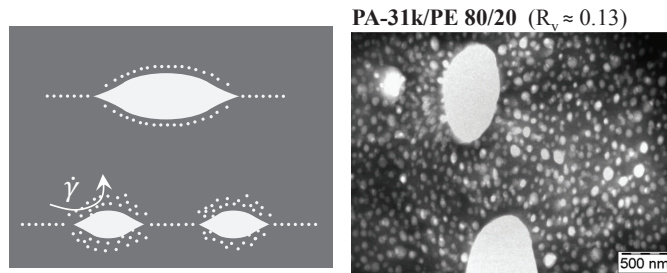


Figure 4.49: Schematic representation of the different steps from the coalescence of two PE droplets to the formation of PA micelles "stripes" in blends PA-3k/MAGPE 50/50, 40/60 and 30/70.

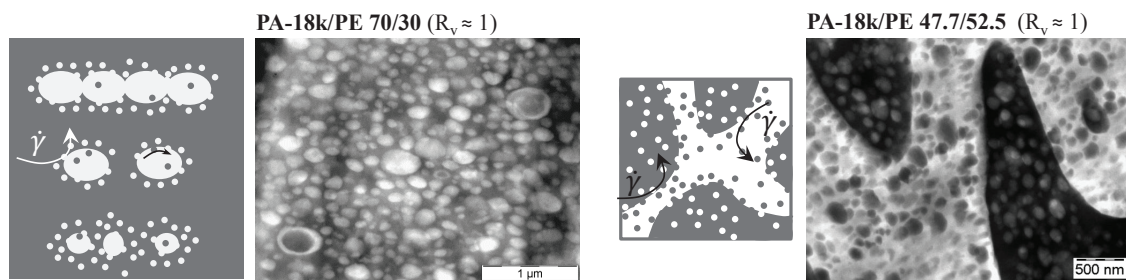
**a)  $R_v < 1$ : Blends PA6-31k/MA-g-HDPE**

Usual break-up mechanisms + Tip-streaming + nanodispersions break-off



**b)  $R_v \approx 1$ : Blends PA6-18k/MA-g-HDPE**

Usual break-up mechanisms + nanodispersions break-off .



**c)  $R_v \ll 1$ : Blends PA6-3k/MA-g-HDPE**

Usual break-up mechanisms + Tip-streaming

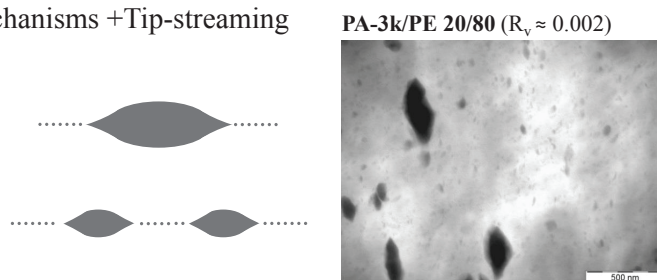


Figure 4.50: Schematic representation of cases where nanodispersions are observed depicted with illustrations with TEM micrographs of different blends.

## 4 General conclusion on morphology development in all the studied systems

### Uncompatibilized binary blends

Figure 4.51 summarizes morphologies obtained for uncompatibilized binary blends PA-31k/PE (left), PA-18k/PE (middle) and PA-3k/PE (right) after batch mini extrusion. A deep analysis of the morphology obtained has been performed and pertinent mechanisms of morphology development have been proposed. In the literature, only few systematic analysis of blends morphology on a large set of compositions are available. To the best of our knowledge, there is no experimental study dealing with the mechanisms of morphology development in polymer blends exhibiting viscosity ratios very far from one. Figure 4.52 summarizes the break-up mechanism proposed to be representative of the morphologies obtained for different viscosity ratios. Figure 4.53 summarizes the coalescence mechanism proposed that proceeds simultaneously to the break-up mechanism.

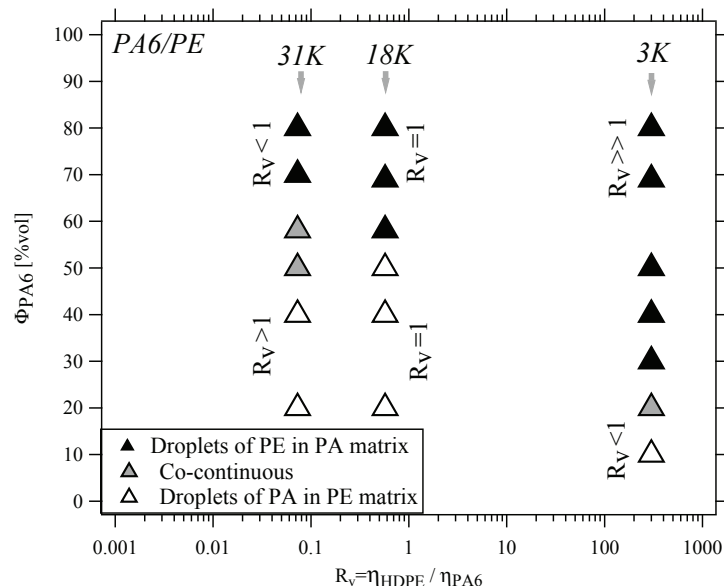


Figure 4.51: Summary of the morphologies observed for uncompatibilized binary blends PA-31k/PE (left), PA-18k/PE (middle) and PA-3k/PE (right) after batch mini extrusion. Blends are represented by triangles as a function of their composition in volume fraction (in the melt state) and viscosity ratio  $R = \eta_{HDPE} / \eta_{PA6}$  of pure components.  $R$  has been measured at 100 rad/s: black triangles are PE droplets in matrix PA, grey, co-continuous morphologies and white, PA droplets in PE matrix.

Main conclusions are:

- For a given couple of polymers (given interfacial tension  $\Gamma$ ), the main parameters that control the morphology development are: the viscosity ratio  $R_v$ , the composition  $\phi$  and the shear rate  $\dot{\gamma}$ .
- When the viscosity ratio changes the mechanism of morphology development also changes:
  - When  $R_v = 1$ , morphology develops by the capillary wave instability break-up

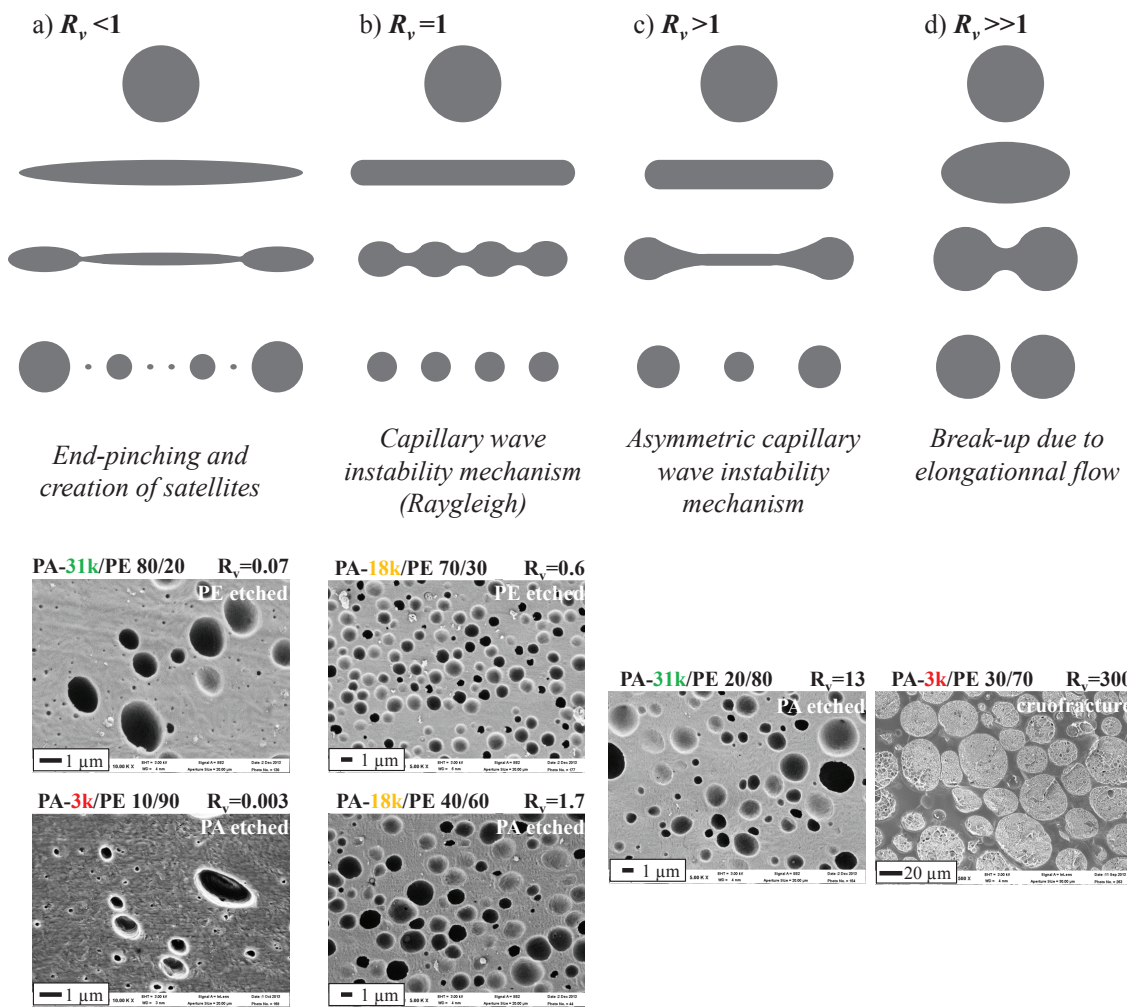


Figure 4.52: Schematic representation of the different droplet break-up mechanisms under shear proposed in uncompatibilized blends as a function of the viscosity ratio ( $R_v$ ) and illustration with SEM micrographs of binary uncompatibilized blends obtained after batch mini-extrusion. The scale of SEM micrographs after minor phase etching or cryofracture has been adapted to the sizes of morphologies.

mechanism (Rayleigh) and coalescence. This leads to homogeneous sizes of morphologies.

- When  $R_v < 1$ , morphology develops by the mechanism of end-pinching with formation of small satellites between droplets. The probability of coalescence favours coalescence of larger domains. This leads to morphologies very heterogeneous in sizes with very small droplets and larger droplets.
- When  $R_v > 1$ , morphology develops by Rayleigh capillary wave instabilities which leads to more homogeneous size distribution of droplets than the end-pinching mechanism. However, the capillary waves development can be delayed due to the fact that the filament is more viscous than the matrix, this leads to less homogeneous sizes than when  $R_v=1$ . When the viscosity ratio is too high, very large drops (few tens of microns) are observed.
- When  $R_v \gg 1$ , droplets break-up was observed even though, theoretically, un-

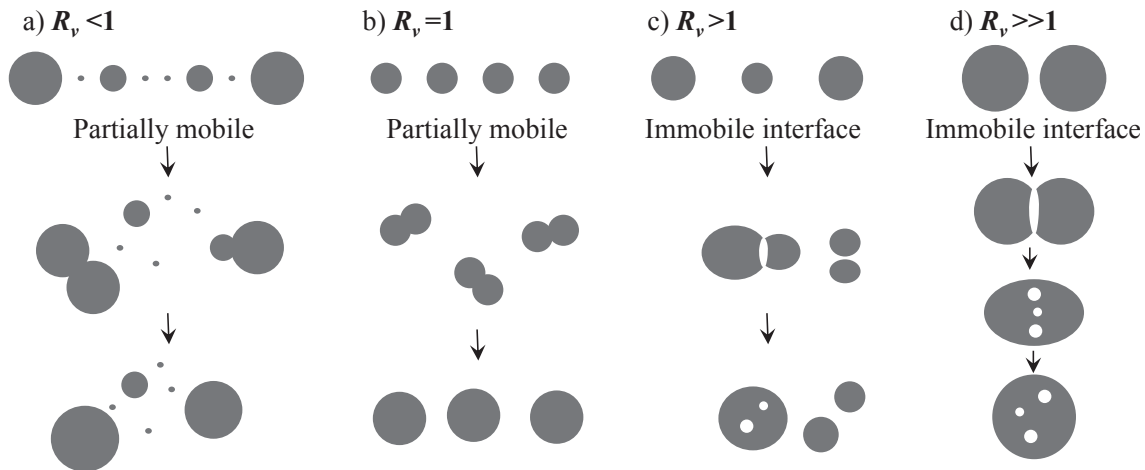


Figure 4.53: Schematic representation of the different coalescence mechanisms under shear proposed in uncompatibilized blends as a function of the viscosity ratio ( $R_v$ ).

der simple shear a viscous droplet cannot be deformed by a fluid droplet when the viscosity ratio is higher than 4. Our results show that zones of elongation are also present in the process. These zones could correspond to the passage through the die or high compression zones between screws. The viscoelastic nature of polymer may also allow break-up at higher viscosity ratios.

- When the matrix phase is more fluid than droplets ( $R_v > 1$ ) sub-dispersions into dispersions were observed: The drainage regime in that case is very unfavorable to coalescence, nevertheless when two droplets coalesce they can trap a film of the matrix in the new larger nodule formed. This film breaks into thinner droplets into the larger droplet.
- The phase inversion composition is observed at different composition for each series: when  $R_v = 1$  it is observed at 50/50 %vol but when  $R_v \neq 1$  it is shifted toward lower composition of the more fluid phase.
  - For PA6-18k/HDPE blends it is observed close to 50/50 %vol.
  - For PA6-3k/HDPE blends it has been shifted to smaller PA6 volume fraction: between 30 and 10%vol.
  - For PA6-31k/HDPE blends it has been shifted to smaller HDPE volume fraction: between 42 and 31%vol.
- The width of the co-continuity widows was larger for PA6-31k/HDPE blends series when  $R_v \neq 1$  than for the PA6-18k/HDPE series when  $R_v = 1$ . Thus when  $R_v$  deviates from one co-continuity windows seems to be larger. We did not deepen the interpretation of this observation since more blends would have been needed to conclude.
- In the case of  $R_v \gg 1$  the global viscosity is artificially increased by the presence of very viscous nodules into a fluid matrix, thus the break-up becomes more efficient when the volume fraction of the dispersed phase increases.

### Reactively compatibilized binary blends

Figure 4.54 summarizes the morphologies obtained for compatibilized binary blends PA-31k/MAGPE (left), PA-18k/MAGPE (middle) and PA-3k/MAGPE (right) after batch mini extrusion. We identified in this work that for compatibilized blends, the position of the phase inversion as well as the global type of morphology, was not changed in compatibilized blends compared to uncompatibilized blends (see figure 4.51). Thus, mechanisms of drop break-up and coalescence which were the only one mechanism in uncompatibilized blends are predominant in the determination of phase inversion composition.

Almost all morphology sizes were reduced (by at least a factor of  $\sim 10$ ) which is consistent with a decrease in interfacial tension due to the creation of copolymers. Coalescence was also greatly inhibited because droplet sizes remained almost unchanged when the concentration of dispersed phase increased. We also observed that when  $Rv < 1$ , tip-streaming could be a break-up mechanism to consider in the morphology development.

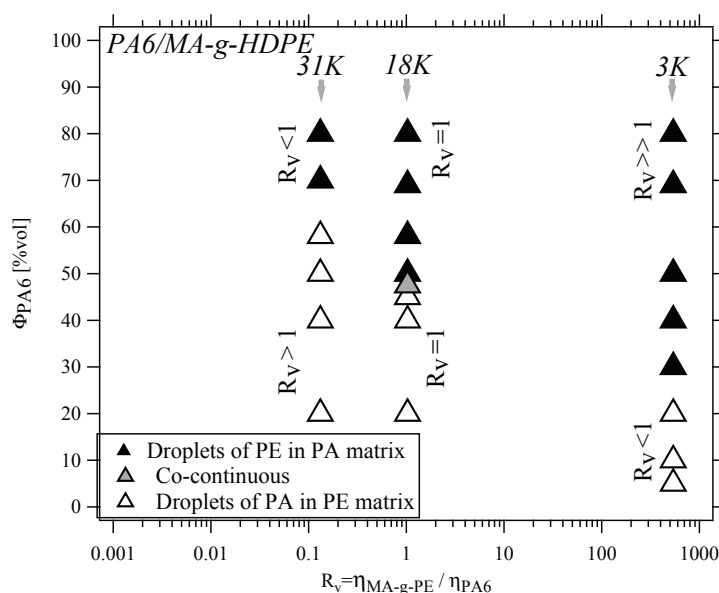


Figure 4.54: Summary of the morphologies obtained for compatibilized binary blends PA-31k/MAGPE (left), PA-18k/MAGPE (middle) and PA-3k/MAGPE (right) after batch mini extrusion. Blends are represented by triangles as a function of their composition in volume fraction (in the melt state) and viscosity ratio  $R = \eta_{MA-g-HDPE} / \eta_{PA6}$  of pure components.  $R$  has been measured at 100 rad/s: black triangles are PE droplets in matrix PA, grey, co-continuous morphologies and white, PA droplets in PE matrix.

However, we showed in this study that another mechanism can happen simultaneously: if the architecture of copolymers created at the interface allows to form a dense chains packing, blocks are stretched on both sides and contribute to the interfacial tension decrease down to zero. This leads to the destabilization of the interface and fluctuations are formed; new interfacial area is created and new reactive moieties can reach the interface for the reaction to progress. The conditions for interfacial fluctuations were studied in chapter 3. Under shear this process is followed by nanodispersions break-off from the interface. The nanodispersions departure is mainly governed by two factors: first, nan-

#### 4. General conclusion on morphology development in all the studied systems

---

odispersions could be broken-off in the phase preferred by the shear rate, i.e. the more viscous phase, and secondly, the copolymer architecture may favour a curvature toward one or the other side. A schematic representation of the nanodispersions break-off was proposed in figure 4.44.

Thus in compatibilized blends, the morphology development which combines both break-up and coalescence and nanodispersions break-off in some cases, led to the following morphologies in the three blend series:

- For blend with PA6-31k,  $\eta_{PA6-31k} > \eta_{MA-g-HDPE}$ , in static conditions the interface was destabilized and the architecture favours a curvature toward the PE side. Nanodispersions of PE in PA matrix were indeed observed at all compositions.
- For blends with PA-18k  $\eta_{PA6-18k} \simeq \eta_{MA-g-HDPE}$ , in static conditions the interface was destabilized but the architecture do not have a preferred curvature (roughly symmetric case). Nanodispersions of both PA in PE and PE in PA were observed at all compositions.
- For blend with PA6-3k,  $\eta_{PA6-3k} \ll \eta_{MA-g-HDPE}$ , in static conditions the interface was not destabilized and the architecture favours a very strong curvature toward the PA side. No nanodispersions of PE in PA were observed. However, very small micelles of PA in PE were observed due to the very curved interface at the ends of sharp tips formed by the mechanism of tip-streaming.

Thus, in compatibilized blends, two mechanisms proceed simultaneously: usual break-up and coalescence mechanisms and nanodispersions break off from interfacial fluctuations. Thus, to control the morphology development in reactively compatibilized blends, one need to know several parameters:

- The viscosity ratio at process temperature and shear rate representative of process conditions.
- The reactivity of functional moieties.
- The molecular parameters of both reactive chains: number average molecular weight  $M_n$ , location and amount of reactive moieties on the chain (end-groups or graft) in order to determine the copolymer architecture.
- The blend composition.
- The shear rate or possibly elongational flow present in the process.

With these informations it is possible to get quite good predictions on the final morphology. Indeed, the viscosity ratio and the blend compositions could allow to know the global kind of morphology. For that, we propose in chapter 5 a model of prediction of phase inversion composition which has demonstrated its efficiency for uncompatibilized and compatibilized blends with a viscosity ratio very far from one. And knowing the copolymer architecture allows to estimate if the interface can be destabilized or not to create fluctuations. If the interface is destabilized, then the knowledge of the viscosity ratio and the architecture are helpful to determine in which phase nanodispersions can be broken-off.



# RHEOLOGICAL BEHAVIOUR IN THE LINEAR REGIME

---

# 5

First of all, generalities on the rheological behaviour of viscoelastic pure polymers and current knowledge on compatibilized blends with copolymers at the interface are reminded. A literature review summarizes the most pertinent models that exist to describe the rheological behaviour dependence on concentration and frequency of polymer blends.

We then analyse the linear rheological behaviour of uncompatibilized and compatibilized blends. The dependence of blend viscoelastic responses on the frequency and on the composition is studied in relation to the observed morphologies (described in the previous chapter).

In the last section, a simple and original rheological model is used to predict the phase inversion composition for both uncompatibilized and compatibilized blends.

## 1 Models for the rheology of non miscible blends

### 1.1 Linear rheological behaviour of a pure polymer

For a material with a relaxation time  $\tau$ , the mechanical response to an imposed stress  $\sigma$  is described by the constitutive equation:

$$\sigma(t) = \int_{-\infty}^t \dot{\gamma}(t')G(t-t')dt' \quad (5.1)$$

With  $G(t) = G_0 \exp(-t/\tau)$  is the time-dependent modulus, which gives the response at time  $t>0$  to an excitation at time  $t=0$ .

For a dynamical (sinusoidal) strain-controlled sollicitation of the form

$$\gamma(\omega) = \gamma_0 \sin \omega t \quad (5.2)$$

in the steady state, the sinusoidal stress response is of the form

$$\sigma(\omega) = G'(\omega)\gamma_0 \sin \omega t + G''(\omega)\gamma_0 \cos \omega t \quad (5.3)$$

$G'(\omega)$  is the dynamic storage modulus (response in phase with the excitation): elastic response.  $G''(\omega)$  is the dynamic loss modulus: dissipated energy per cycle.

Combining equations 5.1, 5.2 and 5.3 it is found:

$$G'(\omega) = \frac{G_0\omega^2\tau^2}{1 + \omega^2\tau^2} \quad G''(\omega) = \frac{G_0\omega\tau}{1 + \omega^2\tau^2} \quad (5.4)$$

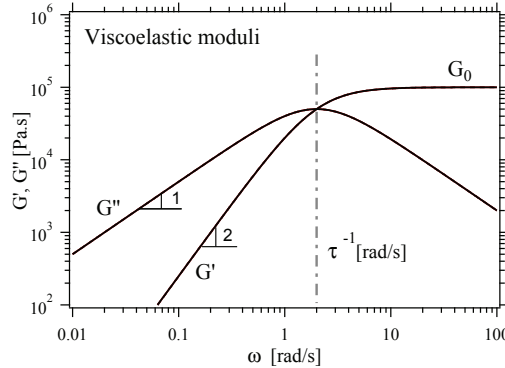


Figure 5.1: Example of the dynamic behaviour of a model viscoelastic liquid with  $\tau$  and  $G_0$  the relaxation time and modulus associated.

Thus, in dynamic rheometry, a relaxation process in a material is characterized by:

- A modulus  $G_0$  at high frequency: expresses the elastic response of the material at short time, before relaxation occurs.
- a **terminal regime at low frequencies (long times), after the material has relaxed, characterized by  $G' \propto \omega^2$  and  $G'' \propto \omega$ .**

The dynamic viscosity  $\eta^*$  is directly dependent on  $G'(\omega)$  and  $G''(\omega)$ :

$$|\eta^*| = \frac{|G^*|}{\omega} = \frac{\sqrt{G'^2 + G''^2}}{\omega} \quad (5.5)$$

### 1.2 Gel-like behaviour

The "gel" states covers a wide range of material. A gel is a material with a long range connectivity into the material provides a temporary elastic response related to a power law distribution of relaxation modes over a wide range of time scales [143, 144]. Two main categories of gels are found: "chemical" gels in which connectivity can be due for example to irreversible covalent crosslinks; "Physical gels" in which the reversible network is due to entanglements, hydrogen or ionic bonds, small crystalline domains...

For both chemical and physical gels, the linear viscoelastic behaviour has been extensively studied. Winter and Chambon [143] showed that the dynamic storage and loss moduli follow a simple power law at the critical-gel point, i.e, at the point where the material start to form a gel:

$$G'(\omega) \propto G''(\omega) \propto \omega^n \quad (5.6)$$

The exponent  $n$  may vary between  $\approx 0$  and 1 depending on the degree of connectivity in the system [145]. The higher the number of contacts (which can be crosslinks or other) the smaller the value of the exponent  $n$ .

Equation 5.6 reflects a power law distribution of relaxation times. At the gel point, the loss tangent ( $\tan\delta = G'(\omega)/G''(\omega)$ ) is independent of the frequency.

### 1.3 Dependence of the rheological behavior of polymer blends on the frequency

The rheological behaviour of polymer blends under shear has been quite extensively studied over the past decades [146, 145, 147]. First, ideal cases, such as emulsions of Newtonian liquid components have been widely studied. The case of polymer blends is more complex due to the viscoelastic behavior of polymers. In dynamic rheometry, a viscoelastic polymer exhibits the typical behaviour where the storage modulus  $G'$  and the loss modulus  $G''$  exhibit, in the terminal regime,  $G' \propto \omega^2$  and  $G'' \propto \omega$  ( $\omega$  being the frequency). The rheological behaviour of a blend of two non miscible viscoelastic polymers is generally characterized by additional relaxation processes as compared to the pure components. These additional relaxations process are the following ones:

- **For both uncompatibilized and compatibilized blends, relaxation processes due to shape relaxations of dispersed droplets under shear are observed.** Indeed, deforming a spherical droplet (at constant volume) increases the interface area, thus increases the energy contained in the material due to the surface tension (see figure 5.2).
  - At high frequency: droplets do not have time to relax and their deformation follows the imposed macroscopic strain. The blend elastic response do not undergo any modification due to the presence of interfaces.
  - At low frequency: droplets have time to relax back to spherical shape within each excitation cycle. This induces a shoulder on the elastic response. The elastic response increases to higher values, corresponding to a dissipated energy per cycle. This relaxation is associated to a modulus  $G$  and a relaxation time  $\lambda$ . Values of  $G$  and  $\lambda$  are discussed in next subsection.

Qualitatively, the modulus for a dispersion of droplets looks like (fig.5.3):



Figure 5.2: Droplet deformation under shear and relaxation.

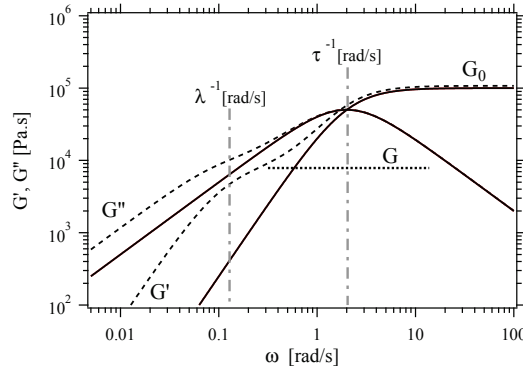


Figure 5.3: Example of the shoulder induced on  $G'$  and  $G''$  in a blend (dotted lines) due to droplet shape relaxation compared to the behaviour of the pure components (solid lines).  $\tau$  is the relaxation of the matrix phase,  $\lambda$  the relaxation time and  $G$  the modulus associated to the droplet shape relaxation.

- For compatibilized blends with copolymers at the interface, an extra **relaxation associated to the interfacial elasticity due to the presence of copolymers** at the interface. For an interface between two immiscible fluids (polymers), the surface tension  $\Gamma$  gives the energy per unit area of interface. Increasing the surface area as shown in figure 5.4 gives an excess energy  $dE = \Gamma dS$ .

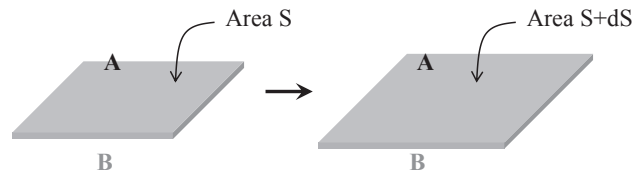


Figure 5.4: Shearing of a copolymer brush at the interface between polymers A and B.

For an interface containing a fixed number of block copolymers, changing the surface area changes the state of the copolymer brush. If the copolymer brush is at its equilibrium configuration, changing the surface area changes the density (coverage) of the brush, which brings it out of equilibrium and thus increases the energy. This is the analogue in 2D of the bulk (compressibility) modulus of a liquid. We shall denote its *interfacial dilatation modulus*. Also block copolymers within the interface may be entangled with polymers from the bulk or with each other, this may result in a *shear modulus of the interface*.

Jacobs et al. [148] and Van Puyvelde et al. [16] papers reference several studies dealing with (1) experimental work regarding the influence of interfacial agents on the rheological behavior of polymer blends and (2) theoretical models developed to describe the rheological properties of compatibilized blends.

#### 1.4 Modeling the contribution of the elastic response of the interfaces: Palierne's model

A model for the linear rheological behaviour of dispersions of droplets in a matrix for viscoelastic fluids has been proposed by Palierne [147][115] and further developed by other authors [148]. Palierne (1990) considers in his model the linear viscoelastic behaviour of "emulsions" of incompressible viscoelastic materials in the presence of an interfacial agent. His model accounts for the three relaxation processes described above (droplets shape relaxation and interfacial shear and dilatation moduli). He has established a linear viscoelastic constitutive equation for the emulsion as a function of the linear viscoelastic behavior of each component: complex shear modulus of the matrix phase  $G_m^*$  and dispersions  $G_d^*$ , the volume fraction and size distribution of the dispersed droplets ( $\phi_i$  and  $R_i$ ) and the interfacial tension ( $\Gamma$ ). In this model, the complex modulus of the emulsion is given by the general equation[147]:

$$G^*(\omega) = G_m^*(\omega) \frac{1 + 3 \sum_i \phi_i \frac{E_i(\omega)}{D_i(\omega)}}{1 - 2 \sum_i \phi_i \frac{E_i(\omega)}{D_i(\omega)}} \quad (5.7)$$

With:

$$\begin{aligned} E_j(\omega) = & [G_d^*(\omega) - G_m^*(\omega)][19G_d^*(\omega) + 16G_m^*(\omega)] + \\ & 4 \frac{\Gamma}{R_i} [5G_d^*(\omega) + 2G_m^*(\omega)] + \frac{\beta'(\omega)}{R_i} [23G_d^*(\omega) - 16G_m^*(\omega)] + \\ & 2 \frac{\beta''(\omega)}{R_i} [13G_d^*(\omega) + 8G_m^*(\omega)] + 24\beta'(\omega) \frac{\Gamma}{R_i^2} + 16\beta''(\omega) \frac{\Gamma + \beta'(\omega)}{R_i^2} \end{aligned} \quad (5.8)$$

and

$$\begin{aligned} D_j(\omega) = & [2G_d^*(\omega) + 3G_m^*(\omega)][19G_d^*(\omega) + 16G_m^*(\omega)] + \\ & 40 \frac{\Gamma}{R_i} [5G_d^*(\omega) + 2G_m^*(\omega)] + 2 \frac{\beta'(\omega)}{R_i} [23G_d^*(\omega) + 32G_m^*(\omega)] + \\ & 4 \frac{\beta''(\omega)}{R_i} [13G_d^*(\omega) + 12G_m^*(\omega)] + 48\beta'(\omega) \frac{\Gamma}{R_i^2} + 32\beta''(\omega) \frac{\Gamma + \beta'(\omega)}{R_i^2} \end{aligned} \quad (5.9)$$

Where,  $G_d^*(\omega)$ ,  $G_m^*(\omega)$   $G^*(\omega)$  are respectively the complex moduli of the dispersed phase, matrix, and blend at frequency  $\omega$ .  $\beta'(\omega)$  is the complex interfacial dilatation modulus and  $\beta''(\omega)$  the complex interfacial shear modulus. Graebbling et al. [115] have shown that for low droplet polydispersity (Ratio of the volume averaged over the number averaged radii  $Rv/Rn < 2$ ), the volume averaged radius  $R$  and the total volume fraction of the dispersed phase could be used quite safely, instead of the summation of droplets radii  $R_i$  and volume fraction  $\phi_i$ . Nevertheless, we have to keep in mind that this assumption has to be used carefully since both uncompatibilized and compatibilized blends can have very polydisperse morphologies.

##### Simplified Palierne's model: Droplet shape relaxation

If we consider a system with no interfacial elasticity due to the presence of copolymers at the interface, i.e. uncompatibilized blends, then we may assume that  $\beta'(\omega) = \beta''(\omega) =$

0. Thus, only the droplets shape relaxation which corresponds to the time required for a droplet to recover its spherical shape after being deformed, is observed. In this case, the complex shear modulus expression for the emulsion 5.7 simplifies to:

$$G^*(\omega) = G_m^*(\omega) \frac{1 + 3 \sum_i \phi_i H_i(\omega)}{1 - 2 \sum_i \phi_i H_i(\omega)} \quad (5.10a)$$

$$H_i(\omega) = \frac{\frac{4\Gamma}{R_i}(2G_m^* + 5G_d^*) + (G_d^* - G_m^*)(16G_m^* + 19G_d^*)}{\frac{40\Gamma}{R_i}(G_m^* + G_d^*) + (2G_d^* + 3G_m^*)(16G_m^* + 19G_d^*)} \quad (5.10b)$$

In this form, Palierne's model predicts the relaxation time associated with droplet shape relaxation as shown by equation 5.11, which induces a shoulder in the linear dynamic moduli as shown in figure 5.5. The relaxation time  $\lambda_s$  associated with this shape relaxation is approximately:

$$\lambda_s = \frac{R_i \eta_m (19R_v + 16)(2R_v + 3 - 2\phi(R_v - 1))}{4\Gamma (10(R_v + 1) - 2\phi(5R_v + 2))} \quad (5.11)$$

The value of the plateau  $G_s$  associated with this shape relaxation is approximately:

$$G_s = 20 \frac{\Gamma}{R_i} \phi \frac{1}{(2R_v + 3 - 2\phi(R_v - 1))^2} \quad (5.12)$$

For example, for an uncompatibilized polymer blends with a surface tension  $\Gamma = 2 \cdot 10^{-2} \text{N/m}$ , a volume fraction of the dispersed phase  $\phi_d = 0.3$  an average drop radius  $R = 1 \mu\text{m}$  and blend components exhibiting the same viscoelastic behaviour ( $\eta_0 = 100 \text{Pa.s}$ ), the droplet shape relaxation  $\lambda_s \approx 0.01 \text{s}$  thus  $\approx 72 \text{ rad/s}$  and the plateau modulus  $G_s \approx 4800 \text{Pa.s}$ . Figure 5.5 shows results of the simplified Palierne's model for this example. The droplets shape relaxation induces a shoulder on both  $G'$  and  $G''$  but much less pronounced on  $G''$ . Thus, viscosity also increases at low frequencies (see eq. 5.5) as shown on figure 5.5 (b) and becomes also dependent on the composition  $\phi_d$ , droplet sizes  $R$  and interfacial tension  $\Gamma$ .

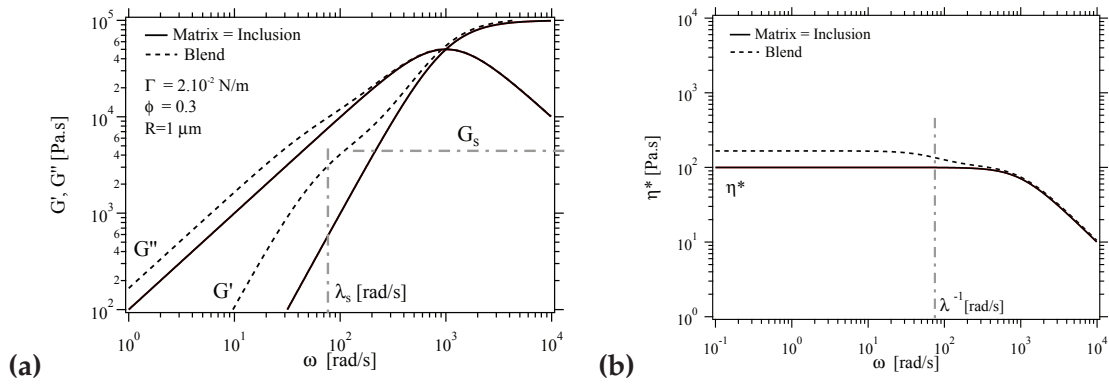


Figure 5.5: Example of the Palierne model applied to a theoretical uncompatibilized blend (i.e.  $\beta'(\omega) = \beta''(\omega) = 0$ ) with  $\eta_m = \eta_d = 100 \text{ Pa}\cdot\text{s}$  to show the impact of blending on the rheological behavior, especially the shoulder on the storage modulus  $G'(\omega)$ . Chosen parameters are reported in the graph.

By changing the parameters of the Palierne's model, the value of the slope of the elastic modulus  $G'$  is not modified, only  $\lambda_s$  or  $G_s$  values can change. At low frequencies,  $G'$  and  $G''$  recover the slope of respectively -2 and -1. This model has been successfully applied to describe the rheological behavior of uncompatibilized polymer blends [115].

### Complete Palierne's model: Droplet shape relaxation and relaxations associated to the copolymer brush at the interface

In the case of compatibilized blend, relaxation processes governed by the relaxation of the copolymer brush at the interface occurs in addition to the droplet shape relaxation. We shall denote two relaxation processes  $\lambda_{\beta'}$  and  $\lambda_{\beta''}$  associated respectively to the interfacial dilatation and shear modulus of the brush at the interface. This results theoretically in additional plateau, generally at lower frequencies. Rienman et al. [149] were the first authors to study this double relaxation. The values of the interfacial dilatation and shear modulus ( $\beta'(\omega)$  and  $\beta''(\omega)$ ) were also discussed in Jacobs et al. [148]. Van Hemelrijck et al. [150] showed that  $\beta''$  decreases when the amount of block copolymer at the interface increases. Figure 5.6 shows a theoretical example of the double relaxation process, the relaxations being very close they are denoted by a single relaxation value  $\lambda_\beta$ .

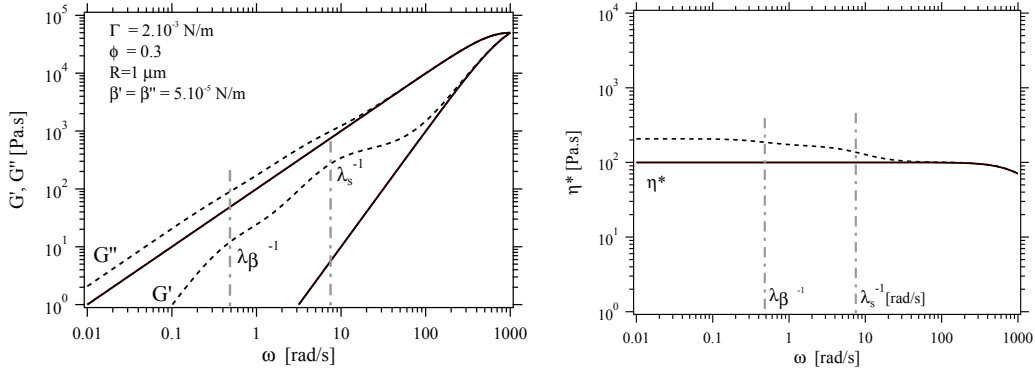


Figure 5.6: Example of the Palierne model applied to a theoretical compatibilized blend (i.e.  $\beta'(\omega) = \beta''(\omega) \neq 0$ ) with  $\eta_m = \eta_d = 100\text{Pa.s}$ . A double relaxation process can be observed on the rheological behavior, especially on the storage modulus  $G'(\omega)$  where two shoulders are observed. Chosen parameters are reported in the graph.

Several research teams mentioned that in polymeric systems, the dilatation of the interface can be neglected thus  $\beta'(\omega) = 0$  [148, 150, 151]. The interface will just undergo the effect of shearing. The interfacial relaxation time due to the presence of copolymers at the interface can thus be calculated as follow:

$$\lambda_\beta = \frac{\lambda_{12}}{2} \left[ 1 + \left( 1 - 4 \frac{\lambda_{11}}{\lambda_{12}} \right)^{0.5} \right] \quad (5.13)$$

With:

$$\lambda_{11} = \frac{R_i \eta_m}{4\Gamma} \frac{(19R_v + 16)(2R_v + 3 - 2\phi(R_v - 1))}{10(R_v + 1) + \frac{\beta''}{\Gamma}(13R_v + 12) - 2\phi \left( (5R_v + 2) + \frac{\beta''}{2\Gamma}(13R_v + 8) \right)} \quad (5.14)$$

$$\lambda_{12} = \frac{R_i \eta_m}{8\beta''} \frac{10(R_v + 1) + \frac{\beta''}{\Gamma}(13R_v + 12) - 2\phi \left( (5R_v + 2) + \frac{\beta''}{2\Gamma}(13R_v + 8) \right)}{(1 - \phi)} \quad (5.15)$$

Some examples of physically compatibilized blends with low amount of compatibilizer (addition of a diblock copolymer at the interface) exhibit very good agreement with the prediction of the Palierne's model[148]. For example, VanHemelrijck et al. (2004)[150] showed very good agreement between experimental results and Palierne's prediction for PDMS/PI blends physically compatibilized with 0.05 to 1% (by weight of the minor phase) of PI-PDMS diblock copolymer.

## 1.5 Dependence of the rheological behaviour of polymer blends on the composition

From a simple point of view, one may expect that the viscosity varies as a function of the concentration of blend component in the case of nodular dispersion following simple mixing rules [152]. However, as we have seen previously, polymer blends have intrinsic viscoelastic properties due to the presence of interfaces. Besides, the presence of a compatibilizer has several consequences on interfaces: size decrease, stabilization, steric repulsion... Thus at high volume fractions of the dispersed phase, strong interactions between droplets may be observed, especially for compatibilized blends, which complicates the evolution of the viscosity.

### 1.5.1 Empirical mixing rules

The simplest mixing rule for incompatible polymers or liquid mixtures is the linear relationship [152]

$$\eta = \eta_A \phi + \eta_B (1 - \phi) \quad (5.16)$$

With  $\eta$  the blend viscosity,  $\eta_A$  and  $\eta_B$  those of components A and B, and  $\phi$  the volume fraction of A. The log linear rule is also used when  $\eta_A$  and  $\eta_B$  differs by orders of magnitude [152],

$$\log \eta = \phi \log \eta_A + (1 - \phi) \log \eta_B \quad (5.17)$$

Finally, one can also find the reciprocal mixing rule which produces a negative deviation [152]

$$\frac{1}{\eta} = \frac{\phi}{\eta_A} + \frac{(1 - \phi)}{\eta_B} \quad (5.18)$$

This last equation is representative of the viscosity of a layered mixture of two newtonian liquids. More complex empirical relations can be found in the literature but are not discussed here. These mixing rules do not take into account the proper morphology, i.e. the presence of interfaces, and thus do not necessarily predict an increase in the viscosity when the volume fraction of the dispersed phase increases. They do not consider any interaction between neighbouring droplets if a nodular morphology is considered.

### 1.5.2 Viscosity of suspensions

To take into account the interactions between droplets, it is interesting to make a parallel between emulsions and polymer blends. The rheological behaviour of ideal cases, such as suspensions of solid droplets in a Newtonian matrix and, later, emulsions of Newtonian components have been widely studied [145]. In the case of polymeric systems the viscoelastic behaviour has to be considered.

In suspensions of rigid spheres in a fluid matrix, there are several forces in balance: Hydrodynamic forces, inter-particle forces (repulsive or attractive), thermal forces (Brownian motion) and inertia (which can be neglected)[116]. Only the hydrodynamic interactions and Brownian motion are considered in what follows. Considering a Newtonian and incompressible matrix in the linear regime, different cases to calculate the viscosity, depending on the volume fraction of monodisperse rigid spheres, were considered:

- Dilute case ( $\phi < 0.03$  typically) (Einstein 1911): no interactions between particles [145].

$$\eta = \eta_m [1 + 2.5\phi] \quad (5.19)$$

Where  $\phi$  is the volume fraction of the dispersion et  $\eta_m$  the viscosity of the matrix.

- Semi-dilute case ( $\phi < 0.10$  typically) (Batchelor 1977 [153]) :

$$\eta = \eta_m [1 + 2.5\phi + 6.2\phi^2] \quad (5.20)$$

- Up to the maximum close packing (Krieger and Dougherty 1959 [154]) :

$$\eta = \eta_m \left[ 1 - \frac{\phi}{\phi_m} \right]^{-[\eta]\phi_{max}} \quad \text{where } [\eta] = \lim_{\phi \rightarrow 0} \left( \frac{\eta - \eta_m}{\phi \eta_m} \right) \quad (5.21)$$

Where  $\phi_m$  is the maximum close packing volume fraction (for monodisperse hard spheres  $\phi_m \simeq 0.63 - 0.64$ ), and  $[\eta]$  is the intrinsic viscosity: for rigid spheres  $[\eta] = 2.5$  (see eq. 5.19). The semi-empirical Krieger and Dougherty model equation (1959) [154] is interesting for us because it covers a large range of compositions, not only dilute systems.

Models presented above are designed for rigid spheres, thus only the viscosity of the matrix phase is taken into account. For polymer blends in the melt state, we have to take into account modifications since we are working with viscoelastic spheres. As an extension of Einstein's equation, Taylor (1932) [8] proposed an expression of the viscosity for the case of diluted elastic spheres in a Newtonian liquid:

$$\eta \simeq \eta_m \left( 1 + 2.5\phi \frac{R_v + 0.4}{R_v + 1} \right) \quad (5.22)$$

Where  $R_v = \eta_d/\eta_m$  is the viscosity ratio and  $\eta_d$  and  $\eta_m$  are the viscosities of the dispersed and the matrix phases respectively. Thus, the total blend viscosity depends not only on the matrix viscosity but also on the dispersed phase.

To account for the the viscoelastic nature of both matrix and dispersions on the whole composition range, Janssen et al. [10] proposed to use a modified Krieger and Dougherty equation for fluid spheres in a viscoelastic matrix, in analogy with Taylor's equation [155] [145]:

$$\eta \simeq \eta_m \left[ 1 - \frac{\phi_d}{\phi_{max}} \right]^{-2.5\phi_{max} \left( \frac{R_v + 0.4}{R_v + 1} \right)} \quad (5.23)$$

With:

- $\eta$  the blend viscosity.
- $\eta_m$  the matrix viscosity.
- $\phi_d$  the volume fraction of the dispersed phase.
- $R_v$  the viscosity ratio between the dispersion and the matrix  $R_v = \eta_d/\eta_m$ .
- $\phi_{max}$  the maximum close packing parameter.

This modified version of the Krieger and Dougherty model will be called in what follows "**the modified KD model**". More precisions concerning the use of this model will be given below. Besides, the origin of the modification from the original Krieger and Dougherty model will be discussed. This equation designed to describe the viscosity of concentrated viscoelastic blends with a nodular morphology shows that when the volume fraction of the dispersed phase increases, the viscosity of the blend increases whatever the value of the viscosity ratio.

## 1.6 Analysis of models to predict viscosity evolution as a function of blend composition

**Palierne's model** [147] appears to be the most pertinent model **to study the blends rheological behaviour as a function of the frequency**, but, can it be used in the whole composition range? We might thus analyse first how does the dynamical moduli predicted with Palierne's model evolve with the composition, i.e. study the mixing rule included

in Palierne's model.

Besides, Janssen et al. [10, 7] proposed an expression, **the modified KD model** (eq. 5.23), that is supposed to account for the viscoelastic nature of blends and describe **the viscosity evolution as a function of the composition**. However, we saw that the viscosity is also frequency dependent. Thus, one may wonder if the modified KD model is valid in the whole frequency range and what are the differences with the mixing rule included in Palierne's model. Besides, it is worth studying the origin of the modification proposed by Janssen et al. from the original KD version (see eq. 5.21).

Thus prior to analysing data, a deeper analysis of models proposed was thus performed. This allowed to study the relevance of the models proposed in the literature to meet our main objective which was to make the link between rheological behaviour and morphologies of reactively binary blends in the whole range of compositions.

### 1.6.1 Mixing rules included in Palierne's model

In the general expression of the dynamical modulus  $G^*$  of the simplified Palierne's model (see eq. 5.10), the term  $H_i(\omega)$  containing two terms:

$$H_i(\omega) = \frac{\frac{4\Gamma}{R_i}(2G_m^* + 5G_d^*) + (G_d^* - G_m^*)(16G_m^* + 19G_d^*)}{\frac{40\Gamma}{R_i}(G_m^* + G_d^*) + (2G_d^* + 3G_m^*)(16G_m^* + 19G_d^*)}$$

Predominates when:
Predominates when:

$\frac{\Gamma}{R} \gg G'$ 
 $\frac{\Gamma}{R} \ll G'$

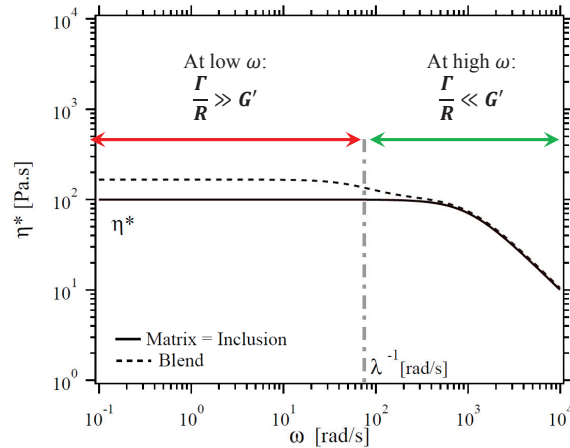


Figure 5.7: Predominance zones of the two terms contained in the value of  $H_i(\omega)$  in the expression of the complex shear modulus of the simplified Palierne's model equation 5.10.

The first terms predominates at low frequencies when interfacial relaxations occurs and affect dynamical moduli (especially the  $G'$  value) and thus the viscosity, and the second term predominates at high frequencies when relaxation processes due to interfacial effects do not affect dynamical moduli. The mixing rules that control the dependence on the dispersed phase concentration considered in Palierne's model can thus be discussed.

- **At high frequencies**, relaxation processes due to interfacial effects do not affect the  $G'$  value. It thus correspond to the cases where  $\Gamma/R \ll G'$  and thus the first term in the value of  $H_i(\omega)$  can be neglected. The complex shear modulus  $G^*(\omega)$  can be calculated with:

$$H_i(\omega) = \frac{(G_d^* - G_m^*)}{(2G_d^* + 3G_m^*)} \quad (5.24)$$

If we make the rough estimate that in the terminal regime the polymer behaves as a newtonian fluid, thus  $G' \ll G''$  and  $G^* \approx G'' \approx \omega\eta^*$ . An estimation of the viscosity evolution as a function of the frequency can thus be made:

$$\eta^*(\omega) = \eta_m^*(\omega) \frac{1 + 3\phi_i \frac{R_v - 1}{2R_v + 3}}{1 - 2\phi_i \frac{R_v - 1}{2R_v + 3}} \quad (5.25)$$

Which corresponds to **Kerner's result in the case of incompressible media** [147].

For very dilute systems,  $\phi \ll 1$ , the complex shear modulus of the simplified Palierne's model in equation 5.10 can be simplified as in equation 5.26.

$$G^*(\omega) = G_m^*(\omega) [1 + 5 \sum \phi_i H_i(\omega)] \quad (5.26)$$

Thus, for very dilute systems, the viscosity evolution as a function of the composition becomes:

$$\eta^*(\omega) \simeq \eta_m^*(\omega) \left( 1 + 2.5\phi_i \frac{R_v - 1}{R_v + 1.5} \right) \quad (5.27)$$

$R_v = \eta_d^*/\eta_m^*$  is the viscosity ratio. We notice here that for the case of rigid spheres in a liquid matrix,  $R_v \rightarrow \infty$  and we find again the Einstein's equation for very diluted systems in equation 5.19.

- **At low frequencies**, relaxation processes due to interfacial effects affect the  $G'$  value it thus corresponds to the case case where  $\Gamma/R \gg G'$  and thus the first term in the value of  $H_i(\omega)$  predominates and the second can be neglected. The complex shear modulus  $G^*(\omega)$  can be calculated with:

$$H_i(\omega) = \frac{(2G_m^* + 5G_d^*)}{(G_m^* + G_d^*)} \quad (5.28)$$

Then by approximating  $G^* \approx G'' \approx \omega\eta^*$ , an estimation of the viscosity evolution as a function of the frequency can be made:

$$\eta^*(\omega) = \eta_m^*(\omega) \frac{1 + 3\phi_i \frac{1}{10} \frac{2 + 5R_v}{1 + R_v}}{1 - 2\phi_i \frac{1}{10} \frac{2 + 5R_v}{1 + R_v}} \quad (5.29)$$

In the case of very diluted systems, this expression becomes:

$$\eta^*(\omega) \simeq \eta_m^*(\omega) \left( 1 + 2.5\phi_i \frac{R_v + 0.4}{R_v + 1} \right) \quad (5.30)$$

This expression correspond to Taylor's equation in equation 5.22 [8].

Thus, we now have the expression of the viscosity evolution as a function of the composition included in Palierne's model for two cases: (1) the case where there is no droplet shape relaxation (high frequencies) and (2) the case where dynamical moduli are modified due to droplet shape relaxation (low frequencies).

### 1.6.2 Modified Krieger and Dougherty model

Krieger and Dougherty [154] proposed an expression for describing the viscosity evolution up to the maximum close packing (see eq. 5.21). Janssen et al. [10, 7] proposed to use a modified version of the semi-empirical KD model to account for elastic contribution of the interface in the value of the viscosity that arise from Taylor's expression (see eq. 5.22).

Thus the intrinsic viscosity  $[\eta]$  of equation 5.21, may be expressed, by using the simplified expression of  $\eta^*(\omega)$  in equation 5.22, by :

$$[\eta] = \lim_{\phi \rightarrow 0} \left( \frac{\eta - \eta_m}{\phi \eta_m} \right) = 2.5 \left( \frac{R_v + 0.4}{R_v + 1} \right) \quad (5.31)$$

Thus, we find the modified Krieger and Dougherty expression ("**modified KD model**") of the viscosity proposed by Janssen et al. :

$$\eta = \eta_m \left[ 1 - \frac{\phi}{\phi_{max}} \right]^{-2.5\phi_{max} \left( \frac{R_v + 0.4}{R_v + 1} \right)} \quad (5.32)$$

However, it has been seen above (subsection 1.6.1) that Taylors equation describes the viscosity evolution for very dilute systems when dynamical moduli are modified due to droplet shape relaxation (low frequencies) (see eq. 5.30). The KD model modified with Taylors expression **may thus be valid at low frequencies, when relaxation processes due to droplet shape relaxation affect the  $G'$  value.**

One can thus wonder what become the KD model at high frequencies, when there is no droplet shape relaxation affecting the dynamical moduli. The same calculation of the intrinsic viscosity  $[\eta]$  of equation 5.21 may be expressed by using the simplified expression of  $\eta^*(\omega)$  in equation 5.27, by :

$$[\eta] = \lim_{\phi \rightarrow 0} \left( \frac{\eta - \eta_m}{\phi \eta_m} \right) = 2.5 \left( \frac{R_v - 1}{R_v + 1.5} \right) \quad (5.33)$$

Thus, another expression of the original Krieger and Dougherty's expression for the blend viscosity is proposed as follow:

$$\eta = \eta_m \left[ 1 - \frac{\phi}{\phi_{max}} \right]^{-2.5\phi_{max} \left( \frac{R_v - 1}{R_v + 1.5} \right)} \quad (5.34)$$

This equation may thus be valid at high frequencies, when relaxation processes due to interfacial effects do not affect the  $G'$  value. This expression will be called in what follows "no relaxation KD model"

Let us discuss the evolution of blends viscosities as a function of the viscosity ratio. We see that for the modified KD model (eq. 5.32), whatever the viscosity ratio, the viscosity will increase in any case. However, for the no relaxation KD model (eq. 5.34), if  $R_v < 1$ , i.e. if droplets less viscous than the matrix are added, the viscosity may decrease compared to the viscosity of the pure component which constitute the matrix.

Thus, since the modified KD model (eq. 5.32) predict one evolution when droplets of A are dispersed in a B matrix and a second one for the opposite case (see figure 5.8 (left)), only the part below the cross section can be represented for the sake of clarity of the results (see figure 5.8 (right)). This representation cannot be used when  $R_v < 1$  when the no relaxation KD model will be used.

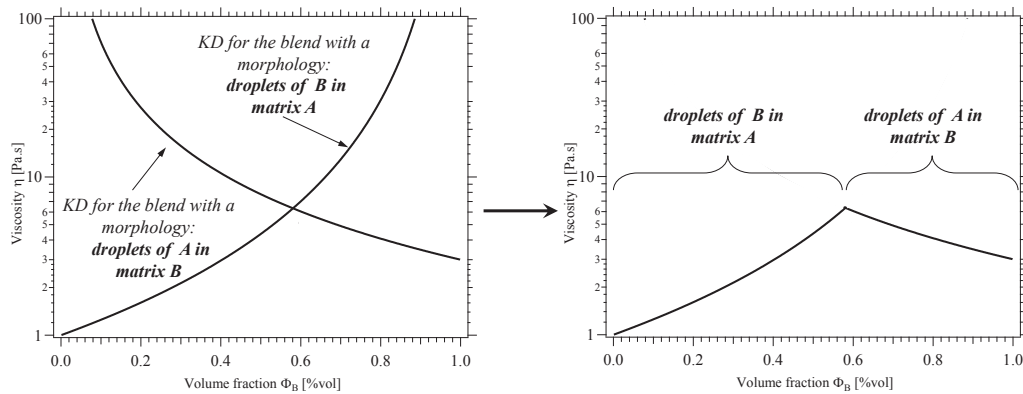


Figure 5.8: Simplified representation of the modified Krieger and Dougherty model which is morphology-based. Example for a polymer B, 3 times more viscous than a polymer A.

### 1.6.3 Comparison between the mixing rules included in Palierne's model and the modified KD model

To compare the mixing rule included in Palierne's model and the modified KD model let us consider only the evolution of a simple blend with droplets of B in a matrix A with a viscosity ratio  $R_v=3$  ( $\eta_A=1$  and  $\eta_B=3$ ). Figure 5.9 (a) shows this evolution when droplets shape relaxations occurred, i.e at low frequencies using the modified KD model (eq. 5.32) and the mixing rule included in Palierne's model (eq. 5.29). Figure 5.9 (b) shows the predicted evolution at high frequency when no droplet shape relaxation occurred using the no relaxation KD model (eq. 5.34) and the mixing rule included in Palierne's model (eq. 5.25).

From figure 5.9, it shall be noticed that for dispersed phase composition lower than 20%vol both models provide the same evolution. However, for more concentrated blends, the mixing rule included in Palierne's model exhibit a more linear evolution while the KD model diverges and adopt a more common shape for concentrated emulsions. This suggest that for more concentrated blends exhibiting a droplet in matrix morphology, Palierne's model may underestimate the blend viscosity. This difference is much less

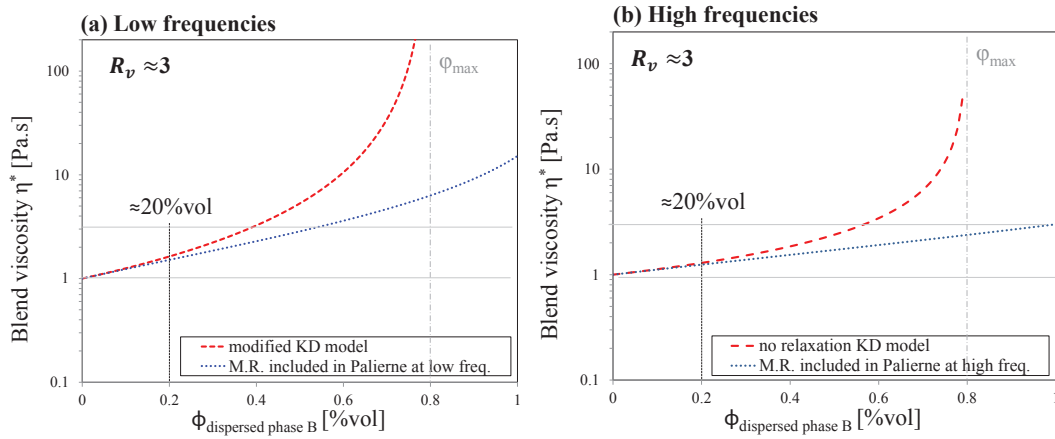


Figure 5.9: Example of the viscosity evolution for a blend with droplets of B in a matrix A with a viscosity ratio  $R_v=3$  ( $\eta_A=1$  and  $\eta_B=3$ ). (a) shows this evolution when droplets shape relaxations occurred, i.e. at low frequencies using the modified KD model (eq. 5.32) and the mixing rule included in Palierne's model (eq. 5.29). (b) shows the predicted evolution at high frequency when no droplet shape relaxation occurred using the no relaxation KD model (eq. 5.34) and the mixing rule included in Palierne's model (eq. 5.25).

pronounced at high frequency where both curves are closer except close to  $\phi_{max}$  where the no relaxation KD model diverges.

## 1.7 Objectives of the chapter

Most commonly in the literature, blends linear viscoelastic behaviour are described by additional relaxation process that affect dynamical moduli: (1) droplet shape relaxation and (2) in case of compatibilized blends, additional slow relaxation processes due to interfacial elasticity (due to the presence of copolymers at the interface). Palierne [147] developed a model that accounts for these effects. However, this model has proven its usefulness in case of dilute blends only (i.e. low volume fraction of the dispersed phase) and low amount of compatibilizers [156, 115, 148, 149, 150].

Besides, to the best of our knowledge, very few systematic studies have been published on the linear viscoelastic behaviour of highly compatibilized blends in the whole composition range [157, 158]. Only few papers report the study of the viscosity evolution as a function of the composition for compatibilized blends [159]. Moreover, all studies concern blends in which the viscosity ratio is close to 1.

We thus defined more precisely pertinent models to describe the rheological behaviour of our blends. From the above analysis, it can be concluded:

- To study the evolution of the viscosity as a function of the composition the expression proposed by Janssen et al., '**the modified KD model**' (eq. 5.32) predict the viscosity evolution only at low frequencies, when droplet shape relaxation have already affected the dynamical moduli. A high frequencies, we proposed another model which does not account for the droplet shape relaxation, the '**no relaxation KD model**' (eq. 5.34). This model has a more physical sense than using only simple mixing rules, like linear mixing rule for example. **We already understand that**

**these models are not designed to describe the viscosity evolution of compatibilized blends at frequencies where other relaxation processes than droplet shape relaxation occurs.**

- After analysing the shape of the evolution of the mixing rule included in Palierne's model we understand that for blend **with a concentration in dispersed phase  $\phi_d$  higher than 20%vol the Palierne's model may underestimate the value of the viscosity and intrinsically of the dynamic moduli.**

A thorough analysis of both uncompatibilized and compatibilized blends linear viscoelastic behaviour dependence on the frequency and on the composition was thus performed. Data were compared to the discussed models. **Our goal was not necessarily to find a model which fits our data, but rather to observe for which conditions our data diverge from the selected models, and try to understand the reason for such a deviation.** This shall provide new elements to know **if morphologies can be inferred based on rheology, or conversely, if we can predict rheology knowing the morphology.**

## 2 Preliminary remarks

### Morphologies of uncompatibilized and compatibilized blends

In chapter 4 blends morphologies were studied. The study of blends rheological behaviour is based on those morphologies. Thus, given the large number of blends studied:

- Uncompatibilized PA6-3k/HDPE, PA6-18k/HDPE and PA6-31k/HDPE blends morphologies are summarized in figure 5.10.
- Compatibilized PA6-3k/MA-g-HDPE, PA6-18k/MA-g-HDPE and PA6-31k/MA-g-HDPE blends morphologies are summarized in figure 5.11.

### Linear viscoelastic behaviour of blend components

In chapter 2, section 5 the rheological behaviour of the three pure polyamides 6 PA6-3k, PA6-18k and PA6-31k (see subsection 5.1) and HDPE and MA-g-HDPE (see subsection 5.2) have been studied. For the polyamide 6:

- PA6-31k exhibits a characteristic behaviour of a viscoelastic polymer, in the terminal regime  $G' \propto \omega^2$  and  $G'' \propto \omega$ .
- PA6-18k exhibits a characteristic behaviour of a viscoelastic polymer within the frequency range  $10 < \omega < 100 \text{ rad/s}$ . At frequencies lower than  $10 \text{ rad/s}$  the storage modulus  $G'$  exhibit a shoulder that could be attributed to the presence of gas bubbles.
- PA6-3k the typical behaviour of viscoelastic polymer is not observed. This may also be due to the presence of gas bubbles.

For both polyolefins shoulders on  $G'$  were also observed at low frequencies. For MA-g-HDPE the shoulders may be due to micelles of MA, which are not miscible with the HDPE backbone. The rheological behaviour of pure components are summarized in figures 5.12, 5.13.

In order to limit the problem of gas bubbles, all blends are dried overnight at  $90^\circ \text{C}$  in order to reach a moisture content in the blend below 1000ppm.

Frequency sweep tests are performed in a frequency range from 0.1 (or 0.05) to 100 rad/s. In blends, any potential plateau observed at low frequencies shall be interpreted very carefully due to the rheological behaviour of blend components. Palierne's model will be used to model blend dynamical rheological behaviour. It needs the input of  $G_m^*$  of the matrix and  $G_d^*$  of the dispersed phase. Thus, the shoulders seen on pure materials are taken into account in the model and affect the calculation.

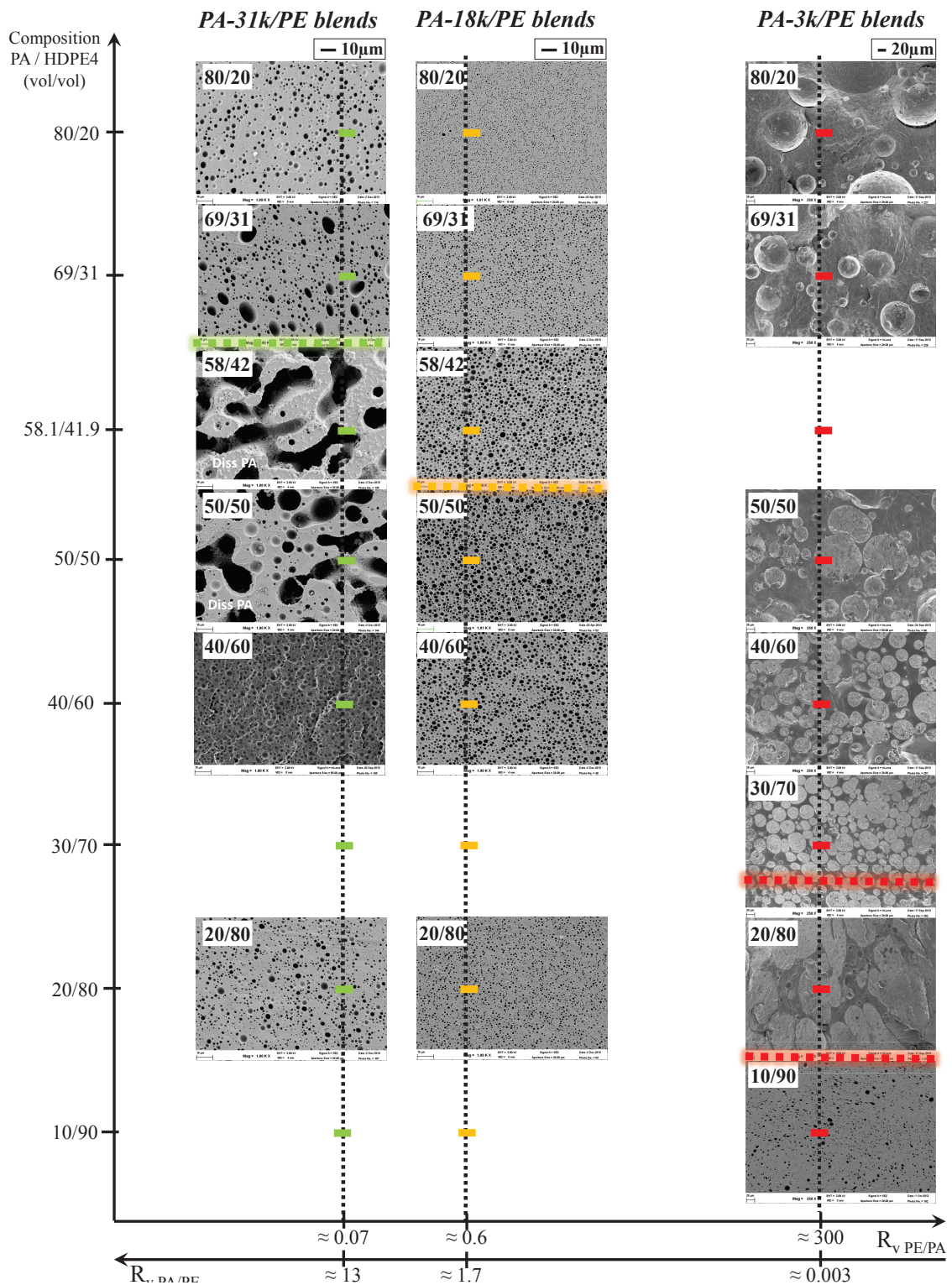


Figure 5.10: Comparison of PA-31k/PE, PA-18k/PE and PA-3k/PE uncompatibilized blends. For a better visualization, SEM micrographs of either minor phase etching or cryofracture are presented. Due to the different characteristic sizes of morphology, different magnification are presented: x1000 for PA-31k/PE and PA-18k/PE blends and x250 for PA-3k/PE blends.

## 2. Preliminary remarks

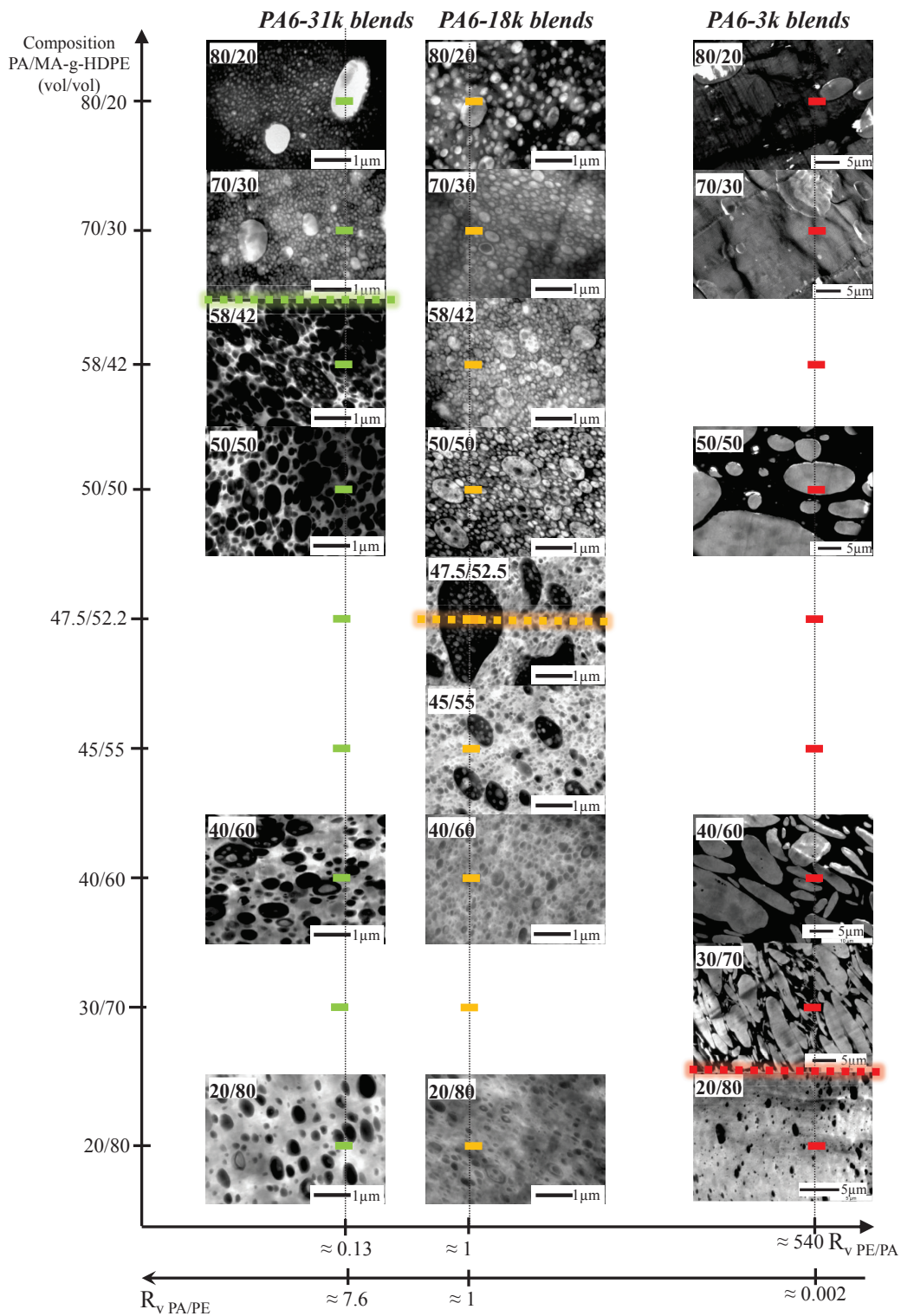


Figure 5.11: Comparison of PA-31k/MAGPE, PA-18k/MAGPE and PA-3k/MAGPE compatibilized blends. TEM micrographs after PA6 staining are presented, PA6 appears in dark. Due to the different characteristic sizes of morphology, different magnification are presented:  $\times 16000$  for PA-31k/PE and PA-18k/PE blends and  $\times 2500$  for PA-3k/PE blends.

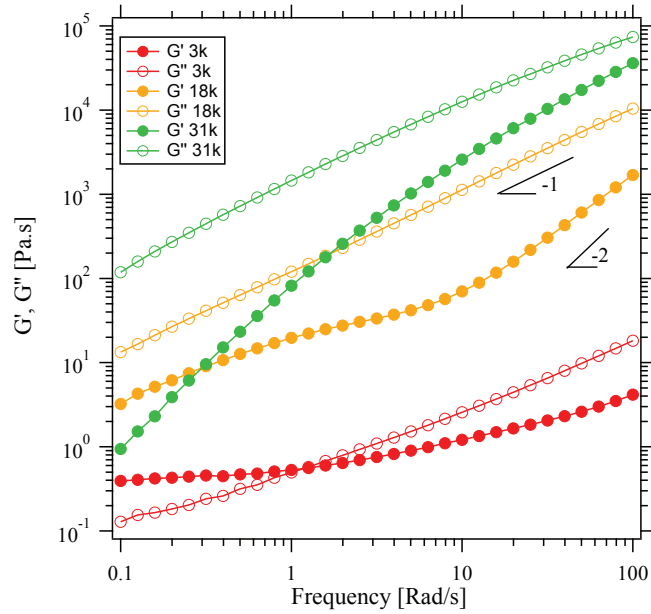


Figure 5.12: Dynamic moduli  $G'$  and  $G''$  as a function of the frequency of PA6-3k, 18k and 31k at 290 °C at constant strain (15%).

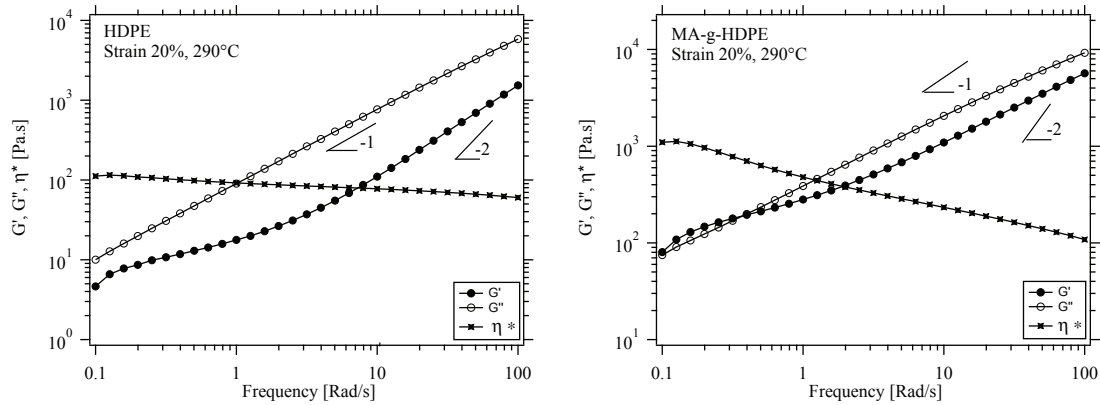


Figure 5.13: Dynamic viscosity  $\eta^*$ , and dynamic modulus  $G'$  and  $G''$  as a function of the frequency of commercial HDPE (left) and MA-g-HDPE (right) at 290 °C at constant strain (20%). Vertical scales are different on each graph.

## 3 Uncompatibilized blends

### 3.1 Evolution of the viscosity with the composition

#### 3.1.1 Experimental results

Dynamic viscosity of PA6-3k/HDPE, PA6-18k/HDPE and PA6-31k/HDPE uncompatibilized binary blends were measured by dynamical rheometry as described in chapter 2 subsection 3.3. Figure 5.14 shows the dynamical viscosity  $\eta^*$  of uncompatibilized blends at high (100 rad/s) and low (1rad/s) frequencies as a function of blend composition  $\phi$  for the three blend series.

For the three blends series, at 100 rad/s, dynamic viscosities evolve monotonically as a function of  $\phi_{PEHD}$ . At lower frequencies (1rad/s), viscosities are higher than at 100 rad/s and exhibit non monotonic variation. The general trend is that, on approaching the phase inversion composition, viscosities increases. For blend exhibiting co-continuous morphologies, viscosities almost do not increase compared to high frequencies. For blends with a viscosity ratio  $R_v \gg 1$ , the viscosity increase is more important at high and low frequencies than any other blend.

#### 3.1.2 Discussion

In order to analyse the viscosity evolution as a function of the blend composition, experimental results were compared at high frequency with the 'no relaxation KD model' (eq. 5.34) and at low frequencies with the 'modified KD model' (eq. 5.32). Mixing rules have been calculated thanks to the dynamic viscosity of pure polymers (HDPE, PA6-3k, PA6-18K and PA6-31k). Results are reported on figure 5.14.

**At high frequency (100 rad/s)**(figure 5.14 (a),(c) and (e)), the model describes quite satisfactorily the viscosity evolution. This is consistent with the fact that, at high frequency, interfaces do not contribute significantly to the viscoelastic response of the blend.

**At low frequency (1 rad/s)** (figure 5.14 (b),(d) and (f)) different cases are observed:

- For blends exhibiting a "droplet in matrix" morphology:
  - When the viscosity ratio  $R_v=1$  or  $R_v < 1$  (i.e.  $\eta_d \approx \eta_m$  or  $\eta_d < \eta_m$  respectively) the modified KD model describes quite satisfactorily the viscosity, even for concentrated blend ( $\phi_d > 20\%$ vol) in the case of blends with PA6-18k. Thus the increase in viscosity on approaching phase inversion is consistent with an increase due to droplet shape relaxation, as explained in subsection 1.6.3. Besides, this confirms that the Palierne's model, which differs from the modified KD model at 20%vol (see subsec. 1.6.3), will probably underestimate results.
  - When the viscosity ratio  $R_v > 1$  (i.e.  $\eta_d > \eta_m$ ) the modified KD model underestimates viscosities.
- Both co-continuous blends with PA6-31K are below the model prediction.

More specific observations are described below:

- For **PA6-18k/HDPE blends** (figure 5.14 (d)), an interesting observation is the nearly symmetrical increase in viscosity when the volume fraction of the dispersed phase

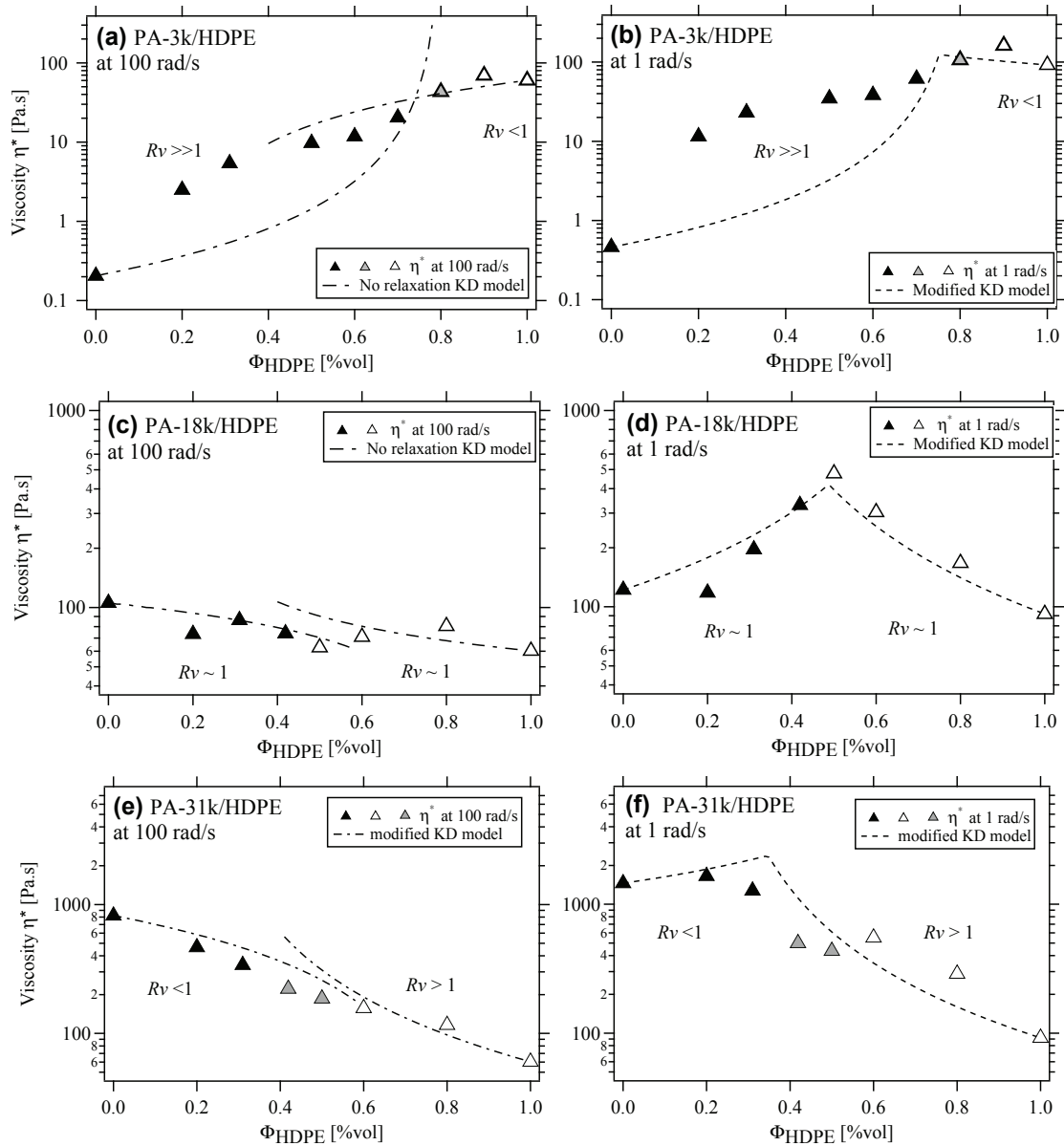


Figure 5.14: Dynamic viscosity (triangles), of PA-3k/HDPE (top), PA-18k/HDPE (middle) and PA-31k/HDPE (bottom) uncompatibilized binary blends measured by cone-plate rheometry: left column, results at 100rad/s and right column, results at 1rad/s. Symbols correspond to different morphologies: black triangles, dispersions of PE in PA, grey triangles, co-continuous morphologies and white triangles, dispersions of PA in PE matrix. Mixing rules calculated from the viscosity of pure components are represented: the modified KD model (equation 5.32- dashed line) and the no relaxation KD model (eq. 5.34- dash and dots line).

increases toward phase inversion. This is very consistent with the symmetrical development of morphology (sizes increase when  $\phi_d$  increases) observed on both sides of phase inversion.

- For **PA6-3k/HDPE blend** (figure 5.14 (a) and (b)), for blends exhibiting a dispersion of PE into a PA6-3k matrix ( $R_v \approx 300$ ) viscosities are much above the model prediction. We observed that the morphology of these blends consists in large viscous droplets separated by relatively thin films, in which drainage may be slow (see chapter 4 subsection 2.2). In such particular morphologies, the overall viscosity may thus be significantly larger than predicted by a simple mean-field models. This could explain the higher viscosities measured.
- Finally for **PA6-31k/HDPE blends** (figure 5.14 (f)) a particular behaviour is observed. For blends with  $R_v > 1$ , the situation is similar to blends with PA6-3k (with  $R_v \gg 1$ ) where viscous droplets are dispersed in a fluid matrix, here  $R_v = 13$ : Although the situation is less critical, the same phenomena may explain the situation. Another interesting observation is that both blends exhibiting a co-continuous morphology, exhibit lower viscosities than other blends. Their viscosity does not increase compared to values at high frequencies, even though they constitute the more concentrated blends. It is an indication that the partially or fully co-continuous nature of the blends morphology, does not lead to the same relaxation process as droplets in matrix morphologies. Huitric et al. [156] observed the same behaviour for uncompatibilized PE/PA12 blends having a viscosity ratio close to unity. Castro et al. [30, 160, 29] observed a drop in  $G'$  modulus at low frequencies for co-continuous blends. This point will be discussed in more details in the study of the complex modulus.

## 3.2 Linear viscoelastic behaviour as a function of the frequency

In this section, the linear viscoelastic behaviour of uncompatibilized blends PA6-3k/HDPE, then PA6-18k/HDPE and finally PA6-31k/HDPE are studied. The variation of the elastic moduli  $G'$  and loss moduli  $G''$  are presented as a function of the frequency  $\omega$ . The viscoelastic response of blends will be discussed in relation to the blend morphologies which have been described in detail in chapter 4 and are summarized in figure 5.10 subsection 2.

### 3.2.1 Blends with PA6-3k

#### Observations

The linear viscoelastic behaviour of uncompatibilized binary blends of PA6-3k/HDPE, elastic modulus  $G'$  and loss modulus  $G''$ , are presented as a function of  $\omega$  in Figure 5.15.

In blends where PA6-3k is the matrix the presence of gas bubbles in pure components slightly affect the loss modulus  $G''$  which exhibit a slope slightly lower than 1. However, only  $G'$  measurements at frequencies higher than  $\sim 10$  rad/s or with values higher than  $\sim 10$  Pa.s should be less affected by gas bubbles. When HDPE is the matrix phase, the presence of gas bubbles do not affect the storage moduli  $G'$  in the frequency range studied. Only  $G'$  measurements at frequencies higher than  $\sim 5$  rad/s or with values higher

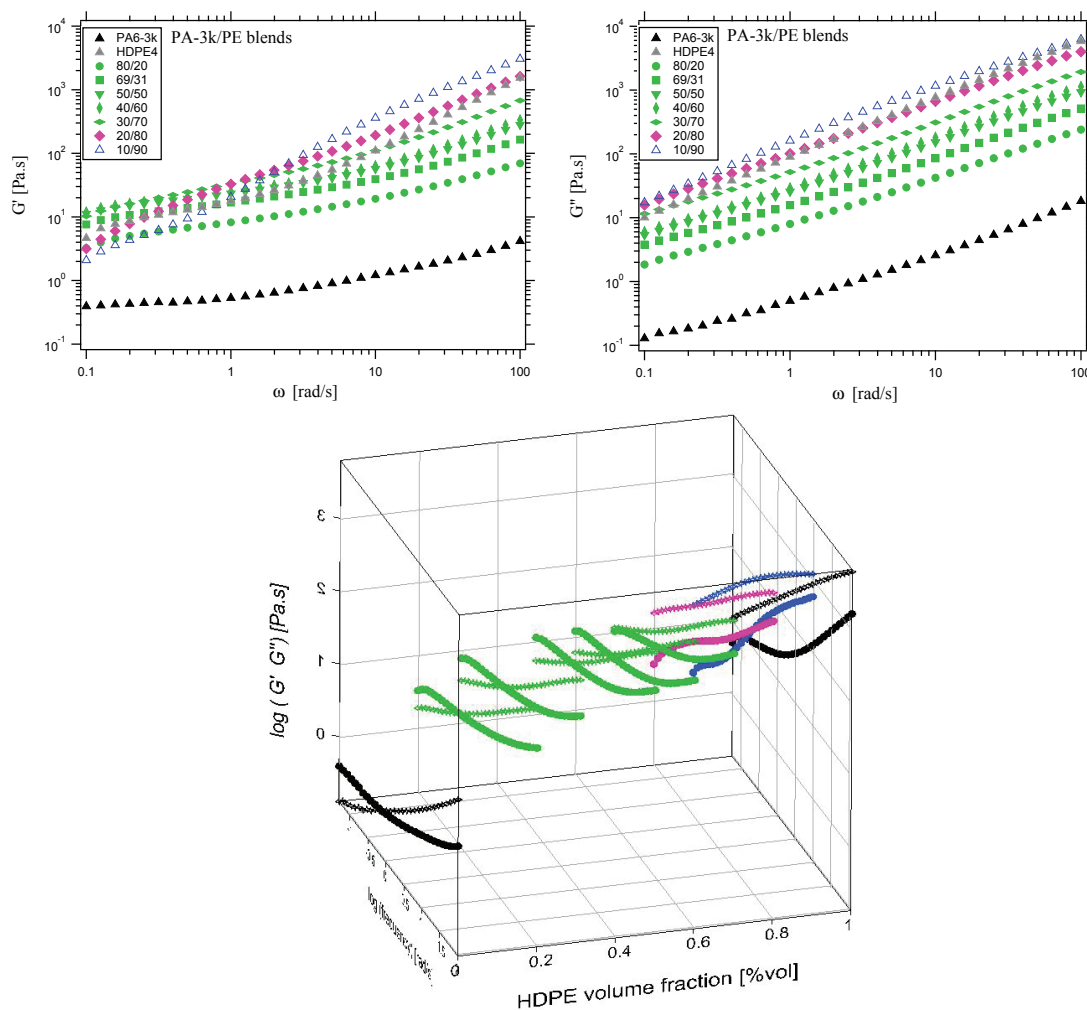


Figure 5.15: Linear viscoelastic behaviour of uncompatibilized binary PA-3k/PE blends. Elastic modulus  $G'$  (left) and loss modulus  $G''$  (right) as a function of the frequency  $\omega$ . Measurements performed at 290 °C. Full symbols (green) correspond to the morphology of dispersion of PE into a PA matrix, crosses (pink) to co-continuous morphology, and empty symbols (blue) to dispersion of PA into a PE matrix. A 3D representation of  $G'$  and  $G''$  as a function of  $\omega$  for the different compositions is also given.

than  $\sim 10$  Pa.s are not affected by gas bubbles.

For blends with a PA6-3K matrix (for the five blends PA-3k/HDPE 80/20 to 30/70, figure 5.16 (a) to (e)), the global frequency variation of  $G'$  and  $G''$  is similar to that of pure PA6-3k. This supports the idea that the PA6-3k remains the matrix phase during the experiment.

In those blends, an interpretation of the  $G'$  value is difficult. Indeed, between 0.1 and 10 rad/s the elastic moduli of each blend show a shoulder and a plateau at around 10 Pa.s consistent with the presence of gas bubbles (see discussion in appendix 1). Bubbles have indeed been observed into the polymer after the rheological experiment.

At frequencies higher than 1 rad/s the  $G''$  values are not perturbed by gas bubbles, they are all quite parallel.

For the co-continuous blend, blend PA-3k/PE 20/80 (figure 5.16 (f)),  $G' < G''$  and they are both roughly parallel.

For the blend with a HDPE matrix (blend PA-3k/PE 10/90, figure 5.16 (g)),  $G' < G''$  and a large shoulder is observed on  $G'$  within the zone between 5 and 100 rad/s.

#### Discussions, modelling

To analyse the linear viscoelastic behaviour of uncompatibilized blends, experimental results are compared to the simplified Palierne's model (see equation 5.10 in section 1). The simplified Palierne's model was calculated using the linear viscoelastic rheological behaviour of pure PA6-3k and HDPE and variable parameters were chosen as follow:

- $\phi$  is the volume fraction.
- The interfacial tension was taken to be approximately  $\Gamma = 10^{-2} \text{N/m}$ .
- The average nodule size  $R$ : the average size was roughly estimated from SEM and TEM pictures and is different for each blends (no image analysis were performed).

The comparison between  $G'$  and  $G''$  and the prediction of the simplified Palierne's model calculated with equation 5.10 are presented as a function the frequency  $\omega$  for each individual blends in figure 5.16 (a) to (g). Different values of  $\Gamma$  and  $R$ , were tested. With realistic parameter values, changes in the model prediction were relatively small. Thus, the most relevant parameter values are presented here.

**For blends with a PA6-3K matrix** (for the five blends PA-3k/HDPE 80/20 to 30/70, figure 5.16 (a) to (e)), the prediction of Palierne's model is much lower than the experimental measurements (more than one decade in any case). The observation of the dynamical moduli allow to precise the interpretation proposed in last subsection (subsec. 3.1) concerning the viscosity evolution of blends with PA6-3k in the case where  $R_v \gg 1$ . The interpretation was that adding more viscous droplets in a fluid matrix increases artificially the mean blend viscosity due to unfavourable drainage regimes. Indeed, we could issue any doubt about the impact of the presence of gas bubbles on the viscosity increase. However, at high frequencies  $G'' > G'$ , thus the measured viscosities are poorly impacted by the presence of gas bubbles, thus the higher moduli measured compared to Palierne's prediction are not an effect of gas bubbles. At low frequencies however ( $\omega < 1 \text{rad/s}$ )  $G'$  overpasses  $G''$  and thus may increase the  $\eta^*$  value (see eq. 5.5).

Besides, the phenomenon of droplet shape relaxation can hardly be considered here to explain the viscosity increase. Indeed, one easily understand that a very fluid matrix could hardly apply a deformation on droplets much more viscous, during the dynamical experiment.

To confirm this interpretation, let us analyse, with the help of the Palierne's model, the values of the relaxation time  $\lambda_s$  and the plateau  $G_s$  theoretically predicted for droplet shape relaxations. They could be estimated respectively with eq. 5.11 and 5.12. Estimations are reported in table 5.1. In all cases, we observed that the value of the estimated plateau  $G_s$  ( $< 0.4 \text{ Pa.s}$  in all cases) are much lower than the experimental values of  $G'$  measured. *This confirms that droplet shape relaxation cannot be the only origin of the viscosity increase and reinforces the interpretation proposed in subsection 3.1..* These difficulties in measuring the plateau induced by droplet shape relaxation in the case of highly viscous droplets in a fluid matrix was mentioned by Graebing et al.[115].

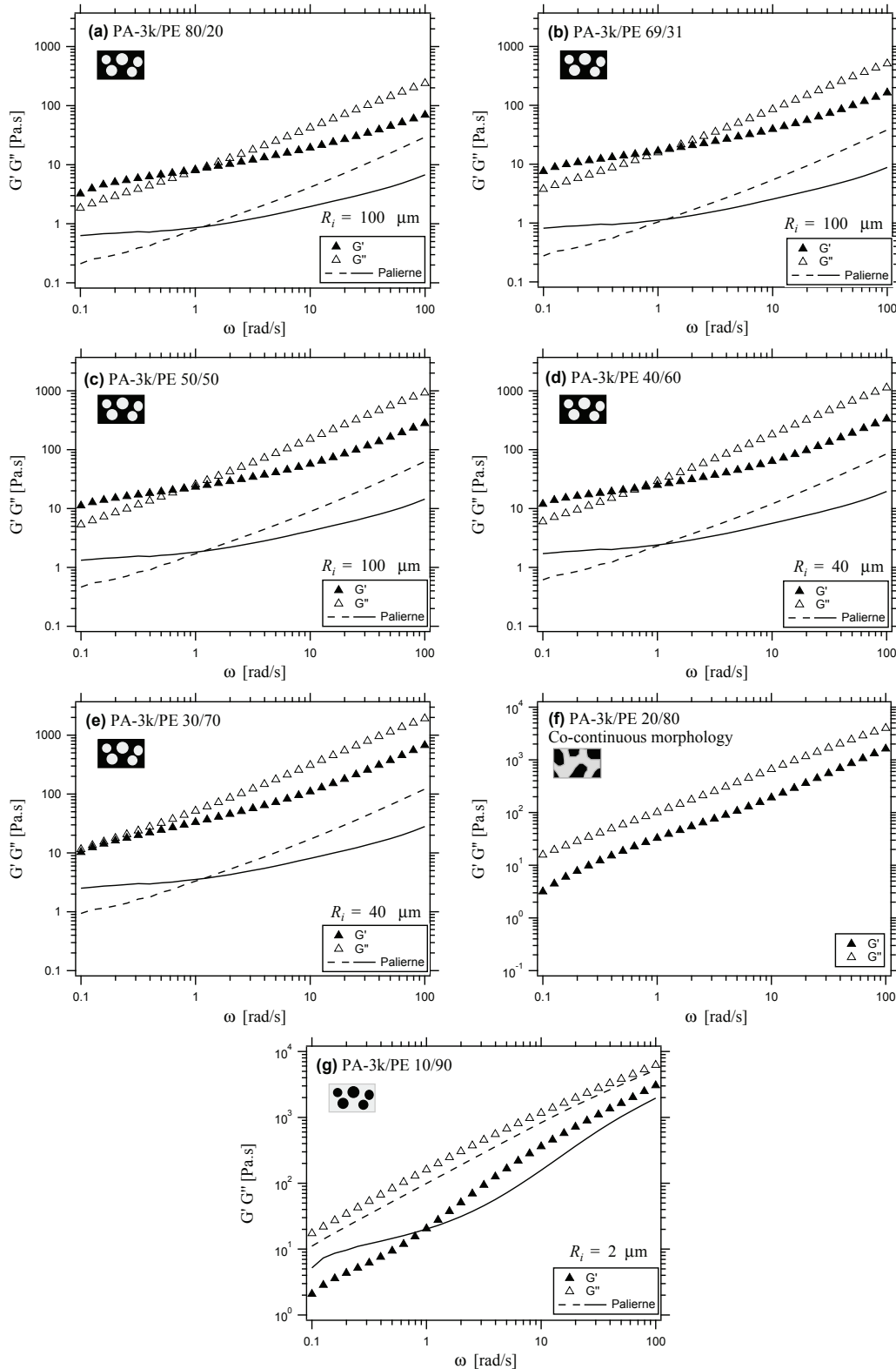


Figure 5.16: Comparison for PA6-3k/HDPE blends between experimental elastic modulus  $G'$  (solid triangle) and loss modulus  $G''$  (empty triangle) and the prediction of the simplified Palierne's model for the elastic modulus (solid line) and loss modulus (dashed line) of equation 5.10 as a function of the frequency  $\omega$ . The interfacial tension  $\Gamma = 10 \text{ mN/m}$  and the value of the average drop radius  $R_i$  is specified for each blend.

### 3. Uncompatibilized blends

**For the co-continuous blend**, blend PA-3k/PE 20/80 (figure 5.16 (f)), frequency variation changes noticeably. We observe that for this blend  $G'$  is almost parallel to  $G''$  (i.e. the loss tangent ( $\tan\delta=G'/G''$ ) is nearly independent of the frequency). This behaviour is similar to a gel like behaviour. The same kind of behaviour are observed for other blends with PA6-18k and PA6-31k and will be discuss below.

**For the blend with HDPE matrix** (blend PA-3k/PE 10/90, figure 5.16 (g)), which exhibits a nodular dispersion of PA6-3k into an HDPE matrix, the prediction of the Palierne's model is much closer to measurements than for other blends of the series. Values of  $G'$  and  $G''$  are nevertheless a little underestimated. Although not well defined, a shoulder between 10 and 100 rad/s with a value of the plateau  $G_s$  a few hundreds Pa.s, is observed on the storage modulus  $G'$ . The estimation of  $\lambda_s^{-1}$  and  $G_s$  (see table 5.1), respectively  $\sim 62$ rad/s and  $\sim 970$  Pa.s, are consistent with the large shoulder observed. In this frequency range, dynamical moduli are not affected by the presence of gas bubbles, this shoulder could thus be attributed to droplet shape relaxation.

Table 5.1: Estimation of  $\lambda_s$  and  $G_s$  for the PA-3k/PE blends with equation 5.11 and 5.12.

PA-3k/PE	80/20	69/31	50/50	40/60	30/70	20/80	10/90
	PE ds 3K						3K ds PE
$R_i$ [m]	1.00E-04	1.00E-04	1.00E-04	1.00E-05	1.00E-05		2.00E-06
$\phi_d$ [%vol]	0.2	0.3	0.5	0.6	0.7		0.1
$\eta_m^*$ [Pa.s]	0.2	0.2	0.2	0.2	0.2	Co-	60
$\Gamma$ [N/m]	0.01	0.01	0.01	0.01	0.01	continuous	0.01
$R_{v\ 100\ rad/s}$	300	300	300	300	300		0.003
$\lambda_s$ [s]	0.57	0.57	0.58	0.06	0.06		0.02
$\lambda_s^{-1}$ [rad/s]	2	2	2	17	17		62
$G_s$ [Pa.s]	0.002	0.003	0.01	0.20	0.41		973

#### 3.2.2 Blends with PA6-18k

##### Observations

The linear viscoelastic behaviour of uncompatibilized binary blends of PA6-18k/HDPE, are presented as a function of  $\omega$  in Figure 5.17.

The presence of gas bubbles in pure components (PA6-18k and HDPE) do no affect the storage moduli  $G''$  in the frequency range studied. However, when PA6-18k is the matrix phase, only  $G'$  measurements at frequencies higher than  $\sim 10$ rad/s or with values higher than  $\sim 10$  Pa.s are not affected by gas bubbles. When HDPE is the matrix phase, only  $G'$  measurements at frequencies higher than  $\sim 5$ rad/s or with values higher than  $\sim 10$  Pa.s are not affected by gas bubbles.

For blends with a dispersed phase concentration  $\phi_d < 30\%$ vol (blends PA-18k/PE 80/20, 69/31 and 20/80, figure 5.18 (a), (b) and (f)),  $G'$  and  $G''$  slightly increase with  $\phi_d$ . For the more concentrated blend PA-18k/PE 40/60 (figure 5.18 (e)), the  $G'$  and  $G''$  increase

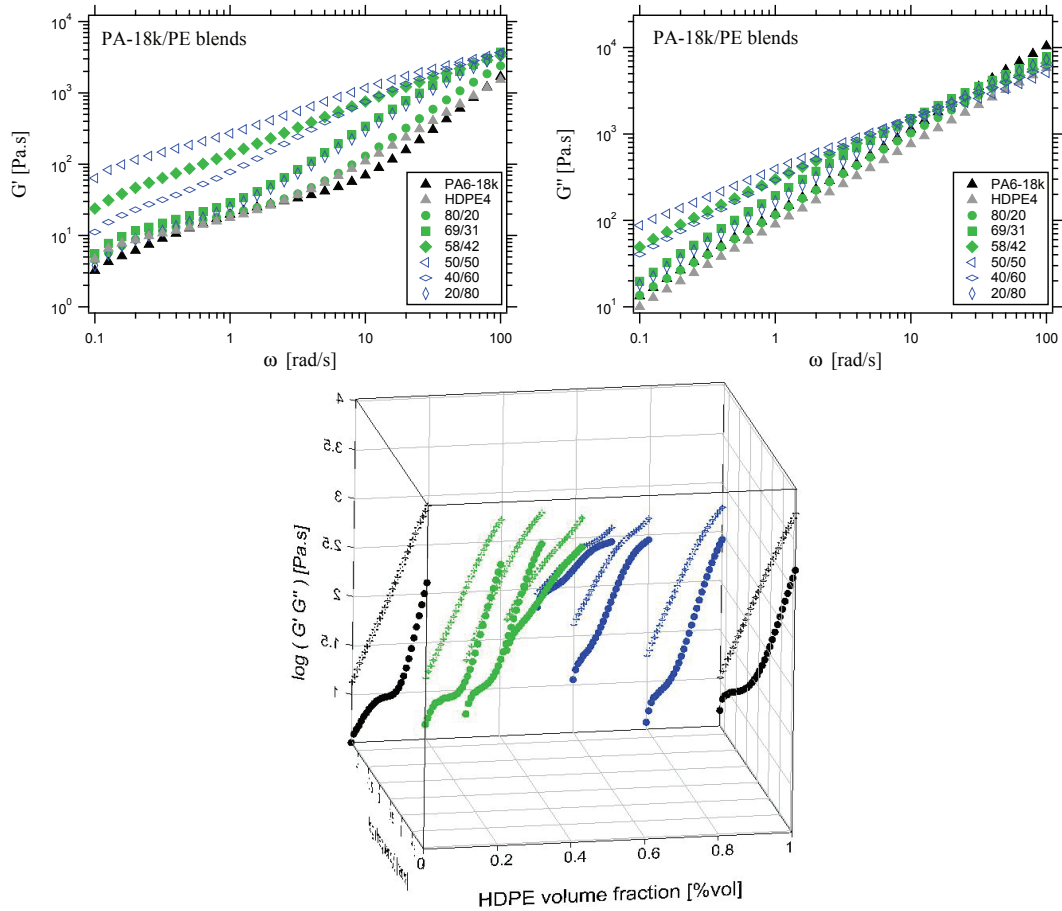


Figure 5.17: Linear viscoelastic behaviour of uncompatibilized binary PA-18k/PE blends. Elastic modulus  $G'$  (left) and loss modulus  $G''$  (right) as a function of the frequency  $\omega$ . Measurements performed at 290 °C. Full symbols (green) correspond to the morphology of dispersion of PE into a PA matrix and empty symbols (blue) to dispersion of PA into a PE matrix. A 3D representation of  $G'$  and  $G''$  as a function of  $\omega$  for the different composition is also given.

is larger especially at lower frequencies. For blends PA-18k/PE 58/42 and 50/50 (figure 5.18 (c) and (d))  $G'$  and  $G''$  are almost parallel and follow a power law: for PA-18k/PE 58/42 blend  $G' \approx G'' \approx \omega^{0.7}$  and for PA-18k/PE 50/50 blends  $G' \approx G'' \approx \omega^{0.57}$ .

### Discussions, modelling

To analyse the linear viscoelastic behaviour of uncompatibilized PA6-18k/HDPE blends, experimental results are compared to the simplified Palierne's model (see equation 5.10 in section 1). The comparison between experimental  $G'$  and  $G''$  and the prediction of the simplified Palierne's model are presented as a function of the frequency  $\omega$  for each individual blends in figure 5.18.

**For blends with a dispersed phase concentration  $\phi_d < 30\% \text{vol}$**  (blends PA-18k/PE 80/20, 69/31 and 20/80, figure 5.18 (a), (b) and (f)),  $G'$  and  $G''$  values are predicted in a rather satisfactory way with Palierne's model. Although not well defined, large shoulders between 10 and 100 rad/s are observed for those three blends. The estimation of  $\lambda_s^{-1}$  and  $G_s$  with Palierne's model (see table 5.1), which are respectively between  $\sim 40$  and 75

### 3. Uncompatibilized blends

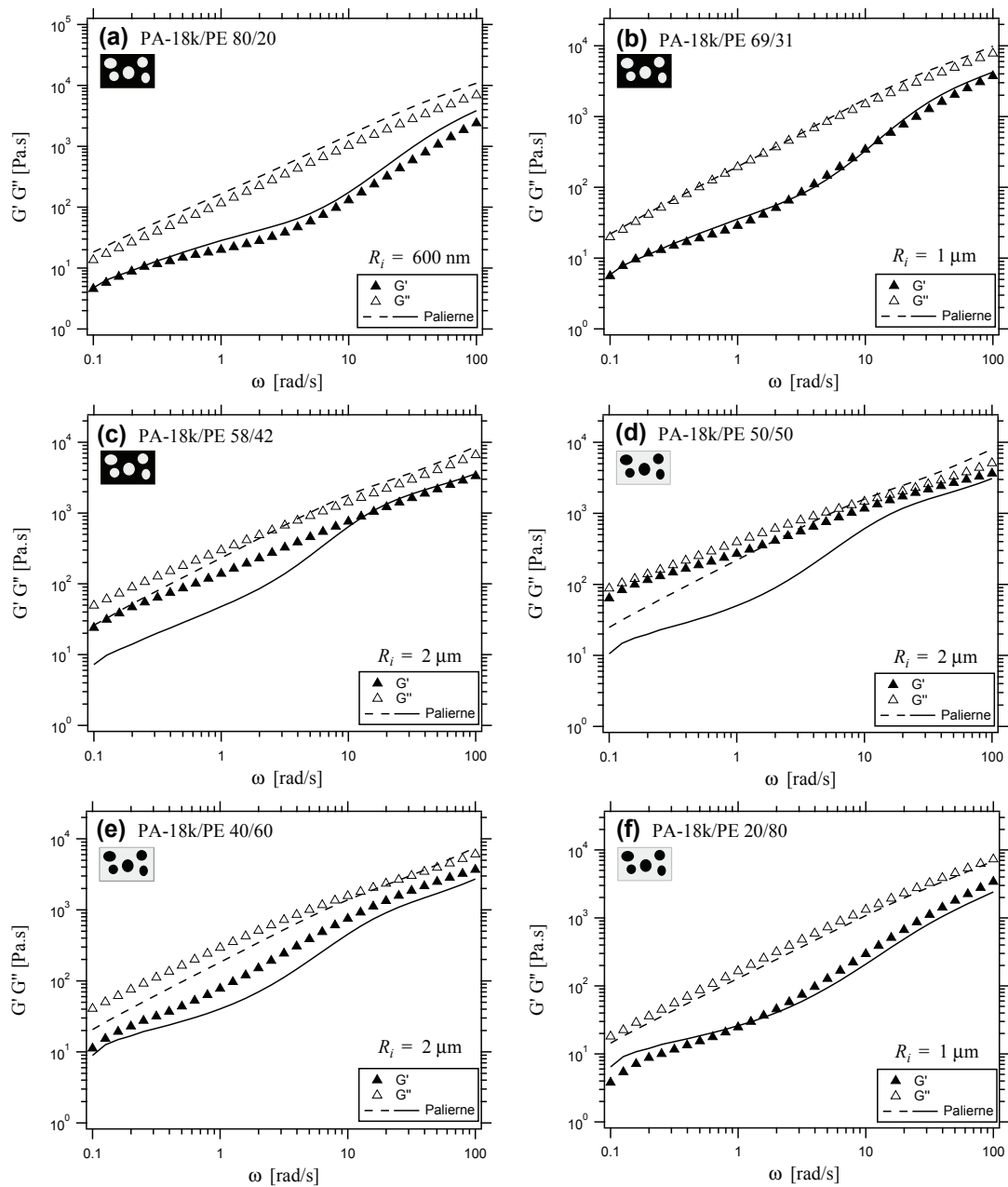


Figure 5.18: Comparison for PA6-18k/HDPE blends between elastic modulus  $G'$  (solid triangle) and loss modulus  $G''$  (empty triangle) and the prediction of the simplified Palierne's model for the elastic modulus (solid line) and loss modulus (dashed line) of equation 5.10 as a function of the frequency  $\omega$ . The interfacial tension is  $\Gamma=10\text{mN/m}$  and the value of the average drop radius  $R_i$  is specified for each blend.

Table 5.2: Estimation of  $\lambda_s$  and  $G_s$  for the PA-18k/PE blends with equation 5.11 and 5.12.

PA-18k/PE	80/20	69/31	58/42	50/50	40/60	20/80
	PE ds 18k			18k ds PE		
$R_i$ [m]	6.00E-07	1.00E-06	2.00E-06	2.00E-06	2.00E-06	1.00E-06
$\phi_d$ [%vol]	0.20	0.31	0.42	0.50	0.40	0.20
$\eta_m^*$ [Pa.s]	105	105	105	60	60	60
$\Gamma$ [N/m]	0.01	0.01	0.01	0.01	0.01	0.01
$R_{v 100 \text{ rad/s}}$	0.60	0.60	0.60	1.70	1.70	1.70
$\lambda_s$ [s]	0.01	0.02	0.06	0.05	0.05	0.02
$\lambda_s^{-1}$ [rad/s]	74	40	18	20	22	51
$G_s$ [Pa.s]	3507	3134	2041	1539	1173	1068

rad/s and between 1000 and 3500 Pa.s, are in qualitative agreement shoulders observed on  $G'$  moduli. In this frequency range, dynamical moduli are not affected by the presence of gas bubbles, these shoulders could thus be attributed to droplet shape relaxation.

**For more concentrated blend PA-18k/PE 40/60** (figure 5.18 (e)), the model underestimates a little the values of  $G'$  and  $G''$ . However, the shoulder observed between 10 and 100rad/s is well consistent with the Palierne's prediction of  $\lambda_s^{-1}$  and  $G_s$  with Palierne's model (see table 5.1). It could thus be attributed to droplet shape relaxation.

Nevertheless, **for the more concentrated blends** (blend PA-18k/PE 58/42 and 50/50, figure 5.18 (c) and (d)), Palierne's model do not predict the linear viscoelastic behaviour in the whole frequency range. Indeed, at high frequency ( $\sim 100$  rad/s) predictions are in agreement with experimental measurements. However, at lower frequencies, the model underestimates values of both  $G'$  and  $G''$ ; the gel-like behaviour is not predicted. The gel-like behaviour of both blends denote the presence of long range connectivities, which leads to a wide distribution of relaxation times, probably involved in the dynamical rheological behaviour.

Castro et al. [30] observed the same behaviour for immiscible uncompatibilized PEO/PVdF-HFP blends. They studied binary blends in the whole composition range and noticed a power law behaviour of the  $G'$  and  $G''$  of two blends, corresponding to the limiting compositions of the co-continuity domain. The microscopic characterization of both blends showed that the dispersed phase was very inhomogeneous with very thin nodules observed concomitantly to large elongated domains. A micrograph of one of the critical composition exhibiting a gel-like behaviour (PEO 25%) is shown in figure 5.19 (after PEO etching). They supposed that elongated domains may even form a 3D paths across the whole sample. They explained the power law dependence of  $G'$  and  $G''$  by the fractal nature of the blend morphology.

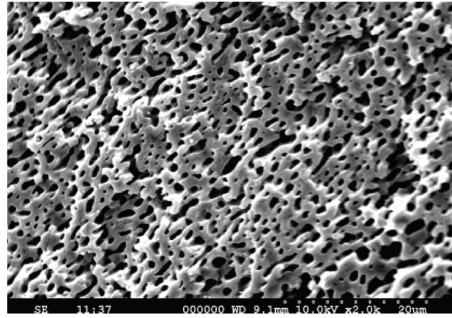


Figure 5.19: SEM micrograph of a PEO/PVdF-HFP blend containing 25% of PEO (after extraction of PEO): limiting compositions of the co-continuity domain[30].

This explanation might be valid in our case, since a fraction of droplets may coalesce and form some 3D path throughout the sample during the rheological measurement. However, our initial morphologies exhibit much more nodular droplets, with more homogeneous sizes as shown in figure 5.20. **Thus, we propose here another explanation of the gel-like behaviour observed that has not been discussed before. Because of the large droplets volume fraction, cooperative relaxation of neighbouring droplets may happen.** Indeed, in figure 5.20, we observe that droplets are very close to each other. This explanation is consistent with the fact that a model like Krieger and Dougherty (modified KD model discussed in subsection 3.1) describes accurately the measured viscosities. Indeed, this model was originally designed to describe the hydrodynamic interactions between droplets and their cooperativity.

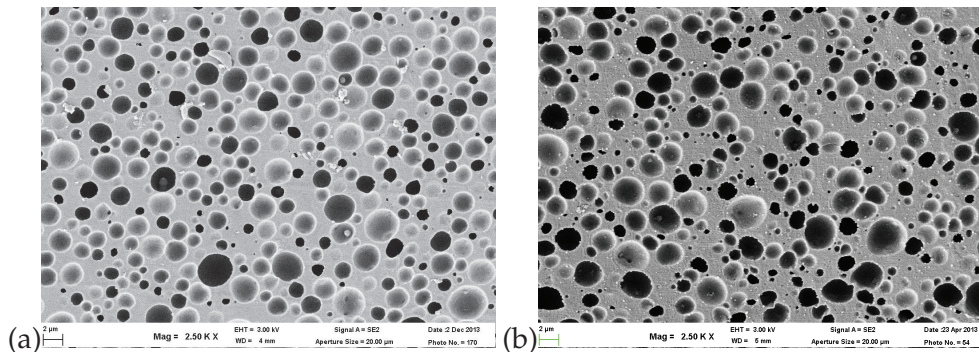


Figure 5.20: SEM micrographs of a PA6-18k/HDPE blends. (a) blend PA-18k/PE 58/42 (after PE etching) and (b) PA-18k/PE 50/50 (after PA etching). Both blends exhibit a gel-like behaviour and are the most concentrated compositions analysed before phase inversion.

#### 3.2.3 Blends with PA6-31k

##### Observations

The linear viscoelastic behaviour of uncompatibilized binary PA6-31k/HDPE blends, elastic modulus  $G'$  and loss modulus  $G''$ , are presented as a function of  $\omega$  in Figure 5.21.

In this case only the storage modulus  $G'$  of pure HDPE is perturbed by the presence of gas bubbles. When HDPE is the matrix phase, only  $G'$  measurements at frequencies higher than  $\sim 5$  rad/s or with values higher than  $\sim 10$  Pa.s are not affected by gas bubbles.

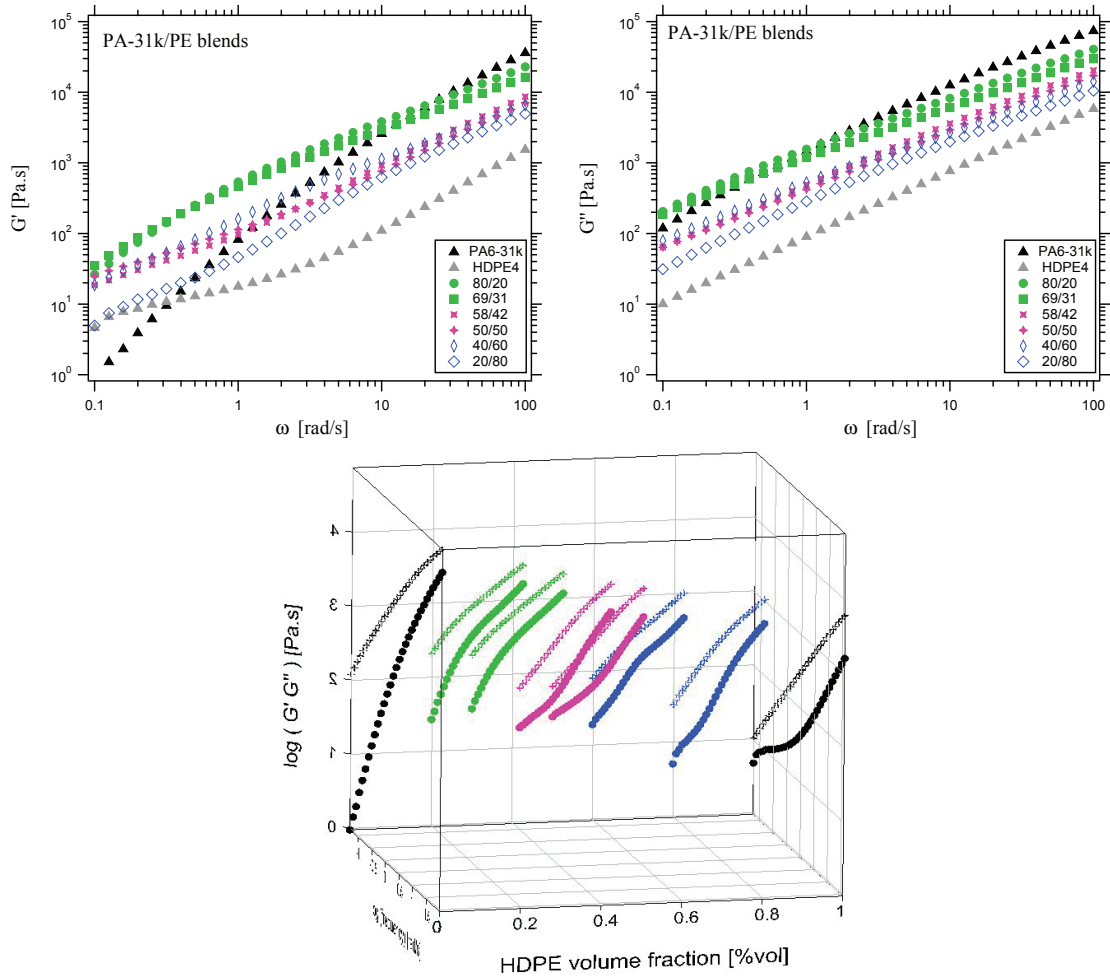


Figure 5.21: Linear viscoelastic behaviour of uncompatibilized binary PA-31k/PE blends. Elastic modulus  $G'$  (left) and loss modulus  $G''$  (right) as a function of the frequency  $\omega$ . Measurements performed at 290 °C. Full symbols (green) correspond to the morphology of dispersion of PE into a PA matrix, crosses (pink) to co-continuous morphology, and empty symbols (blue) to dispersion of PA into a PE matrix.

For blends exhibiting PE droplets in PA (blends 80/20 and 69/31 5.23 (a) and (b)) at high frequencies ( $10 < \omega < 100 \text{ rad/s}$ ),  $G'$  and  $G''$  decreases with  $\phi_d$  compared to pure PA6-31k, on approaching compositions of the co-continuity domain. However at low frequencies ( $0.1 < \omega < 10 \text{ rad/s}$ ),  $G'$  and  $G''$  increases with  $\phi_d$ .

For both blends exhibiting PA droplets in PE (blends 40/60 and 20/80 5.23 (e) and (f)),  $G'$  and  $G''$  increase with  $\phi_d$  in the whole frequency window, and  $G'$  increases particularly at low frequencies on approaching the compositions of the co-continuity domain, .

For both co-continuous blends PA-31k/PE 50/50 and 58/42 (figure 5.23 (c) and (d)) the rheological behaviour is different from the others. At high frequency the moduli vary quite linearly with blend composition following the 'no relaxation KD model' (see discussion in subsec. 3.1). However, at low frequencies, while both  $G'$  and  $G''$  were increasing with  $\phi_d$  for less concentrated blends, for both co-continuous blends, they exhibit lower values . The variation of both  $G'$  and  $G''$  at 1 rad/s is given in figure 5.22.

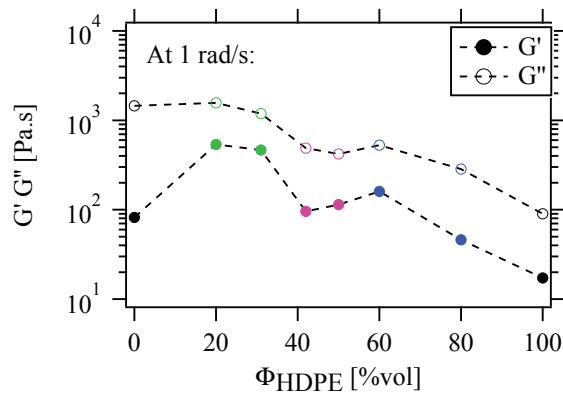


Figure 5.22: Variation of both  $G'$  and  $G''$  for PA6-31k/HDPE blends at 1 rad/s. Green circles: PA droplets in PE, pink, co-continuous morphologies and blue PE droplets in PA matrix.

### Discussion, modelling

Experimental results are compared to the simplified Palierne's model (see equation 5.10 in section 1). Results are presented as a function of the frequency  $\omega$  for each individual blends in figure 5.23.

**For blends with PA6-31k matrix** (blends PA-31k/PE 80/20 and 69/31 (figure 5.23 (a) and (b)), are quite satisfactorily described by the Palierne's model. However, shoulders observed in experimental results are larger than shoulders predicted by Palierne's model. This may arise from the large polydispersity in size of the droplets observed in real experiments, which induce a distribution of droplet shape relaxation times, which is here too large to be taken into account in Palierne's model. Note that for these specific cases, several average droplet sizes were tested for the fits, from  $1\mu\text{m}$  to  $10\mu\text{m}$ : when  $R_i$  increase, the value of  $\lambda_s$  increases and the value of the plateau  $G_s$  decreases. All fits described well a part of the large shoulder observed on the  $G'$  measurement. Estimations of  $\lambda_s$  and  $G_s$  are consistent with experimental measurement of the shoulder observed. This analysis attests that the large shoulder should be attributed to the consequence of droplet shape relaxation.

**For blends with HDPE matrix** (blends PA-31k/PE 20/80 and 40/60 (figure 5.23 (f) and (e)), values of  $G'$  and  $G''$  are underestimated. In that case, the viscosity of the dispersions are higher than the viscosities of the matrix ( $R_v > 1$ ). The situation is similar to the case studied for blends with PA6-3k, even if the viscosity difference between droplets and matrix is much closer to one ( $R_v \approx 300$  for blends with PA6-3k and  $R_v \approx 13$  in the present case). Thus as it was suggested for blends with PA6-3k, when a sollicitation is applied to a blends with more viscous droplets in a less viscous matrix, this may increases the mean blend viscosity due to unfavourable drainage regimes.

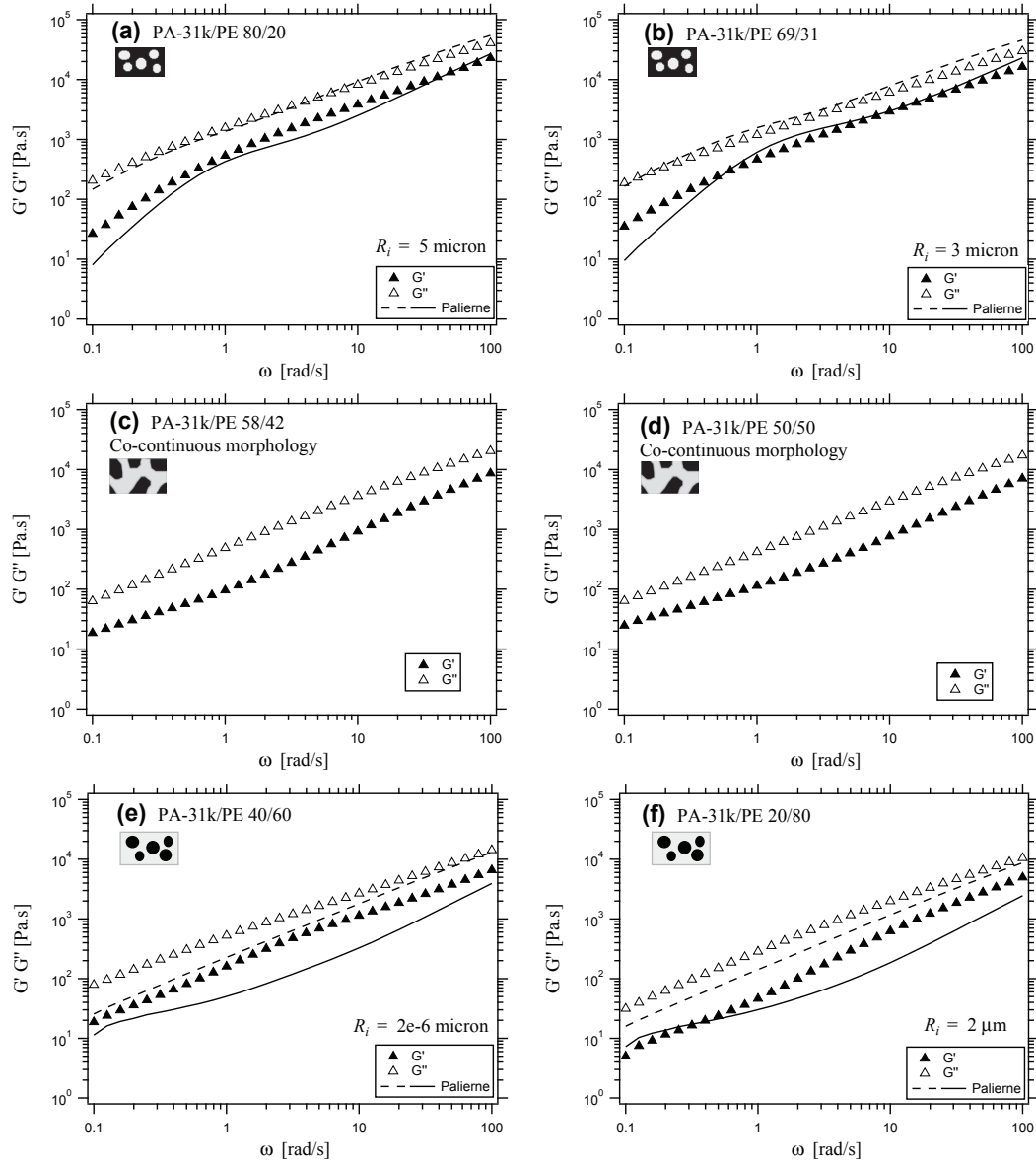


Figure 5.23: Comparison for PA6-31k/HDPE blends between elastic modulus  $G'$  (solid triangle) and loss modulus  $G''$  (empty triangle) and the prediction of the simplified Palieme's model for the elastic modulus (solid line) and loss modulus (dashed line) of equation 5.10 as a function of the frequency  $\omega$ . The interfacial tension  $\Gamma=10\text{mN/m}$  and the value of the average drop radius  $R_i$  is specified for each blend.

### 3. Uncompatibilized blends

Table 5.3: Estimation of  $\lambda_s$  and  $G_s$  for the PA-31k/PE blends with equation 5.11 and 5.12.

PA-31k/PE	80/20 PE ds 31k	69/31	58/42	50/50 31k ds PE	40/60	20/80
$R_i$ [m]	5.00E-06	3.00E-06			2.00E-06	2.00E-06
$\phi_d$ [%vol]	0.2	0.31			0.4	0.2
$\eta_m^*$ [Pa.s]	820	820	co-	co-	60	60
$\Gamma$ [N/m]	0.01	0.01	continuous	continuous	0.01	0.01
$R_{v100}$ rad/s	0.07	0.07			13	13
$\lambda_s$ [s]	0.64	0.43			0.18	0.17
$\lambda_s^{-1}$ [rad/s]	2	2			6	6
$G_s$ [Pa.s]	649	1496			106	34

**For both co-continuous blends** PA-31k/PE 50/50 and 58/42 (figure 5.23 (c) and (d)) the decrease in the  $G'$  coincided with the creation of continuous phases. This phenomenon has also been observed by Castro et al. [29] in the PEO/PVdF-HFP blends. They reported that the aspect of the  $G'$  curve as a function of the composition was very similar to the evolution of interfacial area measured by image analysis which decreases in co-continuous blends.

An hypothesis to explain why the moduli for both co-continuous blends, do not increase as much as for droplets in matrix morphologies at low frequencies may be the following: For co-continuous structures with no compatibilizer at the interface, while a small deformation is applied in the melt state, one may rather observe a global re-organization of the global structure because all domains are supposed to be interconnected. There is thus no creation of interfacial area and thus no relaxation associated compared to the case of deformed droplets. This phenomenon is known in lyotropic continuous phases in which the morphology can be sheared without increasing the surface area [161]. Thus the modulus associated with the shearing of a co-continuous structure is close to zero.

### 3.3 Conclusions

We have studied the dependence of the viscoelastic behaviour of uncompatibilized blends on the composition and the frequency. Our objective was to understand the various complex trends observed in the rheological behaviour of all blends. In this work, despite shoulders observed for pure blends components, we observed strong correlations between blends morphologies and linear rheological behaviours thanks to different models. We were aware that some degree of coalescence may occur during the frequency sweep test. A modest fraction of large droplets may appear in some cases. We assumed that they do not contribute significantly to the results because the relative fraction of associated area is small.

In this study **we applied and completed the model proposed by Janssen et al. [10] to describe the viscosity evolution as a function of the composition.** Indeed, the version proposed by Janssen et al. is only valid at frequencies lower than droplet shape relaxation ( 'modified KD model', equation 5.32). The second version proposed in this

work was valid at high frequencies when droplets do not have enough time to relax ('no relaxation KD model' (eq. 5.34). **This models was successfully applied in the whole composition range when  $R_v < 1$  or  $R_v = 1$ .** However **it should be valid only for uncompatibilized blends** since only the phenomenon of droplet shape relaxation is taken into account.

**We have confirmed that Palierne's model could only be used in the case of diluted blends,  $\phi_d > \sim 30\%$  vol.** The model was **successfully applied only when  $R_v < 1$  or  $R_v = 1$ .** Within this composition range, all phenomena of droplet shape relaxation were observed within the frequency range not perturbed by the presence of gas bubbles. For more concentrated blends, other relaxation phenomena that could be observed in blends are not taken into account in this model. Two interesting observations have been made:

- For compositions very close to phase inversion composition, we observed a nearly gel-like behaviour suggesting strong interaction between droplets that could be cooperative relaxation of neighbouring droplets.
- Besides, we observed a decrease in both  $G'$  and  $G''$  for co-continuous blends as reported by [29].

When  $R_v > 1$ , **both models underestimate the experimental values.** We argued that the higher values measured could not come from droplet shape relaxations. We have no clear explanation for this observation, but we made the hypothesis that the overall viscosity was significantly larger than predicted by models, because very viscous droplets are added to a fluid matrix when  $R_v > 1$ .

This work was necessary to understand the various complex additional relaxation processes that may be observed in compatibilized blends. All uncompatibilized blends studied in this first part constitute the references for the compatibilized blends studied in next section.

## 4 Compatibilized blend

### 4.1 Evolution of the viscosity with the concentration

#### 4.1.1 Experimental results

Figure 5.24 shows dynamical viscosities  $\eta^*$  of compatibilized blends at high (100 rad/s) and low (1rad/s) frequencies as a function of blend composition for the three blend series.

The viscosity evolutions at both high and low frequencies are very different from those of uncompatibilized blends (see section:3.1). For PA6-31k/MA-g-HDPE blends at 100rad/s viscosities evolve quite monotonically with composition. However, for all the other cases, the complex viscosity increases at both low and high frequency compared to pure component on approaching phase inversion composition. A strongly non monotonic variation with  $\phi_d$  is observed in almost all cases at low frequencies, especially for blends with a MA-g-HDPE matrix.

#### 4.1.2 Discussion

In order to analyse the viscosity evolution as a function of the blend composition, experimental results were compared the 'no relaxation KD model' (eq. 5.34) and the 'modified KD model' (eq. 5.32). Results are reported on figure 5.24.

Main conclusion are:

- **At high frequencies (100 rad/s)** (figure 5.24 (a),(c) and (e)) different cases were observed:
  - For blends with PA6-31k, the more diluted blends are well described by the 'modified KD model' and the more concentrated blend by the 'no relaxation KD model'.
  - For blends with PA6-18k, the viscosity evolution is remarkably well described by the 'modified KD model'.
  - For blends with PA6-3k, the modified KD model underestimates the experimental viscosity measurement.
- **A low frequencies (1 rad/s)**, predictions of the modified KD model model were, in all cases, much lower than the measured viscosities.

Figure 5.25 shows a comparison between the viscosity evolution as a function of the composition at 100 rad/s and 1 rad/s for uncompatibilized PA6-18k/HDPE blends and compatibilized PA6-18k/MA-g-HDPE blends. For compatibilized blends we see that the viscosity increases even at 100 rad/s. An explanation could be that, according to eq. 5.11 which allows to estimate the droplet shape relaxation time, when the droplet sizes  $R$  decreases,  $\lambda_s$  decreases and thus  $\lambda_s^{-1}$  increases. Thus because average sizes have decreased in compatibilized blends, droplet shape relaxation happened at higher frequencies, and the increase in viscosity on approaching phase inversion at 100 rad/s is consistent with an increase due to droplet shape relaxation. This would also be consistent with the fact that the modified KD model prediction predicts the viscosity. However the viscosities measured at low frequencies for the compatibilized blends are much higher. The evolution is characteristic of a viscosity increase observed, for example, in case of emulsions

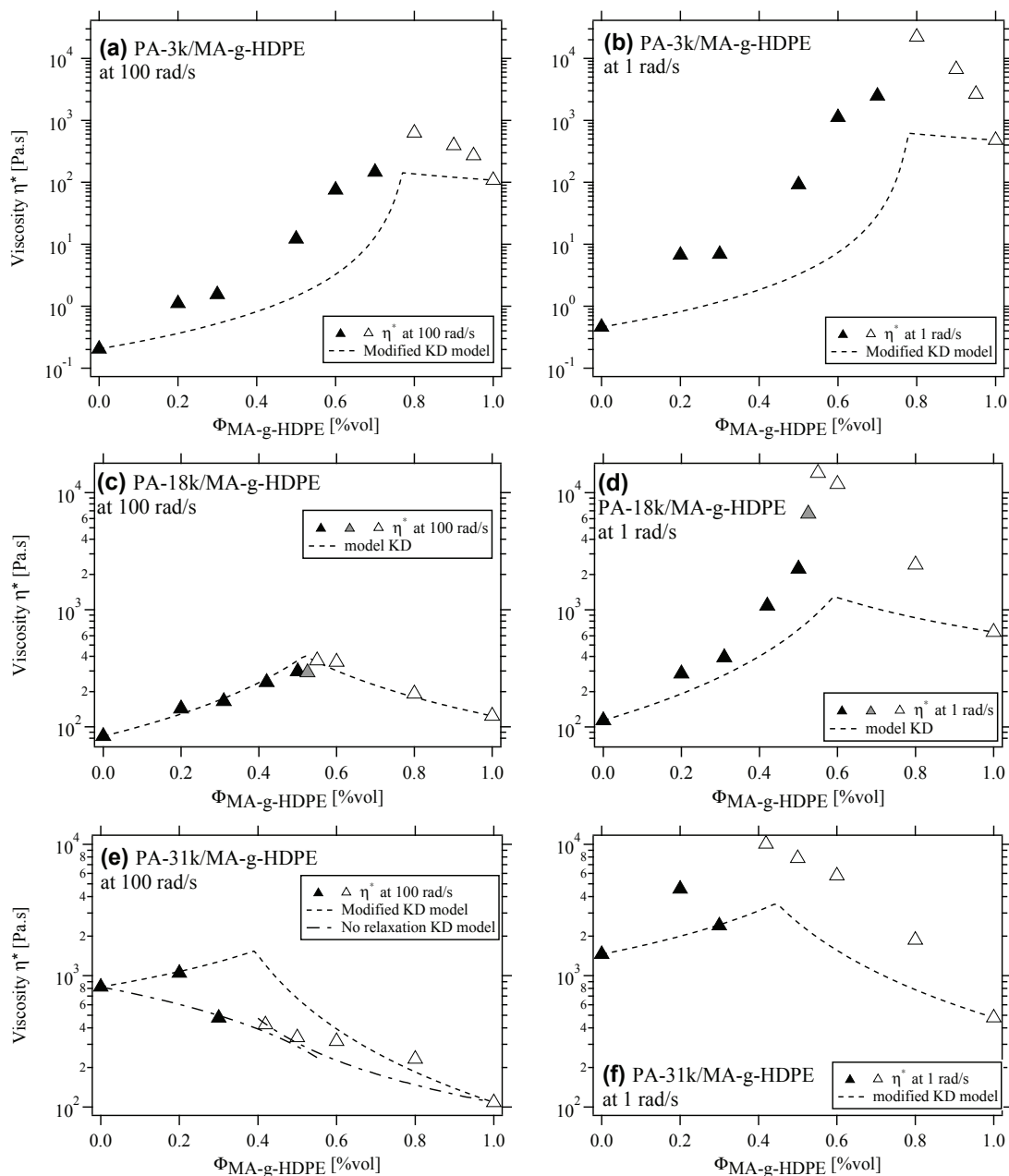


Figure 5.24: Dynamic viscosity (triangles) of PA-3k/MAGPE (a) and (b), PA-18k/MAGPE (c) and (d) and PA-31k/MAGPE (e) and (f) of compatibilized binary blends measured by cone-plate rheometry: left column, results at 100rad/s and right column, results at 1rad/s. Symbols correspond to different morphologies: black triangles, dispersions of PE in PA, grey triangle, co-continuous morphologies and white triangles, dispersions of PA in PE matrix. Mixing rules calculated from the viscosity of pure components are represented: the modified KD model ('modified KD model', equation 5.32- dashed line) and the 'no relaxation KD model' ('no relaxation KD model' (eq. 5.34- dash and dots line).

when interactions (of different natures) are present between droplets. This strongly suggests that interactions between droplet are responsible of the large increase toward the phase inversion composition.

The complete Palierne's model is supposed to describe, in addition to droplet shape relaxations, relaxations associated to the presence of copolymers at the interface (shear and dilatation modulus, see section 1 subsection 1.3). The analysis of the linear viscoelastic behaviour of compatibilized blends as a function of the frequency based on this model should allow to investigate if the very large viscosity enhancement observed for the 3 blends series could be attributed to the presence of copolymers at the interface or, as suggested above, to even stronger interactions.

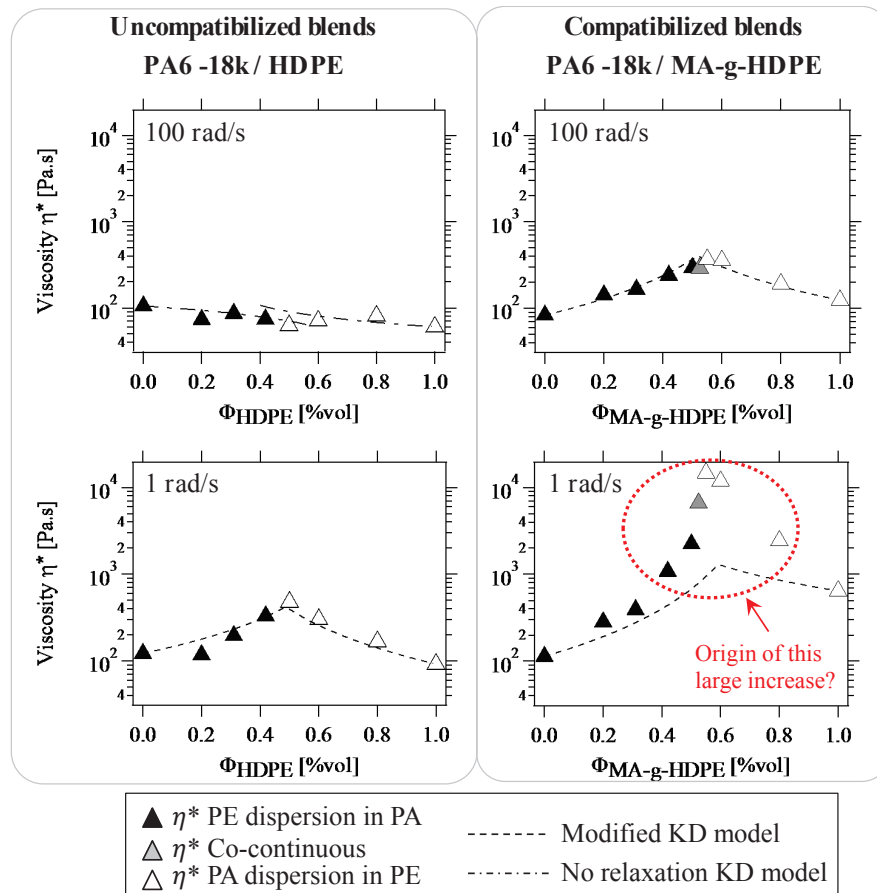


Figure 5.25: Comparison between viscosity evolution as a function of the composition at 100 rad/s and 1 rad/s for uncompatibilized PA6-18k/HDPE blends and compatibilized PA6-18k/MA-g-HDPE blends.

## 4.2 Linear viscoelastic behaviour of compatibilized blends as a function of the frequency

In this section, the linear viscoelastic behaviour of compatibilized blends PA6-3k/MA-g-HDPE, PA6-18k/MA-g-HDPE and PA6-31k/MA-g-HDPE is studied. The variation of the elastic modulus  $G'$  and loss modulus  $G''$  is presented as a function of the frequency  $\omega$ .

The viscoelastic response of blends will be discussed in relation to the blend morphologies which have been described in detail in chapter 4 and are reminded in figure 5.11 section 2.

#### 4.2.1 Blends with PA6-18k

##### Observations

The linear viscoelastic behaviour of compatibilized binary PA6-18k/MA-g-HDPE blends is presented as a function of  $\omega$  in Figure 5.26. Better visualization of the relative positions of  $G'$  and  $G''$  is possible in figure 5.27.

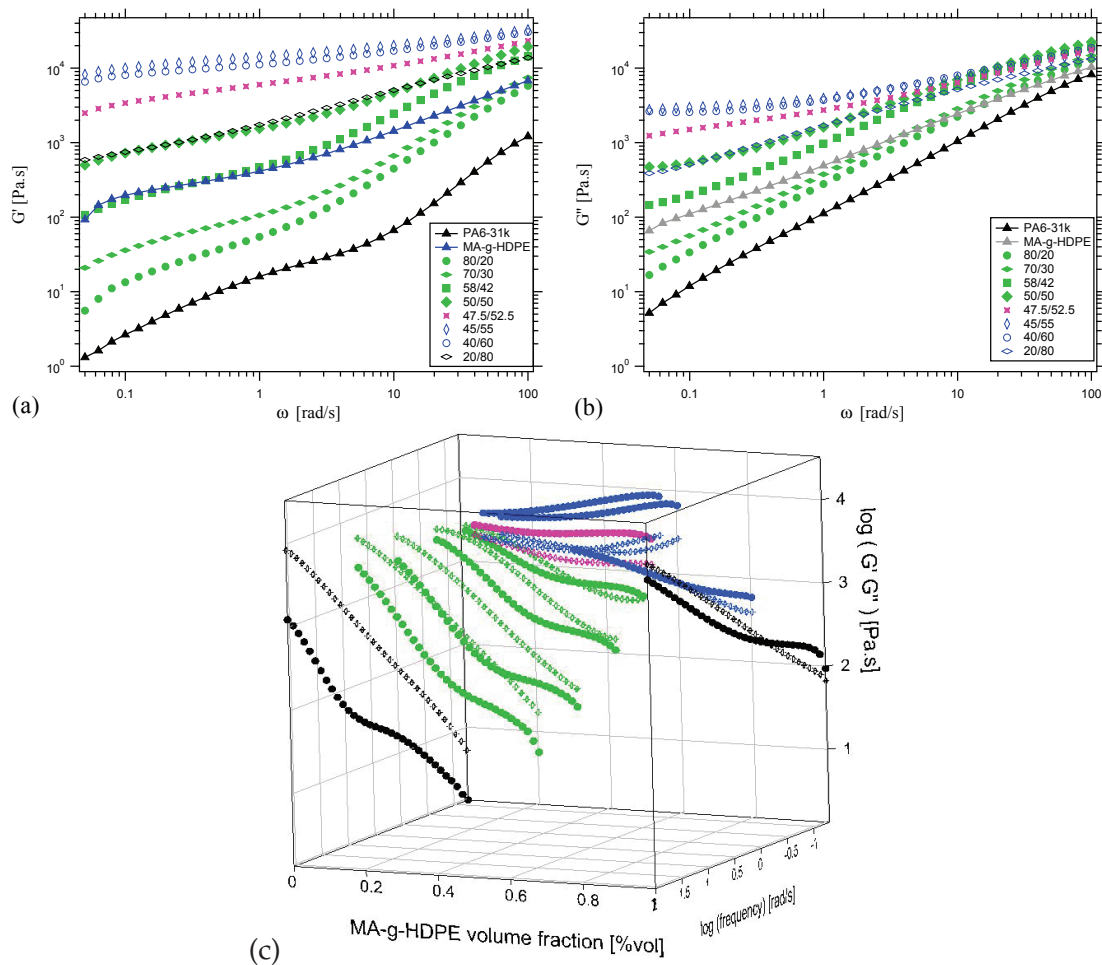


Figure 5.26: Linear viscoelastic behaviour of compatibilized binary PA-18k/PE blends. Elastic modulus  $G'$  (a) and loss modulus  $G''$  (b) and 3D representation of  $G'$  and  $G''$  as a function of the frequency  $\omega$ . Measurements performed at 290 °C. Full symbols (green) correspond to the morphology of dispersion of PE into a PA matrix, crosses (pink) to co-continuous morphology, and empty symbols (blue) to dispersion of PA into a PE matrix.

The presence of gas bubbles in pure components (PA6-18k and HDPE) does not affect the storage moduli  $G''$  in the frequency range studied. However, when PA6-18k is the

matrix phase, only  $G'$  measurements at frequencies higher than  $\sim 10$  rad/s or with values higher than  $\sim 10$  Pa.s are not affected by gas bubbles in this phase. When MA-g-HDPE is the matrix phase, only  $G'$  measurements at frequencies higher than  $\sim 5$  rad/s or with values higher than  $\sim 100$  Pa.s are not affected by gas bubbles in this phase.

The general tendency shows that values of  $G'$  and  $G''$  increase with  $\phi_d$  on approaching phase inversion composition.

**For blends with PA6-18k matrix** (blends PA-18k/MAGPE 80/20 to 50/50 figure 5.27 (a) to (d)), the shoulder on  $G'$  due to gas bubbles is observed for the more diluted blends and disappears when  $\phi_d$  increases. Despite the shoulder in the middle of the frequency range on  $G'$  values, the slope of both  $G'$  and  $G''$  decreases when  $\phi_d$  increases. The relative position of  $G'$  and  $G''$  also varies from a liquid like behaviour for blend 80/20, 70/30 and 58/42 to a nearly gel like behaviour (in the range between 1 and 100 rad/s) for blend 50/50 for which  $G' \propto G'' \propto \omega^{0.56}$  (see respectively figure 5.27 (a), (b), (c) and (d)).

**For the co-continuous blend** PA-18k/MAGPE 47.5/52.5 (figure 5.27 (e)), the blend exhibit a solid-like behaviour where  $G' > G''$ .

**For blends with MA-g-HDPE matrix** (blends PA-18k/MAGPE 45/55 to 20/80 figure 5.27 (f) to (h)) blend 20/80 (h) exhibits the behaviour of a blend at the gel point where  $G'$  is almost equal to  $G''$ ,  $G' = G'' \propto \omega^{0.3}$ , between 0.1 and 100 rad/s. For this blend the  $\tan\delta$  is indeed almost independent of the frequency. For blends 40/60 and 45/55 (fig. 5.27 (g) and (f)) the value of  $G'$  overpass the value of  $G''$ , exhibiting a solid-like behaviour. For blend 45/55,  $G' \propto \omega^{0.2}$ .

#### Discussions, modelling

Experimental results are compared to the extended Palierne's model (see equation 5.7 in section 1) calculated using the linear viscoelastic rheological behaviour of pure PA6-18k and MA-g-HDPE and variable parameters chosen as follow:

- Volume fraction  $\phi$ .
- The interfacial tension was taken at  $\Gamma=10^{-3}$ N/m.
- The average nodule size  $R$ : roughly estimated from SEM and TEM pictures and are different for each blends.
- The dilatation shear modulus of the interface is neglected thus  $\beta'(\omega) = 0$  and the interfacial shear modulus  $\beta''(\omega) = 0.001$ N/m[148]. Note that the chosen value for  $\beta''(\omega)$  does not play a key role on our analysis because in almost all cases the measured moduli are much higher than model's predictions.

The comparison between  $G'$  and  $G''$  and the prediction of the complete Palierne's model are presented as a function of the frequency  $\omega$  for each individual blend in figure 5.27. Different parameters,  $\Gamma$  and  $R$ , were tested. Within the range of realistic parameter values, the changes in the model prediction were relatively small and, as it will be seen, none of the tested values allowed to fit the data. Thus, the most consistent parameter values are presented here.

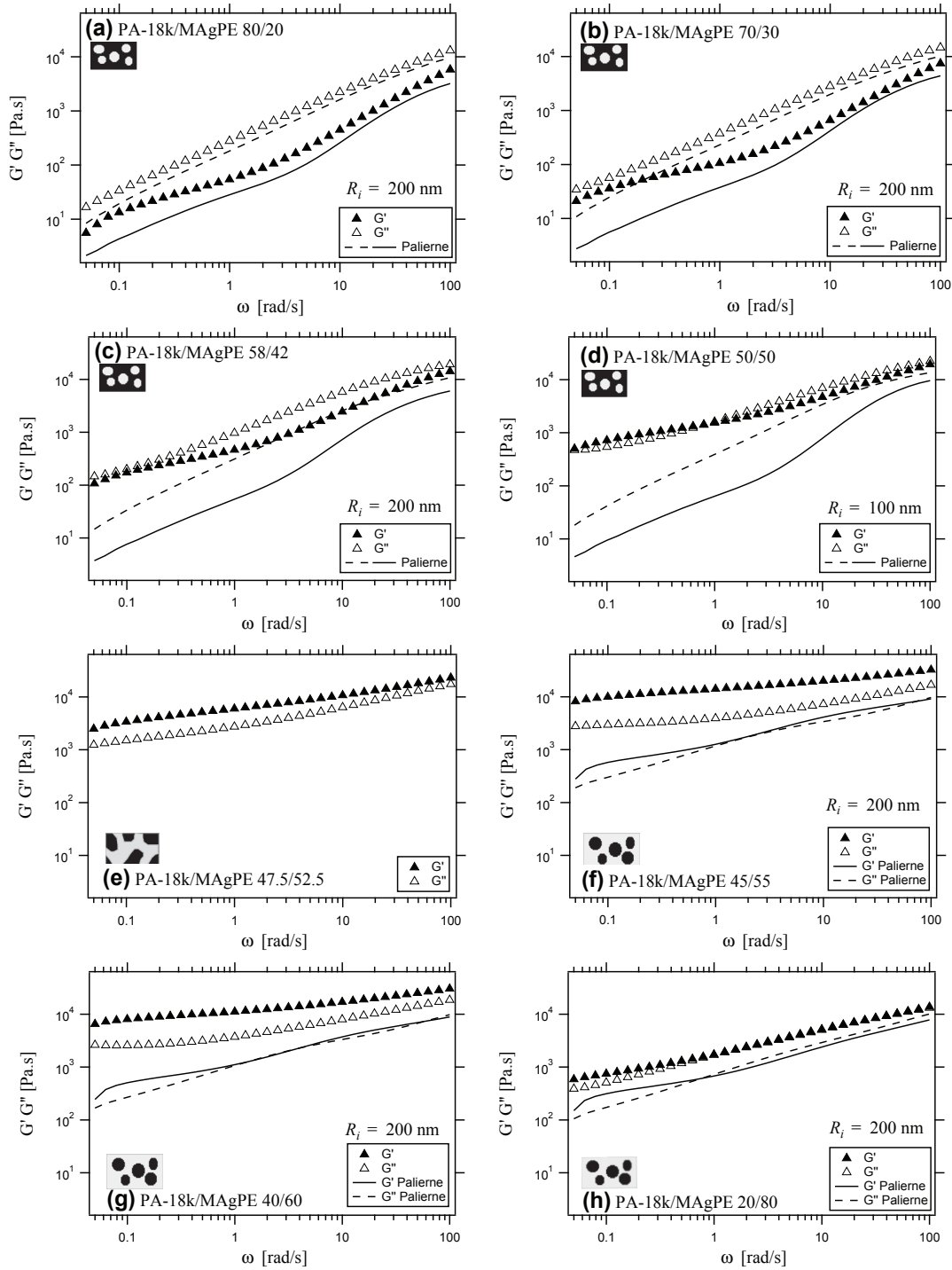


Figure 5.27: Comparison for PA6-18k/MA-g-HDPE blends between elastic modulus  $G'$  (solid triangle) and loss modulus  $G''$  (empty triangle) and the prediction of the complete Palierne's model for the elastic modulus (solid line) and loss modulus (dashed line) (see equation 5.7) as a function of the frequency  $\omega$ . The interfacial tension  $\Gamma = 1 \text{ mN/m}$ ,  $\beta'(\omega) = 0$  and  $\beta''(\omega) = 0.001 \text{ N/m}$ . The value of the average drop radius  $R_i$  is specified for each blend.

The main observation is that **in almost all cases, experimental values are higher than the Palierne's model predictions over the entire frequency range especially at low frequencies.** The difference between model and experimental results increases when  $\phi_d$  increases. Besides we calculated an estimation of relaxation times  $\lambda_s^{-1}$  and value of plateaus  $G_s$  associated to the droplet shape relaxation, as well as the value of  $\lambda_\beta$  associated to the interfacial shear modulus. Both relaxation processes are estimated to be observed within the frequency range from 10 rad/s to 30rad/s and do not justify the large enhancement over the entire frequency rang for almost all blends.

Thus the global morphology of our blends, in which a very large amount of copolymer is created, totally changes the usual relaxations seen in binary blends with a low amount of compatibilizer. **We have here evidences that other relaxation phenomena are responsible of the very large enhancement behaviour of almost all blends.**

Hypothesis on rheological mechanisms will be discussed in subsection 4.3.

### 4.2.2 Blends with PA6-3k

#### Observations

The linear viscoelastic behaviours of compatibilized binary PA6-3k/MA-g-HDPE blends are presented as a function of  $\omega$  in Figures 5.28 and 5.29.

**For blends with PA6-3k matrix** (blends 80/20 to 30/70 figure 5.29 (a) to (e)) we observe that the slope of both  $G'$  and  $G''$  decreases when  $\phi_{MA-g-HDPE}$  increases. Blends 80/20, 70/30 and 50/50 (figure 5.29 (a), (b) and (c)) exhibit a liquid like behaviour. However, blends PA-3k/PE 40/60 and 30/70 (figure 5.29 (d) and (e)) exhibit a gel-like behaviour: for blend 40/60  $G' \propto G'' \propto \omega^{0.45}$  and for blend 30/70  $G'$  overpasses  $G''$  and  $G' \propto G'' \propto \omega^{0.37}$ . For these two blends,  $\tan\delta$  is indeed almost independent of  $\omega$ .

**For blends with a MA-g-HDPE matrix** (blend PA-3k/MAGPE 5/95 to 20/80, figure 5.29 (h), (g) and (f)) exhibiting a PA dispersion in PE matrix the behaviour is also particular. Indeed, for blend 5/95  $\tan\delta$  is almost independent of  $\omega$  and, between 1 and 100rad/s,  $G' = G'' \propto \omega^{0.5}$ . Both blends 10/90 and 20/80 exhibit a solid like behaviour where  $G'$  is much higher than  $G''$ .

#### Discussion, modelling

As for blends with PA6-18k,  $G'$  and  $G''$  of blends with PA6-3k were compared to the complete Palierne's model (see equation 5.7). The Palierne's model was calculated using the linear viscoelastic rheological behaviour of pure PA6-3k and MA-g-HDPE and the same variable parameter as for PA6-18k ( $\Gamma=1\text{mN/m}$ ,  $\beta'(\omega) = 0$ ,  $\beta''(\omega) = 0.001$  and  $R_i$  different for each blends).

The comparison between  $G'$  and  $G''$  and Palierne's model predictions are presented as a function of the frequency  $\omega$  for each individual blend in figure 5.29. As for the case of PA6-18k/MA-g-HDPE blends, experimental results are much higher than Palierne's model predictions. Thus the global morphologies of our blends, in which a very large amount of copolymer is created, totally changes the usual relaxations seen in binary blends with a low amount of compatibilizer. We have here evidences that other relaxation phenomena are responsible for the gel-like behaviour of almost all blends. Hypothesis on rheological mechanisms will be discussed in subsection 4.3.

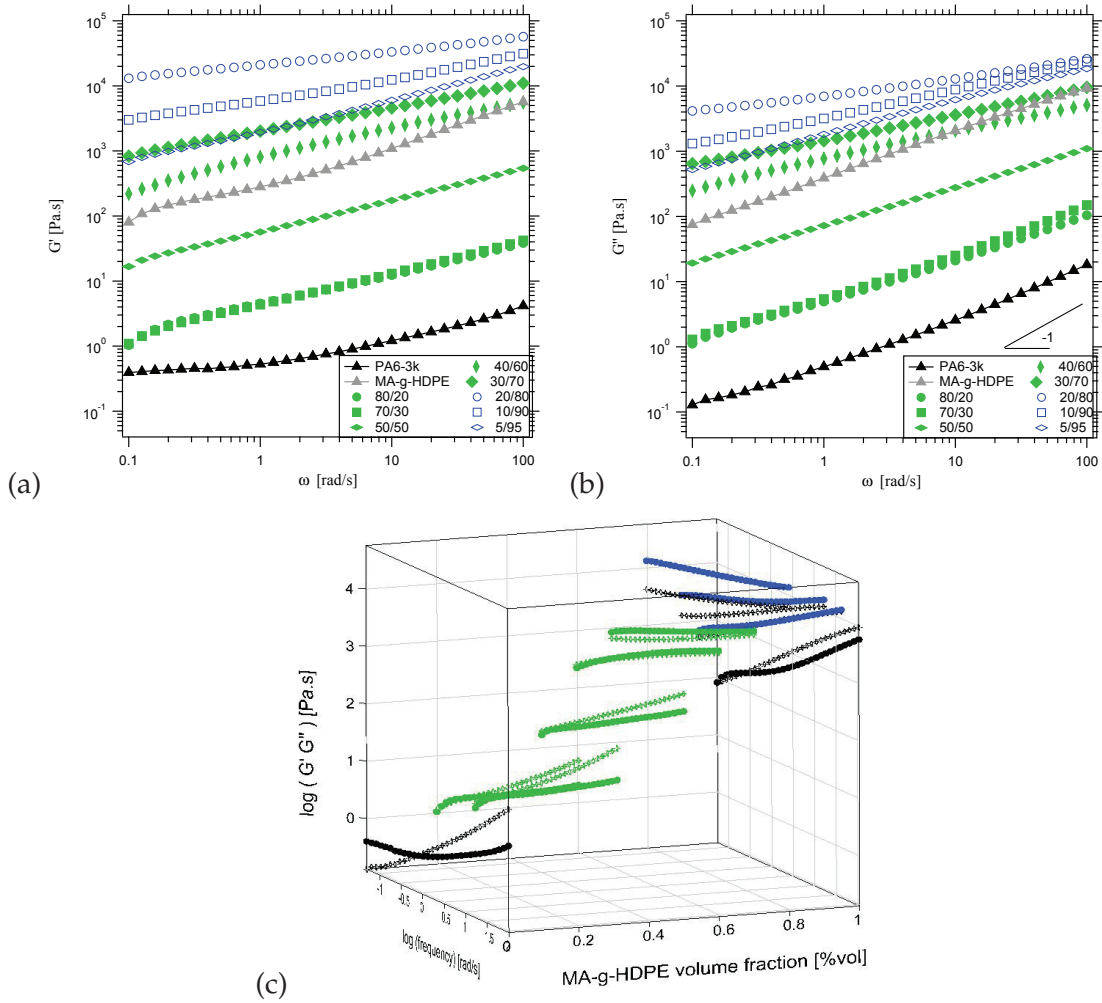


Figure 5.28: Linear viscoelastic behaviour of uncompatibilized binary PA-3k/PE blends. Elastic modulus  $G'$  (a), loss modulus  $G''$  (b) 3D representation of  $G'$  and  $G''$  (c) as a function of the frequency  $\omega$ . Measurements performed at 290 °C. Full symbols (green) correspond to the morphology of dispersion of PE into a PA matrix and empty symbols (blue) to dispersion of PA into a PE matrix.

## 4. Compatibilized blend

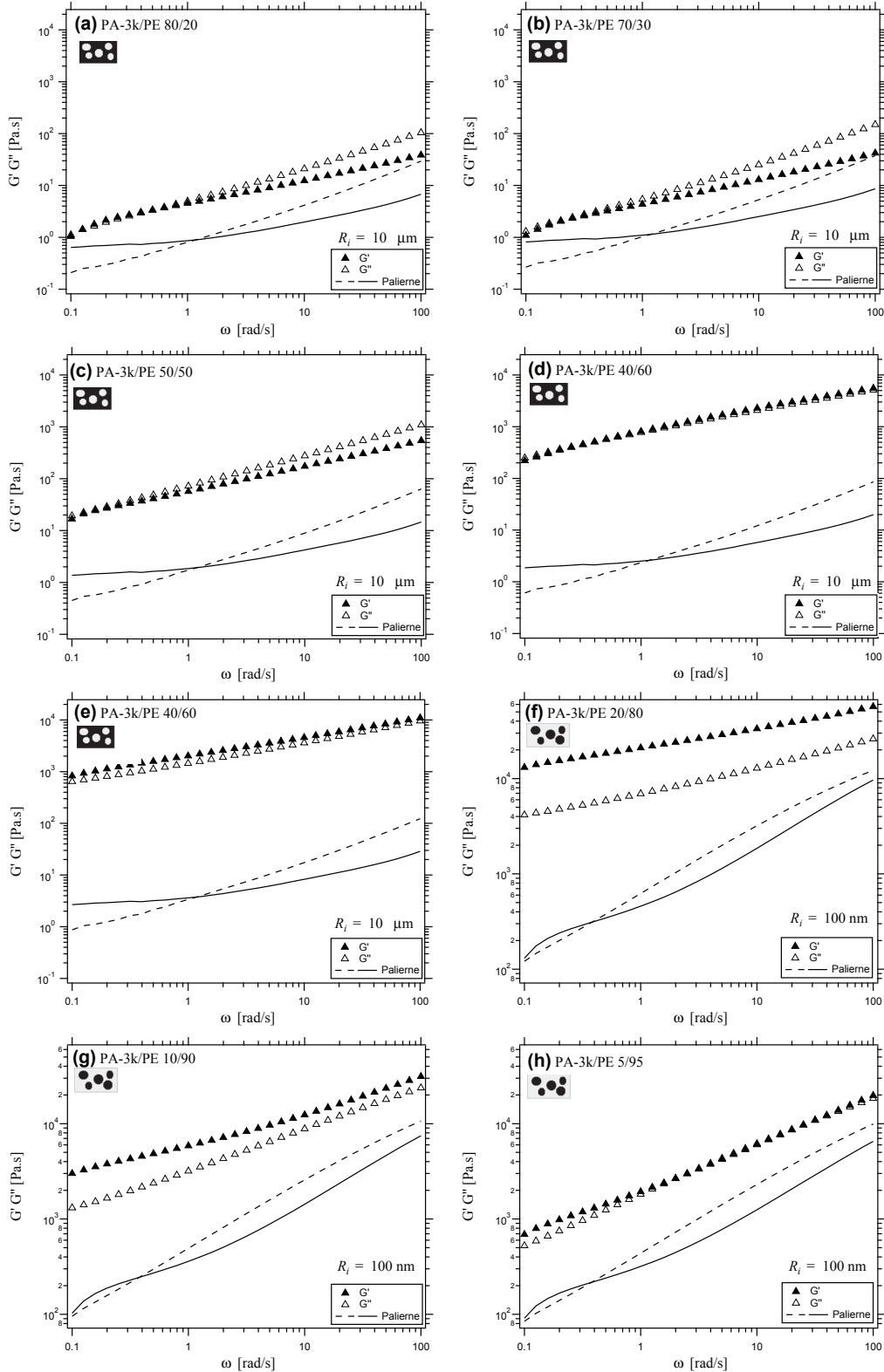


Figure 5.29: Comparison for PA6-3k/MA-g-HDPE blends between elastic modulus  $G'$  (solid triangle) and loss modulus  $G''$  (empty triangle) and the prediction of the complete Palierne's model for the elastic modulus (solid line) and loss modulus (dashed line) (see equation 5.7) as a function of the frequency  $\omega$ . The interfacial tension  $\Gamma=1\text{mN/m}$ ,  $\beta'(\omega) = 0$  and  $\beta''(\omega) = 0.001\text{N/m}$ . The value of the average drop radius  $R_i$  is specified for each blend.

### 4.2.3 Blends with PA6-31k

#### Observations

The linear viscoelastic behaviour of compatibilized binary blends of PA6-31k/MA-g-HDPE are presented as a function of  $\omega$  in figures 5.30 and 5.31.

**Blends with a PA6-31k matrix** (blends PA-31k/MAGPE 80/20 and 70/30 (figure 5.31 (a) and (b)) exhibit a liquid-like behaviour ( $G' < G''$ ) and both viscoelastic moduli  $G'$  and  $G''$  observe a large enhancement at low frequencies.

**Blend PA-31k/MAGPE20/80 with a MA-g-HDPE matrix** (figure 5.31 (f)) shows the typical gel state behaviour:  $G' \sim G'' \sim \omega^{0.54}$ . **The three other blends exhibiting a PA dispersion in PE** (blends PA-31k/MAGPE 40/60 and 58/42, figure 5.31 (c) (d) and (e)) show a solid-like behaviour:  $G'$  overpasses  $G''$  and the slope of  $G'$  decreases between 0.1 and 10 rad/s when  $\phi_d$  increases.

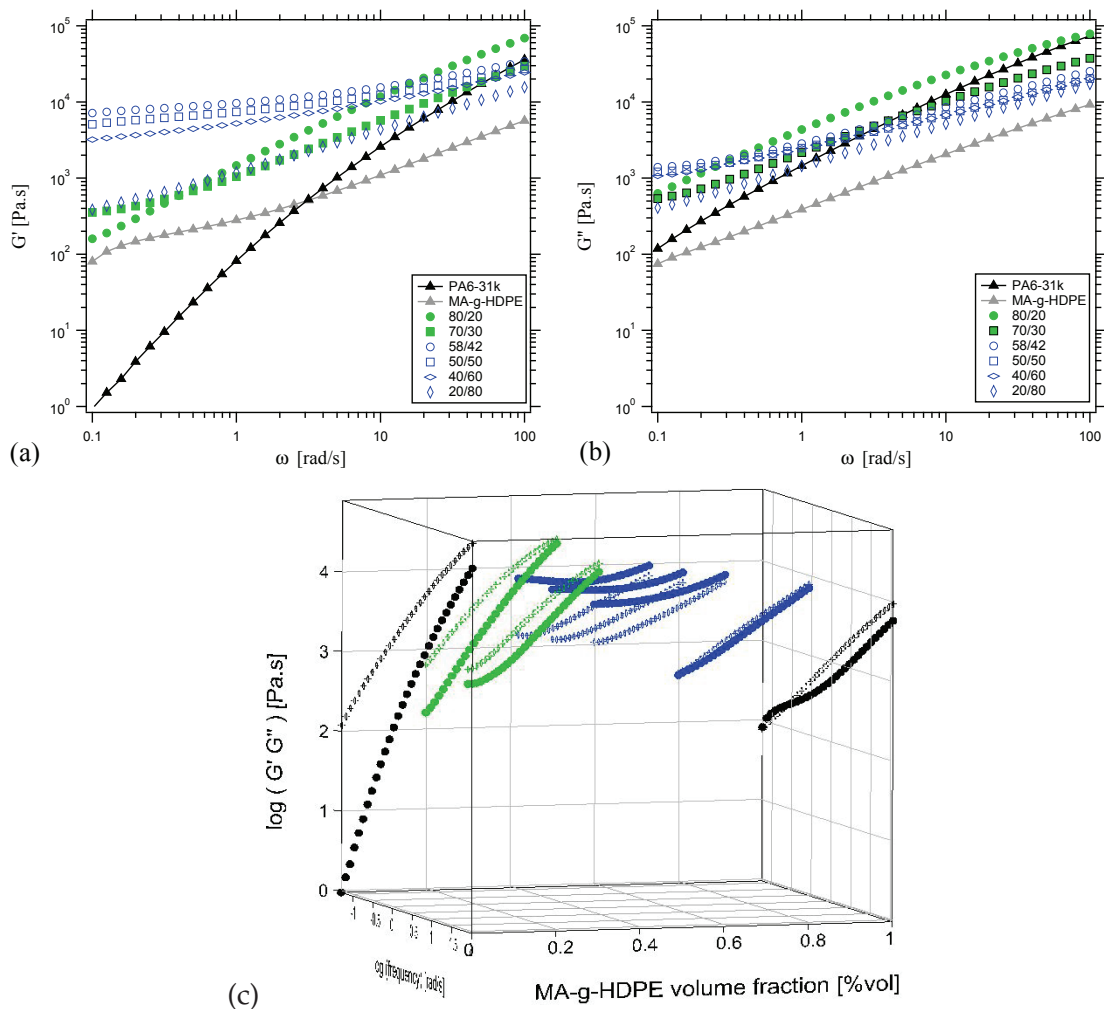


Figure 5.30: Linear viscoelastic behaviour of uncompatibilized binary PA-31k/PE blends. Elastic modulus  $G'$  (a) and loss modulus  $G''$  (b) as a function of the frequency  $\omega$ . Measurements performed at 290 °C. Full symbols (green) correspond to the morphology of dispersion of PE into a PA matrix and empty symbols (blue) to dispersions of PA into a PE matrix.

##### **Discussion, modelling**

$G'$  and  $G''$  of blends with PA6-31k were compared to the complete Palierne's model (see equation 5.7). The Palierne's model was calculated using same variable parameters as for PA6-18k ( $\Gamma=1\text{mN/m}$ ,  $\beta'(\omega) = 0$ ,  $\beta''(\omega) = 0.001$  and different  $R_i$  for each blends).

The comparison between  $G'$  and  $G''$  and Palierne's model predictions are presented as a function of the frequency  $\omega$  for each individual blends in figure 5.23. Once again, we observe that experimental results are higher than the Palierne's model predictions especially at low frequencies where blend moduli are much above prediction. Thus, same conclusions as for blends with PA6-18k and 3k are made and hypothesis on rheological mechanisms will be discussed in subsection 4.3.

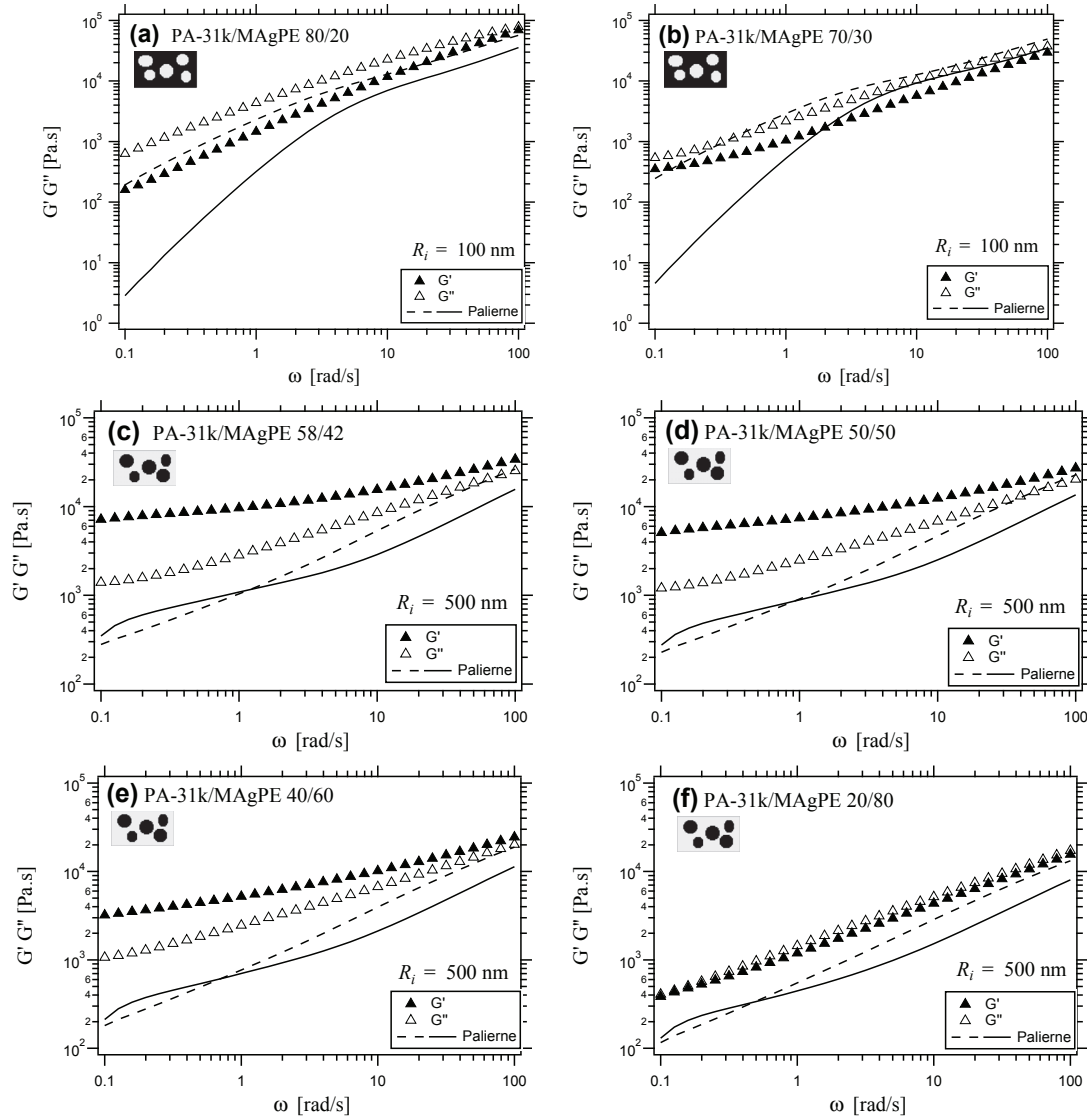


Figure 5.31: Comparison for PA6-31k/MA-g-HDPE blends between elastic modulus  $G'$  (solid triangle) and loss modulus  $G''$  (empty triangle) and the prediction of the complete Palierné's model for the elastic modulus (solid line) and loss modulus (dashed line) (see equation 5.7) as a function of the frequency  $\omega$ . The interfacial tension  $\Gamma=1\text{mN/m}$ ,  $\beta'(\omega) = 0$  and  $\beta''(\omega) = 0.001\text{N/m}$ . The value of the average drop radius  $R_i$  is specified for each blend.

### 4.3 Hypothesis on rheological mechanisms

For the three compatibilized blend series, we have seen that, in almost all cases, the experimental measurement of blends linear rheological behaviours were higher than the prediction of the Palierne's model over the entire frequency range. Indeed, even for dilute blends, the Palierne's model did not describe successfully the linear viscoelastic behaviour. It means that relaxation processes described by Palierne's model (droplet shape relaxation and interfacial relaxation due to the presence of copolymers) are probably not the only relaxation processes involved in the blends rheological response.

Such enhancements of moduli at low frequencies have been observed in several systems: bloc copolymers [162, 163, 164], suspensions of rigid particles [165] and polymer gels [143, 144].

For the three compatibilized blends systems studied in this work the following behaviour was observed:

- For blends with a matrix of PA6, the linear rheological behaviour gets closer to the characteristic description of a gel-like behaviour when the volume fraction of the dispersed phase increased.
- For blends with a matrix of MA-g-HDPE, for concentrated blends  $G'$  may even overpass  $G''$ .

As a consequence, it means that it exists in our material something which creates a "network" able to transmit the stresses imposed on the material. Indeed, isolated droplets are unable to transmit the mechanical energy responsible of the moduli enhancement.

The following tentative of explanation may be proposed: percolating paths having very long relaxation times with a high associated modulus exist in concentrated blends. This percolating network may thus be directly related to the blend morphology. Indeed, we have seen in chapter 4 that when the volume fraction of the dispersed phase is increasing, in all cases, distances between nodules are also decreasing. In some cases, distances are or the order of twice the radius of gyration of the bloc grafted at the interface. Thus nodules may interact with each-other to create this percolating network. The larger the number of contacts, the larger the associated modulus. However the nature of the contacts has to be discussed.

In the case of PA6-18k/MA-g-HDPE and PA6-31k/MA-g-HDPE blends, branches grafted on the outside of nodules may interact with each other as represented in figure 5.32:

- When PA6 grafted branches are on the outside the nature of interactions could be brush entanglement. The entanglement network created due to the proximity of nodules may create the long range connectivity responsible of the stresses transmission. The number of entangled points increases with the concentration due to the larger number of droplets. The system may be able to relax and flow at very long relaxation times. Indeed, PA6 are linear chains with only one reactive end-group which form linear grafted blocks. The hypothetical relaxation time cannot be observed within the experimental frequency window. The network created can be called a "*viscoelastic percolating network*" and is schematically depicted in figure 5.32 (a).

- When MA-g-HDPE branches are outside droplets, (see figure 5.32 b) ) they may entangle or even form trapped entanglements or direct bridges between droplets. This creates a percolating network which cannot, or with low probability, disentangle. This may explain the solid-like behaviour ( $G' > G''$ ) observed in almost all compatibilized blends with a dispersion of PA into a MA-g-HDPE matrix. This hypothesis is also valid in the case of PA6-3k/MA-g-HDPE for blends exhibiting PA6-3k dispersions into MA-g-HDPE matrix.
- For all cases, the slope of  $G'(\omega)$  decreases when  $\phi_d$  increases, thus when the number of "contacts" (entanglements, trapped entanglements or direct bridges) between droplets increases. Thus the more interconnected nodules via "contacts" of external brushes, the higher the value of  $G'$  and the smaller the slope. This is consistent with the behaviour observed in the literature for a gel [145, 163]. The creation of nanodispersions in the systems, helps for the creation of the connectivity between nodules. However, for example, blends with PA6-31k (20/80 to 58/42) which exhibit only few nanodispersions, show that only a very thin distance between nodules combined with a very large density of copolymers at the interface can create the percolating network and exhibit a very large increase in viscoelastic moduli. Figures 5.33 and 5.34 show examples of compatibilized blends in which a viscoelastic percolating network may be created by the entanglement of external brushes.

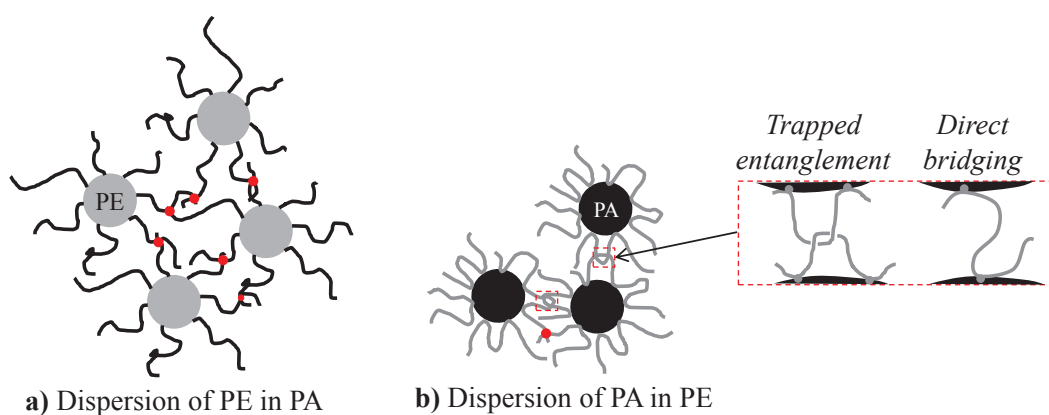


Figure 5.32: Schematic representation of (a) the viscoelastic percolating network created by the entanglement of linear PA6 block copolymer chains grafted on the outside of droplets in reactively compatibilized blends and (b) the percolating network created by entanglement of the grafted HDPE chains and/or trapped entanglements or direct bridging that can be created during blend rheological development.

The nature of the network created by morphologies with droplets of MA-g-HDPE into PA6-3k matrix could hardly be explained by only entanglements. Indeed, the number average molecular weight of PA6-3k ( $M_n \approx 3000 \text{ g/mol}$ ) is close to the molecular weight between entanglements  $M_e \approx 2 \text{ kg/mol}$  [59]. The morphology observed in those blends is particular and exhibits large PE elongated droplets with very thin films of PA6 between droplets. There is thus a large area of contact between copolymer layers at the interface of PE nodules. A storage of energy into the copolymer layer present at the interface may be at the origin of the large moduli enhancement, however, its nature has yet to be defined.

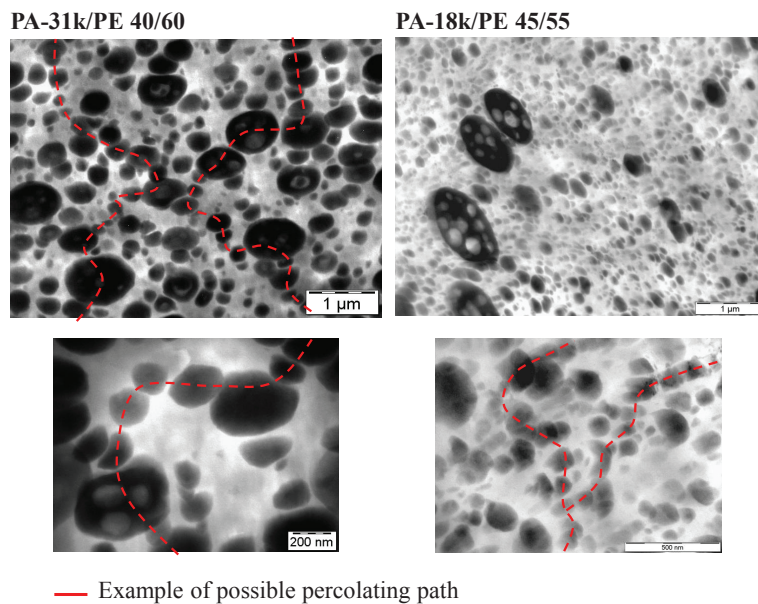


Figure 5.33: Example of compatibilized blends (name and composition on the figure) with MA-g-HDPE matrix, in which a viscoelastic percolating network can be created by the entanglement of MA-g-HDPE chains grafted on the outside of PA6 droplets. A red line has been drawn to guide the eyes.

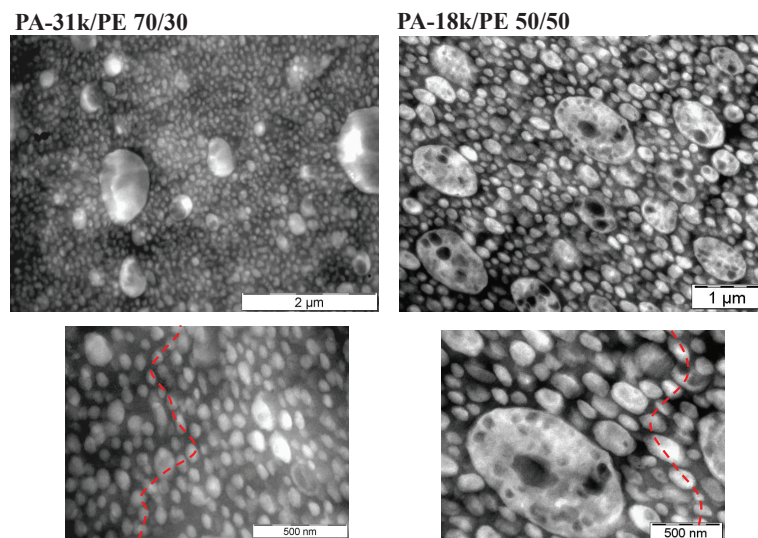


Figure 5.34: Example of compatibilized blends (name and composition on the figure) with a PA6 matrix, in which a viscoelastic percolating network can be created by the entanglement of linear PA6 chains grafted on the outside of PA6 droplets. A red line has been drawn to guide the eyes.

Only few studies have reported such a behaviour for compatibilized polymer blends [166, 112, 167, 168, 169]. Sailer [166, 112] have studied Styrene-acrylonitrile copolymers (SAN) / Polyamide 6 (PA6) blends, reactively compatibilized by styrene-acrylonitrile-maleic anhydride terpolymers (SAMMA), this leads to the creation of graft copolymers at the interface. The molecular weights are respectively  $Mn_{PA6}=23\text{kg/mol}$ ,  $Mn_{SAN}=43.4\text{kg/mol}$  and  $Mn_{SANMA}=52\text{kg/mol}$ . The linear viscoelastic behaviour of blend with PA6/ SAN/ SANMA (70/25.2/4.8%wt with a ratio MA/NH<sub>2</sub>=0.47) exhibit a power law behaviour characteristic for the critical gel state. This blend exhibits a thin SAN dispersion into PA6 matrix. They interpreted the rheological behaviour by a long range connectivity of molecular motions between numerous and close by domains of SAN into PA6. This connectivity being created by molecular interactions between the grafted PA6 grafted chains on SAN domains. **However the nature of these interactions was not explicitly discussed.** Besides, different PA6 chain lengths were not tested.

Maani et al. [169] studied thermoplastic olefin blends of polypropylene (PP) and ethylene octene copolymers (EC) reactively compatibilized. They observed an increase in the storage modulus slope at low frequency when increasing the amount of compatibilization. They attributed this behaviour to copolymers on the interface of each particles, which favours the formation of a percolated structure. **Once again the nature of the interaction was not further discussed.**

Both Sailer et al. and Maani et al. used a modified version of Zener model based on parallel combination of the Maxwell model to fit their data. They succeeded in describing the modulus enhancement at low frequencies. However, this did not give any additional information about the nature of interactions and the reasons for the increase at low frequencies.

## 5 Prediction of phase inversion

### 5.1 Literature on the prediction of phase inversion composition

Various empirical and semi-empirical models have been proposed that relate the composition at phase inversion to the viscosity ratios of the blend components [17, 20, 28].

A first, heuristic model was proposed by Paul and Barlow [170] and then generalized by Miles and Zureck [171]. The volume fractions  $\phi_1$  and  $\phi_2 = 1 - \phi_1$  at phase inversion are directly related to the viscosity ratio,  $R_v$ :

$$R_v = \frac{\eta_1(\dot{\gamma})}{\eta_2(\dot{\gamma})} = \frac{\phi_1}{\phi_2} \quad (5.35)$$

Where  $\eta$  and  $\dot{\gamma}$  are respectively the viscosity and the shear rate.

An alternative model with a more complicated function of the viscosity ratio was developed by Metelkin and Blekht [172]:

$$\frac{\phi_1}{\phi_2} = R_v [1 + 2.25 \ln R_v + 1.81 (\ln R_v)^2] \quad (5.36)$$

D. Bourry et al proposed a model to take into account the elasticity, relating the ratio  $\phi_1/\phi_2$  to the ratio of either the elastic moduli  $G'_i$  or the loss factors  $\tan \delta_i = G''_i/G'_i$  [173]:

$$\frac{\phi_1}{\phi_2} = \frac{G'_2}{G'_1} \text{ and } \frac{\phi_1}{\phi_2} = \frac{\tan \delta_1}{\tan \delta_2} \quad (5.37)$$

All these models converge to the composition at phase inversion of 50/50(vol/vol) when the viscosity ratio between phases is close to 1. Omonov and al. [28] proposed a figure which summarizes some of the empirical and semi-empirical models used for the prediction of phase inversion composition and region of co-continuity of polymer blends as a function of the viscosity ratio in the range of 0.1-10 (Figure 5.35).

**Experimentally, in polymer blends, a single phase inversion composition is not observed but rather a range of compositions exhibiting a co-continuous morphology.** The phase inversion composition occurs within this co-continuity window. Detection of a single phase inversion composition by experimental measurement is thus difficult. **Indeed, it is difficult to rationalize all observations in the literature with a single model.** It was observed in the literature that:

- Often, the experimental determination of phase inversion composition does not fit exactly with any of the rheological models proposed above [28, 160, 174].
- Co-continuity is often observed within a large range of compositions which can vary from 5 to 60vol%,: it makes the detection of the phase inversion composition even more complex [20, 160, 174].

For example, Castro and al. (2003) [160] studied POE/PVdF-HFP uncompatibilized blends exhibiting ratios of viscosity and elasticity close to 1. By solvent extraction and microscopy techniques, they determined quantitatively a range of composition corresponding to the co-continuity window: from 45 to 55vol%. They compared their experimental results to models based on viscosity or elasticity ratios of blend components. For some models (Miles and Zureck (1988)[171] and Bourry and Favis (1998)[173]), the prediction

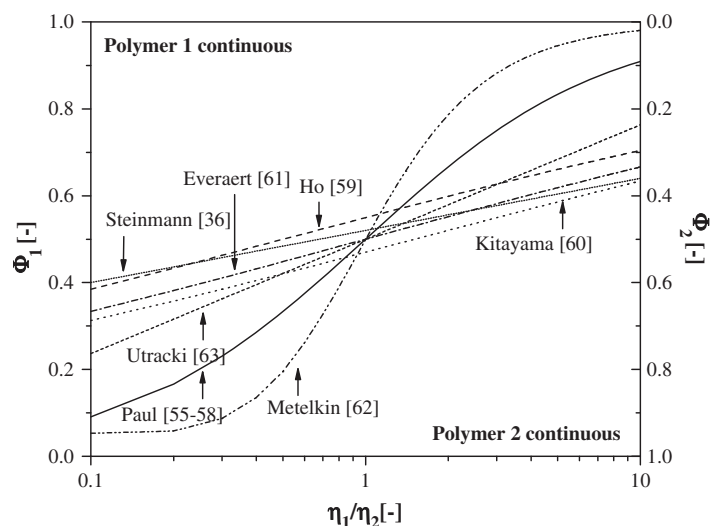


Figure 5.35: Different semi-empirical models describing the phase inversion volume fraction as a function of the viscosity ratio of binary polymer blends. The references mentioned in the figure correspond to the references of Omonov and al.'s paper[28].

of phase inversion composition was in good agreement with the observed range of composition for co-continuity but the experimental determination of a single phase inversion composition was not possible since they obtained a range of composition.

For compatibilized blends, the prediction of phase inversion composition becomes even more complex. The previously described models do not involve the interfacial tension, assuming that the presence of an interfacial agent in compatibilized systems would not affect the phase inversion composition, but only change the average domain size. Then, the nature and/or architecture of the interfacial agent is not considered. To the best of our knowledge, models of phase inversion composition prediction are generally not used with compatibilized systems. Dedecker and al. (1997) [174], for example, compared uncompatibilized PA6/PMMA with PA6/(PMMA/SMA20) reactively compatibilized blends exhibiting viscosity ratios close to 1 (SMA20 being the reactive compatibilizer). The main conclusion of their work was: (1) the region of co-continuity was quite broad on the non-compatibilized blends and this interval was dramatically reduced with compatibilization and (2) phase inversion was shifted to lower PA6 contents in the compatibilized blends even though the viscosity ratio did not change.

This shows that the prediction of the exact phase inversion composition is difficult because co-continuity is observed within a range of composition, which can be large and is affected when blends are compatibilized. Besides, for uncompatibilized and compatibilized blends exhibiting viscosity ratios very different from one, the prediction of phase inversion composition with the help of rheological models has not been extensively studied and usually the predictions of classical models do not agree with experimental results.

Meijer et al. [7] suggested to use the modified Krieger and Dougherty (KD) model (see equation 5.23) to predict the phase inversion composition. To the best of our knowledge, the first study in the determination of phase inversion composition by using the

KD model was performed in our lab by Argoud et al. [125]. Indeed, in this work, this method has successfully been applied for numerous reactively compatibilized polymer blends of PA6/HDPE/MA-g-HDPE to predict phase inversion composition. The viscosity ratio of the studied blends was always close to 1 (from 0.5 to 1.5). In this chapter, section 3 and 4, the modified KD model was compared to the blend viscosity evolution of both uncompatibilized and compatibilized blends (see respectively subsections 3.1 and 4.1). For uncompatibilized blends, it has been shown that at frequencies lower than the droplet shape relaxation times, the KD model described quite satisfactorily the viscosity evolution of blends with PA6-18k for a viscosity ratio close to 1. When the viscosity ratio was lower than unity, the KD model was also quite satisfactory. However when  $R_v > 1$ , the viscosity was not described by the KD model. For compatibilized blends, the KD model described very satisfactorily the behaviour of blends with PA6-18k at 100 rad/s and at low frequencies, for the three blends series, only the shape of the KD model was reproduced but at higher values. We will show here that, even if the KD model does not describe exactly blends viscosities, it constitute a very good method for the prediction of phase inversion composition for very different viscosity ratios.

## 5.2 Modified Krieger and Dougherty model for the prediction of blend morphology: phase inversion composition

The modified KD model is reminded first (see also eq. 5.23):

$$\eta \simeq \eta_m \left[ 1 - \frac{\phi_d}{\phi_{max}} \right]^{-2.5\phi_{max} \left( \frac{R_v + 0.4}{R_v + 1} \right)} \quad (5.38)$$

With:

- $\eta$  the blend viscosity.
- $\eta_m$  the matrix viscosity.
- $\phi_d$  the volume fraction of the dispersed phase.
- $R_v$  the viscosity ratio between the dispersion and the matrix  $R_v = \eta_d / \eta_m$ .
- $\phi_{max}$  the maximum close packing parameter.

The idea is to predict the viscosity of an emulsion of two viscoelastic polymers A and B: the modified Krieger and Dougherty model can predict the effective viscosity of both an A in B emulsion and B in A emulsion depending on the A/B composition. A way to rationalize phase inversion in polymer blends is to consider that "a flowing system will choose the emulsion with the lower viscosity" [7], i.e. the system should minimize its energy by choosing the less viscous morphology for each composition and/or set of material parameters.

For example, if we consider a viscosity ratio  $R_v = \eta_B / \eta_A = 3$  between polymers B and A as shown in figure 5.36, it is possible to calculate the viscosity evolution of the emulsion of both B in A (solid line) and A in B (dotted line) as a function of the volume fraction of B in the blend. Then, according to equation 5.23:

- Rheological behavior of the blends for all compositions is described by the lower parts of both curves and,
- the intersection of both curves where  $\eta_{(AinB)} = \eta_{(BinA)}$  defines **the phase inversion composition**.

In a first approximation, and for the sake of simplicity, the maximum close packing density parameter  $\phi_{max}$  was chosen equal to one. This may be justified by the fact that, in polymeric blends, droplets are polydisperse in size and deformable. Figure 5.36 illustrates this prediction for three values of  $R_v$  (3, 30 and 300).

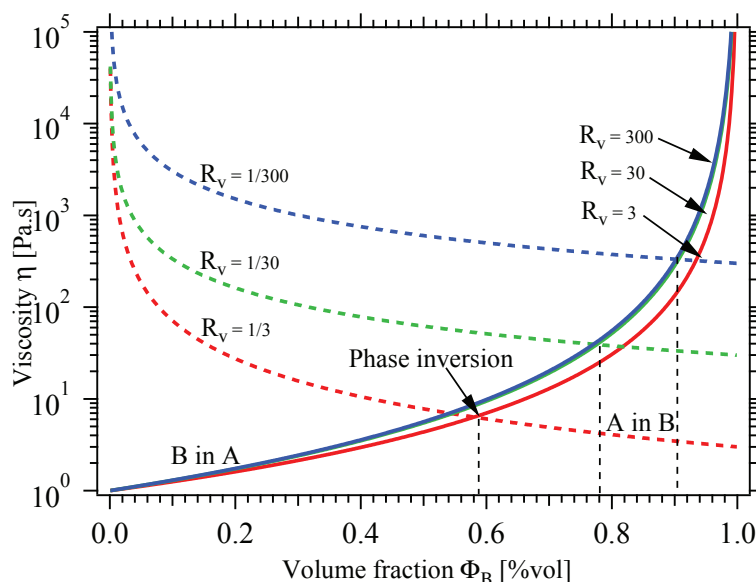


Figure 5.36: Viscosity of the emulsion of A in B (dotted lines) and B in A (solid lines) as a function of volume fraction of polymer B for different viscosity ratios  $R_v = \eta_i/\eta_m$ . For dotted lines  $R_v = \eta_A/\eta_B$ : 1/3 (red), 1/30 (green) and 1/300 (blue) with  $\phi_{max}=1$ . Curves predicted from the modified Krieger and Dougherty model (eq. 5.38).

Determination of the phase inversion composition as a function of the viscosity ratio of polymers A and B leads to the master curve of figure 5.37. The blend morphology can be predicted from this master curve at any composition as a function of the viscosity ratio between polymers A and B:

- At compositions above the phase inversion curve, the morphology prediction is droplets of B in A.
- Close to the phase inversion curve, the morphology is hardly predictable since co-continuity occurs over a range of compositions[20][28]. Nevertheless we can expect the morphology to be co-continuous or nearly co-continuous.
- At compositions below the phase inversion curve, the morphology prediction is droplets of A in B.

At  $R_v$  far from unity, this master curve is strongly influenced by the value of  $\phi_{max}$ .

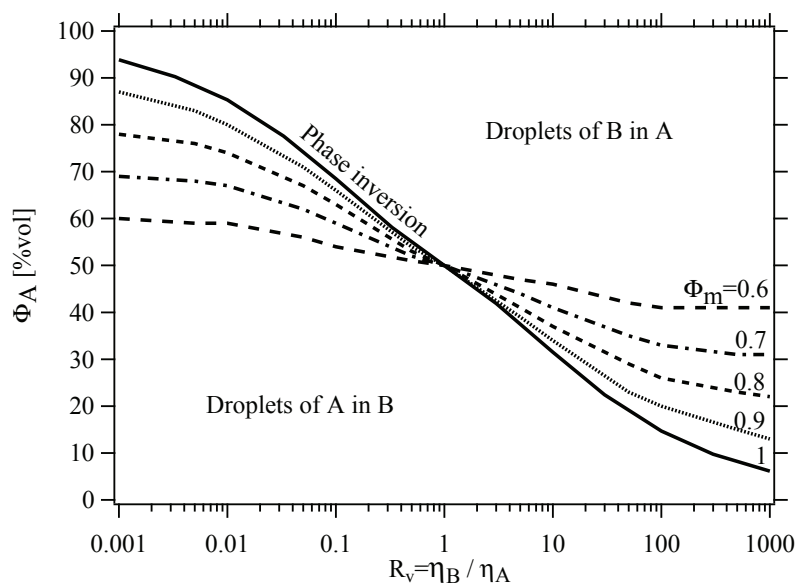


Figure 5.37: Master curve predicted from the modified Krieger and Dougherty model: prediction of the blend morphology at any composition as a function of the viscosity ratio between polymer A and B. Different curves illustrate the influence of  $\phi_{max}$  value.

### 5.3 Application to compatibilized and uncompatibilized blends of this study

On figures 5.38 and 5.39 the prediction of phase inversion composition of the modified KD model with several  $\phi_{max}$  are reported as well as blends, represented by triangles, with their respective morphologies: black triangles are dispersions of PE in PA matrix, grey triangles are co-continuous morphologies and white triangles are dispersions of PA in PE matrix.

Figure 5.38 shows the comparison for uncompatibilized binary blends PA-31k/PE, PA-18k/PE and PA-3k/PE. The morphology of blends PA-31k/PE 58/42 and 50/50 blends appears as co-continuous but more precisions given by the microscopy (see chapter 4 subsection 2.3) and the rheological measurements (see subsection 3.2.3) showed that the PE phase "supports" the morphology of blends, i.e. the PE phase is more continuous than the PA phase. Thus the phase inversion in blends PA-31k/PE happened between 58%vol and 70%vol of PA-31k. Thus, **with values of  $\phi_{max}$  between 0.8 and 0.9 the prediction of KD model is in very good agreement with the morphologies observed even at viscosity ratios very different from 1.**

Figure 5.39 shows the comparison for compatibilized binary blends PA-31k/MAGPE, PA-18k/MAGPE and PA-3k/MAGPE. **With  $\phi_{max} = 0.8$  the prediction of KD model is in very good agreement with the morphologies observed for the three series of compatibilized blends.**

Even if the viscosity evolution as a function of blends concentration was not in agreement with all the viscosity evolution measured for both compatibilized and uncompatibilized blends, the Krieger and Dougherty model used for the prediction of phase inversion composition with  $\phi_{max}=0.8$ , appears to be a very good qualitative model compared

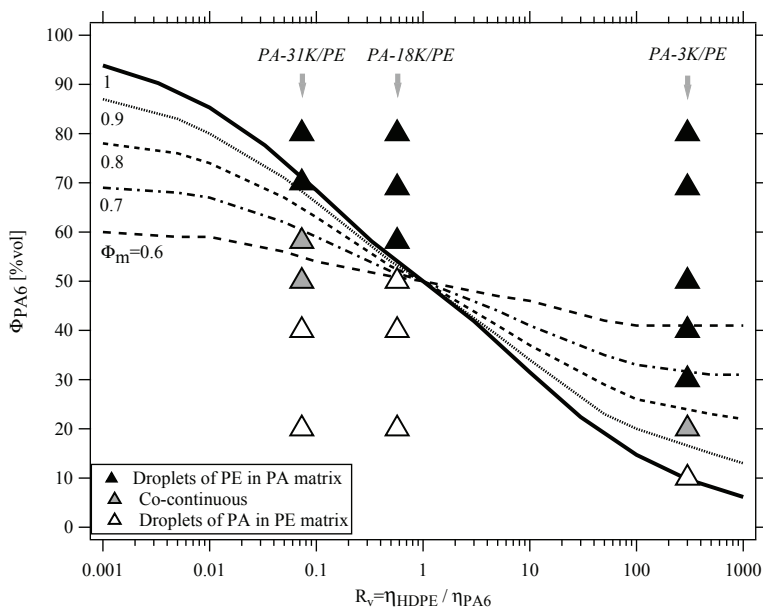


Figure 5.38: Prediction of phase inversion composition with the modified KD model compared to the morphologies observed for UNCOMPATIBILIZED binary blends PA-31k/PE, PA-18k/PE and PA-3k/PE. The solid and dotted lines represent the mastercurves of phase inversion composition predicted by the modified KD model for different  $\phi_{max}$ . Blends are represented by triangles as a function of their composition in volume fraction (in the melt state) and viscosity ratio  $R_v$  of pure components.  $R_v$  have been measured at 100rad/s at 290 °C.

to the experimental results of this study. The value of  $\phi_{max}=0.8$  is in agreement with the value proposed by Meijer et al. [7]. It is also consistent with the fact that in polymeric blends, droplets can be deformed and can also be polydisperse in size, and thus,  $\phi_{max}$  can overpass the critical value of 0.74 for monodisperse hard spheres. **This model can thus be used for highly compatibilized blends as well as uncompatibilized blends in a broad range of viscosity ratios to predict the morphology of a blend. It only requires: (1) the viscosity ratio of pure components measured at a shear rate representative of process conditions and (2) the composition in volume fractions (calculated with densities of pure components in the melt state).**

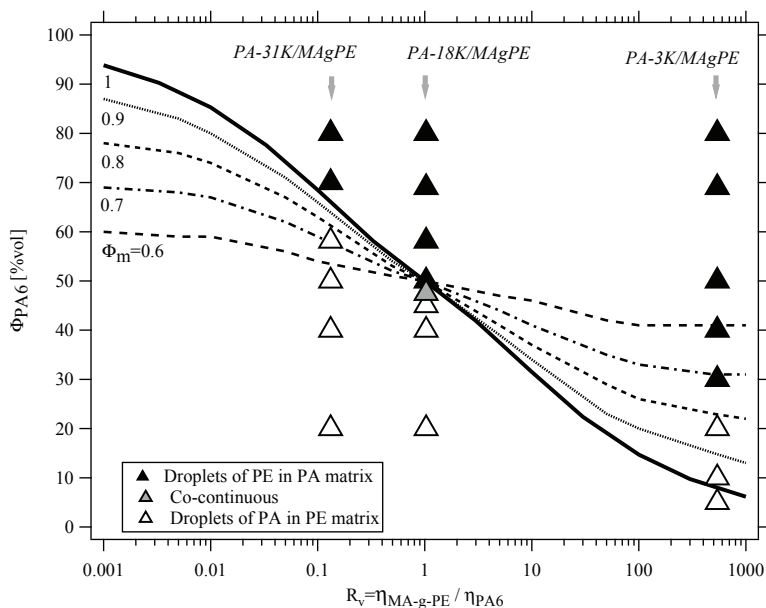


Figure 5.39: Prediction of phase inversion composition with the modified KD model compared to the morphologies observed for COMPATIBILIZED binary blends PA-31k/MAGPE, PA-18k/MAGPE and PA-3k/MAGPE. The solid and dotted lines represent the mastercurves of phase inversion composition predicted by the modified KD model for different  $\phi_{max}$ . Blends are represented by triangles as a function of their composition in volume fraction (in the melt state) and viscosity ratio  $R_v$  of pure components.  $R_v$  have been measured at 100rad/s at 290 °C.

## 6 Conclusion

The main objective of this work was to make the link between rheological behaviour and morphologies of both uncompatibilized and reactively compatibilized binary blends.

In this study the rheological behaviour of uncompatibilized and compatibilized binary blends were studied, over a broad composition range and for systems with viscosity ratio ( $R_v$ ) of one and different from one. The other interest for binary PA6/MA-g-HDPE blends, was to study the effect of a large amount of copolymers at the interface and their architecture, on the rheological response. **The various complex trends of blends linear viscoelastic behaviour were analysed and strong correlations were found with blends morphologies of both compatibilized and uncompatibilized blends**, despite the intrinsic artefact on linear viscoelastic behaviour of pure blend components.

Blends linear viscoelastic behaviour ( $G'$ ,  $G''$  and  $\eta^*$ ) were compared to pertinent models: Palierne's models for the evolution of  $G'$  and  $G''$  as a function of the frequency and modified versions of the Krieger and Dougherty model for the evolution of  $\eta^*$  as a function of the composition (volume fraction of the dispersed phase  $\phi_d$ ).

For uncompatibilized blends with  $R_v \leq 1$ , when  $\phi_d < 30\% \text{vol}$  when, blends rheological behaviours were typical of blends where droplets shape relaxations are observed. For more concentrated blends other interaction phenomena between droplets happened. Palierne's model failed in predicting the data of concentrated blends.

For blends with  $R_v > 1$ , data were underestimated by models. The experimental data, higher than the one expected, indicate that when viscous droplets are added to a fluid matrix the viscosity is probably increased due to unfavourable drainage regimes. The rheological measurements were consistent with the morphology observed.

For compatibilized blends, even at low concentrations, a large increase in dynamical moduli, and especially the storage modulus  $G'$ , were observed at low frequencies. This enhancement increases with  $\phi_d$ : when PA6 was the matrix the moduli increased and for the more concentrated blends exhibited a gel-like behaviour; when MA-g-HDPE was the matrix a gel or solid-like behaviour was observed in almost all cases. In all cases Palierne's model failed in predicting the data. This behaviour suggested the presence of strong interactions between neighbouring droplets which creates a percolating network.

The nature of interactions was discussed. For blend with PA6-18k and PA6-31k as matrix, the creation of a viscoelastic percolating network due to PA6 grafted chains entanglements between PE droplets was proposed. For all blends with MA-g-HDPE as matrix, entanglements, or even trapped entanglements or direct bridging between neighbouring PA droplets could explain de gel or solid like behaviour. For blend with PA6-3k as matrix, the nature of the interactions is still in discussion. Interactions are thus strongly correlated to the distances between droplets and thus to the morphology.

Thus, based on the rheological measurements, quantitative informations on the morphology can be extracted for blends  $\phi_d < 30\% \text{vol}$  and  $R_v \leq 1$  in uncompatibilized blends thanks to the Palierne's model. Qualitative ideas should be deduced for more concentrated blends. For compatibilized blends, large enhancement at low frequencies is an indication of droplets interactions and thus that small distance between nodules are ob-

served. The higher the enhancement, the higher the number of "contacts" via interactions between nodules.

Conversely, thanks to this study, the rheological behaviour of blends can be qualitatively deduced from the morphology.

In last section, we proposed a model base on a modified Krieger and Dougherty model to predict the phase inversion composition. This model was successfully applied for very compatibilized blends as well as uncompatibilized blends in a broad range of viscosity ratio. It only requires: (1) the viscosity ratio of pure components measured at a shear rate representative of process conditions and (2) the composition in volume fraction calculated with densities of pure components in the melt state.



# GENERAL CONCLUSION

---

The first objective of this work was to identify parameters that control the multi-scale blend morphology developed in reactively compatibilized polymer blends and, especially, that control the formation of nanodispersions. In the first part of this work, we attempted to discriminate the effects due to shearing (drop break-up and coalescence) and due to the chemical reaction of compatibilization on the morphology development in reactively compatibilized blends.

Four polyamide 6 (PA6) of different controlled molecular weights were synthesized for the present work. Two polyolefins were used: One Maleic Anhydride grafted High Density Polyethylene (MA-g-HDPE), for the binary compatibilized blends, and one HDPE, for the binary uncompatibilized blends chosen so that its viscosity is close to that of MA-g-HDPE (at 290 °C and 100rad/s).

The chemical compatibilization reaction was first studied alone in static conditions between thin films of PA6 and MA-g-HDPE annealed at 290 °C for different times. The interest was to understand the consequence of the creation of copolymers at the interface and the effect of the copolymer architecture.

For the case of relatively high PA6 chains ( $M_n \approx 10000\text{g/mol}$  to  $31000\text{g/mol}$ ), the nucleation and growth of ordered microphase separated copolymer domains at flat interfaces were observed after only 10 min annealing. Quite symmetrical patterns (lamellae or cylinders) were observed. However, no interfacial destabilization was observed with shorter PA6 chains ( $M_n \approx 3000\text{g/mol}$ ) even after 60 minutes annealing.

It appeared that interfacial destabilization are initiated due to the fast chemical reaction at the interface, and the creation of a dense brush of copolymers at the interface that decreases the interfacial tension to zero (or even negative values). The formation of the dense brush depends essentially on the copolymer architecture symmetry. Copolymers created with PA6-10k, 18k and 31k favours the creation of quite symmetrical copolymers which allows the formation of a dense copolymer brush, whereas, copolymers created with PA6-3k favour a very strong curvature toward the PA6 blocks (micelles of PA). The creation of a dense copolymer brush at a flat interface for this last case is thus not possible. The architecture of the copolymer created at the interface also affects the microstructures formed as a result of interface destabilization.

**For the first time in compatibilized polyamide/polyethylene blends, it was shown that the symmetry of the formed copolymer is critical for the interfacial destabilization.**

The morphology development only due to rheological processes, i.e. only mechanisms of drop break-up and coalescence, was then studied. The objective was to identify

the different mechanisms of morphology development, for blends with viscosity ratios between the dispersed and the matrix phase,  $R_v$ , close and very different from one.

Uncompatibilized blends of HDPE and PA6 (PA6-3k, 18k and 31k) of different chain length, thus viscosities, were studied. In order to perform systematic studies, blends composition were varied over a wide range of composition. Besides, the viscosity ratio were calculated from viscosity of pure blend components at 100 rad/s and 290 °C to be the most representative of process conditions.

For blends with  $R_v \approx 1$ , quite homogeneous morphologies created by Rayleigh capillary waves instabilities were observed. Sizes increases with the volume fraction of the dispersed phase ( $\phi_d$ ) and phase inversion was close to 50/50%vol. When  $R_v \neq 1$ , the phase inversion composition was shifted to lower volume fraction of the more fluid phase composing the blend.

When  $R_v < 1$ , very heterogeneous morphologies were observed with a bimodal size distribution (droplets of few hundreds of nanometers and nodules of few microns). They may be created by the mechanism of end-pinching which favours the formation of small satellites between droplets. For moderate values of  $R_v$  ( $R_v$  close to 10) more heterogeneous morphologies than when  $R_v \approx 1$  were observed, because of the delayed creation of Rayleigh capillary waves instabilities on the more viscous thread. Blends with very high viscosity ratios ( $R_v \gg 1$ ) exhibited morphologies with droplets separated by very thin films, resulting from very unfavourable drainage mechanisms which are discussed. In this case, coalescence is thus highly inhibited.

The morphology development that combines both effects of shearing and compatibilization reaction was then studied with compatibilized blends. The MA-g-HDPE was used instead of the HDPE: by changing only the molecular weight of the linear PA6 in binary blends, the viscosity ratio as well as the copolymer architecture created at the interface were varied at the same time.

Compositions of phase inversion remained unchanged compared to uncompatibilized blends. In all blends, as it was expected, sizes were greatly reduced as well as coalescence. In blends with PA6-18k, nanodispersions of both PA in PE and PE in PA were observed in almost all compositions, and especially close to phase inversion. For blends with PA6-31k, nanodispersions were mainly observed into the PA6 phase. PE dispersions in PA6-31K were found both when PA6-31k constituted the matrix or the dispersed phase. PA6-3k nanodispersions were only observed when the PA was the dispersed phase.

**We thus observed that nanodispersions are not formed equivalently on each side of the interface depending on the system studied. Even though the classical mechanisms of drop break-up and coalescence control the global type of morphology (dispersion, co-continuity...), sizes and distributions of nanodispersions could not be explained only by these classical mechanisms.**

A detailed comparison between compatibilized blends and their corresponding uncompatibilized blends, as well as with the reaction in static conditions, was thus performed.

One of the main observations was that the morphology created in static conditions (lamellar or cylindrical structure) were not created in reactive blends, even if the same precursor where used.

This was explained by the fact that, under shear, the interface is not under equilibrium

---

conditions. Thus, the very first interfacial fluctuations, which, in static conditions, initiated the ordered morphology growth, are broken-off from the interface under shear. We observed that **two main parameters controlled the nanodispersion creation: (1) First, the copolymer architecture** which not only controls interfacial destabilizations, but also may favour a curvature of the interface for the nanodispersions. **(2) Secondly, the viscosity ratio**, indeed, nanodispersions may be broken-off into the more viscous phase. If  $R_v=1$ , they may be broken-off equivalently on both sides.

**Based on this work the morphology can thus be predicted if the following parameters are known**

- **The reactivity of the reactive moieties attached on homopolymers,**
- **The viscosity ratio at the shear rate and temperature representatives of process conditions,**
- **Molecular parameters ( $M_n$ , copolymer architecture...),**
- **The composition**
- **The shear rate or eventually the presence of elongational flow in the process.**

The second objective of this work was to understand the impact of this multi-scale morphology on blends rheological behaviour. Improving the knowledge on the relationships between formulation, morphology and rheology of reactively compatibilized blends could lead to future improvements in both product formulation and process characteristics.

The linear viscoelastic rheological behaviours of uncompatibilized and compatibilized binary blends were studied. They depend strongly on the frequency and on the composition.

For uncompatibilized blends with  $R_v \leq 1$ , when  $\phi_d < 30\% \text{vol}$ , blends rheological behaviours were typical of blends where droplets shape relaxations are observed. For more concentrated blends other interaction phenomena between droplets happened. A gel-like behaviour was observed for compositions very close to phase inversion (in blends with PA6-18k), and a drop in both dynamical moduli values was observed for co-continuous blends (in blends with PA6-31k). Palierne's model failed in predicting the data of concentrated blends. However, a model based on the Krieger and Dougherty model was well adapted to describe the viscosity evolution as a function of the composition at both high and low frequencies.

For blends with  $R_v > 1$ , data were underestimated by models. The experimental data, higher than the expected ones, indicate that when viscous droplets are added to a fluid matrix the viscosity is increased due to unfavourable drainage regimes. The rheological measurements were consistent with the morphology observed.

**For compatibilized blends, even at low concentrations, a large increase in dynamical moduli, and especially the storage modulus  $G'$ , were observed at low frequencies.** This enhancement increases with  $\phi_d$ : when PA6 was the matrix the moduli increased and for the more concentrated blends exhibited a gel-like behaviour; when MA-g-HDPE was the matrix a gel or solid-like behaviour was observed in almost all cases. In all cases Palierne's model failed in predicting the data. **This behaviour suggested the presence of strong interactions between neighbouring droplets which creates a percolating network.**

The nature of interactions was discussed. They appear to be strongly correlated to the distances between droplets and thus to the morphology. For blend with PA6-18k and PA6-31k as matrix, the creation of a viscoelastic percolating network due to PA6 grafted chains entanglements between PE droplets was proposed. For all blends with MA-g-HDPE as matrix, entanglements, or even trapped entanglements or direct bridging between neighbouring PA droplets could explain de gel or solid like behaviour. For blend with PA6-3k as matrix, the nature of the interactions is still in discussion.

Finally we proposed a **model based on a modified Krieger and Dougherty model to predict the phase inversion composition**. This model was successfully applied for very compatibilized blends as well as uncompatibilized blends in a broad range of viscosity ratio.

To conclude, parameters that control the formation the multi scale morphology in binary reactively compatibilized blends, and particularly the nanodispersions, were identified. Besides, the impact of such morphologies on blends viscoelastic behaviour were studied. The relationships between formulation, morphology and rheological properties of reactively compatibilized blends have thus been established. This knowledge will help tuning polymer blend morphologies so as to meet properties compromises targeted (processability, permeability, mechanical, cost. . . ).

#### **Perspectives:**

To go deeper in the scientific understanding it would probably be necessary to observe, in real time, structural evolutions, either under static annealing (interfacial destabilization) or under shear. It should be of great interest to combine in-situ rheology or static annealing with optical or scattering observations.

It would be very interesting to vary independently the viscosity ratio and the architecture of the copolymer which is formed, in order to validate our hypothesis on the formation of nanodispersions.

Concerning the rheological behaviour, one important issue would be to elucidate the nature of the interactions that are responsible for the gel or solid-like behaviour. For this it would certainly be important to extend the frequency range towards lower frequencies, e.g. creep experiments.

# BIBLIOGRAPHY

---

- [1] L. Leibler. Emulsifying effects of block copolymers in incompatible polymer blends. *Makromolekulare Chemie, Macromolecular Symposia*, 16:1–17, 1988.
- [2] L. Leibler. Block copolymers at interfaces. *Physica A*, 172:258–268, 1991.
- [3] G. H. Fredrickson, A. J. Liu, and F. B. Bates. Entropic corrections to the Flory-Huggins theory of polymer blends: architectural and conformational effects. *Macromolecules*, 27(9):2503–2511, 1994.
- [4] Elian M Masnada, Grégoire Julien, and Didier R Long. Miscibility maps for polymer blends: Effects of temperature, pressure, and molecular weight. *Journal of Polymer Science Part B: Polymer Physics*, 52(6):419–443, 2014.
- [5] L. A. Utracki. *Thermodynamics of polymer blends*, pages 123–194. Kluwer Academic Publishers, Dordrecht, Boston, London, 2003.
- [6] P. G. De Gennes. *Scaling concepts in polymer physics*. Cornell University Press, Ithaca, London, 1979.
- [7] H. E. H. Meijer, J. M. H. Janssen, and P. D. Anderson. *Mixing of immiscible liquids*, pages 1–147. Carl Hanser Verlag, Munchen, 2009.
- [8] G.I. Taylor. The viscosity of a fluid containing small drops of another fluid. In The royal society, editor, *The royal society*. Royal Society, 1932.
- [9] H. Grace. Dispersion phenomena in high viscosity immiscible fluid systems and applications of static mixers as dispersion devices in such systems. *Chemical engineering Communication*, 14(225-277), 1982.
- [10] J. M. H. Janssen and H. E. H. Meijer. Dynamics of liquid-liquid mixing: A 2-zone model. *Polymer Engineering and Science*, 35(22):1766–1780, 1995.
- [11] H.A. Stone, B.J. Bentley, and L.G. Leal. An experimental study of transient effects in the breakup of viscous drops. *Journal of Fluid Mechanics*, 173:131–158, 1986.
- [12] H.A. Stone and L.G. Leal. Relaxation and breakup of an initially extended drop in an otherwise quiescent fluid. *Journal of Fluid Mechanics*, 198:399–427, 1989.
- [13] P. H. M. Elemans, J. M. H. Janssen, and H. E. H. Meijer. The measurement of interfacial tension in polymer/polymer systems: The breaking thread method. *Journal of Rheology*, 34(8):1311–1325, 1990.

- [14] M. Tjahjadi, H.A. Stone, and J.M. Ottino. Satellite and subsatellite formation in capillary breakup. *Journal of Fluid Mechanics*, 243:297–317, 1992.
- [15] L. A. Utracki. *Polymer blends handbook*, volume 1. Kluwer Academic Publishers Dordrecht, The Netherlands, 2002.
- [16] P. Van Puyvelde and P. Moldenaers. Rheology and morphology development in immiscible polymer blends. *The British Society of Rheology*, pages 101–145, 2005.
- [17] A. Fabre-Argoud. *Control and stabilization of morphologies in reactively compatibilized polyamide6/high density polyethylene blends*. Thesis, Universite Claude Bernard, 2011.
- [18] U. Sundararaj and C. W. Macosko. Drop breakup and coalescence in polymer blends: the effects of concentration and compatibilization. *Macromolecules*, 28:2647–2657, 1995.
- [19] G.D.M. MacKay and S.G. Mason. The gravity approach and coalescence of fluid drops at liquid interfaces. *Can. J. Chem. Eng.*, 41:203–219, 1963.
- [20] C. Harrats and N. Mekhilef. *Cocontinuous phase morphologies: predictions, generation, and practical applications*, book section 3, pages 91–132. CRC Press Taylor and Francis Group, Boca raton, London, New York, 2006.
- [21] Petra Pötschke and DR Paul. Formation of co-continuous structures in melt-mixed immiscible polymer blends. *Journal of Macromolecular Science, Part C: Polymer Reviews*, 43(1):87–141, 2003.
- [22] J. A. Galloway and C. W. Macosko. Comparison of methods for the detection of cocontinuity in poly(ethylene oxide)/polystyrene blends. *Polymer Engineering and Science*, 44(4):714–727, 2004.
- [23] T. S. Omonov, C. Harrats, G. Groeninckx, and P. Moldenaers. Anisotropy and instability of the co-continuous phase morphology in uncompatibilized and reactively compatibilized polypropylene/polystyrene blends. *polymer*, 48:5289–5302, 2007.
- [24] J. R. Bell, K. Chang, C. Lopez-Barron, C. W. Macosko, and D. M. Morse. Annealing of cocontinuous polymer blends: effect of block copolymer molecular weight and architecture. *Macromolecules*, 43:5024–5032, 2010.
- [25] S. Chaput, C. Carrot, M. Castro, and F. Prochazka. Co-continuity interval in immiscible polymer blends by dynamic mechanical spectroscopy in the molten and solid state. *Rheol Acta*, 43:417–426, 2004.
- [26] J. A. Galloway, K. J. Koester, B. J. Paasch, and C. W. Macosko. Effect of sample size on solvent extraction for detecting cocontinuity in polymer blends. *polymer*, 45:423–428, 2003.
- [27] H. Pernot. *Polymeres nanostructure a base de polyethylene et de polyamide synthetises par extrusion reactive: conception et proprietes*. Thesis, Universite Pierre et Marie Curie, 2003.
- [28] T. S. Omonov, C. Harrats, P. Moldenaers, and G. Groeninckx. Phase continuity detection and phase inversion phenomena in immiscible polypropylene/polystyrene blends with different viscosity ratios. *polymer*, 48:5917–5927, 2007.

- [29] M. Castro, C. Carrot, and F. Prochazka. Experimental and theoretical description of low frequency viscoelastic behaviour in immiscible polymer blends. *polymer*, 45:4095–4104, 2004.
- [30] M. Castro, F. prochazka, and C. Carrot. Cocontinuity in immiscible polymer blends: a gel approach. *Journal of Rheology*, 49(1):149–160, 2004.
- [31] A. Pyun, J. R. Bell, K. H. Won, B. M. Weon, S. K. Seol, J. H. Je, and C. W. Macosko. Synchrotron x-ray microtomography for 3d imaging of polymer blends. *Macromolecules*, 40:2029–2035, 2007.
- [32] C. Lopez-Barron and C. W. Macosko. Characterizing interface shape evolution in immiscible polymer blends via 3d image analysis. *Langmuir*, 25(16):9392–9404, 2009.
- [33] Jacques Huitric, Michel Moan, Pierre J Carreau, and Nicolas Dufaure. Effect of reactive compatibilization on droplet coalescence in shear flow. *Journal of Non-Newtonian Fluid Mechanics*, 145(2):139–149, 2007.
- [34] H. K. Jeon, C. L. Zhang, and C. W. Macosko. Premade vs. reactively formed compatibilizers for pmma/ps melt blends. *Macromolecules*, 46:12422–12429, 2005.
- [35] C. W. Macosko, P. Guégan, A. K. Khandpur, A. Nakayama, P. Marechal, and T. Inoue. Compatibilizers for melt blending: premade block copolymers. *Macromolecules*, 29:5590–5598, 1996.
- [36] Julien Ville. *Alliages de thermoplastiques immiscibles Polyéthylène/Polyamide chargés de nanoparticules d'argile: relations structure–morphologie–rhéologie*. Thesis, Université de Bretagne occidentale-Brest, 2009.
- [37] S.S. Velankar, P. Van Puyvelde, J. Mewis, and P. Moldenaers. Effect of compatibilization on the breakup of polymeric drops in shear flow. *Journal of Rheology*, 45(4):1007–1019, 2001.
- [38] Y. T. Hu, D.J. Pine, and L. Gary Leal. Drop deformation, breakup, and coalescence with compatibilizer. *Physics of fluids*, 12(13):484–489, 2000.
- [39] C.D. Eggleton, T.M. Tsai, and K.J. Stebe. Tip streaming from a drop in the presence of surfactants. *Physical Review Letters*, 87(4):048302(4), 2001.
- [40] S. T. Milner and H. Xi. How copolymers promote mixing of immiscible homopolymers. *journal of Rheology*, 40(4):663–687, 1996.
- [41] S. T. Milner. How do copolymer compatibilizers really work? *MRS bulletin*, 22(1):38–42, 1997.
- [42] S. P. Lyu, T. D. Jones, F. B. Bates, and C. W. Macosko. Role of block copolymers on suppression of droplet coalescence. *Macromolecules*, 35:7845–7855, 2002.
- [43] A. Steurer and G. P. Hellmann. Reactive blending: Inhomogeneous interface grafting in melts of maleinated polystyrene and polyamides. *Polymers for Advanced Technologies*, 9:297–306, 1998.

- [44] Z. Yin, C. Koulic, C. Pagnouille, and R. Jérôme. Reactive blending of functional ps and pmma: Interfacial behavior of in situ formed graft copolymers. *Macromolecules*, 34:5132–5139, 2001.
- [45] M. Freluche. *Copolymères greffés et matériaux nanostructurés à base de poly(méthacrylate de méthyle) et de polyamide-6*. Thesis, Université Pierre et Maire Curie, 2005.
- [46] L. Gani, S. Tencé-Girault, M. Milléquant, S. Bizet, and L. Leibler. Co-continuous nanostructured blend by reactive blending: incorporation of high molecular weight polymers. *Macromolecular Chemistry and Physics*, 211:736–743, 2010.
- [47] Ian W Hamley. *Developments in block copolymer science and technology*. Wiley Online Library, 2004.
- [48] L. Leibler. Theory of microphase separation in block copolymers. *Macromolecules*, 13:1602–1617, 1980.
- [49] F. B. Bates and G. H. Fredrickson. Block copolymer thermodynamics: Theory and experiment. *Annual Review of Physical Chemistry*, 41:525–557, 1990.
- [50] D. A. Hajduk, P. E. Harper, S. M. Gruner, C. C. Honeker, G. Kim, E. L. Thomas, and L. J. Fetters. The gyroid: a new equilibrium morphology in weakly segregated diblock copolymers. *Macromolecules*, 27:4063–4075, 1994.
- [51] R. A. Segalman. Patterning with block copolymer thin films. *Materials Science and Engineering*, 48:191–226, 2005.
- [52] M. W. Matsen and F. B. Bates. Unifying weak- and strong-segregation block copolymer theories. *Macromolecules*, 29(4):1091–1098, 1996.
- [53] A. K. Khandpur, S. Förster, F. B. Bates, W. Hamley, A. J. Ryan, W. Bras, K. Almdal, and K. Mortensen. Polyisoprene-polystyrene diblock copolymer phase diagram near the order-disorder transition. *Macromolecules*, 28:8796–8806, 1995.
- [54] S. M. Mai, J. P. A. Fairclough, N. J. Terrill, S. C. Turner, W. Hamley, A. J. Ryan, and C. Booth. Microphase separation in poly(oxyethylene)-poly(oxybutylene) diblock copolymers. *Macromolecules*, 31:8110–8116, 1998.
- [55] S. P. Gido, C. Lee, D. J. Pochan, S. Pispas, W. Mays, and N. Hadjichristidis. Synthesis, characterisation, and morphology of model graft copolymers with trifunctional branch points. *Macromolecules*, 29:7022–7028, 1996.
- [56] C. Lee, S. P. Gido, Y. Poulos, N. Hadjichristidis, N. Beck Tan, S. F. Trevino, and W. Mays. Pi-shaped double-graft copolymers: effect of molecular architecture on morphology. *polymer*, 39(19):4631–4638, 1997.
- [57] S. T. Milner. Chain architecture and asymmetry in copolymer microphases. *Macromolecules*, 27:2333–2335, 1994.
- [58] D. J. Pochan, S. P. Gido, S. Pispas, W. Mays, A. J. Ryan, J. P. A. Fairclough, W. Hamley, and N. J. Terrill. Morphologies of microphase-separated a<sub>2</sub>b simple graft copolymers. *Macromolecules*, 29:5091–5098, 1996.

- [59] L. J. Fetters, D. J. Lohse, D. Richter, T. A. Witten, and A. Zirkel. Connection between polymer molecular weight, density, chain dimensions, and melt viscoelastic properties. *Macromolecules*, 27(17):4637–4647, 1994.
- [60] T. Hashimoto, H. Tanaka, and H. Hasegawa. Ordered structure in mixtures of a block copolymer and homopolymers. 2. effects of molecular weights of homopolymers. *Macromolecules*, 23:4378–4386, 1990.
- [61] K. R. Shull and K. I. Winey. Homopolymer distribution in lamellar copolymer/homopolymer blends. *Macromolecules*, 25:2637–2644, 1992.
- [62] H. Tanaka, H. Hasegawa, and T. Hashimoto. Ordered structure in mixtures of a block copolymer and homopolymers. 1. solubilization of low molecular weight homopolymers. *Macromolecules*, 24:240–251, 1991.
- [63] S. Koizumi, H. Hasegawa, and T. Hashimoto. Spatial distribution of homopolymers in block copolymer microdomains as observed by a combined sans and saxs method. *Macromolecules*, 27:7893–7906, 1994.
- [64] S. Koizumi, H. Hasegawa, and T. Hashimoto. Ordered structure of block copolymer/homopolymer mixtures. 5. interplay of macro- and microphase transitions. *Macromolecules*, 27:6532–6540, 1994.
- [65] M. W. Matsen. Phase behavior of block copolymer/homopolymer blends. *Macromolecules*, 28:5765–5773, 1995.
- [66] P. K. Janert and M. Schick. Phase behavior of binary homopolymer/diblock blends: temperature and chain length dependence. *Macromolecules*, 31:1109–1113, 1998.
- [67] K. I. Winey, E. L. Thomas, and L. J. Fetters. Isothermal morphology diagrams for binary blends of diblock copolymer and homopolymer. *Macromolecules*, 25:2645–2650, 1992.
- [68] K. I. Winey, E. L. Thomas, and L. J. Fetters. The ordered bicontinuous double-diamond morphology in diblock copolymer/homopolymer blends. *Macromolecules*, 25:422–428, 1992.
- [69] P. K. Janert and M. Schick. Phase behavior of ternary homopolymer/diblock blends: Influence of relative chain lengths. *Macromolecules*, 30:137–144, 1997.
- [70] P. K. Janert and M. Schick. Phase behavior of ternary homopolymer/diblock blends: Microphase unbinding in the symmetric system. *Macromolecules*, 30:3916–3920, 1997.
- [71] L. Yang, S. P. Gido, J. W. Mays, S. Pispas, and N. Hadjichristidis. Phase behavior of i2s single graft block copolymer/homopolymer blends i 2. *Macromolecules*, 34:4235–4243, 2001.
- [72] G. H. Fredrickson and S. T. Milner. Time dependent reactive coupling at polymer-polymer interfaces. *Macromolecules*, 29:7386–7390, 1996.
- [73] B. O’Shaughnessy and U. Sawhney. Reaction kinetics at polymer-polymer interfaces. *Macromolecules*, 29:7230–7239, 1996.

- [74] B. O'Shaughnessy and D. Vavylonis. Reactive polymer interfaces: How reaction kinetics depend on reactivity and density of chemical groups. *Macromolecules*, 32:1785–1796, 1999.
- [75] G. H. Fredrickson. Diffusion-controlled reactions at polymer-polymer interfaces. *Physical Review Letters*, 76(18):3440–3443, 1996.
- [76] H. T. Oyama and T. Inoue. Kinetics and mechanism of coupling of functionalized chains at the immiscible polymer-polymer interface. *Macromolecules*, 34:3331–3338, 2001.
- [77] J. S. Schulze, J. J. Cernohous, A. Hirao, T. P. Lodge, and C. W. Macosko. Reaction kinetics of end-functionalized chains at a polystyrene/poly(methyl methacrylate) interface. *Macromolecules*, 33:1191–1198, 2000.
- [78] J. Jiao, E. J. Kramer, S. De Vos, M. Muller, and C. Koning. Polymer interface instability caused by a grafting reaction. *polymer*, 40:3585–3588, 1999.
- [79] Z. Yin, C. Koulic, H. K. Jeon, C. Pagnoulle, C. W. Macosko, and R. Jérôme. Effect of molecular weight of the reactive precursors in melt reactive blending. *Macromolecules*, 35(24):8917–8919, 2002.
- [80] Z. Yin, C. Koulic, C. Pagnoulle, and R. Jérôme. Probing of the reaction progress at a pmma/ps interface by using anthracene labeled reactive ps chains. *Langmuir*, 19:453–457, 2003.
- [81] C. W. Macosko, H. K. Jeon, and T. R. Hoyer. Reactions at polymer-polymer interfaces for blend compatibilization. *Progress in Polymer Science*, 30:939–947, 2005.
- [82] C. A. Orr, J. J. Cernohous, P. Guégan, A. Hirao, H. K. Jeon, and C. W. Macosko. Homogeneous reactive coupling of terminally functional polymers. *polymer*, 42:8171–8178, 2001.
- [83] P. Guegan, C. W. Macosko, T. Ishizone, A. Hirao, and S. Nakahama. Kinetics of chain coupling at melt interfaces. *Macromolecules*, 27:4993–4997, 1994.
- [84] H. K. Jeon, C. W. Macosko, B. Moon, T. R. Hoyer, and Z. Yin. Coupling reactions of end- vs mid- functional polymers. *Macromolecules*, 37:2563–2571, 2004.
- [85] E. Helfand and Y. Tagami. Theory of the interface between immiscible polymers. ii. *The Journal of Chemical Physics*, 56(7):3592–3601, 1972.
- [86] T. D. Jones, J. S. Schulze, C. W. Macosko, and T. P. Lodge. Effect of thermodynamic interactions on reactions at polymer-polymer interfaces. *Macromolecules*, 36:7212–7219, 2003.
- [87] A. V. Berezkin and Y. V. Kudryavtsev. Simulation of end-coupling reactions at a polymer-polymer interface: The mechanism of interfacial roughness development. *Macromolecules*, 44:112–121, 2011.
- [88] B. J. Kim, G. H. Fredrickson, and E. J. Kramer. Analysis of reaction kinetics of end-functionalized polymers at a ps-p2vp interface by dsims. *Macromolecules*, 40:3686–3694, 2007.

- [89] C. Ligoure and L. Leibler. Thermodynamics and kinetics of grafting end-functionalized polymers to an interface. *Journal de physique*, 51:1313–1328, 1990.
- [90] S. P. Lyu, J. J. Cernohous, F. S. Bates, and C. W. Macosko. Interfacial reaction induced roughening in polymer blends. *Macromolecules*, 32:106–110, 1999.
- [91] C. L. Zhang, T. P. Lodge, and C. W. Macosko. Interfacial morphology development during ps/pmms reactive coupling. *Macromolecules*, 38:6586–6591, 2005.
- [92] H. Y. Kim, U. Jeong, and J. K. Kim. Reaction kinetics and morphological changes of reactive of polymer-polymer interface. *Macromolecules*, 36:1594–1602, 2003.
- [93] P. A. Bhadane, A. H. Tsou, J. Cheng, and B. D. Favis. Morphology development and interfacial erosion in reactive polymer blending. *Macromolecules*, 41:7549–7559, 2008.
- [94] C. L. Zhang, L. F. Feng, J. Zhao, H. Huang, S. Hoppe, and G. H. Hu. Efficiency of graft copolymers at stabilizing co-continuous polymer blends during quiescent annealing. *polymer*, 49:3462–3469, 2008.
- [95] C. Harrats, K. Dedeker, G. Groeninckx, and R. Jérôme. Reactively and physically compatibilized immiscible polymer blends: stability of the copolymer at the interface. *Macromol.Symp.*, 198:183–196, 2003.
- [96] F. B. Bates, W. W. Maurer, P. M. Lipic, M. A. Hillmyer, K. Almdal, K. Mortensen, G. H. Fredrickson, and T. P. Lodge. Polymeric bicontinuous microemulsions. *Physical Review Letters*, 79(5):849–852, 1997.
- [97] H. K. Jeon and J. K. Kim. The effect of the amount of in situ formed copolymers in the final morphology of reactive polymer blends with an in situ compatibilizer. *Macromolecules*, 31:9273–9280, 1998.
- [98] H. Y. Kim, D. Y. Ryu, U. Jeong, D. H. Kho, and J. K. Kim. The effect of chain architecture of in situ formed copolymers on interfacial morphology of reactive polymer blends. *Macromolecular rapid communications*, 26:1428–1433, 2005.
- [99] J. K. Kim, H. Kang, K. Char, K. Katsov, G. H. Fredrickson, and E. J. Kramer. Interfacial roughening induced by the reaction of end-functionalized polymers at a ps/p2vp interface: quantitative analysis by dsims. *Macromolecules*, 38:6106–6114, 2005.
- [100] A. V. Berezkin, D.V. Guseva, and Y.V. Kudryavtsev. Formation of linear and graft block copolymers at a polymer/polymer interface: How copolymer brush and microdomain morphology control heterogeneous reactions. *Macromolecules*, 45(21):8910–8920, 2012.
- [101] A. V. Berezkin and Y. V. Kudryavtsev. End-coupling reactions in incompatible polymer blends: From droplets to complex micelles through interfacial instability. *Macromolecules*, 46:5080–5089, 2013.
- [102] J. Ibuki, P. Charoensirisomboon, T. Chiba, T. Ougizawa, T. Inoue, M. Weber, and E. Koch. Reactive blending of polysulfone with polyamide: a potential for solvent-free preparation of the block copolymer. *polymer*, 40:647–653, 1999.

- [103] P. Charoensirisomboon, T. Chiba, S. I. Solomko, T. Inoue, and M. Weber. Reactive blending of polysulfone with polyamide: a difference in interfacial behavior between in situ formed block and graft copolymers. *polymer*, 40:6803–6810, 1999.
- [104] P. Charoensirisomboon, T. Chiba, T. Inoue, and M. Weber. In situ formed copolymers as emulsifier and phase-inversion-aid in reactive polysulfone/polyamide blends. *polymer*, 41:5977–5984, 2000.
- [105] P. Charoensirisomboon, T. Inoue, and M. Weber. Interfacial behavior of block copolymers in situ-formed in reactive blending of dissimilar polymers. *polymer*, 41:4483–4490, 2000.
- [106] P. Charoensirisomboon, T. Inoue, and M. Weber. Pull-out of copolymer in situ-formed during reactive blending: effect of the copolymer architecture. *polymer*, 41:6907–6912, 2000.
- [107] L. Pan, T. Chiba, and T. Inoue. Reactive blending of polyamide with polyethylene: pull-out of in-situ formed graft copolymer. *polymer*, 42:8825–8831, 2001.
- [108] L. Pan, T. Inoue, H. Hayami, and S. Nishikawa. Reactive blending of polyamide with polyethylene: pull-out of in situ-formed graft copolymers and its application for high-temperature materials. *polymer*, 43:337–343, 2002.
- [109] H. Pernet, M. Baumert, F. Court, and L. Leibler. Design and properties of co-continuous nanostructured polymers by reactive blending. *Nature Materials*, 1:54–58, 2002.
- [110] M. Freluche, I. Iliopoulos, J. J. Flat, A. V. Ruzette, and L. Leibler. Self-organised materials and graft copolymers of polymethymethacrylate and polyamide-6 obtained by reactive blending. *polymer*, 46:6554–6562, 2005.
- [111] J. Zhang, S. Ji, J. Song, T. P. Lodge, and C. W. Macosko. Flow accelerates interfacial coupling reactions. *Macromolecules*, 43(18):7617–7624, 2010.
- [112] C. Sailer and U.A. Handge. Reactive blending of polyamide 6 and styrene-acrylonitrile copolymer: influence of blend composition and compatibilizer concentration on morphology and rheology. *macromolecules*, 41:4258–4267, 2008.
- [113] Johannes Brandrup, Edmund H Immergut, Eric A Grulke, Akihiro Abe, and Daniel R Bloch. *Polymer handbook*. Wiley New York, 1999.
- [114] JG Fatou, C Vasile, and R Seymour. Handbook of polyolefins, synthesis and properties, 1993.
- [115] D. Graebling, R. Muller, and J. F. Paliarne. Linear viscoelastic behavior of some incompatible polymer blends in the melt. interpretation of data with a model of emulsion of viscoelastic liquids. *Macromolecules*, 26:320–329, 1993.
- [116] C. W. Macosko. *Rheology principles, measurements, and applications*. Advances in interfacial engineering. Wiley-VHC, Inc, New York, Chichester, Weinheim, Brisbane, Singapore, Toronto, 1994.
- [117] H.M. Laun. Das viskoelastische Verhalten von polyamide-6-schmelzen. *Rheologica acta*, 18:478–491, 1979.

- [118] P. Parrini, D. Romanini, and G.P. Righi. Melt rheology of some aliphatic polyamide. *Polymer*, 17:377–381, 1976.
- [119] Y.P. Khanna, P.K. Han, and E.D. Day. New developments in the melt rheology of nylons. i: Effect of moisture and molecular weight. *polymer Engineering and Science*, 36(13):1745–1996, 1996.
- [120] S. Acierno and P. Van Puyvelde. Rheological behavior of polyamide 11 with varying initial moisture content. *Journal of Applied Polymer Science*, 97:666–670, 2005.
- [121] D.J. Dijkstra. Guidelines for rheological characterization of polyamide melts (iupac technical report). *Pure and Applied Chemistry*, 81(2):339–349, 2009.
- [122] M.A. Schaffer, K.B. Mcauley, and M.F. Cunningham. Prediction of water solubility in nylon melts based in flory-huggins theory. *Polymer Engineering and Science*, 43(3):639–646, 2003.
- [123] K. R. Shull, E. J. Kramer, G. Hadziannou, and W. Tang. Segregation of block copolymers to interfaces between immiscible homopolymers. *Macromolecules*, 23:4780–4787, 1990.
- [124] K. R. Shull, A.J. Kellock, V.R. Deline, and S.A. MacDonald. Vanishing interfacial tension in an immiscible polymer blend. *J.Chem.Phys.*, 97(3):2095–2104, 1992.
- [125] A. Argoud, L. Trouillet-Fonti, S. Ceccia, and P. Sotta. Morphologies in polyamide 6/high density polyethylene blends with high amounts of reactive compatibilizer. *European Polymer Journal*, 50:177–189, 2014.
- [126] Maurice Kleman. Points, lines and walls in liquid crystals, magnetic systems and various ordered media. *John Wiley and Sons*, 1982.
- [127] M. Buchanan, J. Arrault, and M. Castes. Swelling and dissolution of lamellar phases: Role of bilayer organization. *Langmuir*, 14:7371–7377, 1998.
- [128] M. Buchanan, S.U. Egelhaaf, and M.E. Cates. Dynamics of interface instabilities in nonionic lamellar phases. *Langmuir*, 16:3718–3726, 2000.
- [129] M. Haran, A. Chowdhury, C. Manohar, and J. Bellare. Myelin growth and coiling. *Colloid and Surfaces A: Physicochemical and Engineering Aspects*, 205:21–30, 2002.
- [130] L. Reissig, D.J. Fairhurst, J. Leng, M.E. Cates, A.R. Mount, and S.U. Egelhaaf. Three-dimensional structure and growth of myelins. *Langmuir*, 26(19):15192–15199, 2010.
- [131] L.-N.; Zou. Myelin figures: The buckling and flow of wet soap. *Physical Review E*, 79(6):061502, 2009.
- [132] I. W. Hamley. *The Physics of Block Copolymers*. Oxford University Press, New York, 1988.
- [133] E. Helfand and Z.R. Wasserman. Block copolymer theory. 4. narrow interphase approximation. *Macromolecules*, 9(6):879–888, 1976.
- [134] E. Helfand. Block copolymer theory. iii. statistical mechanics of the microdomain structure. *Macromolecules*, 8(4):552–556, 1975.

- [135] L. J. Fetters, D.J. Lohse, and R. H. Colby. *Chain Dimensions and Entanglement Spacings*, in *Physicla Properties of Polymer Handbook*. Springer, 2007.
- [136] K.M.B. Jansen, W.G.M. Agterof, and J. Mellema. Droplet breakup in concentrated emulsions. *Journal of Rheology*, 45(1):227–236, 2000.
- [137] E. Klaseboer, J. Ph. Chevaillier, C. Gourdon, and O. Masbernat. Film drainage between colliding drops at constant approach velocity: Experiments and modeling. *Journal of colloid and interface science*, 229:274–285, 2000.
- [138] L. A. Utracki and G. Z. H. Shi. *Compounding polymer blends*, pages 577–650. Klumer Academic Publishers, Dordrecht, Boston, London, 2003.
- [139] A.V. Machado, J.A. Covas, and M. Van Duin. Chemical and morphological evolution of pa6/epm/epm-g-ma blends in a twin screw extruder. *Journal of polymer science: part A: Polymer chemistry*, 37(9):1311–1320, 1999.
- [140] L.A. Pinheiro, C.S. Bittencourt, and S.V. Canevarolo. Real time assessment of the compatibilization of polypropylene/polyamide 6 blends during extrusion. *polymer Engineering and Science*, 50(4):826–834, 2010.
- [141] C. Scott and C. W. Macosko. Model experiments for the interfacial reaction between polymers during reactive polymer blending. *Journal of polymer science: Part B: Polymer physics*, 32(2):205–213, 1994.
- [142] V. Yquel, A.V. Machado, J.A. Covas, and J.J. Flat. Contribution of the melting stage to the evolution of the morphology and chemical conversion of immiscible polyamide/polyethylene blends in twin-screw extruders. *Journal of Applied Polymer Science*, 114(3):1768–1776, 2009.
- [143] F. Chambon and H.H. Winter. Linear viscoelasticity at the gel point of a crosslinking pdms with imbalanced stoichiometry. *Journal of Rheology*, 31(8):683–697, 1987.
- [144] H.H. Winter. The critical gel state: The universal material state between liquid and solid, 2002.
- [145] R.G. Larson. *The structure and rheology of complex fluids*. Oxford University Press, Inc, New york, Oxford, 1999.
- [146] C. W. Macosko. *Rheology: Principle, Measurements, and Applications*. Wiley, 1994.
- [147] J. F. Palierne. Linear rheology of viscoelastic emulsions with interfacial tension. *Rheologica acta*, 29:204–214, 1990.
- [148] U. Jacobs, M. Fahrlander, J. Winterhalter, and C. Friedrich. Analysis of palierne’s emulsion model in the case of viscoelastic interfacial properties. *Journal of Rheology*, 43(6):1495–1509, 1999.
- [149] R.-E. Riemann, H. J. Cantow, and C. Friedrich. Interpretation of a new interface-governed relaxation process in compatibilized polymer blends. *macromolecules*, 30:5476–5484, 1997.
- [150] E. Van Hemelrijck and P. Van Puyvelde. Interfacial elasticity and coalescence suppression in compatibilized polymer blends. *Journal of Rheology*, 48(1):143–158, 2004.

- [151] E. Van Hemelrijck and P. Van Puyvelde. The effect of block copolymer architecture on the coalescence and interfacial elasticity on compatibilized polymer blends. *Journal of rheology*, 49(3):783–798, 2005.
- [152] N. Grizzuti, G. Buonocore, and G. Iorio. Viscous behavior and mixing rules for an immiscible model polymer blend. *journal of Rheology*, 44(1):149–164, 1999.
- [153] G.K. Batchelor. The effect of brownian motion on the bulk stress in a suspension of spherical particles. *Journal of fluid mechanics*, 83(01):97–117, 1977.
- [154] I.M. Krieger and T.J. Dougherty. A mechanism for non-newtonian flow in suspensions of rigid spheres. *Trans. Soc. Rheol.*, 3:137, 1959.
- [155] R. Pal. Rheology of polymer-thickened emulsions. *Journal of Rheology*, 36:1245, 1992.
- [156] J. Huitric, P. Médéric, M. Moan, and J. Jarrin. Influence of composition and morphology on rheological properties of polyethylene/polyamide blends. *Polymer*, 39(20):4849–4856, 1998.
- [157] W. Wang, Y. Shangguan, L. Zhao, J. Yu, L. HE, H. Tan, and Q. Zheng. The linear viscoelastic behaviors of nylon1212 blends toughened with elastomer. *Journal of Applied Polymer Science*, 108(3):1744–1754, 2007.
- [158] W. Wang, Y. Cao, J. Wang, and Q. Zheng. Rheological characterization and morphology of nylon 1212/functional elastomer blends. *Journal of Applied Polymer Science*, 112(2):953–962, 2008.
- [159] J.D. Martin and S.S. velankar. Effects of compatibilizer on immiscible polymer blends near phase inversion. *Journal of Rheology*, 51(4):699, 2007.
- [160] M. Castro, C. Carrot, and F. Prochazka. Morphologie co-continue dans un mélange de polymères incompatibles: Poe/pvdf-hfp. *Rheologie*, 4:32–39, 2003.
- [161] R Bruinsma. Elasticity and excitations of minimal crystals. *Journal de Physique II*, 2(3):425–451, 1992.
- [162] J. H. Rosedale and F. S. Bates. Rheology of ordered and disordered symmetric poly(ethylenepropylene)-poly(ethylethylene) diblock copolymers. *Macromolecules*, 23:2329–2338, 1990.
- [163] Y. He, P.G. Boswell, P. Bühlmann, and T. P. Lodge. Ion gels by self-assembly of a triblock copolymer in an ionic liquid. *the journal of physical chemistry B*, 111:4645–4652, 2007.
- [164] R. H. Colby. Block copolymers, melt rheology of. *Encyclopedia of materials: Science and technology*, pages 727–730, 2001.
- [165] P.F. Luckham and M.A. Ukeje. Effect of particule size distribution on the rheology of dispersed systems. *Journal of colloid and interface science*, 220:347–356, 1999.
- [166] C. F. Sailer. *Blends of polyamide 6 and styrenic polymers: influence of reactive compatibilization on melt rheology and morphology*. Thesis, Friedrich-Alexander-Universität Erlangen-Nürnberg, 2008.

- [167] C. DeLeo, K. Walsh, and S.S. Velankar. Effect of compatibilizer concentration and weight fraction on model immiscible blends with interfacial crosslinking. *Journal of Rheology*, 44(4):713–731, 2011.
- [168] C. DeLeo and S.S. Velankar. Morphology and rheology of compatibilized polymer blends: Diblock compatibilizers vs crosslinked reactive compatibilizers. *Journal of rheology*, 52:1385–1404, 2008.
- [169] A. Maani, B. Blais, M-C. Heuzey, and P. J. Carreau. Rheological and morphological properties of reactively compatibilized thermoplastic olefin (tpo) blends. *Journal of rheology*, 56:625–647, 2012.
- [170] D.R. Paul and J.W. Barlow. Polymer blends. *Journal of macromolecular Science, Part C: Polymer Reviews*, 18(1):109–069, 1980.
- [171] I.S. Miles and A. Zurek. Preparation, structure, and properties of two-phase co-continuous polymer blends. *Polym. Eng. Sci.*, 28:796–805, 1988.
- [172] Metelkin V.I. and V.S. Blekht. Formation of a continuous phase in heterogeneous polymer mixtures. *Colloid Journal of the USSR*, 46:425–429, 1984.
- [173] D. Bourry and B. D. Favis. Cocontinuity and phase inversion in hdpe/ps blends: Influence of interfacial modification and elasticity. *Journal of polymer science: Part B: Polymer physics*, 36:1889–1899, 1998.
- [174] K. Dedecker and G. Groeninckx. Reactive compatibilization of a/(b/c) polymer blends. part 2: Analysis of the phase inversion region and the co-continuous phase morphology. *Polymer*, 39(21):4993–5000, 1998.
- [175] C. Cocquet. *Contrôle de la morphologie de matériaux polyamide cellulaires par la cinétique chimique et la rhéologie*. Thesis, Université Claude Bernard Lyon 1, 2012.
- [176] F. Wolff and H. Münstedt. Artefacts of the storage modulus due to bubbles in polymeric fluids. *Rheologica acta*, 52(4):287–289, 2013.
- [177] C. W. Macosko, H. K. Jeon, and J. S. Schulze. Block copolymers and compatibilization: Reactively formed. *Encyclopedia of materials: Science and technology*, pages 683–688, 2001.

# APPENDIX

---

## 1 APPENDIX: Linear viscoelastic behaviour of blend components

### Linear viscoelastic behaviour of PA6

Palierne's model allows to estimate the relaxation time and of the plateau value induced by the shape relaxation of dispersed droplets into a polymeric matrix (this model is described in more details in chapter 5). The averages values of viscosity the PA6-18k matrix is  $\eta_{18k}^* = 105$  Pa.s (resp. PA6-3k  $\eta_{3k}^* = 0.2$  Pa.s).

During the experiments on pure PA6, we observed, between the cone and the plate, visible gas bubbles into the material of the order of about 0.5mm ( $R \approx 500\mu\text{m}$ ). By making the approximation that the volume fraction of those vapour bubbles are  $\phi \approx 20\%$ vol and  $\eta_{vapour}^* \approx 0$  Pa.s and the interfacial tension  $\Gamma = 16\text{mN/m}$  [175]:

- For PA6-18k, the droplet shape relaxation  $\lambda_s \approx 4.8\text{s}$  thus  $1/\lambda_s \approx 0.2\text{Hz}$  (Estimated with equation 5.11). The associated plateau is  $G_s \approx 11\text{Pa.s}$  (Estimated with equation 5.12).
- For PA6-3k, the droplet shape relaxation  $\lambda_s \approx 0.01\text{s}$  thus  $1/\lambda_s \approx 110\text{Hz}$  (Estimated with equation 5.11). The associated plateau is  $G_s \approx 11\text{Pa.s}$  (Estimated with equation 5.12).

Thus values of  $\lambda_s$  and  $G_s$  are in agreement with the observed behaviour of the loss modulus of PA6-18k. Thus shoulders observed are in agreement with the presence of gas bubbles. The same observation was made by Dijkstra et al. [121]. Wolff et al. [176] studied the artefacts of the storage modulus due to bubbles in polymeric fluids. They studied a PDMS silicon oil with and without air bubbles and noticed a bending of  $G'$ . The loss modulus  $G''$  was not influenced at all. The shape relaxation of bubbles induces an increase in the storage modulus  $G'$ .

A solution to remove this shoulder would be to dry the PA6 sample as much as possible before rheological experiments. However complications due to the polycondensation equilibrium are observed. We tested different initial moisture contents and performed time and frequency sweep tests. For example, for PA6-18k (see figure 40), when the initial moisture content was too low, the shoulder on  $G'$  was almost removed but the viscosity was higher than the expected one ( $\eta^* \approx 200$  Pa.s). Conversely, when the sample was very wet the viscosity measured was too low ( $\eta^* \approx 60$  Pa.s). Besides, the time sweep tests showed different percentages of viscosity increase (due to post-condensation) for the different initial moisture amount. The viscosity increase is more important for dry samples. Thus kinetics of post-condensation are probably modified by the initial moisture content. Thus, drying the sample does not lead necessarily to the more accurate value of viscosity.

For the PA6-3k, even for very dry samples we did not succeed in removing the shoulder. The measured value are above the sensitivity limits of the rheometer and several geometries were tested and gave the same results.

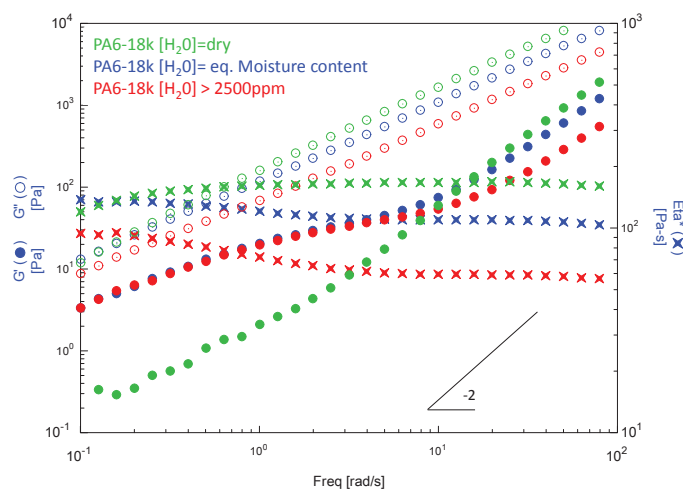


Figure 40: Linear viscoelastic behaviour of PA6-18k preliminary dried at different moisture amount.

This shows the influence of the initial moisture amount not only on the polycondensation equilibrium but also on the presence of gas bubbles.

### Linear viscoelastic behaviour of HDPE

As in the case of PA6, the shoulder could be due the presence of air bubbles into the polymer. These air bubbles being trapped between pellets during the melting stage. Thus the pure HDPE acts like a biphasic blend, and air bubbles which constitute the dispersed phase, can undergo shape relaxation while shearing. The elastic modulus  $G'$  is thus affected and a shoulder can be observed. We estimated  $\lambda_s$  and  $G_s$  with Palierne's model (see chapter 5). With an average values of viscosity the HDPE matrix  $\eta_m^* = 60$  Pa·s and  $\eta_{air}^* \approx 0$  Pa·s,  $\phi_{air} = 0.2$ , the diameter of air bubble  $R = 500 \mu\text{m}$  and the interfacial tension  $\Gamma = 16 \text{mN/m}$  [175]:

- The droplet shape relaxation  $\lambda_s \approx 2.3 \text{s}$  thus  $1/\lambda_s \approx 0.43 \text{Hz}$  (Estimated with equation 5.11).
- The plateau associated to this relaxation  $G_s \approx 10 \text{Pa}$  (Estimated with equation 5.12).

The values of  $\lambda_s$  and  $G_s$  are in agreement with the observed behaviour of the loss modulus of HDPE. Some measurements have been performed at lower temperature, which is usually the case for polyolefins, and the plateau was not seen anymore. This reinforces the idea that the shoulder observed is due to gas bubbles.

## 2 APPENDIX: Properties of PA6-10k (chap 3)

This polyamide 6, called PA6-10k ( $M_n \approx 10000$  g/mol), has been synthesized at the Solvay's R& I Center Lyon. The synthesis protocol has been modified to obtain PA6-10k: a mono-functionnal comonomer (called Blocker End Group amine  $BEG_{amine}$ ) which reacts at chains ends with a part of carboxylic acids end groups of the PA6 chains, has been used. It thus allows to control the progression of the PA6 synthesis reaction and reduces the sensitivity of these short PA6 chains to hydrolysis and condensation reactions. PA6-10k properties are given in table 4. The number average molecular weight is calculated from end-groups measurement.

Table 4: PA6-10k characteristics after synthesis.

Name	AEG [NH <sub>2</sub> ] (mmol/kg)	$M_{n_{equilibrium}}$ (g/mol)
<b>PA6-10k</b>	97	$\approx 10300$

### 3 APPENDIX: Consistency with force measurement on process tool during compounding

Blends are prepared by compounding in a batch co-rotating twin screw extruder (microcompounder DSM), that is in a strongly non linear regime. The estimated shear rate for blending is  $\dot{\gamma} = 100\text{s}^{-1}$ . During compounding the screw speed is fixed at 100 rpm and the force applied on the screw by the microcompounder to maintain this screw speed is measured. This force is related to the torque, and thus, to the stress imposed into the blend in which the morphology is being formed. The stress is representative of the viscosity of the blends. Thus, the measured torque varies with the viscosity in the blend.

An example of force measurement during the compounding experiment as a function of time for pure HDPE is shown in figure 41. The curve is divided in three zones corresponding to the characteristic steps of the compounding. The average force during compounding is measured on the second zone (steady state).

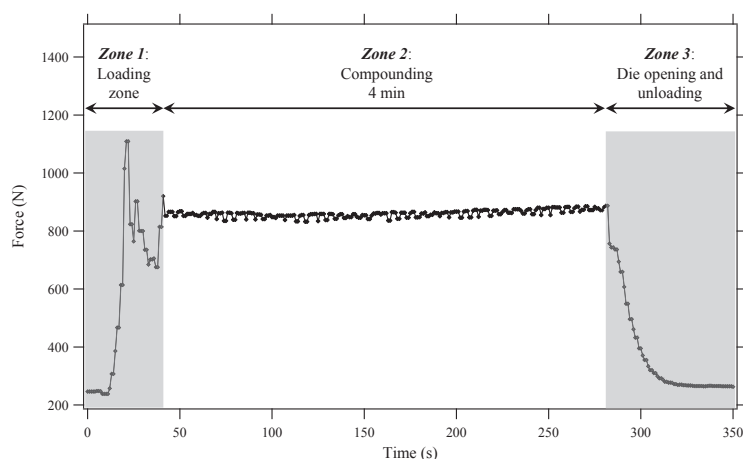


Figure 41: Force measured during the compounding process with the microcompounder as a function of the time for pure HDPE.

Figures 42 and 43 show the average value of the plateau measured in the steady state during compounding for respectively, uncompatibilized and compatibilized blends. The dynamical viscosity measured at 100 rad/s (290 °C, strain 15%) in linear dynamical rheometry are also shown as comparisons. The shape of the complex viscosities measured at 100 rad/s in the linear regime are qualitatively in agreement with the shape of the evolution of average forces measured in steady state during compounding in the microcompounder. This is observed for both compatibilized and uncompatibilized blends.

Measurements presented in chapter 5 are performed in the linear regime. The Cox-Merz rule can be applied for pure components of our blends and shows that  $\eta(\dot{\gamma} = 100\text{s}^{-1}) = \eta^*(\omega = 100\text{rad/s})$ . The direct measurement of blend viscosities in the non-linear regime is impossible because the deformation would be too high and the morphology greatly modified.

The present comparison shows that the viscosity measured in the linear regime at 100rad/s is representative of the blend viscosity of blends during compounding in the strongly non linear regime.

3. APPENDIX: Consistency with force measurement on process tool during compounding

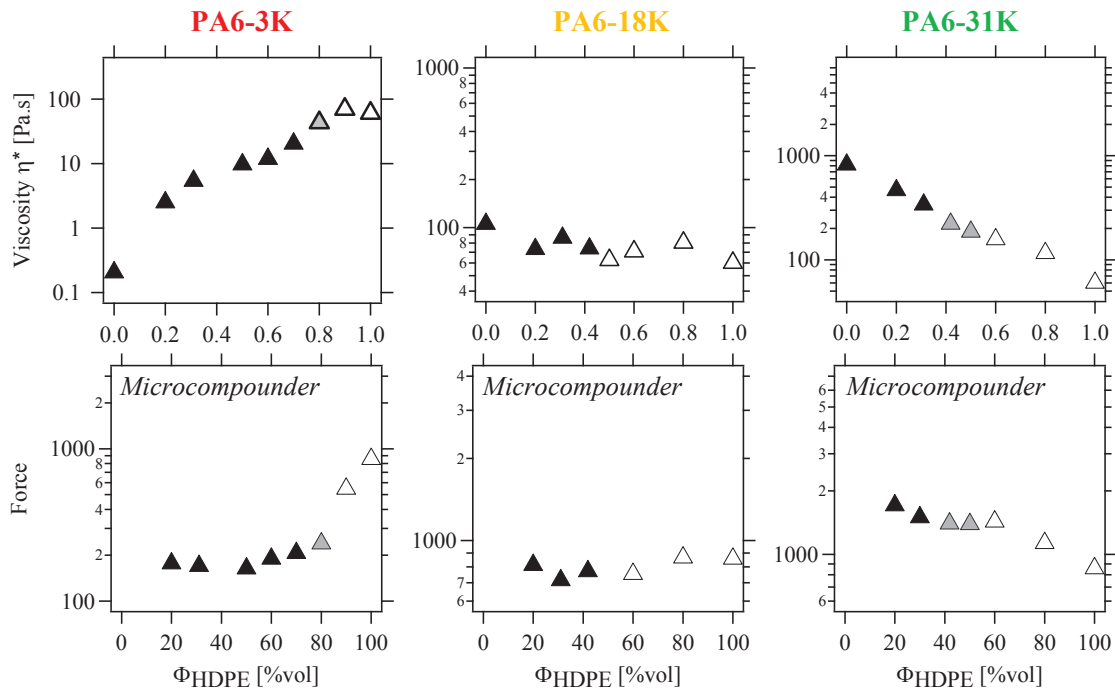


Figure 42: Comparison between complex viscosities measured at 100 rad/s in the linear regime by dynamic rheometry and average force measured in steady state during compounding in the microcompounder for UNCOMPATIBILIZED blends.

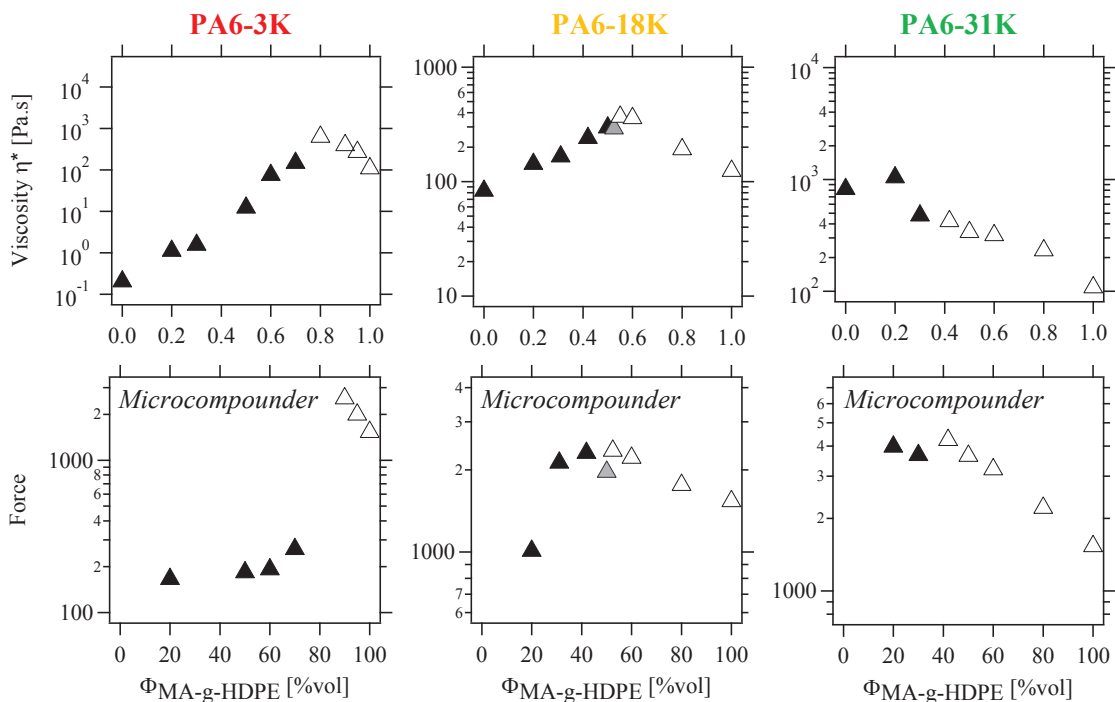


Figure 43: Comparison between complex viscosities measured at 100 rad/s in the linear regime by dynamic rheometry and average force measured in steady state during compounding in the microcompounder for COMPATIBILIZED blends.



## RÉSUMÉ EN FRANÇAIS

---

Le mélange de polymères est une solution pour fabriquer de nouveaux matériaux présentant des compromis de propriétés intéressants. Cette technique permet d'atteindre une combinaison de performances souhaitées, à partir de plusieurs matériaux aux propriétés individuelles complémentaires. Cependant, la quasi-totalité des polymères sont incompatibles, ce qui se caractérise par deux phases distinctes, une morphologie grossière et instable et une mauvaise adhésion entre les phases[15]. Il est alors nécessaire de les rendre compatibles afin de diminuer la tension interfaciale et donc de diminuer les tailles de morphologies et d'éviter la coalescence des dispersions[20]. La compatibilisation permet aussi de stabiliser les morphologies, d'augmenter l'adhésion entre les phases et donc les propriétés à l'état solide. Plusieurs méthodes de compatibilisation existent. On dénote parmi celles-ci la compatibilisation physique, qui consiste à ajouter un copolymère préformé au mélange ou encore l'ajout de nano-charges, venant se placer à l'interface et permettant de réduire les tensions interfaciales [35, 36]. Industriellement, la voie la plus utilisée est la compatibilisation réactive. Elle consiste à créer in-situ la molécule compatibilisante directement à l'interface, par une réaction chimique entre des espèces réactives situées directement sur les homopolymères constituant le mélange [177]. Certaines réactions se sont montrées très efficaces pour les temps courts de processing rencontrés par exemple en extrusion réactive. Dans ce travail de thèse nous sommes intéressés au développement des morphologies dans les mélanges binaires de Polyamide 6 (PA6) et de Polyéthylène greffé anhydride maléique (MA-g-HDPE). Lors de l'extrusion réactive, les bouts de chaînes amine viennent réagir à l'interface avec les groupements anhydride maléique greffés sur la chaîne PEHD pour former des copolymères greffés à l'interface.

Les propriétés des mélanges de polymères incompatibles dépendent des morphologies développées lors de la mise en œuvre. Pour contrôler les morphologies, il est essentiel de mieux comprendre les mécanismes mis en jeu lors de la préparation. Notre objectif est d'améliorer les connaissances sur les liens entre la formulation, la morphologie et les propriétés rhéologiques de ces mélanges.

Des études antérieures réalisées dans notre laboratoire ont montré que des morphologies multi-échelles pouvaient être créées dans les mélanges de polymères compatibilisés par voie réactive. Ces morphologies sont dues au fait de l'existence de deux mécanismes concomitants de développement des morphologies [17]: (1) D'une part, les mécanismes standards de rupture de gouttes et coalescence des domaines de polymères sous cisaillement, contrôlés par des mécanismes rhéologiques. Ces mécanismes conduisent à la formation de divers types de morphologies (dispersion, co-continuité. . .) dont la taille moyenne est de plusieurs centaines de nanomètres voire plusieurs microns. (2) D'autre part, des mécanismes plus locaux d'accumulation de copolymères aux interfaces dus à

la réaction chimique, qui conduisent à la formation de nano-dispersions de quelques dizaines de nanomètres à la fois de PA6 dans le PE et de PE dans le PA6. Il en résulte des morphologies complexes, avec de larges distributions des tailles de domaines.

Le but principal de la thèse est d'être capable de maîtriser finement les morphologies obtenues et, en particulier, d'identifier les paramètres permettant de contrôler la formation de nano-dispersions dans les mélanges compatibilisés par voie réactive. Pour cela, le fil conducteur de la thèse a été, dans un premier temps, de discriminer le rôle des mécanismes usuels de rupture de goutte et coalescence et des mécanismes dus à la réaction à l'interface sur les mécanismes de développement des morphologies. Puis, dans un second temps, d'étudier l'interaction de ces deux paramètres sur le développement des morphologies dans les mélanges compatibilisés par voie réactive.

Le second objectif a été de comprendre l'impact de cette morphologie multi-échelle sur le comportement rhéologique des mélanges.

## Chapitre 1: État de l'art (page 7)

Le premier chapitre de cette thèse présente une étude bibliographique centrée sur le développement des morphologies dans les mélanges de polymères incompatibles, et plus particulièrement les mélanges compatibilisés.

Le mécanisme de rupture et coalescence de gouttelettes sous cisaillement est le plus décrit dans la littérature [8]. Ce mécanisme a beaucoup été étudié pour une unique goutte d'un fluide Newtonien dans une matrice Newtonienne. La déformation et la rupture d'une goutte sont régies par le nombre capillaire représentant le ratio entre les forces de cisaillement et les forces interfaciales [7].  $Ca_{crit}$ , défini comme le nombre capillaire critique pour la rupture d'une goutte, est fonction du ratio de viscosité  $R_v$  [9].  $R_v$  représente le ratio entre la viscosité de la phase dispersée et la viscosité de la phase matrice  $R_v = \eta_d/\eta_m$ . Pour des mélanges viscoélastiques, les exemples de travaux ayant étudié le développement des morphologies pour des mélanges présentant un ratio de viscosité proche de 1 sont nombreux [16]. Le mécanisme principalement décrit est le mécanisme d'instabilités capillaire de Rayleigh, qui conduit à la rupture d'un filament en de plus fines gouttelettes. Lorsque,  $R_v < 1$ , les exemples sont beaucoup moins nombreux. Il apparaît que des mécanismes tels que le "end-pinching" conduisant à des morphologies de tailles polydisperses peuvent se développer. Dans le cas de fluides Newtoniens, un  $R_v > 4$  ne permet pas de casser les nodules sous simple cisaillement, cependant un cisaillement élongationnel le permet plus facilement. On ne connaît pas précisément l'impact de la nature viscoélastique des matériaux sur ces valeurs critiques. Il n'existe pas, ou très peu, d'études systématiques du développement des morphologies pour des ratios de viscosités éloignés de 1 et sur toute la gamme de composition.

La description usuelle de l'effet de la compatibilisation sur le développement des morphologies est la suivante: les copolymères créés à l'interface décroissent la tension interfaciale et permettent donc la rupture en de plus fines gouttelettes [37]. Ils permettent aussi de réduire, voire d'éliminer, les phénomènes de coalescence [42, 40]. Cela permet de stabiliser les morphologies et d'améliorer l'adhésion à l'interface à l'état solide. Dans la littérature, on trouve essentiellement des exemples de mélanges présentant de faibles taux de compatibilisation. Une vision récemment développée est de synthétiser

---

des mélanges de polymères entièrement nanostructurés par extrusion réactive [27, 45].

Afin de mieux comprendre les propriétés de la couche de copolymères formée à l'interface, une étude sur les caractéristiques thermodynamiques des copolymères blocs a été menée [48]. Il apparaît que lorsque des copolymères greffés sont formés à l'interface, ce qui est notre cas, l'étude de ces copolymères peut être menée en considérant une unité constitutive du copolymère greffé: 2 blocs de la chaîne constituant le squelette et un bras des greffons, appelé copolymère Y [55] (cf. figure 1.21). Un critère de symétrie qui définit l'architecture favorisant une interface plane est proposée [57] (cf. equation 1.17).

Les paramètres contrôlant la cinétique de réaction chimique à l'interface ont été résumés. Il s'agit principalement de la réactivité intrinsèque des fonctions réactives, de leur concentration, de la longueur des homopolymères (masses molaire  $Mn$ ) sur lesquelles elles sont attachées, du cisaillement... Il apparaît qu'une fois la brosse de copolymères créée à l'interface, celle-ci peut créer une barrière énergétique empêchant la réaction de progresser. Sous certaines conditions, cette barrière énergétique peut-être franchie grâce à la formation spontanée de rugosités d'interface.

Une étude récente effectuée dans notre laboratoire a montré que, en plus de la morphologie micrométrique développée par les mécanismes de rupture de goutte et coalescence, un second mécanisme dû à la réaction chimique de compatibilisation à l'interface, pouvait conduire à la formation de nano-dispersions. Ces nano-dispersions peuvent être très nombreuses et observées dans les deux phases. Dans de nombreux cas de la littérature, les nanodispersions sont bien présentes, mais ne sont pas prises en compte dans les discussions.

Quelques études ont observé que les rugosités interfaciales, mentionnées précédemment, ou même le départ spontané de micelles depuis l'interface, pouvaient se produire en conditions de recuit statique [90, 78, 79]. Des études de simulation numérique ont aussi montré la formation de structure types de copolymères à l'interface [87]. Sous cisaillement, certaines études montrent la formation de nanodispersions (quelques dizaines de nanomètres), en plus de morphologies plus grossières (quelque micromètres) [93, 27, 111]. Cependant, aucune études systématique n'a été effectuée pour faire le lien avec les morphologies observées dans les mélanges compatibilisés par voie réactive. De plus les mécanismes conduisant à la déstabilisation de l'interface ne sont pas encore bien compris. A notre connaissance, aucune équipe de recherche universitaire n'a déjà essayé de contrôler la formation de ces nano-dispersions.

Cette revue de la littérature conduit à la conclusion que, même si des mécanismes de formation de ces nano-dispersions ont déjà été proposés dans quelques études, il n'y a toujours pas consensus sur ce point.

## **Chapitre 2: Matériaux et techniques expérimentales (page 57)**

Nous avons étudié des mélanges binaires de polyamides 6 (PA6) et de polyéthylène haute densité non réactif (PEHD) ou greffé anhydride maléique (PEHD-g-AM). Les mélanges ont été préparés par extrusion réactive (microcompounder) à 290 °C. Lors de la compatibilisation réactive, les extrémités de chaînes PA6 réagissent avec les fonctions anhydride maléique pour former un copolymère greffé sur la chaîne PEHD à l'interface (cf. fig. 44).

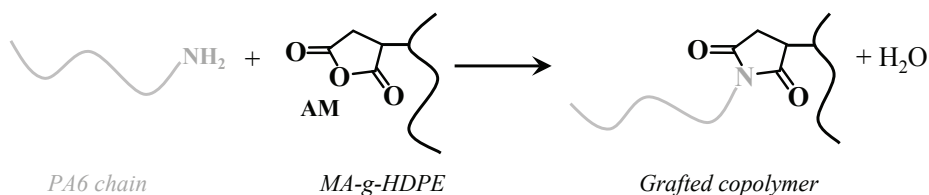


Figure 44: Compatibilization reaction

Nous avons formulé des mélanges en variant stratégiquement les paramètres de formulation: en changeant seulement la masse molaire du PA6 linéaire dans les mélanges binaires, le ratio de viscosité ainsi que l'architecture du copolymère créé à l'interface sont modifiés. Ainsi:

- Trois polyamide 6 (PA6) de longueur de chaîne contrôlées (différentes masses molaires) ont été synthétisés: PA6-3k, PA6-18k et PA6-31k avec respectivement:  $M_n \approx 3000$  g/mol, 18000 g/mol et 31000 g/mol.
- Deux polyoléfines commerciales ont été utilisées: un polyéthylène haute densité greffé anhydride maléique (MA-g-HDPE), pour les mélanges binaires compatibilisés et un PEHD, pour les binaires mélanges non-compatibilisés, choisi de telle sorte que sa viscosité soit proche de celle du MA-g-HDPE (à 290 °C et à 100 rad/s).

Toutes les compositions mentionnées dans ce travail sont des compositions en fraction volumique à l'état fondu, c'est à dire, calculées avec la densité des polymères purs à 290 °C. De plus, le ratio de viscosité a été calculé à partir de la viscosité des composants purs du mélange à 100 rad/s et 290 °C afin d'être le plus représentatif possible des conditions de procédé et de mise en forme.

L'observation des mélanges par microscopie électronique à balayage (SEM), après dissolution sélective de la phase minoritaire ou bien après cryofracture, a permis d'observer les morphologies de tous les mélanges. Les mélanges compatibilisés ont aussi été caractérisés par microscopie électronique en transmission (TEM) après optimisation des conditions de marquage. Une attention particulière a été portée à l'observation des nanodispersions. Les mesures rhéologiques sur les matériaux purs et mélanges ont été faites en rhéométrie dynamique à 290 °C.

La température de mise en œuvre étant élevée (290 °C), notamment pour les PEHDs; et le PA6 étant sensible à la reprise en eau, une étude a été menée pour étudier la stabilité des polymères utilisés durant le procédé de préparation et pendant les expériences de rhéologie dynamique. L'étude a montré que les masses molaires moyenne des PE pouvaient évoluer pendant l'extrusion, cependant les deux PE restent stables pendant les mesures de rhéologie. Les PA6 par contre n'évoluent pas de manière significative pendant le procédé, mais beaucoup plus pendant les mesures de rhéologie. Ceci est du au déséquilibre de l'équilibre de post-condensation, induit par le séchage continu du flux d'azote dans le four du rhéomètre, et le contact du PA6 à la pression atmosphérique.

Le comportement viscoélastique linéaire des composants purs des mélanges sont finalement présentés. En raison de sa sensibilité à l'humidité, une attention particulière a été portée au comportement rhéologique des polyamide 6. Les résultats des mesures

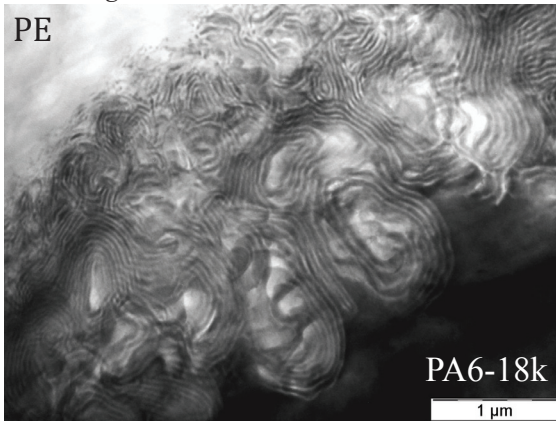
dépendent fortement de la quantité d'humidité initiale. Ainsi, malgré l'épaulement observé pour le PA6-18k et 3k aux basses fréquences, nous avons décidé de réaliser nos mesures rhéologiques sur des PA6 séchés au taux d'eau à l'équilibre à 290 °C. En ce qui concerne les polyoléfines, nous avons remarqué un épaulement aux basses fréquences sur de module élastique  $G'$  à la fois pour le HDPE et le MA-g-HDPE. *Dans les mélanges, tout plateau observé aux basses fréquences, doit donc être interprété avec beaucoup d'attention.*

### Chapitre 3: Réaction de compatibilisation en conditions statiques (page 85)

Dans la troisième partie, nous nous sommes focalisés sur les mécanismes liés à la réaction chimique à l'interface. Pour cela, nous avons réalisé des sandwichs de films de PA6 de longueurs variables et de PEHD-g-AM, que nous avons fondus pendant des durées variables (10, 10+15 et 10+60 minutes) pour initier la réaction chimique, en conditions statiques. Pour cette étude un quatrième polyamide 6 (PA6-10k,  $M_n \approx 10000$ g/mol) a été utilisé. Les interfaces obtenues ont été observées par microscopie électronique.

Après seulement 10 minutes de recuit, nous observons des domaines de structures de copolymères à l'équilibre formés à l'interface. Ces structures sont observées aux interfaces pour les systèmes avec les chaînes de PA6 de plus hautes masses molaires (PA6-10k, 18k et 31k) (cf. fig. 45), tandis qu'aucune morphologie particulière ne s'est formée aux interfaces avec des chaînes plus courtes (PA6-3k).

Sandwich **PA6-18k** and MA-g-HDPE  
Annealing 10+15min



Sandwich **PA6-31k** and MA-g-HDPE  
Annealing 10+15min

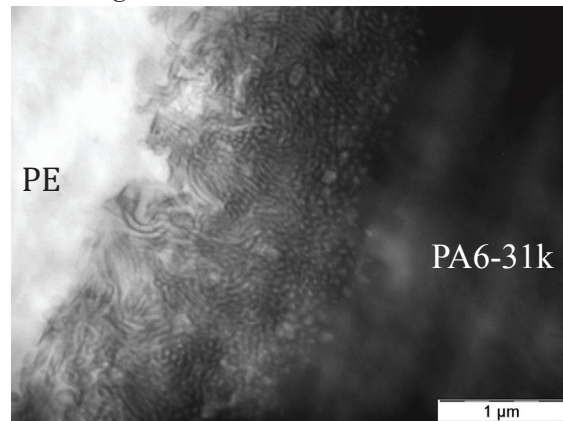


Figure 45: Morphologies obtenues après recuit static pendant 10+15 minutes pour des sandwichs avec le PA-18k (gauche) and PA6-31k (droite). La phase sombre est le PA6 marqué.

L'initiation de la déstabilisation interfaciale, ainsi que les morphologies des microstructures obtenues ont été discutées. Il apparaît que le paramètre le plus critique est l'architecture des copolymères créés à l'interface. Nous proposons le mécanisme suivant: les homopolymères réactifs réagissent rapidement pour former des copolymères à l'interface plane, il se forme une brosse de copolymères à l'interface. La diminution de la tension interfaciale est directement liée à l'étirage des blocs. Quand la densité de la brosse atteint des valeurs au moins égales à la valeur d'équilibre, la tension interfaciale

devient nulle ou négative et des fluctuations d'interface apparaissent. L'air interfaciale formée permet alors à de nouvelles fonctions réactives de venir réagir à l'interface. On observe alors la croissance de microstructures à partir de l'interface.

L'architecture des copolymères créés par les systèmes avec du PA6-10k, 18k et 31k sont proches de l'architecture symétrique qui favorise une courbure spontanée de l'interface nulle. Ainsi, à une interface plane, une couche dense de copolymères peut être formée pour initier les fluctuations interfaciales. En revanche, l'architecture des copolymères formés dans le système avec le PA6-3k, favorise une très forte courbure du côté des blocs de PA6 (micelles de PA). Ainsi, à une interface plane, une brosse dense de copolymères ne peut pas être formée des deux côtés de l'interface et ne peut donc pas engendrer de déstabilisation de l'interface. L'énergie libre de la brosse de copolymères formée avec le PA6-3k a été étudiée. Il a été montré que seule une interface très incurvée vers les chaînes de PA6 (de quelques dizaines de nm) pourrait conduire à la formation d'une brosse dense de copolymères dans ce cas. En conséquence, il ne se développe pas de morphologies spécifique de copolymères en conditions statique.

L'architecture du copolymère créé à l'interface affecte également les microstructures formées à la suite de la déstabilisation de l'interface. Pour les systèmes avec 10k, 18k et 31k, des morphologies globalement symétriques ont été observés (lamelles, cylindres...). Les structures observées sont similaires aux figures de myéline observées par exemple dans les surfactants mis en présence d'eau [131]. Les densités des copolymères à l'interface (couverture) ont été estimées à partir de la longue période des structures formées. Elles sont en accord avec la densité de copolymères blocs purs. Les morphologies observées sont qualitativement en accord avec les prédictions de Milner [57] et en remarquable accord avec les prédictions de Berezkin et al. obtenu par simulations "Dissipative Particle Dynamics" (DPD) [87, 100].

Pour la première fois dans des systèmes PA/PE, la nucléation et la croissance de structures ordonnées à l'interface en conditions statiques ont été observées. Cette observation confirme que des structures sub-micrométriques peuvent se former sous l'effet de la réaction chimique pendant la préparation des mélanges de polymères réactifs en extrusion, en plus des mécanismes de nature rhéologique (instabilités de Taylor et de Rayleigh).

## Chapitre 4: Morphologies (page 109)

Le développement des morphologies dans les mélanges non-compatibilisés et compatibilisés ont ensuite été étudiés. Une étude systématique a été menée en variant la composition des mélanges sur toute la gamme de compositions accessible.

Dans les mélanges non-compatibilisés PA6/HDPE, des morphologies typiques (dispersions de PE dans PA ou PA dans PE et morphologies co-continues) de l'ordre du micromètre ont été observées. La figure 4.3 page 114 résume ces morphologies. La composition à l'inversion de phase a été observée à des compositions différentes selon le ratio de viscosité ( $R_v$ ): près de 50/50 % vol lorsque  $R_v \approx 1$  et décalés aux plus faibles fractions volumiques de la phase la plus fluide lorsque  $R_v \neq 1$ .

Différents mécanismes de rupture de gouttes basés sur les phénomènes d'instabilités capillaires peuvent expliquer les morphologies obtenues selon le ratio de viscosité (résumés schématiquement figure 4.52 ainsi que pour la coalescence figure 4.53):

- Lorsque  $R_v \approx 1$ , le mécanisme de Rayleigh conduit effectivement à la rupture en de plus petites gouttelettes de tailles et de dispersion homogènes.
- Lorsque  $R_v < 1$ , le mécanisme de "end-pinching" avec la formation de satellites entre les gouttelettes est très pertinent pour décrire les morphologies observées. Ce mécanisme conduit à la formation de morphologies avec des tailles très hétérogènes. En effet, des nodules avec une distribution de tailles bimodale (des nodules de  $\approx 100-200\text{nm}$  et des nodules de l'ordre du micromètre) ont été observés. Cela s'explique par le fait que l'onde capillaire à la surface du filament se développe très rapidement sur un filament moins visqueux que la matrice qui l'entoure.
- Le cas  $R_v > 1$  a été étudié dans une très large gamme ( $R_v=1.7, 13$  and  $300$ ). La rupture de goutte a été observée même dans le cas où  $R_v > 4$ , ce qui n'est théoriquement pas possible sous simple cisaillement. Il semble donc que des flux elongationnels étaient présents lors du mélange en extrusion. Ceci combiné à la nature viscoélastique des phases pouvant modifier la valeur critique  $R_v \approx 4$ .

Pour le cas où le ratio de viscosité n'était pas trop éloigné de 1 ( $R_v=13$ ), la formation des instabilités capillaires est probablement retardée car le filament est plus visqueux que la matrice. Cela conduit à des morphologies proches de celles observées quand  $R_v = 1$  mais avec des tailles plus grossières et hétérogènes.

Lorsque le ratio de viscosité était largement supérieur à 1 ( $R_v=300$ ), de très larges gouttes (quelques dizaines de microns de diamètre) séparées parfois par de très fins films de matrice (quelques centaines de nanomètres d'épaisseur) ont été observées. Cet exemple a permis d'illustrer le régime de drainage très défavorable rencontré lorsque des gouttelettes très visqueuses sont dispersées dans une matrice très fluide (cf. sous-section 2.2 page 119).

Dans les mélanges PA6/MA-g-HDPE compatibilisés, les compositions à l'inversion de phase ont été inchangées par rapport aux mélanges non-compatibilisés. La figure 4.19 page 4.19 résume ces morphologies. Cela signifie que les mécanismes rhéologiques de rupture de gouttes et coalescence contrôlent, dans tous les cas, le type de morphologies (i.e. dispersion de PA dans PE ou PE dans PA). En outre, comme attendu, les tailles ont été considérablement réduites et la coalescence a été inhibée. Cependant, nous observons des nanodispersions, qui ne se forment pas de manière équivalente de chaque côté de l'interface:

- Dans les mélanges avec le PA6-18k, des nanodispersions de PE dans PA et PA dans PE ont été observées à toutes les compositions et surtout pour les compositions proches de l'inversion de phase (cf. figure 4.27).
- Pour les mélanges avec du PA6-31K, des nanodispersions de PE ont été principalement observées dans la phase PA6-31k, à la fois lorsque le PA constituait la phase matrice ou la phase dispersée (cf. figure 4.33).
- Des nanodispersions de PA6-3k n'ont été observées que lorsque le PA était en phase dispersée dans les mélanges PA6-3k/MA-g-HDPE (cf. figure 4.38).

Une comparaison détaillée des mélanges compatibilisés et des compositions correspondantes de mélanges non compatibilisés, ainsi que des morphologies obtenues en conditions statiques a été effectuée. Une des principales observations a été de constater que les morphologies créées en conditions statiques (structure lamellaire ou cylindrique), n'ont pas été créées dans les mélanges compatibilisés, même si les mêmes précurseurs ont

été utilisés. Ceci a été expliqué par le fait que, sous cisaillement, l'interface n'est pas dans des conditions d'équilibre, contrairement au cas statique. Ainsi, les premières fluctuations d'interface qui, en conditions statiques, ont initié la croissance de microstructures ordonnées, sont arrachées à l'aide du cisaillement. Une représentation schématique est donnée figure 4.44 page 166.

Nous avons identifié que deux paramètres principaux semblaient contrôler la création de nanodispersions: (1) Tout d'abord, l'architecture du copolymère qui contrôle non seulement la déstabilisation de l'interface, mais peut aussi favoriser une courbure de l'interface pour la création des nanodispersions. (2) En second lieu, le ratio de viscosité, en effet, les nanodispersions sont arrachées favorablement dans la phase plus visqueuse. Si  $R_v=1$ , elles peuvent être arrachées de manière équivalente de chaque côté de l'interface.

En conclusion, nous avons montré à travers l'étude de la réaction de compatibilisation en conditions statiques et des morphologies des mélanges non compatibilisés et compatibilisés sous cisaillement, que la morphologie d'un mélange peut être qualitativement prédite si les paramètres suivants sont connus:

- La réactivité intrinsèque des fonctions réactives pour la compatibilisation.
- Le ratio de viscosité à la température et au cisaillement représentatifs des conditions procédé.
- Les paramètres moléculaires des composants du mélange ( $M_n$ , architecture du copolymère formé...)
- La composition
- Le cisaillement et éventuellement les flux elongationnels présents dans le procédé de mélangeage.

## Chapitre 5: Comportement rhéologique dans le domaine linéaire (page 181)

Dans cette dernière partie, nous avons étudié les propriétés rhéologiques des mélanges finaux. Nous discutons les mécanismes de relaxation observés, en particulier ceux liés aux interfaces et aux interactions entre nodules, en lien avec les morphologies des mélanges.

Avant l'analyse des données expérimentales, un rappel des modèles disponibles dans la littérature pour décrire le comportement rhéologique des mélanges de polymères est donné. Pour décrire le comportement en fréquence, il existe le modèle de Palierne qui décrit quantitativement et qualitativement les différents phénomènes de relaxation observés dans les mélanges de polymères: les phénomènes de relaxations de forme observés aux basses fréquences ainsi que, dans le cas des mélanges compatibilisés, des phénomènes de relaxations interfaciales associés à la présence d'une brosse de copolymères à l'interface (cf. eq 5.7 et pour la version simplifiée eq. 5.10). Pour décrire l'évolution de la viscosité des mélanges en fonction de la composition, Janssen et al. [10, 7] ont proposé un modèle basé sur le modèle de Krieger Dougherty (KD) valable sur une large gamme de composition[154]. Une analyse de ces modèles a permis d'affiner leurs domaines de validités. Ainsi, nous discutons le fait que le modèle de Palierne ne décrit pas l'augmentation de viscosité de mélanges concentrés en fonction de la composition, et donc ne semble être valide que pour des mélanges peu concentrés. Nous montrons aussi que le modèle proposé par Janssen et al. semble prendre en compte la relaxation de

---

forme des gouttelettes et donc serait valide aux basses fréquences. Nous affinons le modèle et proposons une expression de ce modèle ne prenant pas en compte les relaxations de forme et donc valide aux hautes fréquences.

Les comportements viscoélastiques linéaires de nos mélanges non-compatibilisés et compatibilisés ont été étudiés. Ils dépendent fortement de la fréquence et de la composition, mais aussi du ratio de viscosité entre les phases.

### Mélanges non-compatibilisés:

**Pour les mélanges avec  $R_v \leq 1$ ,** lorsque  $\phi_d < 30\%$  vol, le comportement rhéologique des mélanges en fonction de la fréquence montrait un comportement typique de mélanges pour lesquels des relaxations de forme de gouttelettes sont observées (cf. fig 5.18 (a, b and f), fig 5.23 (a and b) and fig 5.16 (g)). Le modèle de Palierne simplifié a permis de décrire de manière très satisfaisante ce comportement. Pour des mélanges plus concentrés, le modèle de Palierne n'était plus adapté pour décrire le comportement ce qui implique l'existence d'autres phénomènes de relaxations, dues par exemple à des interactions entre nodules, se passent (cf. fig 5.18 (c, d and e) and fig 5.23 (c and d)). En effet, les modules, et notamment  $G'$  sont augmentés aux basses fréquences.

L'augmentation de la viscosité pour les mélanges plus concentrés était bien prédite par le modèle de KD modifié. Nous avons noté deux observations intéressantes:

- Pour des compositions montrant des morphologies nodulaires très proches de la composition à l'inversion de phase, un comportement type gel a été observé dans le cas des systèmes avec le PA6-18k ( $R_v \approx 1$ ). Nous avons attribué ce comportement gel à des phénomènes de relaxations coopératives des nodules très proches les uns des autres, créant ainsi un réseau à longue distance.
- De plus pour des mélanges dont la morphologie était partiellement co-continue (mélanges avec le PA6-31k), nous avons observé une chute des modules et de la viscosité aux basses fréquences. Ce phénomène avait également été observée par Castro et al. [30].

**Pour les mélanges avec  $R_v > 1$ ,** les modules et viscosités expérimentaux sont plus élevés que ceux attendus dans les modèles (cf. fig 5.23 (e and f) and fig 5.16 (a to e)). Une hypothèse a été émise pour expliquer cette augmentation des modules et de la viscosité consécutive à l'ajout de nodules de viscosité élevée dans une matrice plus fluide: elle pourrait être due à des régimes de drainage défavorables en accord avec la morphologie observée au chapitre 4 (cf. résumé chapitre 4 à la page 271).

### Mélanges compatibilisés:

Pour les mélanges compatibilisés, même à de faibles concentrations en phase dispersée, une augmentation importante des modules dynamiques, et en particulier du module de stockage  $G'$ , ont été observées dans les basses fréquences (cf. fig. 5.27, 5.29 and 5.31). Cet accroissement augmente avec  $\phi_d$ :

- Lorsque la matrice est du PA6, les modules augmentent jusqu'à montrer un comportement type gel ( $G' \propto G'' \propto \omega^n$ ) pour les mélanges les plus concentrés.
- Lorsque la matrice est du MA-g-HDPE, un comportement type gel ou même solide ( $G' > G''$ ) a été observé.

Dans tous les cas le modèle de Paliere ne décrit pas ce comportement. Cela suggère donc la présence de fortes interactions entre les gouttelettes voisines qui créent un réseau de percolation.

La nature des interactions a été discutée. Pour des mélanges ayant du PA6-18k ou PA6-31k comme matrice, la création d'un réseau de percolation viscoélastique créé par l'enchevêtrement des greffons de PA6 en surface des nodules de PE très proches a été proposée. Pour tous les mélanges avec MA-g-HDPE comme matrice, des enchevêtrements simples, des enchevêtrements piégés ou même du pontage direct des chaînes de PEHD greffées entre gouttelettes voisines de PA, pourraient expliquer les comportements type gel ou même solide. Pour les mélanges avec le PA6-3k comme matrice, la nature des interactions est encore en discussion. Les interactions sont ainsi fortement corrélées aux distances entre les gouttelettes et donc à la morphologie.

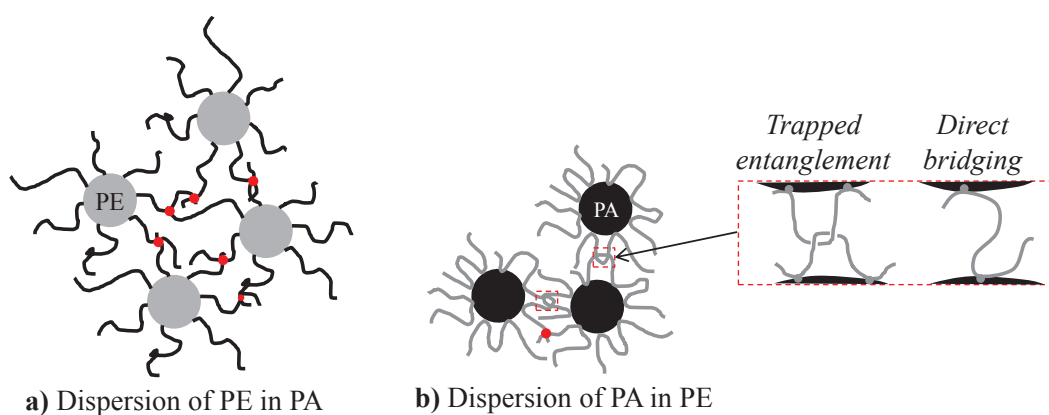


Figure 46: Schematic representation of (a) the viscoelastic percolating network created by the entanglement of linear PA6 block copolymer chains grafted on the outside of droplets in reactively compatibilized blends and (b) the percolating network created by entanglement of the grafted HDPE chains and/or trapped entanglements or direct bridging that can be created during blend rheological development.

Nous avons ainsi vu que des indications sur la morphologie des mélanges pouvaient être directement déduites des mesures de rhéologies dans le domaine linéaire.

Ainsi, sur la base des mesures rhéologiques, des informations quantitatives sur la morphologie peuvent être extraites pour les mélanges  $\phi_d < 30\%$  vol et  $R_v \leq 1$  dans les mélanges non-compatibilisés grâce aux fits du modèle de Paliere. Pour les mélanges plus concentrés, les modèles ne prédisent plus le comportement. En conséquence, seules des informations qualitatives peuvent éventuellement être déduites, par exemple le comportement gel traduisant la proximité au domaine de co-continuité.

Pour les mélanges compatibilisés, la forte augmentation des modules aux basses fréquences est une indication de l'interaction des gouttelettes entre elles et donc que la faible distance entre les nodules qui peut être attendue. Plus la pente des modules est faible, plus le nombre de «contacts» par les interactions entre les nodules est grand.

Inversement, grâce à cette étude, les comportements rhéologiques des mélanges peuvent être déduits de manière qualitative de la morphologie.

Dans la dernière section de ce chapitre, nous proposons un modèle de prédiction de la composition à l'inversion de phase. Ce modèle est basé sur le modèle modifié de

---

Krieger et Dougherty proposé par Janssen et al. [10] (cf. section 5 page 233). Nous avons montré que ce modèle était particulièrement adapté pour prédire la composition à l'inversion de phase pour toutes les séries de mélanges étudiés dans ce travail, et notamment pour les mélanges fortement compatibilisés avec un ratio de viscosité très différent de 1. L'utilisation de ce modèle nécessite de connaître la viscosité des composants purs à la fréquence représentative des conditions de procédé (dans notre cas 100 rad/s) et d'utiliser les fractions volumiques en phases fondues.

## Conclusion

Au vue de ces résultats, nous proposons une vision plus complète des paramètres permettant de contrôler la formation des morphologies multi-échelle dans les mélanges de polymères compatibilisés par voie réactive et en particulier de la formation des nanodispersions. De plus, cette étude apporte de nouveaux éléments sur le comportement rhéologique des mélanges compatibilisés par voie réactive. L'intérêt de l'étude est d'avoir étudié des mélanges avec des rapports de viscosité proches et très différents de un et sur toute la gamme de composition (i.e. avec une concentration en phase dispersée grande).

Ainsi les relations entre la formulation, les morphologies et les propriétés rhéologiques des mélanges compatibilisés par voie réactive ont été établis. Cette connaissance pourra aider à contrôler les morphologies de mélanges afin de répondre à des compromis de propriétés visés pour l'application (processabilité, perméabilité, propriétés mécaniques...).





---

## Résumé: Développement des morphologies et comportement rhéologique des mélanges Polyamide 6 / Polyéthylène Haute Densité compatibilisés par voie réactive

---

L'enjeu de ce travail est de comprendre les paramètres contrôlant les mécanismes de développement des morphologies et notamment la formation des nanodispersions pour des mélanges binaires de polyamides 6 de différentes masses molaires et de polyéthylène haute densité greffé anhydride maléique, mis en œuvre par extrusion réactive. Le choix stratégique des matériaux a permis de balayer une large gamme de rapports de viscosité ainsi que différentes architectures de copolymères formés à l'interface.

Les mécanismes de nature rhéologique ont été isolés méthodiquement des mécanismes dus à la réaction à l'interface en étudiant, d'une part, des mélanges non compatibilisés PA6/PEHD, puis l'effet de la réaction de compatibilisation seule en condition statique. Différents mécanismes de rupture de gouttes basés sur des instabilités capillaires sont proposés selon le rapport de viscosité. L'observation de microstructures ordonnées de copolymères aux interfaces en condition statique démontre la déstabilisation de l'interface fortement relié à la symétrie des copolymères formés.

Les propriétés rhéologiques des mélanges sont étudiées ensuite. Les mécanismes de relaxation observés sont discutés, en particulier ceux liés aux interfaces et aux interactions entre nodules, en lien avec les morphologies des mélanges. Dans les mélanges compatibilisés, le comportement type gel ou solide-élastique (forte augmentation de l'élasticité aux basses fréquences), pour les mélanges concentrés, suggère la création d'un réseau percolant d'interactions entre nodules voisins. Enfin, un modèle performant de prédiction de la composition à l'inversion de phase à partir du comportement rhéologique est proposé.

**Mots clés:** Polyamide – Polyéthylène – Mélanges de polymères – Compatibilisation réactive – Morphologie – Rhéologie – Interface – Copolymère

---

## Abstract: Morphology Development and Rheological Properties of Reactively Compatibilized Polyamide 6 / High Density Polyethylene Blends

---

The aim of this work is to understand the parameters that control the morphology development mechanisms, and especially, the formation of nanodispersions. This study deals with binary blends of polyamide 6 of different molecular weights and maleic anhydride grafted high density polyethylene, processed by reactive extrusion. The strategic choice of blend components allowed to cover a wide range of viscosity ratio and various copolymer architectures formed at the interface.

Mechanisms controlled by classical rheological laws were methodically isolated from mechanisms specific to the compatibilization reaction at the interface by studying, on the one hand, uncompatibilized PA6/HDPE blends, and on the other hand, the effect of the compatibilization reaction in static condition. Different drop break-up mechanisms based on capillary instabilities are proposed depending on viscosity ratios. The observation of ordered microphase separated copolymer domains at the interfaces in static condition attests of the spontaneous interface destabilization, strongly related to the copolymer asymmetry.

Blends rheological properties are then studied. The different relaxation mechanisms obtained are discussed, especially those related to the interfaces and interactions between droplets, relatively to blends morphologies. In compatibilized blends, gel-like or solid-elastic behavior (strong elasticity increase at low frequencies) for concentrated blends, suggest the creation of a percolating network of interactions between neighboring droplets. Finally, an efficient model for predicting the phase inversion composition from the rheological behavior is proposed.

**Keywords:** Polyamide – Polyethylene – Polymer blend – Reactive compatibilization – Morphology – Rheology – Interface – Copolymer